



Seismic and Electrical Properties of Unconsolidated Sediments

Saowapa Suksawat

**A Thesis Submitted in Partial Fulfillment of the Requirements for the Degree of
Master of Science in Geophysics
Prince of Songkla University
2015**

Copyright of Prince of Songkla University

Thesis Title Seismic and electrical properties of unconsolidated
sediments
Author Miss Saowapa Suksawat
Major Program Geophysics

Major Advisor

.....
(Dr. Helmut Dürrast)

Examining Committee

.....Chairperson
(Dr. Decho Phueakphum)

.....Committee
(Dr. Chutharmard Kaewmano)

.....Committee
(Dr. Helmut Dürrast)

The Graduate School, Prince of Songkla University, has approved this thesis as partial fulfillment of the requirements for the Master of Science Degree in Geophysics.

.....
(Assoc. Prof. Dr. Teerapol Srichana)
Dean of Graduate School

This is to certify that the work here submitted is the result of the candidate's own investigations. Due acknowledgement has been made of any assistance received.

.....Signature
(Dr. Helmut Dürrast)
Major Advisor

.....Signature
(Saowapa Suksawat)
Candidate

I hereby certify that this work has not been accepted in substance for any degree, and is not being currently submitted in candidature for any degree.

..... Signature
(Saowapa Suksawat)
Candidate

ชื่อวิทยานิพนธ์	คุณสมบัติคลื่นไหวสะเทือนและไฟฟ้าของตะกอนร่วน
ผู้เขียน	นางสาวเสาวภา สุขสวัสดิ์
สาขาวิชา	ธรณีฟิสิกส์
ปีการศึกษา	2557

บทคัดย่อ

ชั้นผิวดินระดับตื้นมีความลึกประมาณ 100 เมตร ประกอบด้วยตะกอนร่วนเป็นองค์ประกอบสำคัญ วัสดุที่มีรูพรุน เช่น กรวด ทราย ทรายแป้ง ดินเหนียว และเศษหิน เป็นแหล่งกำเนิดดินถล่ม และแหล่งดินที่สำคัญสำหรับการเกษตร สำหรับการศึกษาครั้งนี้เก็บตัวอย่างดินตะกอนร่วนด้วยวิธีถูกรบกววน เก็บตัวอย่างจากชั้นหินฐานถึงชั้นผิวดิน บริเวณเทือกเขาคอหงส์ อำเภอหาดใหญ่ จังหวัดสงขลา จำนวนสองสถานที่ที่ลักษณะชั้นหินฐานต่างกัน คือ หินทรายและหินแกรนิต ตรวจสอบคุณสมบัติของตัวอย่าง เช่น องค์ประกอบหลักโดยเครื่องวิเคราะห์การเลี้ยวเบนรังสีเอกซ์ การกระจายตัวของขนาดตะกอนโดยวิธีร่อนผ่านตะแกรงสำหรับขนาดทรายและกรวด และวิธีตกตะกอนโดยใช้ไฮโดรมิเตอร์สำหรับขนาดทรายแป้งและดินเหนียว ความหนาแน่นของแร่ ความหนาแน่นรวม ความพรุน โครงสร้างโดยกล้องจุลทรรศน์อิเล็กตรอนแบบส่องกราดค่าสัมประสิทธิ์การซึมได้ สภาพต้านทานไฟฟ้าและความเร็ว สภาพต้านทานไฟฟ้าและความเร็วคลื่นพีและคลื่นเอสพิจารณาภายใต้เงื่อนไขการทดลองโดยการเพิ่มความอิ่มตัวของน้ำ (0-100%) ของตัวอย่าง โดยทั่วไปค่าสภาพต้านทานไฟฟ้าจะแปรผกผันกับความอิ่มตัวของน้ำ การคำนวณและการจำลองค่าสภาพต้านทานไฟฟ้าของตะกอนดินเหนียวอาศัยสมการ Archie ที่มีการปรับปรุงโดย Sen และคณะ (2531) สำหรับการวัดค่าอัตราความเร็วมีการลดลงของตัวอย่างตะกอนพบว่าคลื่นพีและคลื่นเอสมีแล้ว โนมลดลงเมื่อมีความอิ่มตัวของน้ำเพิ่มขึ้นสามารถอธิบายได้ด้วยผลกระทบของ Biot-Gassmann การเพิ่มขึ้นของความหนาแน่นเนื่องจากน้ำแทนที่อากาศในช่องว่างส่งผลกระทบมากกว่าการเพิ่มขึ้นของค่าบัลก์มอดูลัส การสร้างแบบจำลองของความเร็วคลื่นไหวสะเทือนได้รับอิทธิพลจากความเค้นประสิทธิผลรวมมากกว่าความเค้นชั้นดินที่ปิดทับเพียงอย่างเดียว ผลที่ได้ค่อนข้างเหมาะสมกับข้อมูลในห้องปฏิบัติการ

Thesis Title Seismic and electrical properties of unconsolidated sediments
Author Miss Saowapa Suksawat
Major Program Geophysics
Academic Year 2014

ABSTRACT

The shallow subsurface, a few hundred meters in depth, comprises mainly of unconsolidated sediments, a porous material, with gravel, sand, silt, clay, and rock fragments, and it is the source for the region of landslide hazards, and the main resource in agriculture, soil. For this study disturbed samples of unconsolidated sediments from different layers from bedrock to the top soil layer were taken from two location of the Khao Khohong mountain range near Hat Yai District, Songkhla Province. The two sample sites comprise different bedrock lithologies, sandstone and granite. The dried samples were characterized as following: main composition (X-ray diffraction), grain size distribution (sieve analysis for sand and hydrometer method for clay and silt content), mineral density (water pycnometer), bulk density, porosity, as well as pore structure (scanning electron microscopy), hydraulic conductivity, electrical resistivity and seismic velocity. Electrical resistivity and P-wave (V_P) and S-wave velocities (V_S) under controlled conditions (pulse transmission ultrasonic technique) were determined under laboratory conditions with increasing water saturation (0–100%) of the sample. In general, the electrical resistivity decreases with increasing water content, it of clay bearing sediments is the combination of electrolytic (water) and colloidal (wet clay) conductivity. Therefore, we used the modified Archie equation proposed by Sen et al. (1988) to model the laboratory derived data. Result of velocity, the decrease of the P- and S-wave velocities with increasing water saturation can be explained by the Biot-Gassmann effect, as the increase in the bulk density due to water replacing air in the pores is larger than the increase in the effective bulk moduli of the overall granular material. Modeling of the seismic velocities used the total effective stress rather than the net overburden stress alone, resulting in a relatively good fit of the laboratory data.

ACKNOWLEDGEMENTS

This thesis could be finished because many people gave me their supervision, support, and advice. First of all, I would like to express my deep gratitude to my advisor, Dr. Helmut Dürrast. He supervised me closely since I started to plan this work until it was finished. He gave me knowledge and he understood my mistakes.

I would like to thanks the Graduate School, Prince of Songkla University (PSU) for a supporting research fund, also to the Department of Physics, Faculty of Science, Prince of Songkla University. I would like to thanks the Department of Mining and Materials Engineering, and the Department of Civil Engineering, Faculty of Engineering, Prince of Songkla University, the Department of Earth Science, Faculty of Natural Resources, Prince of Songkla University, the Scientific Equipment Center, Prince of Songkla University, and the School of Geotechnology, Institute of Engineering, Suranaree University of Technology and Henrike Schmidt, with DAAD RISE.

I would like to thanks many of my friends and students in both Geophysics Programs at Prince of Songkla University. Finally, my deepest thanks are going to my family who always stood beside me.

Saowapa Suksawat

CONTENT

	PAGES
ABSTRACT (IN THAI)	v
ABSTRACT (IN ENGLISH).....	vi
ACKNOWLEDGEMENTS	vii
CONTENT	viii
LIST OF TABLES	xi
LIST OF FIGURES	xiii
CHAPTER 1 INTRODUCTION	1
1.1 Introduction	1
1.2 Unconsolidated sediments	2
1.2.1 Unconsolidated sediment characteristics	3
1.2.1.1 Grain	3
1.2.1.2 Pores	4
1.2.2 Physical properties of unconsolidated sediments	5
1.2.2.1 Density and porosity	5
1.2.2.2 Saturation.....	7
1.2.2.3 Hydraulic conductivity	7
1.2.3 Electrical resistivity	8
1.2.3.1 Archie’s law and modified Archie’s law	9
1.2.3.2 Clay effect	11
1.2.4 Seismic velocities and elastic properties	12
1.2.4.1 Seismic velocities	12
1.2.4.2 Elastic properties	13
1.3 Objective.....	15
CHAPTER 2 METHODOLOGY	16
2.1 Study area	16
2.2 Sampling method.....	16
2.3 Density analysis.....	18
2.4 Porosity analysis.....	20
2.5 Grain size analysis.....	21
2.5.1 Sieve analysis	22
2.5.2 Hydrometer analysis	23

CONTENT (CONTINUED)

	PAGES
2.6 X-ray diffraction	28
2.7 Scanning electron microscopy	29
2.8 Hydraulic conductivity	31
2.9 Electrical resistivity	35
2.9.1 Electrical resistivity laboratory measurement	35
2.9.2 Electrical resistivity modeling	37
2.10 Ultrasonic velocities method	41
2.11 Elastic parameters.....	44
CHAPTER 3 RESULTS.....	47
3.1 Study area	47
3.2 Outcrops	49
3.3 Sample description	51
3.4 Density and Porosity.....	58
3.5 Grain size distribution	60
3.5.1 Grain size distribution	60
3.5.2 Texture.....	63
3.6 Composition	65
3.7 Microstructure	67
3.8 Hydraulic conductivity	72
3.9 Electrical resistivity and water saturation.....	73
3.10 Velocity and water saturation	78
3.11 Elastic analysis	82
CHAPTER 4 DISCUSSION AND CONCLUSION.....	87
4.1 Physical properties of sediments	87
4.2 Parameters in resistivity modeling	90
4.3 Parameters in velocity modeling	93
4.3.1 Total and effective stress	94
4.4 Applicability of work	101
REFERENCES.....	102

CONTENT (CONTINUED)

	PAGES
APPENDICES	110
APPENDICES A OBSERVED AND CALCULATED DATA.....	111
APPENDICES B XRD GRAPH OF SAMPLES	130
APPENDICES C SEM OF SAMPLES	150
APPENDICES D DATA FOR CALCULATION OF VELOCITY	165
 PUBLICATION	 168
 VITAE.....	 182

LIST OF TABLES

TABLE	PAGES
1.1 Comparison of some often used pore size classification schemes exhibiting variations in the ranges depending on the authors (Siegesmund and Dürrast, 2011)	5
1.2 Mineral density from Baker Atlas (1985) and Schlumberger (2000).....	5
1.3 Range in values of porosity of unconsolidated sediments (Morris and Johnson, 1967).....	6
2.1 Sieve analysis determination of sample (KB_5_2)	23
2.2 Hydrometer analysis of sample (KH_3_2).....	26
2.3 Joint Committee for Powder Diffraction Standards (JCPDS) of KB_5_2.....	29
3.1 Sediment samples from granite site.....	53
3.2 Description of sediment samples from granite site	54
3.3 Sediment samples from sandstone site	55
3.4 Description of sediment samples from sandstone site.....	57
3.5 XRD results of unconsolidated sediment samples	65
3.6 Comparison between seismic velocities and sediment characteristics at different levels of water saturation, here sample KB_7_2	81
3.7 Comparison between seismic velocities and sediment characteristics at different levels of water saturation, here sample KH_2_2	82
4.1 Composition of samples from the granite site	87
4.2 Composition of samples from the sandstone site	88
4.3 Physical and theoretical properties and model parameters of sands and clays for seismic velocity calculations	98
A.1 Density and porosity	111
A.2 Grain size distribution	112
A.3 Soil texture.....	113
A.4 Hydraulic conductivity	114
A.5 Resistivity from measurement	117
A.6 Velocity from measurement	123
A.7 Elastic moduli.....	127

LIST OF TABLES (CONTINUED)

TABLE	PAGES
D.1. Physical and theoretical properties and model parameters of sands and clays for seismic velocity calculations, sand at 10 cm and clay at 1 m depth to emphasize the contribution of interparticle stresss (Crane, 2013).....	167

LIST OF FIGURES

FIGURES	PAGES
1.1 Structure of shallow subsurface with different horizons and different terminology related to agriculture, geology, and civil engineering.....	2
1.2 Schematic figure of grains and pores of sediments (USGS, 2013)	3
1.3 Mean range of density for sedimentary rocks (Schön, 2011).....	6
1.4 Definition of porosity (Schön, 2011), V =volume; Φ =porosity	6
1.5 Porosity of granular materials (Modified from Davis and De Wiest, 1966).....	7
1.6 Range of hydraulic conductivity values for geological materials (modified from Driscoll, 1986, and Todd, 1980)	8
1.7 Clay classified by mode of distribution after Schlumberger, 1987 see IHRD, 2014	8
1.8 Electric double layers (Substect, 2013)	11
2.1 Study locations in Khao Khohong mountain range in Hat Yai District, Songkhla Province (modified from Sheet 5123III, Series L7018, Chngwat Songkhla, Royal Thai Survey Department, 1997)	17
2.2 Sample of unconsolidated sediments from Khao Khohong Mountain. Bedrock is a sand/siltstone, red point is sample	17
2.3 Samples of unconsolidated sediments collected by tool in-situ and samples were put in a plastic bag	18
2.4 (a) Pycnometer or specific gravity bottle 25 mL, (b) sample filled into pycnometer, (c) recorded the weight, (d) distilled water added to fill the pycnometer with sample, and (e) pycnometer was filled with distilled water only	20
2.5 (a) sieves (Solids Wiki, 2012), (b) mechanical sieve shaker (QAQC LAB, 2012).....	22
2.6 Sieve analysis determination of sample (KB_5_2), black square is sand, green square is granular, red square is pebble size	23
2.7 (a) 30 % Hydrogen peroxide, (b) beaker on hot plate and under a fume hood, (c) gas bubbles of sample, and (d) sediment samples were dried	24
2.8 (a) 100 mL of 5 % calgon and sediment sample, (b) metal milkshake cup and shaker, (c) moved plunger up and down through the cylinder, (d) sediment solution and blank, (e) reading of the hydrometer, and (f) reading of the temperature.....	25

LIST OF FIGURES (CONTINUED)

FIGURES	PAGES
2.9 Triangle with the textural classification, red circle is sample of KH_3_2	27
2.10 International Powder Diffraction File (PDF) database of KB_5_2.....	29
2.11 X-ray Diffractometer, PHILIPS, The Netherlands.....	29
2.12 (a) Sample before and after gold coating, (b) sputtering equipment, (c) Scanning Electron Microscope, Quanta 400, (d) image of sample of KH_1_2.	31
2.13 (a) SEM image of sample of KB_6_3, (b) graph of KB_6_3 from EDS software (Oxford, England).....	31
2.14 Darcy's experiment (Brown, 2013). Z represents vertical and 1 horizontal dimension direction	32
2.15 Schematic diagrams of falling head permeability test.....	34
2.16 Steps of measurement the hydraulic conductivity: (a) First place one porous stone on the inner support ring in the base of the chamber, (b) placed a filter paper on top of the porous stone, (c) placed chamber on top the filter paper, (d) poured sediment samples into the lower chamber, (e) placed the filter paper, porous stone and support ring on top surface of the sediment samples, (f) placed top of chamber, and (g) shows the assembled falling head permeability test.....	34
2.17 Comparisons between resistivity from laboratory for a NaCl solution (red square) and resistivity from Schlumberger (2000) for a NaCl solution (blue diamond).....	35
2.18 (a) Schematic diagram of the electrical laboratory measurements, (b) photo of the sediment samples in the box	36
2.19 Correlation between electrical resistivity and water saturation of KH_1_2	37
2.20 Correlation between electrical resistivity and water saturation of KB_8_2, blue circle is resistivity from laboratory and red line is resistivity model using Archie's law	39
2.21 Correlation between electrical resistivity and water saturation of KH_1_2, blue circle is resistivity from laboratory and blue line is resistivity model calculated using modified Archie's law	39

LIST OF FIGURES (CONTINUED)

FIGURES	PAGES
2.22 Correlation between electrical resistivity and water saturation of KH_1_2, blue circle is resistivity from laboratory, blue line is the resistivity calculated model with $m=1.25$, red line is the resistivity model when m is lower than 1.25 and the green line is the resistivity model when m is larger than 1.25.....	40
2.23 Correlation between electrical resistivity and water saturation of KH_1_2, black circle is resistivity from laboratory, red line is resistivity model with $n=2.55$, blue line is resistivity model when n is lower, and green line is resistivity model when n is higher than 2.55	40
2.24 Schematic diagrams of the seismic laboratory measurements	42
2.25 (a) Equipment set up in laboratory, (b) Sonic Viewer-170, (c) 63 kHz P-wave (right) and 33 kHz S-waves transducers (left).....	43
2.26 Velocity of KB_7_2, blue crystal is V_P , red square is V_S	44
2.27 Elastic moduli of KB_7_2 , red square is bulk moduli, green triangle is shear moduli, blue crystal is Young's moduli, yellow circle is Poisson's ratio	46
3.1 Geological map of study area in UTM grid (modified from Mineral Resources, Thailand, sheet 5123 III, Changwat Songkhla, 2006), 1 is granite site, 2 is sandstone site, C is quartzitic sandstone, Tr_{gr} is biotite – muscovite – grained, Q_c is colluvium deposits, Q_a is alluvial deposits.....	48
3.2 (a) Granite site, view to east (b) out crop of granite and hornfels, (c) granite intrusion in hornfels.....	50
3.3 Sandstone site, view to north.....	50
3.4 Stereo Net plots of (a) layering, (b) fault and joint of the sandstone site Planes are shown as great circles and as poles	51
3.5 Photos and relative location of the sediment samples from the granite site.....	52
3.6 Photos of the sediment samples from the granite site; sample (a) KB_1_2, (b) KB_2_2, (c) KB_3_2, (d) KB_4_2, (e) KB_5_2, (f) KB_6_2, (g) KB_7_2, (h) KB_8_2, (i) KB_9_2, (j) KB_2, and (k) KB_5.....	53

LIST OF FIGURES (CONTINUED)

FIGURES	PAGES
3.7 Photos of the sediment samples from sandstone site, (a) sandstone site, view to East, (b) northern profile, (b) central profile, and (d) southern profile	56
3.8 Photos of the sediment samples from the sandstone site; sample (a) KH_1_2, (b) KH_2_2, (c) KH_3_2, (d) KH_4_2, (e) KH_5_2, (f) KH_6_2, (g) KH_7_2, (h) KH_8_2, (i) KH_9_2, (j) KH_10_2, (k) KH_11_2, (l) KH_12_2, (m) KH_1, (n) KH_2, (o) KH_3, (p) KH_4, (q) KH_8, (r) KH_9, and (s) KH_13	56
3.9 Density and porosity of samples from the granite site, green histogram is mineral density, blue histogram is bulk density, purple histogram is porosity, (a) samples KB_2_2, KB_4_2, KB_5_2, and KB_7_2, (b) samples KB_1_2, KB_8_2 and KB_9_2.....	58
3.10 Density and porosity of samples from sandstone site, green histogram is mineral density, blue histogram is bulk density, purple histogram is porosity, (a) northern profile, (b) central profile, and (c) southern profile	59
3.11 Influence of (a) grain size, (b) sorting and (c) clay content on the porosity of sediments material (Kirsch et al, 2006)	60
3.12 Grain size distribution of samples from the granite site; blue line - KB_2_2, green line - KB_4_2, red line - KB_5_2, purple line - KB_7_2.....	61
3.13 Grain size distribution of samples from the granite site and beach sand, blue line - KB_1_2, green line - KB_8_2, red line - KB_5_2, violet line – beach sand	61
3.14 Grain size distribution of sandstone site, blue line - KH_1_2, green line - KH_2_2, red line - KH_3_2.....	62
3.15 Grain size distribution of sandstone site, blue line - KH_5_2, green line - KH_6_2, red line - KH_7_2.....	63
3.16 Grain size distribution of sandstone site, blue line - KH_9_2, green line - KH_10_2, red line - KH_11_2.....	63
3.17 Triangle with the textural classification of samples from granite site.....	64
3.18 Triangle with the textural classification of samples from sandstone site.....	64

LIST OF FIGURES (CONTINUED)

FIGURES	PAGES
3.19 Micro structures of sample from the granite site, (a) – (b) sample KB_1_2, (c)-(d) sample KB_4_2, (e) sample KB_5_2, and (f) sample KB_9_2.....	68
3.20 Micro structure of samples from the sandstone site, (a) – (c) sample KH_1_2, (d) sample KH_2_2 and (e) – (f) sample KH_4_2	68
3.21 Micro structures and composition of sample after with water saturation, (a)-(b) sample KB_4_2, (c) sample KH_1_2, (d) sample KH_5_2, (e) sample KH_6_2, and (f) sample KH_7_2.....	69
3.22 Composition of sample by EDX, sample (a) beach sand, (b) KB_1_2, and (c) KB_6_2	70
3.22 Composition of sample by EDX, sample (d) KB_7_2, (e) KH_1_2, and (f) KH_5_2.....	71
3.23 Hydraulic conductivity of samples from the granite site, (a) samples KB_2_2, KB_4_2, KB_5_2, and KB_7_2, (b) samples KB_1_2, KB_8_2 and KB_9_2 and beach sand.....	72
3.24 Hydraulic conductivity of samples form the sandstone site, (a) northern profile, (b) central profile, and (c) southern profile	73
3.25 Resistivity of samples from the granite site with increasing water saturation, (a) sample KB_2_2, (b) sample KB_4_2, (c) sample KB_5_2, and (d) sample KB_7_2	74
3.26 Resistivity of samples from the granite site with increasing water saturation, (a) sample KB_1_2, (b) sample KB_8_2, (c) sample KB_9_2, and (d) sample beach sand	75
3.27 Resistivity of samples from the sandstone site with increasing water saturation (a) northern profile, (b) central profile, and (c) southern profile	76
3.28 Relation between grain size distribution, m, and n	77
3.29 Velocity of beach sand, blue crystal is V_P , red square is V_S	78
3.30 Velocity of samples from the granite site, blue crystal is V_P , red square is V_S , (a) KB_1_2, (b) KB_4_2, (c) KB_7_2, and (d) KB_9_2	79
3.31 Velocity of samples from the sandstone site, blue crystal is V_P , red square is V_S , (a) KH_1_2, (b) KH_2_2, (c) KH_3_2, and (d) KH_7_2.....	79
3.32 Photos of sample KB_7_2 with increases water saturation.....	81

LIST OF FIGURES (CONTINUED)

FIGURES	PAGES
3.33 Photos of sample KH_2_2 with increases water saturation	82
3.34 Elastic moduli of beach sand, red square is bulk moduli, green triangle is shear moduli, blue crystal is Young's moduli, yellow circle is Poisson's ratio.....	83
3.35 Elastic moduli of samples from the granite site (a) KB_1_2, (b) KB_4_2, (c) KB_7_2, (d) KB_9_2, red square is bulk moduli, green triangle is shear moduli, blue crystal is Young's moduli, yellow circle is Poisson's ratio.....	84
3.36 Elastic moduli of samples from the sandstone site (a) KH_1_2, (b) KH_2_2, (c) KH_3_2, (d) KH_7_2, red square is bulk moduli, green triangle is shear moduli, blue crystal is Young's moduli, yellow circle is Poisson's ratio.....	85
4.1 (a) density, KB_m is mineral density of granite site, KH_m is mineral density of sandstone site, KB_b is bulk density of granite site, and KH_b is bulk density of sandstone site, (b) porosity, blue column is granite site and pink column is sandstone site.....	88
4.2 Percent of grain size, purple is clay, green is silt, red is sand, and blue is gravel (a) granite site, (b) sandstone site	89
4.3 Relations between porosity and hydraulic conductivity, (a) granite site, and (b) sandstone site.....	90
4.4 Resistivity modeling (a) granite site, and (b) sandstone site.....	91
4.5 Box plot of resistivity modeling parameter: m is cementation factor, n is saturation exponent, and a is a constant, blue column is granite site and pink column is sandstone site	92
4.6 Velocities of KH samples (sandstone site) with increasing water saturation, red line is V_S and blue line is V_P	93
4.7 Schematic drawing of net overburden stress for a sediment with grain to grain contacts.....	96
4.8 Water meniscuses at one point of contact between two particles (Farouk et al., 2004)	96

LIST OF FIGURES (CONTINUED)

FIGURES	PAGES
4.9 V_P and V_S calculated over a range of water saturation for sand at 10 cm depth and clay at 1 m depth to emphasize the contribution of interparticle stresses (Crane, 2013) using the parameter shown in Appendix, Table D1	99
4.10 V_P and V_S calculated over a range of water saturation for beach sand and sample KB_7_2 using the parameter shown in Table 4.1	99
4.11 V_P and V_S are calculated over a range of water saturation for sand and clay, the blue line is V_P , and the red line is V_S	99
4.12 Comparisons between granite site and sandstone site, (a) velocity, and (b) resistivity.....	100

CHAPTER 1

INTRODUCTION

1.1 Introduction

Rainfall-induced landslides are a common problem in sub-tropical Thailand due to deep weathered rocks and sediments and a rainy season with heavy and prolonged rainfall. Almost every rainy season landslide occurrences are reported in mountainous or hilly areas, with larger landslides occurred in Khao Phanom, Krabi Province, Chayia, Surat Thani Province, Lang Suan, Chumphon Province, and Kathu in Phuket Province in 2011, with the loss of lives and livelihoods (The Nation, 2011).

Landslides induced by heavy rainfall usually occur in areas where the slope angles are steeper than the friction angle of the soil or sediment. The reason is that only within a certain range of water saturation these slopes are stable. This is when the effect of suction creates an apparent cohesion between the soil and sediment particles and by this increases the shear resistance between the soil or sediment particles (e.g., Fredlund and Rahardjo, 1993; Springman et al., 2003). If the saturation gets above a certain or critical value both parameters, suction and shear resistance, are significantly reduced (e.g. Pagano et al., 2010). Especially heavy rainfalls results in higher water saturation that may exceed a critical limit in certain parts of a slope, and by this starting the local failure, which consequently is leading to a landslide or debris flow (e.g. Sassa et al., 2010).

The shallow subsurface comprises of rocks, sediments and soils. Sediments are formed slowly as rock erodes into small pieces near the earth's surface. Organic matter decays and mixes with inorganic material (rock particles, minerals and water) to form sediments. Sediment was made up of distinct horizontal layers; they range from rich, organic upper layers (humus and topsoil) to underlying rock layers (subsoil, weathering and bedrock) as shown in Figure 1.1. The O-horizon or organic matter was made up mostly of leaf litter and humus (decomposed organic matter) and dark colored layer. The A-horizon is called topsoil, which is organics mixed with mineral matter. This layer was depleted of iron, clay, aluminum, organic compounds, and other soluble constituents. The B-horizon called the subsoil as it reflects chemical or physical alterations of the parent material. This layer accumulates iron, clay, aluminum and organic compounds, a process referred to as illuviation. The C-horizon called weathering rock fragment and consists of slightly broken up bedrock. Bedrock is called the R-horizon and it is comprised of continuous masses of hard rock.

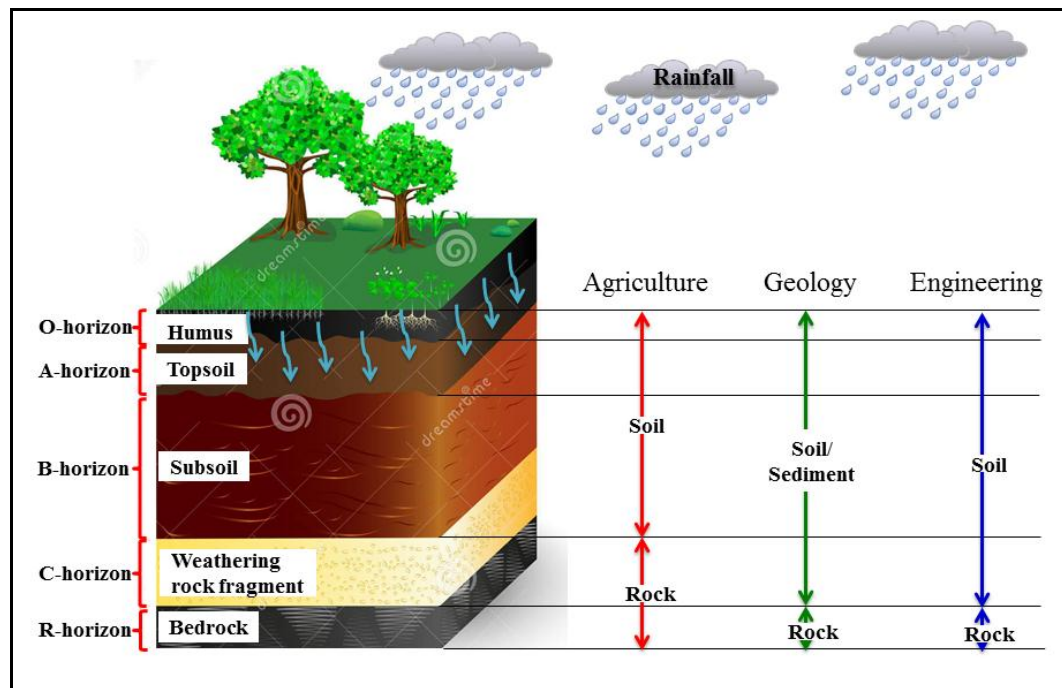


Figure 1.1 Structure of shallow subsurface with different horizons and different terminology related to agriculture, geology, and civil engineering.

1.2 Unconsolidated sediments

Unconsolidated sediments are deposits which were formed by secondary sedimentation of weathered rocks and their fragments, and they were not compacted and lithified. The coarsest sediments are those produced by land sliding and glaciation which may transport fragments of rock. Such very large fragments might be further eroded during river transportation to gravel and boulder size. These fragments disintegrate to smaller size grains; the grains tend to be largely of single minerals. The composition and type of mineral will depend upon the source rock and the degree of abrasion suffered during transportation. Thus, the most common sand-forming mineral is quartz, but in limestone areas the grains may be predominantly calcareous. If there are local sources of less erosion resistant minerals, such as mica, these may be found mixed with more resistant minerals transported from distant sources. Grains of all sizes will rounded by abrasion during transportation and the degree of roundness achieved is of geotechnical significance; angular grains tend to interlock and give greater shear strength than more rounded grains. The distribution of grain sizes in sediment may vary (Piece, 2009).

Unconsolidated sediments can be classified into non-cohesive material (e.g., sand, gravel) and cohesive material (e.g., clay, loam). The differences in the

elastic behavior of these two groups are based on various physical conditions at the contacts of the rock particles. For the first group, conditions are controlled by friction effects, whereas for the second group, physio-chemical phenomena are dominant (Schön, 2011). In summary, unconsolidated sediments are solid fragmental material from weathering of rocks and transported and deposited by air, water and that forms in layers on the Earth's surface at ordinary temperatures, unconsolidated form e.g., sand, gravel, silt, mud, alluvium (Immoor, 2006).

1.2.1 Unconsolidated sediment characteristics

Sediment characteristics can be classified into grain composition, grain size, grain shape, grain arrangement, pore size, pore shape, pore filling, and degree of saturation as shown in Figure 1.2. The main physical properties of sediments are porosity, density (bulk and mineral density), hydraulic conductivity, electrical resistivity, and seismic velocities.

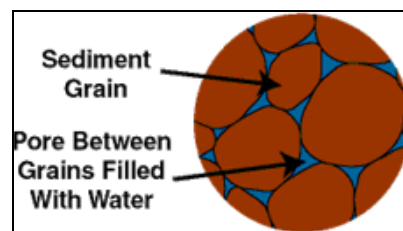


Figure 1.2 Schematic figure of grains and pores of sediments (USGS, 2013).

1.2.1.1 Grain

Grains of sediment compose mainly of quartz, clay, feldspar, and rock fragment. The sediment grains size occurs in a wide range of sizes from microns to centimeters. Grain size uses the assumption that the particle is roughly circular and measured as diameter. Grain size distribution is a fundamental characteristic of sediment particles, as it provides important clues to the sediment provenance, transport history, and depositional environment. Wentworth (1922) divided sediments into four size categories based on grain diameter: cobble/boulder (size larger 64 mm), gravel (size 2-64 mm), sand (size 0.063-2 mm) and clay (size less than 0.063 mm) (Alden, 2013).

Grain shape is mainly the result of erosion processes, defined numerically by sphericity and roundness, where a rock broke up through weathering and transportation. Sphericity measures the degree to which a particle approaches a spherical shape. It was defined as the ratio between the diameter of a sphere with the same volume as the particle and the diameter of the circumscribed sphere, and it is

low to high sphericity. The sphericity of a particle is usually determined by measuring the three linear dimensions of the particle (longest, intermediate, and shortest diameters). Roundness refers to the sharpness of the corners and edges of a grain. It was defined the ratio of the average radius of curvature of the corners to the radius of the largest inscribed circle. It is arguer to roundness.

Clay minerals result mainly from the weathering of other rock forming minerals. Kaolinite, for example, results from the weathering of feldspars in granitic rocks. Clay micas are a common constituent of clays and range, with increasing degradation, from the primary muscovite to the secondary sericite, and to illite at the end of the series. Muscovite has a low content of combined and adsorbed water but together with interstitial water it increases to the end of the series. The montmorillonite group of clay minerals, known by the earlier term 'smectites', are known for their capacity to expand on taking in water and give rise to extreme swelling. Members of the chlorite group of clay minerals also have a capacity for swelling. Organic deposits of plant remains may be laid down in swampy environments to form highly compressible peat deposits. Plant remains may also be mixed intimately with clays to form organic clays and have a significant influence on the behavior of these materials (Freitas, 2009)

1.2.1.2 Pores

Pore space properties are important for the characterization of pore volume (e.g. pores, cracks) fractions of the fluids (porosity, saturation, bulk volume of fluids), properties controlling fluid distribution in the pore space and fluid flow under the influence of a pressure gradient (permeability). Laboratory techniques (standard and special core analysis) deliver fundamental properties, whereas thin sections and microscopic or scanning electron microscopic (SEM) investigations are used for description and computer aided analysis (Schön, 2011). For the description of the pore space, different classification schemes were developed depending mainly on the application (Fitzner and Basten, 1994) such as based on the separation of ideal single pore types by applying the pore geometry and the pore genesis, using the location of the pore in relation to the solid particles, and condition of well fluids or gases can transmission through the pore system.

The size of a pore is given by its pore radius, which is determined from the radius of a cylinder representing the ideal form of a pore. Various pore size classifications have been published over time, with some shown in Table 1.1, mainly dividing the pore space into micro-, meso-, and macropores. However, there is no

consistent classification scheme as the boundaries between the classes vary (Siegesmund and Dürrast, 2011).

Table 1.1 Comparison of some often used pore size classification schemes exhibiting variations in the ranges depending on the authors (Siegesmund and Dürrast, 2011).

	Micropores (μm)	Mesopores (μm)	Macropores (μm)	Large pores (μm)
De Quervain (1967)	<5	5–200 (fine pores)	200 –2,000 (coarse pores)	>2,000
Dubinín (1979)	0.003 to 0.0032 – 0.0012 to 0.0014	0.2 to 0.4 – 0.003 to 0.0032	<0.2–0.4	
UPAC (Gregg and Sing1982)	<0.002	0.002–0.05	>0.05	
Klopfer (1985)	<0.1	0.1–1,000 (capillary pores)	>1,000	
DIN 66131 (1993)	<0.002	0.002–0.05	>0.05	
Kodikara et al. (1999)	1 to 30		10–1,000	

1.2.2 Physical properties of unconsolidated sediments

1.2.2.1 Density and porosity

Density (ρ) of a substance is its mass per unit volume (see Section 2.3). Figure 1.3 gives an overview about the density values of sedimentary rocks. There are two main groups with respect to density controlling factors: density of pore-free sediments is determined by their mineral composition and density of porous sediments is controlled by mineral composition (grain density), porosity, and composition of pore content (saturation) (Schön, 2011). Table 1.2 shows some density values from Baker Atlas (1985) and Schlumberger (2000). Density decreases with increasing porosity, decreasing water saturation, decreasing pressure and increasing temperature.

Table 1.2 Mineral density from Baker Atlas (1985) and Schlumberger (2000).

Mineral	Density (g/cm^3)	Mineral	Density (g/cm^3)
Quartz	2.65	Illite	2.64
Microcline	2.56	Montmorillonite	2.06
Muscovite	2.83	Hematite	5.27
Kaolinite	2.59		

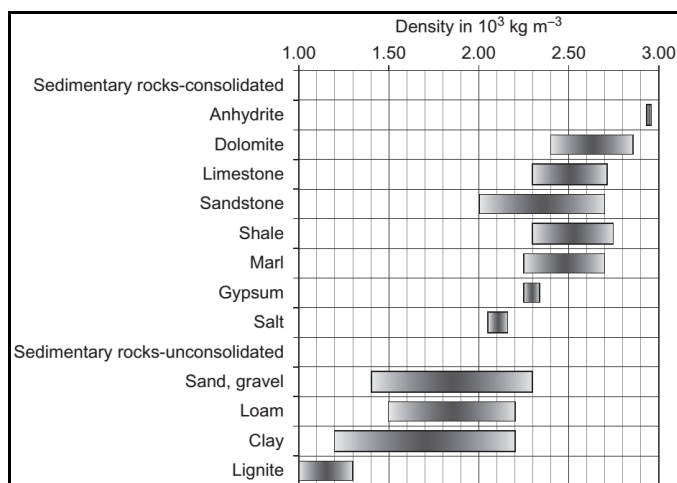


Figure 1.3 Mean range of density for sedimentary rocks (Schön, 2011).

Porosity (ϕ) is defined as the ratio of pore space in sediment to the total volume of sediments shown in Figure 1.4 (see Section 2.4). The porosity of sediment depends on the grains shape, the packing of the grains, and the size distribution of the grains. For sediments consisting of a number of differently sized grains (see Figure 1.5), the smaller grains will sit in the pores between the larger grains, and so the porosity will be lower than it would be in sand made of only one of the grain sizes shown in Figure 1.5. Likewise, angularity of the grains will tend to cause them to pack less efficiently, and so will increase the porosity of the sediment. Larger grains have large pore spaces, whereas smaller grains have many small pore spaces. Typical ranges in porosity for a variety of earth materials are given in Table 1.2. Porosity also decreases nonlinearly with depth or correspondingly compaction (Schön, 2011).

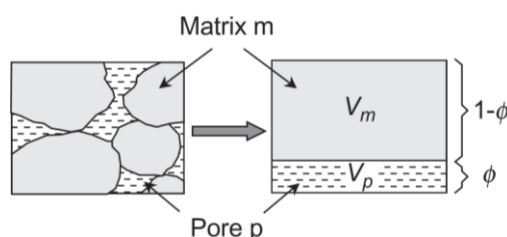


Figure 1.4 Definition of porosity (Schön, 2011), V =volume; Φ =porosity.

Table 1.3 Range in values of porosity of unconsolidated sediments (Morris and Johnson, 1967).

Material	Porosity (%)	Material	Porosity (%)
Gravel, coarse	24-37	Sand, coarse	31-46
Gravel, medium	24-44	Sand, medium	29-49
Gravel, fine	25-39	Sand, fine	26-53
Silt	34-61	Clay	34-60

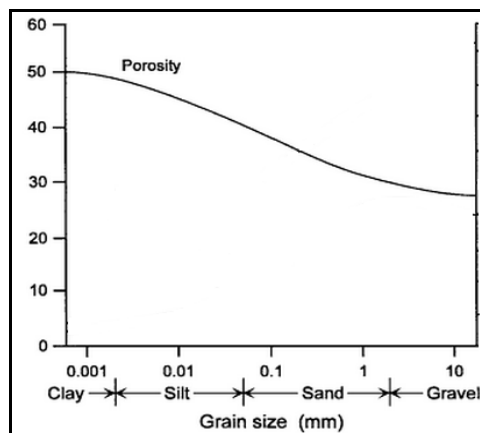


Figure 1.5 Porosity of granular materials (Modified from Davis and De Wiest, 1966).

1.2.2.2 Saturation

The pore space is filled with fluids (air and water). If more than one fluid is present, the spatial distribution of the different fluids depends on the physical properties of the material, on the fluid properties, and on interactions between the fluids and between fluids and solids (Schön, 2011). For the description of the volume fraction of a fluid in a porous media, the term saturation (S) is used and defined as follows

$$S = \frac{\text{fluid volume}}{\text{pore volume}} \quad (1.1)$$

1.2.2.3 Hydraulic conductivity

Hydraulic conductivity (K) is a property that water is the fluid moves through a material (see Section 2.8). Typical ranges of hydraulic conductivity for the main geological materials are shown in Figure 1.6, with hydraulic conductivity decreases with smaller grain size.

The hydraulic conductivity, decreases with increasing effective pressure (nonlinear) and decreasing porosity, because the fluid channels are progressively closed. The amount of clay in the sediment plays a role due to the small size of clay minerals, whereas it is important whether the clay shows a dispersed or laminated distribution. For the first case a relatively monotonic reduction in the hydraulic conductivity can be expected as with increasing clay content. For the second case, the hydraulic conductivity perpendicular to the clay layers will see a sharp decrease, whereas parallel to the layers the hydraulic conductivity is controlled by the sand and clay content (see Figure 1.7, Schön, 2011).

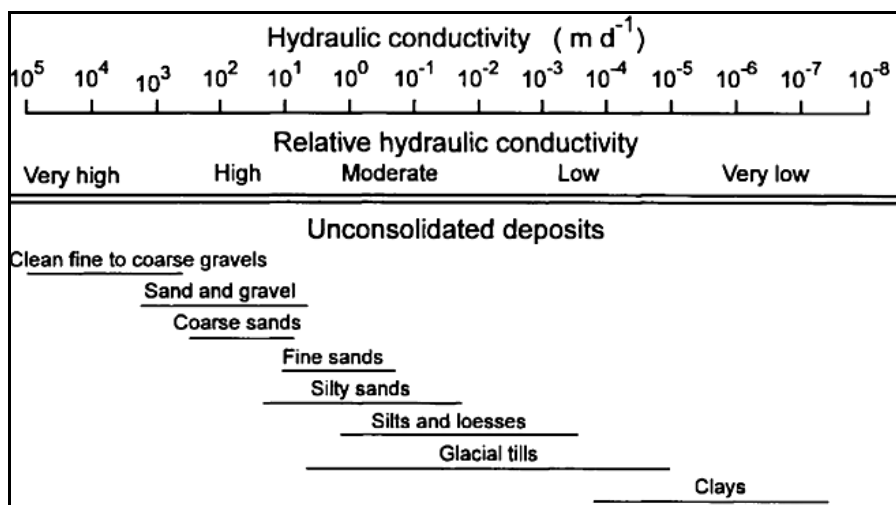


Figure 1.6 Range of hydraulic conductivity values for geological materials (modified from Driscoll, 1986, and Todd, 1980).

The distribution of clay and sand can be classified into four groups shown in Figure 1.6. Clean sands are made up of relatively pure, well washed sand, they contain essentially no clay minerals or shales, and consist solely of sand grains. Laminar clays are thin layers of clay between sand units. Structural clays are clay particles constitute part of the rock matrix, and are distributed within it. Dispersed clays are clay in the open spaces between the grains of the clastic matrix.

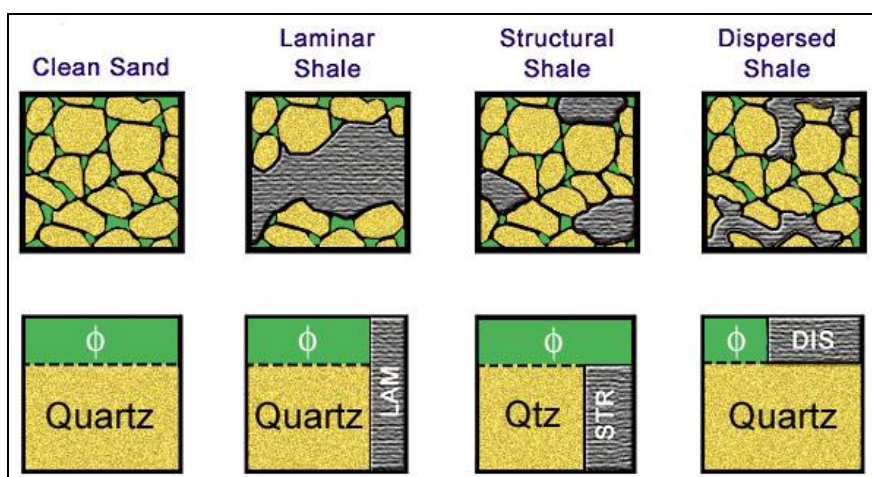


Figure 1.7 Clay classification by mode of distribution after Schlumberger, 1987, see also IHRD, 2014.

1.2.3 Electrical resistivity

Electrical resistivity (ρ) or its inverse the electrical conductivity (σ) is a bulk property of material describing how well that material allows electric currents to

flow through it (see Section 2.9). The electrical resistivity is a function of soil properties, including the nature of the solid constituents (particle size distribution, mineralogy), arrangement of voids (porosity, pore size distribution, connectivity), degree of water saturation, electrical resistivity of the fluid (solute concentration) and temperature. The water solution resistivity is a function of the ionic concentration, and the resistivity of the solid grains is related to the electrical charges density at the surface of the constituents (Samouëlian et al., 2005).

Materials, porosity and chemical content of water filling the pore spaces are more important in resistivity than the conductivity of mineral grains of which the material itself is composed (Dobrin and Savit, 1988; Brovelli and Cassiani, 2010, 2011). The electrical conductivity is related to the particle size by the electrical charge density at the surface of the solid constituents. In clay soil, the electrical charges located at the surface of the clay particles lead to greater electrical conductivity than in coarse-textured soils because of the magnitude of the specific surface (Fukue et al., 1999). The electrical resistivity in clean sands and gravels occurs primarily in the fluids filling the pores. In clay, electrical conduction occurs in the pores and on the surfaces of electrically charged clay particles (Revil and Glover, 1997, 1998; Revil et al. 1998).

1.2.3.1 Archie's law and modified Archie's law

The porosity can be obtained for the electrical property via the Archie's law, which for a saturated soil without clay is written as

$$F = \frac{\rho}{\rho_w} = a\phi^{-m} \quad (1.2)$$

where F is the formation factor, ρ is the resistivity of the formation, ρ_w is the resistivity of the pore-water, a is a constant, Φ is the porosity, and m is the cementation exponent. In general, the exponent m and the parameter a is controlled by the pore channel geometry with respect to the electrical current flow and is therefore a kind of pore textural property. Archie (1942) found characteristic values of 1.3 for unconsolidated sands and 1.8–2.0 for consolidated sandstones.

Electrical currents in soils are mainly electrolytic, i.e. based on the displacement of ions in pore-water. Electrical current in soils depends on the amount of water in the pores and on its quality. The relationship between the electrical resistivity and water saturation was a modified form of the previous Equation (1.2),

taking into account that the porosity can be filled by another medium as water. The water saturation was expressed in function

$$S_w^n = \frac{F\rho_w}{\rho} \quad (1.3)$$

The combining with the Equation (1.2) and (1.3)

$$\rho = a\rho_w\phi^{-m}S_w^{-n} \quad (1.4)$$

where S_w is the saturation degree, and n is a parameter related to the saturation degree. It is controlled by the distribution of the conducting of fluid in the pore space and depends on the texture, wetting properties, and saturation history caused by capillary effects.

Equation (1.4) was established to be valid for medium to coarse-grained soils. It assumes that the characteristic of the solid phase does not influence the electrical conduction. For fine-textured soils, the electrical resistivity of the solid matrix cannot be neglected. The electrical current in clay is not only conducted by the free pore-water but also by the adsorbed water at the clay particle surface.

The electrical properties of clay minerals surrounded by an electrolyte (water) act as a second conductivity component in addition to the electrolytic conductivity of the formation water in the connected pore space. The constants of the empirical law such that the conductivity of water saturated shaly sand is completely determined by porosity, clay charge contribution per unit pore volume (Q_v) and water conductivity (σ_w). Empirical laws may apply for electrolytic conduction in other porous charged systems such as ionomers, ion exchange resins, bone, etc. (Sen et al., 1988). The simple formula is as following

$$\sigma = 1/F[\sigma_w + AQ_v/(1 + CQ_v/\sigma_w)] + EQ_v \quad (1.5)$$

where constants A and C are products of factors which depend on rock (formation) geometry and the effective mobility of the cations near the surface, $A = \mu_{DL}m$, where μ_{DL} is the mobility of the ions in the double layer ($\mu_{DL} = 1.94$) and m is a surface tortuosity factor, $C = 0.7/Q_v$ S/m, and $EQ_v \approx 0$. The combination with Equation (1.4) and (1.5) for electrical resistivity of clay bearing gives

$$\sigma = S^n \phi^m a^{-1} [\sigma_w + A Q_v / (1 + C Q_v / \sigma_w)] \quad (1.6)$$

1.2.3.2 Clay effect

Electrical conduction in porous media occurs by the movement of ions through electrolytic pore water in the void and surface charge (Bryson, 2005). Ions can be displaced under the application of electrical potential through the pores with electrolytic water. Electrical conductivity depends on pore fluid conductivity as well as surface charge in clay soils (it is a net negative charge, see Figure 1.). Cations are attracted by the clay particles and the particle surface layer is an adsorbed layer of fixed ions. The cations produce high concentration around the solid particles. To equalize charge concentration, they try to diffuse throughout the structure. Negative electrical charge of the solid particles restricted the diffusion and anions are also excluded from the negative force of the particles. The adsorbed layers are relatively mobile ions and they consist both of positive and negative charges. The charged surface and distributed charge surface together is known as diffuse layer (Rinaldi and Cuestas, 2002; Kibria, 2011).

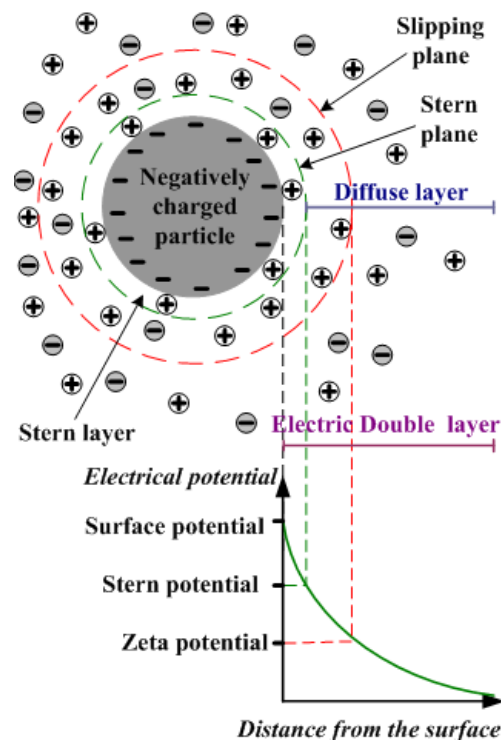


Figure 1.8 Electric double layers (Substect, 2013).

Cation exchange capacity (CEC) is the physical origin of clay-water interface conductance (usually in milliequivalent per 100 g of dry clay). Clay minerals have a negative surface charge with ability to adsorb ions and to create a double layer if the pore fluid is an electrolyte. This ability of clay mineral to form the electric double layer is basis of the cation exchange. During the formation of clay through weathering, positive charges (cations Ca^{2+} , Mg^{2+} , Na^+ , and K^+) are adsorbed on the clay surface. CEC measures the number of cations that are required to neutralize the clay particle.

1.2.4 Seismic velocities and elastic properties

Seismic velocity methods are one of the most used geophysical methods in shallow subsurface investigation. It is based on elastic (mechanical) properties (such as bulk modulus, shear modulus, Young's elasticity modulus, Lamé's constant and Poisson's ratio) and density (Telford et al., 1990) (see Section 2.10). Velocity is a parameter exhibiting a large range of values sensitive to various factors like the nature of material, component (minerals, matrix component), porosity, density, moduli, and the water or fluid saturation. Compressional (P-wave) and shear wave (S-wave) velocities through sediments are governed by various factors, including lithological properties such as formation texture (size, shape, type, packing, sorting and distribution of grains), and the amount of clays, compaction, consolidation, and cementation.

As a result of compaction both the compressional and shear wave velocities increase due to an enhanced stiffness among the grains (Schön, 2011). Compressional wave velocities are also controlled also by the type of pore fluid (gas, liquid). It increases from air to water, and it shows very small changes with increasing saturation up to about 80-85%, and then the velocity abruptly increases. Shear wave velocities are not strongly controlled by the type of pore fluid and a small decrease is not influenced by the pore filling because its shear modulus is zero (Schön, 2011). Velocity values in unconsolidated sediments are distinctly lower than in consolidated sediments. With increasing clay content, the velocity generally decreases in unconsolidated sediments. Velocity decreases with increasing porosity and increase water saturation and pressure (Schön, 2011).

1.2.4.1 Seismic Velocities

Velocity models of the shallow subsurface better explain velocities when total effective stresses are considered. Current constitutive elastic models that

predict velocities in granular materials simplify the effect of total effective stress by equating it to net overburden stress. The methodology calculates elastic moduli of granular matrices in shallow subsurface environments by total effective stress into Hertz Mindlin theory and calculates the elastic moduli by extending Biot Gassmann theory to include pressure effects induced by water saturation changes. Seismic velocities are given by

$$V_P = \sqrt{\frac{K_{eff} + \frac{4}{3}\mu_{eff}}{\rho_{bulk}}} \quad (1.7)$$

$$V_S = \sqrt{\frac{\mu_{eff}}{\rho_{bulk}}} \quad (1.8)$$

where V_P is the P-wave velocity, V_S is the S-wave velocity, μ_{eff} is the effective shear modulus, K_{eff} is the effective bulk modulus, and ρ_{bulk} is the bulk density.

1.2.4.2 Elastic properties

In contrast to the consolidation test, the results of which are usually plotted in the form of void ration-versus-log pressure curve for unconsolidated sediments, the stress-strain characteristics of sediments define the elastic nature of the material. The stress-strain behavior of any sediment depends on a number of factors including mass properties, fluid saturation, particle arrangements, and type of strain condition, stress history, confining pressure, shear stress, and duration of the loading.

Biot-Gassmann theory effectively explains the changing pore fluid influences velocity of elastic waves as a result of changing elastic moduli and changing density. Shear modulus is independent on the fluid type; the effective shear modulus is equal to the shear modulus of the granular matrix (Gassmann, 1951), with

$$\mu_{eff} = \mu_{matrix} \quad (1.9)$$

$$K_{eff} = K_{matrix} + \frac{\left(1 - \frac{K_{matrix}}{K_0}\right)^2}{\frac{\phi}{K_{pore}} + \frac{1-\phi}{K_0} - \frac{K_{matrix}}{K_0^2}} \quad (1.10)$$

where, μ_{matrix} is the shear modulus of the granular matrix, K_0 is the bulk modulus of the grains, K_{matrix} is the bulk modulus of the skeletal matrix and K_{pore} is the bulk modulus of the pore space. The *eff* subscript is used to differentiate the elastic moduli of the bulk granular material from the elastic moduli of the granular matrix, pore space, or individual grains. Matrix subscripts are used instead of the dry subscript used in conventional Biot-Gassmann fluid substitution equations. The bulk modulus of the pore space (K_{pore}) can be calculated as

$$\frac{1}{K_{pore}} = \frac{S_w}{K_{water}} + \frac{1-S_w}{K_{air}} \quad (1.11)$$

where S_w is the water saturation, K_{water} is the bulk modulus of water ($K_{water}= 2.2$ GPa), and K_{air} is the bulk modulus of air ($K_{air} = 0.00014$ GPa). The two moduli and density can be used to determine the seismic velocities (Ikelle and Amundsen, 2005).

Matrix elasticity is calculated using Hertz-Mindlin theory (Mindlin and Deresiewicz, 1953). It is used to calculate the elastic moduli of elastic granular materials in terms of porosity, grain contact geometry, grain elasticity, and grain contact stress, with

$$K_{matrix} = \left[\frac{n^2 (1-\phi)^2 \mu^2}{18\pi^2 (1-\nu)^2} P \right]^{1/3} \quad (1.12)$$

$$\mu_{matrix} = \frac{5-4\nu}{5(2-\nu)} \left[\frac{3n^2 (1-\phi)^2 \mu^2}{2\pi^2 (1-\nu)^2} P \right]^{1/3} \quad (1.13)$$

where n is the grain coordination number ($n=1$), μ is the grain shear modulus, ν is the grain Poisson's ratio, and P is the total effective stress.

The total effective stress (Lu and Likos, 2006) (see Appendix D) represents the average stress carried by the granular matrix and was first defined as total stress minus pore pressure (Terzaghi, 1943). Total effective stress equates to the sum of net overburden stress and interparticle stresses (Bishop, 1959; Lu and Likos, 2006). Interparticle stresses can be classified into stresses in fully saturated media (σ_{CO}), that confer cohesion to sediments, and stresses in unsaturated media that result as water saturation changes (σ_S , soil suction stress) (Lu and Likos, 2006).

1.3 Objective

The objectives of this study were firstly to understanding the physical properties of unconsolidated sediments through investigations of various physical properties (porosity, density, hydraulic conductivity and water saturation), as well as geophysical (seismic velocity and electrical conductivity) and related geomechanical properties (elastic) of soils and sediments from the study area. Secondly, to understand changes in the electrical and seismic properties of these unconsolidated sediments with clay in relation to increasing water saturation through laboratory investigations. Based on those data possible relationships were developed, which then might be applied, for example, for electrical based sensor systems of early landslide warning systems, or the interpretation of soil moisture measurements in agriculture.

It has to be noted that this study aims to understand relationships between different parameters and properties and not tries to determine in situ properties of the sediment samples as this cannot be done with disturbed samples. However, natural sediment samples will be taken from different locations and outcrops in order to get realistic sample material. Disturbed sample means that various properties, for example bulk density and hydraulic conductivity, are different between laboratory measurements aimed in this study and the natural conditions at the site; but as explained above this is not an objective of this study.

CHAPTER 2 METHODOLOGY

2.1 Sample sites

For this study disturbed samples of unconsolidated sediments from different layers from bedrock to the top soil layer were taken from two sites of the Khao Khohong mountain range in Hat Yai District, Songkhla Province, Southern Thailand, as shown in Figure 2.1. The two sample sites comprise different bedrock lithology, the first site at UTM 0666802 0779972 (all UTM locations in WGS-84, Zone 47), mainly granite at a mountain site in different states of weathering. The second site is at UTM 0666927 0774098, mainly sandstone with different layers from bedrock to top soil. Before the field surveys previous studies, geological map and topographic map were analyzed to identify outcrop location, mainly outcrops of shallow unconsolidated sediments. Field observation of the selected outcrops focuses on the identification of lithology, different layers, structures, stratigraphy and geologic processes were studied and recorded. Detailed photos were taken, sketched structures, description of geology, made grids, and measured strike directions of faults. In addition, a beach sand sample from Samila beach, Songkhla Province was collected as sediment containing almost only sand and almost no clay.

2.2 Sampling method

Sediment samples classify being either disturbed or undisturbed. The disturbed sample has been changed sufficiently that tests of structural properties of the sediment will not be representative of in-situ conditions, and only properties of the sediment grains can be accurately determined. The undisturbed sample is close enough to the conditions of the sediment in-situ to allow tests of structural properties of the sediments to be used to approximate the properties of the sediments in-situ (Citizendum, 2007). For this study, from the first site samples (mainly granite) have been randomly collected around the area and the second site samples (mainly sandstone) have been collected as a profile from the top layer to the bottom layer (see Figure 2.2). The top layer (KH_1_2), the second layer (KH_2_2) and bottom layer (KH_3_2).

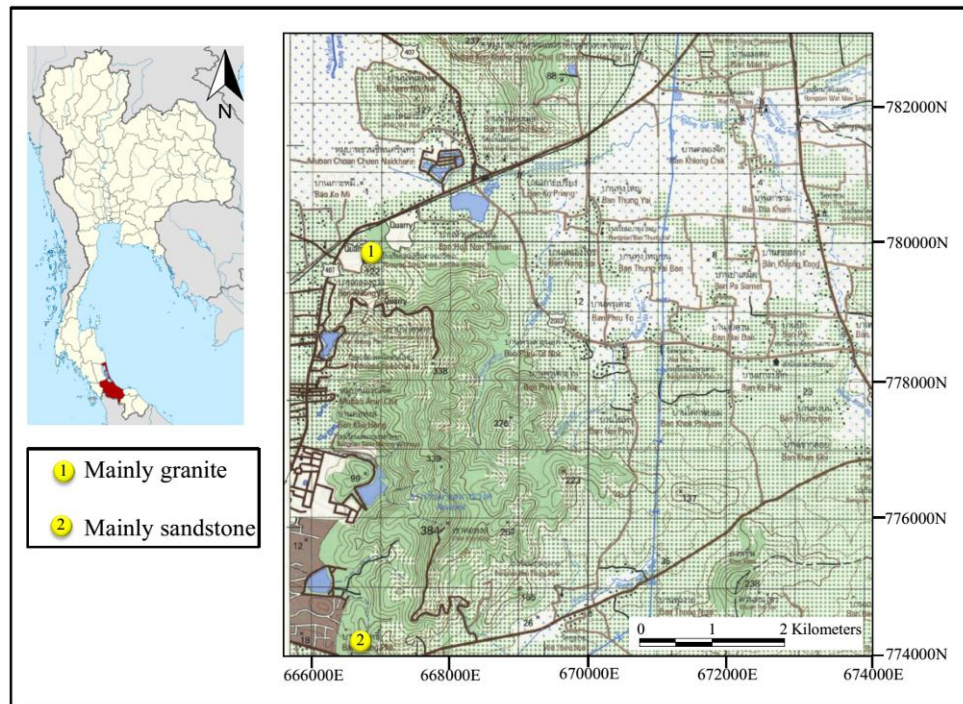


Figure 2.1 Sample site in Khao Khohong mountain range in Hat Yai District, Songkhla Province (modified from Sheet 5123III, Series L7018, Changwat Songkhla, Royal Thai Survey Department, 1997).

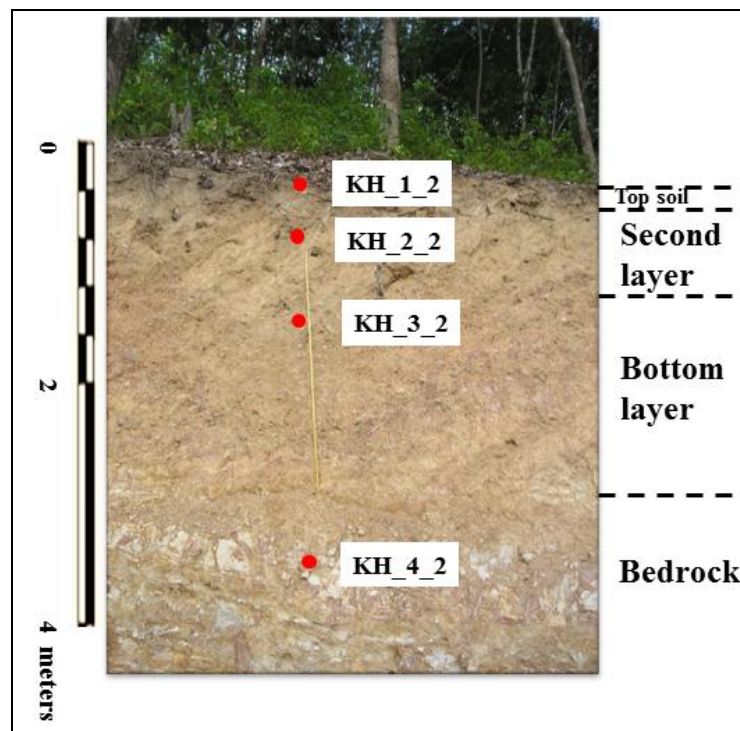


Figure 2.2 Sample of unconsolidated sediments from Khao Khohong Mountain. Bedrock is a sand/siltstone, red points are sample site.

The unconsolidated sediment samples were taken as disturbed samples by shovel as shown in Figure 2.3; samples have been obtained by digging out unconsolidated sediments from the site. The unconsolidated sediment samples were two kilogram per sample and put in a plastic bag, labeled with data of sample and notes were taken about composition, grain size, grain shape, color, texture, and sedimentary structures. The first sample site has nine samples and the second sample site has twelve samples, with some samples being rocks. Samples were carried to laboratory, taken out of the plastic bag and air dried in a room over several weeks.



Figure 2.3 Samples of unconsolidated sediments collected by tool in-situ and samples were put in a plastic bag.

2.3 Density analysis

Theory

Density of a substance is its mass per unit volume. The symbol most often used for density is ρ . Density is defined as mass (m) divided by volume (V), as it follows from Equation 2.1, the SI unit of density is kg/m^3 or g/cm^3 is another unit commonly used in a laboratory.

$$\rho = \frac{m}{V} \quad (2.1)$$

The density of a material can be separated into the matrix density (ρ_m) depends on the components (mineral), and the bulk density (ρ_b) stated with respect to the porosity of a material (e.g. Siegesmund and Dürrast, 2011). Density of minerals is

controlled by their elemental composition and internal bonding and structure. Density of porous sediments is controlled by the mineral composition (grain density), porosity, and saturation (Schön, 2011). The bulk density ρ_b considering dry-sediments conditions is defined as the ratio of the mass of the solid phase m_s to the volume of the whole body V , with

$$\rho_b = \frac{m_s}{V} \quad (2.2)$$

and the matrix density of the sediments ρ_s is determined by the ratio of the mass of solid phase m_s to its volume V_s

$$\rho_m = \frac{m_s}{V_s} \quad (2.3)$$

Methodology

The mineral density was determined by the pycnometer methods using water, following ASTM D854 - Standard Test Methods for Specific Gravity of Soil Solids by Water Pycnometer (AASHTO T100 - Standard Method of Test for Specific Gravity of Soils). First, recorded the weighted the mass of the empty clean and dry pycnometer, then the dry sediments sample filled into the pycnometer and the mass was about 5 g. Distilled water was added to fill the about half to three-fourth of the pycnometer (with sample), removing entrapped air, added to fill the pycnometer until full and weighted. Finally, the pycnometer was filled with distilled water only and weighted again (see Figure 2.4). This method was done at the Department of Mining and Materials Engineering, Faculty of Engineering, Prince of Songkla University. The specific gravity of sediment sample was calculated follow

$$\text{Specific Gravity} = \frac{W_p - W_{ps}}{W_p - W_{ps} - W_{psw} + W_w} \quad (2.4)$$

where W_p is the mass of the empty clean pycnometer in g, W_{ps} is the mass of the empty pycnometer and the dry sediment sample in g, W_{psw} is the mass of the pycnometer, dry sediment sample, and water in g, and W_w is the mass of pycnometer and water in g.

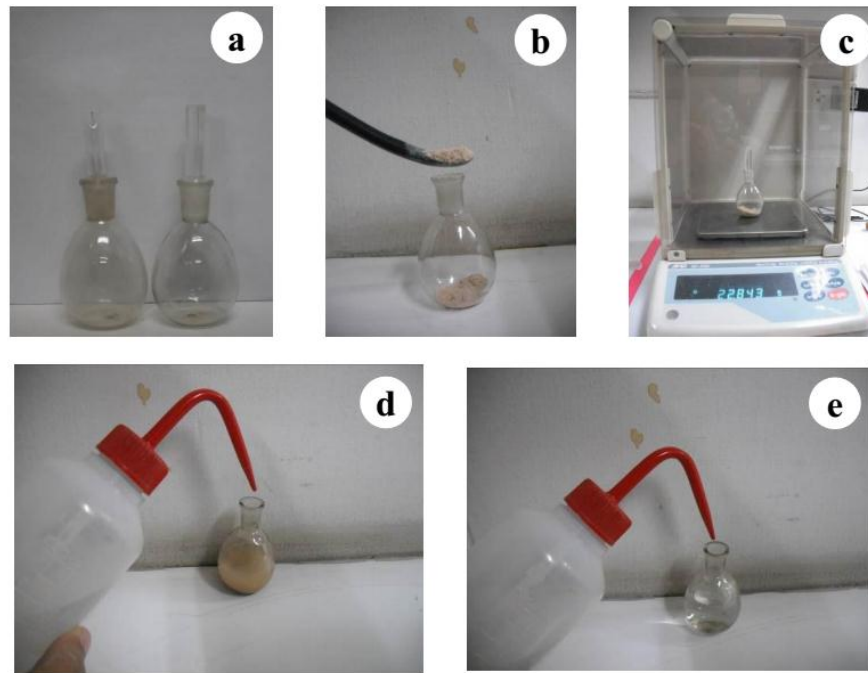


Figure 2.4 (a) Pycnometer or specific gravity bottle 25 mL, (b) sample filled into pycnometer, (c) recorded the weight, (d) distilled water added to fill the pycnometer with sample, and (e) pycnometer was filled with distilled water only.

Density of sediment samples (g/m^3) were calculated from the specific gravity of the sediment sample multiplied by density of water (g/m^3). For example, sample KB_5_2 with 23.882 g mass of empty clean pycnometer, 29.452 g mass of empty pycnometer and dry sediment sample, 52.208 g mass of pycnometer, dry sediment sample and water, 48.788 g mass of pycnometer and water, the specific gravity is $(23.822 - 29.452)/(23.822 - 29.452 - 52.208 + 48.788) = 2.59$, density is $2.59 \times 1.00 = 2.59 \text{ g}/\text{cm}^3$.

The bulk density of a sample was obtained by measuring the dimensions of a geometric sample container filled with the sediment and by this getting the volume and weight of the dry sample, calculated from Equation 2.2. For example, sample KB_5_2 with 441.5 g mass of dry sediment sample, 262.1 cm^3 volume of dry sediment sample, bulk density is $441.5/262.1 = 1.68 \text{ g}/\text{cm}^3$.

2.4 Porosity analysis

Theory

Porosity is an intrinsic property of every material, the symbol most often used for porosity is ϕ . It refers to the amount of empty space within a material,

exists between the grains of minerals and influences most physical sediment properties, e.g., elastic wave velocities, electrical resistivity, or density (Schön, 2011). Porosity is a measure of the total void spaces in a material, and is the volume of voids over the total volume, between 0 and 1. The value for total porosity can be calculated from

$$\phi = \left(1 - \frac{\rho_b}{\rho_m}\right) \times 100\% \quad (2.5)$$

or defined by the ratio of the volume of its pores V_p to the total volume of the body

$$\phi = \frac{V_p}{V} \times 100\% \quad (2.6)$$

Methodology

For the porosity measurement, first the sediment sample was filled into a beaker with the volume recorded. Then, slowly and carefully the water was poured into the beaker until the water just reaches the top of the sediment sample; it was recorded how much water was used. The porosity was calculated by dividing the volume of water that was used by the total volume of the sediment sample, expressed as percentage. For example, sample KB_5_2 with 1.68 g/cm³ bulk density, 2.59 g/cm³ mineral density, porosity is $1 - (1.68/2.59) = 0.35$ (part of 1).

2.5 Grain Size Analysis

For analyzing the grain size distribution of unconsolidated sediments, the distributions of the coarse particles (gravel and sand, larger than 63 μm) were determined by sieve analysis. Fine particles (silt and clay, smaller than 63 μm) were analyzed by the hydrometer method. Grain sizes can occur in a wide range of sizes from micrometer to centimeters, and the assumption is that the particles are roughly circular with the diameter measured. The method used to determine the grain size distribution in the laboratory followed the ASTM D 422- Standard Test Method for Particle-Size Analysis of Soils (AASHTO T88 - Standard Method of Test for Particle Size Analysis of Soils), however with some slight modifications.

2.5.1 Sieve analysis

Theory

Usually data on sand and gravel fractions have been obtained from sieve analysis, which has marked theoretical and experimental limitations in the way it provides size data. Sieving sorts on the basis of smallest cross-sectional diameter (the plane of the intermediate and short axes- the diagonal length between mesh corners determines the intermediate axis length). Since most sedimentary particles are not spherical, the number of particles that pass through a given sieve is time dependent; there will always be more grains that could pass through a given sieve if they were to land with just the right orientation on the mesh (Blott and Pye, 2001).

Methodology

The sieve analysis followed ASTM C136 - Standard Test Method for Sieve Analysis of Fine and Coarse Aggregates (AASHTO No. T 27 Sieve Analysis of Fine and Coarse Aggregates). Dry sediment samples were mixed and reduced to an amount suitable for testing and selected sieves with suitable openings to get the information required for the material to be tested. The sieves were set in order of decreasing size of opening from top to bottom (see Figure 2.5) and weighed samples are poured into a top sieve which has the largest screen opening. The stack of sieves was then shaken by a mechanical sieve shaker, usually for several minutes. After the shaking is complete the sediment samples on each sieve weighed and recoded show in Table 2.1. The weight of the sample of each sieve is then divided by the total weight to give a percentage retained on each sieve. This method was done at the Department of Civil Engineering, Faculty of Engineering, Prince of Songkla University.

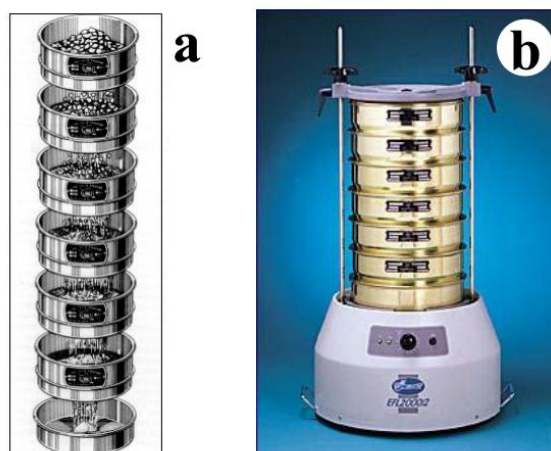


Figure 2.5 (a) Sieves (Solids Wiki, 2012), (b) sieve shaker (QAQC LAB, 2012).

Table 2.1 Sieve analysis determination of sample (KB_5_2).

Sieve No.	Weight of Sample Retained (g)	Cumulative Weight of Sample Retained (g)	Cumulative Retained (%)	Percent Passing (%)
1 1/2"	0.00	0.00	0.00	100.00
1"	20.00	20.00	4.49	95.51
3/8"	63.00	83.00	18.65	81.35
#4	67.00	150.00	33.71	66.29
#10	78.00	228.00	51.24	48.76
#40	112.00	340.00	76.40	23.60
#200	45.00	385.00	86.52	13.48
Pan	60.00	445.00	100.00	0.00

The results of the grain size analyses were presented in a semi logarithmic plot known as particle-size distribution curves. In the semi logarithmic scale, the particle sizes were plotted on the log scale, the percent finer was plotted in arithmetic scale show in Figure 2.6.

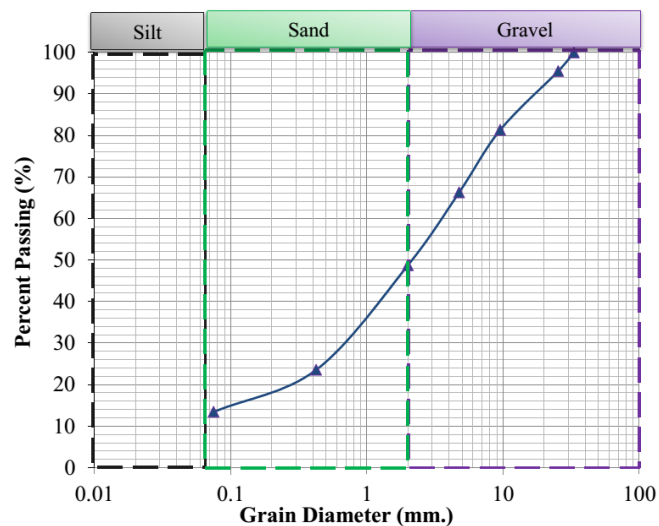


Figure 2.6 Sieve analysis determination of sample (KB_5_2), black square is sand, green square is granular, red square is pebble size.

2.5.2 Hydrometer analysis

Theory

The hydrometer analysis were used to determine the particle size distribution in a soil that is finer than 0.075 mm, which is the smallest standard size opening in the sieve analysis. The procedure was based on the sedimentation of soil

grains in water. It was expressed by Stokes Law, which the velocity of the soil sedimentation was based on the soil particles shape, size, weight, and viscosity of the water. Thus, the hydrometer analysis measured the change in specific gravity of a soil-water suspension as soil particles settle out over time. This method followed ASTM D 422- Standard Test Method for Particle-Size Analysis of Soils (AASHTO T88 - Standard Method of Test for Particle Size Analysis of Soils).

Methodology

In the hydrometer method the first step was to remove the organic matter in the chemical pre-treatment of the sediments as show in Figure 2.7; then the weight was determined and recorded, with 50 g of dry sediment samples and 100 g for sandy sediments, and then transferred into a beaker; then 5 mL of 30% hydrogen peroxide (H_2O_2) were added, followed by distilled water. Adding was done slowly as it will help to prevent excessive foaming. Then the beaker was put on a hot plate (temperature 90 °C) and under a fume hood, while the samples were closely observed for several minutes if there are much gas bubbles. Then hydrogen peroxide was added (5 mL for one time) and repeated until little or no reaction occurs. Then the sediment samples were dried at 105 °C for about 1-2 days; the weight of the dry sediment samples was recorded again (Gee and Bauder, 1987).

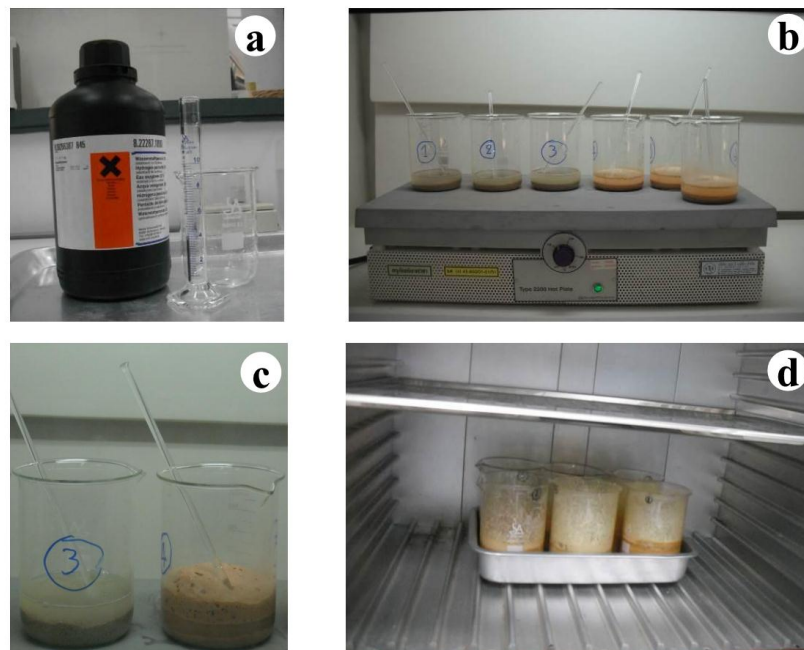


Figure 2.7 (a) 30% Hydrogen peroxide, (b) beaker on hot plate and under a fume hood, (c) gas bubbles of sample, and (d) sediment samples were dried.

The next steps are shown in Figure 2.8. 100 mL of 5 % calgon (50 g of sodium hexametaphosphate ($\text{Na}_6(\text{PO}_3)_6$) and 8.3 g of sodium carbonate (Na_2CO_3) per 1 liter of distilled water) as well as distilled water were added to the sediment samples. The sediment solution was transferred to a dispersion cup (metal milkshake cup) and shaken for about 1 min, then the sediment solution was transferred to a cylinder and water was added up to the 1 liter-mark. Then a plunger was moved up and down through the cylinder for 25-30 plunges; the plunger was removed quickly but gently. In the next step the hydrometer (ASTM NO. 152H, with Bouyoucos scale in g/L) was put into the sediment solution immediately after the plunger was removed from the cylinder and a stop watch was started. A reading of the hydrometer and temperature was done at 50 seconds, and again after 2 hours show in Table 2.2. A 100 ml mixture of the 5% calgon and 900 mL of distilled water was put in a 1,000 mL cylinder; this mixture is used as a blank. Here the reading of the hydrometer and temperature was also recorded at 50 seconds and again after 2 hours (Gee and Bauder, 1987). This method was done at the Department of Earth Science, Faculty of Natural Resources, Prince of Songkla University.

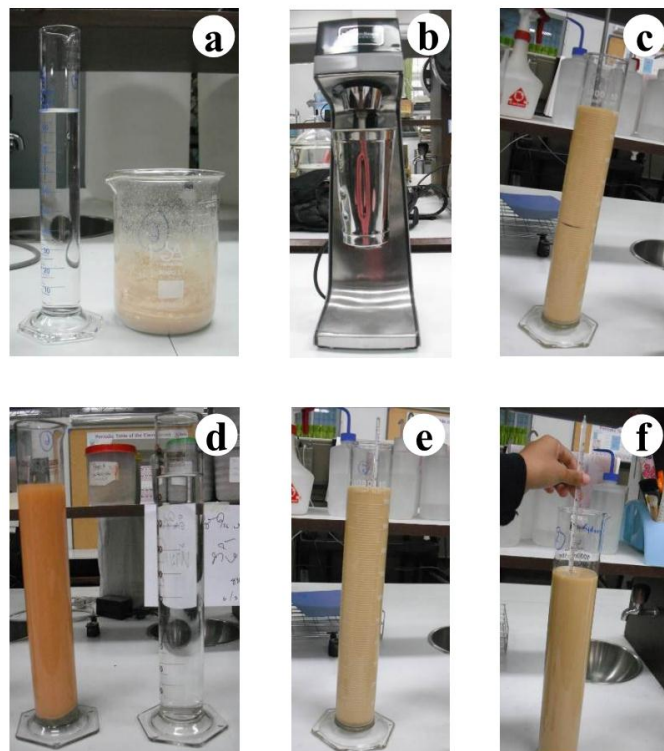


Figure 2.8 (a) 100 mL of 5 % calgon and sediment sample, (b) metal milkshake cup and shaker, (c) moved plunger up and down through the cylinder, (d) sediment solution and blank, (e) reading of the hydrometer, and (f) reading of the temperature.

The value of the hydrometer reading of the sediment solution correction (R_s^*) at time 50 seconds or 2 hours (g/L) is as follow

$$R_s^* = R_s + 0.36(T - 20) \quad (2.7)$$

where, T is the reading temperature of sediment solution at time 50 seconds or 2 hours (g/L), with 20 is ASTM 152H hydrometers calibrated at 20 °C directly in terms of sediment solution concentration, R_s is the density of sediment solution at time 50 seconds or 2 hours (g/L) from

$$R_s = R - R_c \quad (2.8)$$

where R is the hydrometer reading of the sediment solution at time 50 seconds or 2 hours (g/L), R_c is the calgon from temperature correction at time 50 seconds or 2 hours (g/L) with

$$R_c = A - 0.5(T - B) \quad (2.9)$$

where A is the hydrometer reading of calgon at time 50 seconds or 2 hours (g/L), T is the temperature reading of the sediment solution at time 50 seconds or 2 hours (g/L), and B is the temperature reading of calgon at time 50 second or 2 hour (g/L).

Table 2.2 Hydrometer analysis of sample KH_3_2.

Name	Weight (g)	Reading hydrometer at 50 sec (g/L)	Reading temperature at 50 sec (g/L)	Reading hydrometer at 2 hrs (g/L)	Reading temperature at 2 hrs (g/L)
calgon	-	10.00	23.00	10.00	20.00
KH_3_2	49.43	46.00	24.00	37.50	21.50

For example, for sample KH_3_2 with the calgon from temperature correction at time 50 seconds is $10.00 - 0.5(24.00 - 23.00) = 9.50$ g/L; calgon from temperature correction at time 2 hours = $10.00 - 0.5(21.50 - 20.00) = 9.25$ g/L; density of sediment solution at time 50 seconds is $46.00 - 9.50 = 36.50$ g/L; density of sediment solution at time 2 hours is $37.50 - 9.25 = 28.25$ g/L; the reading of the hydrometer of the sediment solution correction at time 50 seconds is $36.50 + 0.36(24.00 - 20) = 37.94$ g/L; and the reading of the hydrometer of the sediment solution

correction at time 2 hours is $28.25+0.36(21.50-20)=28.79$ g/L. The results of the grain size analyses are presented in percentage of clay, silt, and sand follow

$$\text{clay fraction: } \% \text{ clay} = \left(\frac{R_S^* \text{ at } 2\text{hr}}{\text{weight of dry sample(g)}} \times 100 \right) \quad (2.10)$$

$$\text{silt fraction: } \% \text{ silt} = \frac{R_S^* \text{ at } 50\text{s} - R_S^* \text{ at } 2\text{hr}}{\text{weight of dry sample(g)}} \times 100 \quad (2.11)$$

$$\text{sand fraction: } \% \text{ sand} = 100 - \left(\frac{R_S^* \text{ at } 50\text{s}}{\text{weight of dry sample(g)}} \times 100 \right) \quad (2.12)$$

For example, for sample KH_3_2 the percentage of clay is $(28.79/49.43) \times 100\% = 58.24\%$, the percentage of silt is $[(37.94 - 28.79)/49.43] \times 100\% = 18.51\%$, and the percentage of sand is $100 - [(37.94/49.43) \times 100\%] = 23.24\%$. The amount of each particle fraction, sand, silt and clay, determines the sediment texture and present in textural triangle for sediment textural analysis classification, for example, sample KH_3_2 is clay as shown in Figure 2.9.

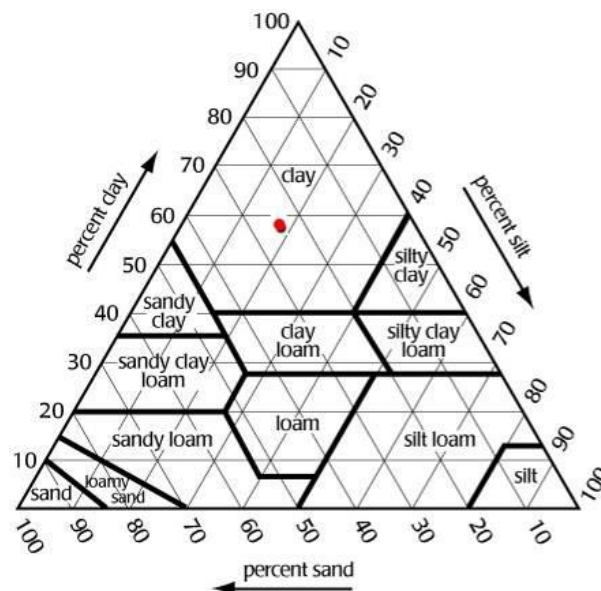


Figure 2.9 Triangle with the textural classification, red circle is sample of KH_3_2.

The results from the sieve analysis and hydrometer method were compared by using the value of the sand grain size for comparative calculations.

2.6 X-Ray Diffraction

Theory

X-ray diffraction (XRD) is the most widely used technique for mineral identification, particularly for minerals of very small size, where X-rays are diffracted by the atomic layers in crystals. As each different mineral has a distinct set of atomic layer spacing (called d spacing), a suite of measurements can be used to identify the mineral (Harris and White, 2008). All crystalline minerals in a sample can be identified from one XRD scan, provided that they are present in sufficient abundance; however, XRD will not detect non-crystalline components (e.g., the allophane clays) in a sample because they have no regular atomic planes. The relationship between the wavelengths of the X-ray used, the angle between the incident and the diffracted X-rays, and the distance between the atomic layers causing the diffraction is given by the Bragg's law equation

$$2d \sin \theta = n\lambda \quad (2.13)$$

where d is the atomic layer spacing (in angstrom units) between the diffracting planes, θ is half the angle between the incident X-ray and the diffracted X-rays, n is an integer ($n=1$ for first-order diffraction peaks, 2 for second-order peaks, etc.), λ is the wavelength of the radiation used, for $Cu_{K\alpha}$ radiation ($\lambda = 1.5418 \text{ \AA}$) (Lewis and McConchie, 1994).

Methodology

Samples for the powder diffraction studies were finely ground ($<5 \mu\text{m}$) and completely homogeneous. The fine powder was prepared for analysis by packing the powder into the well (about 2 mm deep) of a sample holder designed to fit into the goniometer. This method was done at the Scientific Equipment Center, Prince of Songkla University and the X-ray diffractometer as shown in Figure 2.11 was X'Pert MPD, PHILIPS, Netherlands. Data were collected from random orientation powder samples using a $Cu-K\alpha$ source at 40 kV and 30 mA from 5° to 90° 2θ in 0.05° steps 0.154 nm (CuK_{α}) of wavelength, and $3^\circ/\text{min}$ of scan speed. Information gained from diffraction angles and relative peak intensities were used to establish structural details of the minerals using the *International Powder Diffraction File* (PDF) database (see Figure 2.10), compiled by the *Joint Committee for Powder Diffraction Standards* (JCPDS) show in Table 2.3.

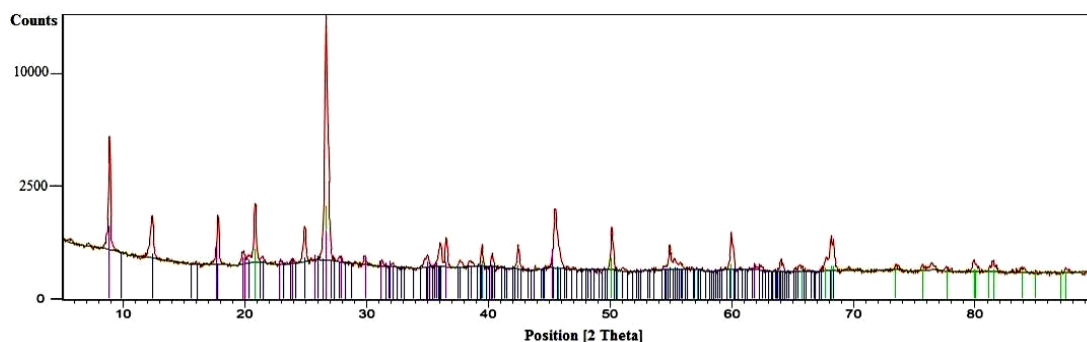


Figure 2.10 International Powder Diffraction File (PDF) database of KB_5_2.

Table 2.3 Joint Committee for Powder Diffraction Standards (JCPDS) of KB_5_2.

Sample Name	JCPDF No.	Chemical Name	Chemical Formula
KB_5_2	03-065-0466	Quartz low, syn	SiO_2
	01-080-0886	Kaolinite 1\ITA\RG	$\text{Al}_2(\text{Si}_2\text{O}_5)(\text{OH})_4$
	00-026-0911	Illite-2\ITM\RG#1[NR]	$(\text{K},\text{H}_3\text{O})\text{Al}_2\text{Si}_3\text{AlO}_{10}(\text{OH})_2$



Figure 2.11 X-ray Diffractometer, PHILIPS, The Netherlands.

2.7 Scanning electron microscopy

Theory

The scanning electron microscope (SEM) uses electrons instead of light to form an image (Schweitzer, 2010). Accelerated electrons carry significant amounts of kinetic energy, and this energy is dissipated as signals produced by electron-sample interactions. These signals include secondary electrons, backscattered electrons (BSE), diffracted backscattered electrons (EBSD), photons (characteristic

X-rays that are used for elemental analysis and continuum X-rays), visible light (cathodoluminescence–CL), and heat. Secondary electrons can show morphology and topography on samples and backscattered electrons are for illustrating contrasts in composition in multiphase samples. X-ray generation is produced by inelastic collisions of the incident electrons with electrons in discrete orbitals (shells) of atoms in the sample (Swapp, 2013).

Methodology

As the SEM utilizes vacuum conditions and uses electrons to form an image, special preparations must be done to the sample. All water must be removed from the samples because the water would vaporize in the vacuum. All metals are conductive and require no preparation before being used. All non-metals need to be made conductive by covering the sample with a thin layer of conductive material. This is done by using a device called a sputter coater. The sputter coater uses an electric field and argon gas shown in Figure 2.12 (b). The sample is placed in a small chamber that is at a vacuum. Argon gas and an electric field cause an electron to be removed from the argon, making the atoms positively charged. The argon ions then become attracted to a negatively charged gold foil. The argon ions knock gold atoms from the surface of the gold foil. These gold atoms fall and settle onto the surface of the sample producing a thin gold coating (Schweitzer, 2010). This method was done at the Scientific Equipment Center, Prince of Songkla University and a Scanning Electron Microscope, Quanta 400, FEI, Czech Republic was used (see Figure 2.12 (c)). Test condition used following mode: high vacuum, voltage: 20.00 kV, detector: Silicon Drift Detector (SDD) and Everhart Thornley Detector.

Backscattered electron images in the SEM displayed compositional contrast that results from different atomic number elements and their distribution. Energy dispersive spectroscopy (EDS) allows to identify what those particular elements are and their relative proportions. Initial EDS analysis usually involves the generation of an X-ray spectrum from the entire scan area of the SEM. Below in Figure 2.13 is a secondary electron image of a sample and the corresponding X-ray spectra that was generated from the entire scan area. The Y-axis shows the counts and the X-axis shows the energy level of those counts. The EDS software is from Oxford (England).

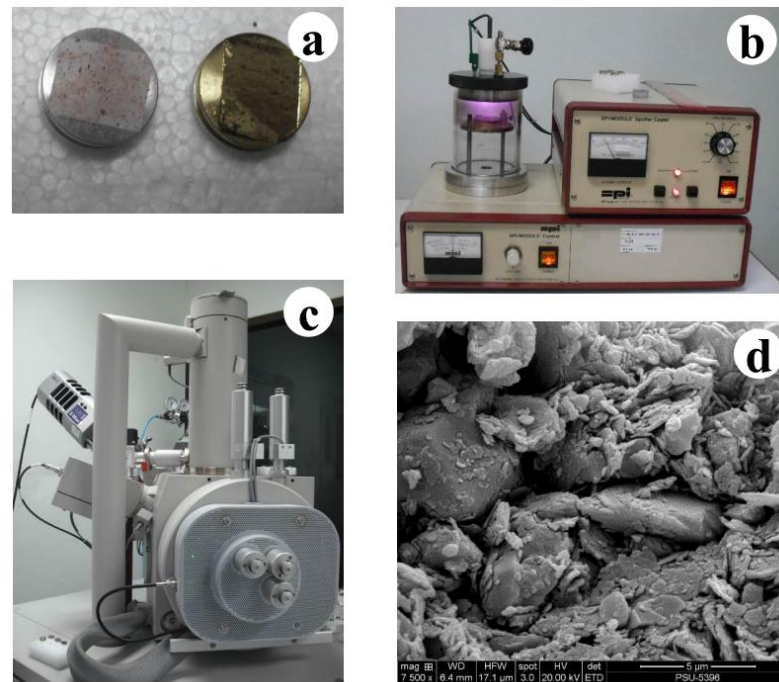


Figure 2.12 (a) Sample before and after gold coating, (b) sputtering equipment, (c) Scanning Electron Microscope, Quanta 400, (d) image of sample of KH_1_2.

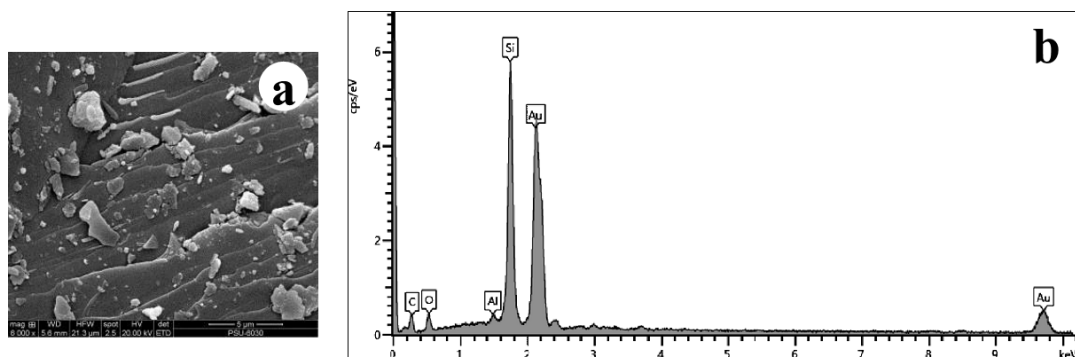


Figure 2.13 (a) SEM image of sample of KB_6_3, (b) graph of KB_6_3 from EDS software (Oxford, England).

2.8 Hydraulic conductivity

Theory

Hydraulic conductivity (K) is a property that provides information about the speed water moves through a material. It is directly related to the porosity and permeability of the material and the density of the water (Herod, 2011). Darcy's law states that the velocity water flows through a material is dependent on the material, which it flows through and the hydraulic gradient, which is the difference in

water level between two points of measurement divided by the distance between them (Herod, 2011).

$$Q = -KA \left(\frac{h_{in} - h_{out}}{L} \right) \quad (2.14)$$

where Q is the discharge or the amount of water that flows out of a material over a set amount of time, K is the hydraulic conductivity, A is the cross sectional area perpendicular to the flow, L is flow path length, h is hydraulic head, Δ denotes the change in h over the path L and $(h_{in}-h_{out})/L$ is the hydraulic gradient (i) (Herod, 2011). Figure 2.14 shows the Darcy's experiment.

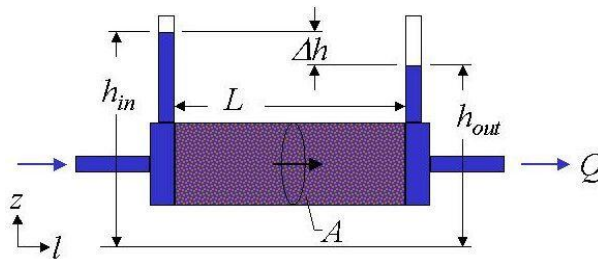


Figure 2.14 Darcy's experiment (Brown, 2013). Z represents vertical and l horizontal dimension direction.

Permeability characterizes the ability of sediment to transmit a fluid or a gas. It connects the fluid/gas flow rate with the applied pressure gradient and the fluid/gas viscosity and controlled by the connected passages of the pore space. For a given hydraulic head gradient, a higher the permeability means a higher fluid/gas velocity. Permeability as defined by Darcy's law is in fact a property of both the soil and the fluid (Barends, 2013).

$$K = \frac{\kappa v}{\mu} \quad (2.15)$$

where κ is the intrinsic permeability in m^2 , K is the hydraulic conductivity in m/s , v is the volumetric weight of the fluid and μ is the dynamic viscosity of the fluid.

The hydraulic conductivity of sediment depends on several factors e.g. fluid viscosity, pore size distribution, grain size distribution; void ratio, roughness of mineral and degree of sediment saturation. Other major factors that affect the permeability of clays are the ionic concentration and the thickness of layers of water held to the clay. Two standard laboratory tests are used to determine the hydraulic

conductivity of sediment, the constant head test (for coarse grained sediment) and the falling head test (for fine grained sediment) (e.g., Das, 2006).

Methodology

A falling head permeability test device was designed and built at the Department of Physics, Faculty of Science, Prince of Songkla University, shown in Figure 2.15 and 2.16, following ASTM D5084-03 Standard Test Methods for Measurement of Hydraulic Conductivity of Saturated Porous Materials Using a Flexible Wall Permeameter. First, the inside diameter of the upper and lower chambers were measured, and then the average inside diameter of the chambers calculated and recorded. A porous stone was placed on the inner support ring in the base of the chamber; then a filter paper was placed on top of the porous stone and the chamber on top of the filter paper. The mixed sediment sample was poured into the lower chamber until full; the top surface of the sediment samples was leveled and a filter paper, the upper porous stone, the support ring and upper chamber were placed as shown in Figure 2.16. The sediment samples length and diameter inside the standpipe was measured and recorded. Water flows from the standpipe through the sediment. The initial head difference h_1 at time $t=0$ was recorded, and water flows through the sediments specimen such that final head difference at time $t=t_1$ is h_2 , temperature and time were recorded. The flow rate of the water through the specimen at any time t can be given by

$$K = \frac{aL}{At} \ln \frac{h_1}{h_2} \quad (2.16)$$

where, K is Hydraulic conductivity in cm/sec, a is cross-section of tube in cm^2 , L is height of soil sample in cm, A is cross-section of soil sample in cm^2 , t is time of test in second, h_1 is height of water table at time t_0 in cm, h_2 is height of water table at time t_1 in cm.

Accordingly, the inside diameter of the chambers was 9.7 cm, the inside diameter of the standpipe 0.58 cm, 73.90 cm^2 was the area of the sediment sample (A), and 0.26 cm^2 the area of the standpipes (a). For example, sample KH_1_2, the length of the sediment samples 11.60 cm, 244.2 seconds was the recorded time, 4 cm the height of the water table at time t_0 , 120 cm the height of water table at time t_1 , therefore $6.0 \times 10^{-3} \text{ cm/sec}$ was the hydraulic conductivity for this sample following Equation 2.16.

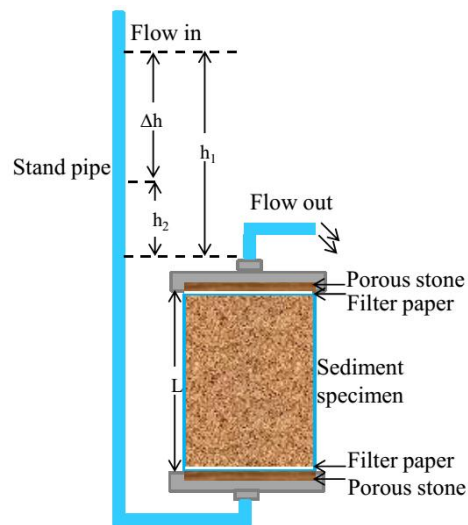


Figure 2.15 Schematic diagrams of falling head permeability test.

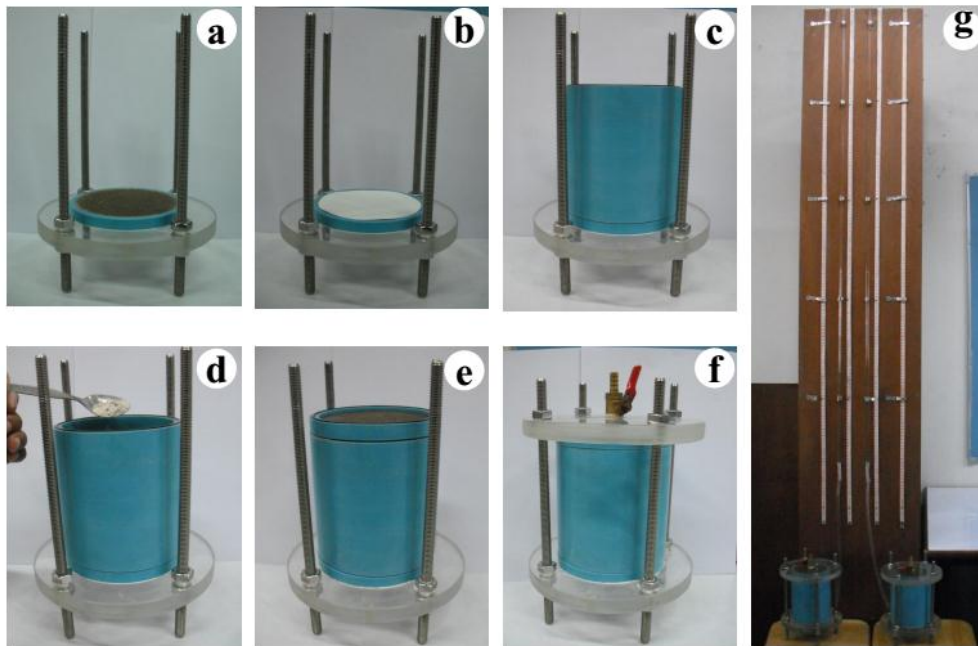


Figure 2.16 Steps of measurement the hydraulic conductivity: (a) First placed one porous stone on the inner support ring in the base of the chamber, (b) placed a filter paper on top of the porous stone, (c) placed chamber on top the filter paper, (d) poured sediment samples into the lower chamber, (e) placed the filter paper, porous stone and support ring on top surface of the sediment samples, (f) placed top of chamber, and (g) shows the assembled falling head permeability test.

2.9 Electrical resistivity

The electrical resistivity ρ (in unit Ohm-m) relates the electrical potential and current to the geometrical dimension of the specified region; it is the inverse of the conductivity. Assuming a homogeneous cylindrical solid of length L in meters and cross section area A in square meters, having resistance R in ohms between the end faces, the resistivity can be expressed by the follow equation (Telford et al., 1990)

$$\rho = \frac{RA}{L} \quad (2.17)$$

2.9.1 Electrical resistivity laboratory measurement

Electrical resistivity measurements in the laboratory were modified from the ASTM G187 - Standard Test Method for Measurement of Soil Resistivity Using the Two-Electrode Soil Box Method (AASHTO T 288-91 Standard Method of Test for Determining Minimum Laboratory Soil Resistivity). The sediment box has a length of 0.078 m; 0.052 m was the width, and 0.065 m the height, so 0.003 m² the area, and 0.043 m of area divided by the width. This method using the sediment box was tested with a salt (NaCl) solution with different concentrations. Figure 2.17 shows the comparison between the resistivity from the laboratory using the sediment box and resistivity from Schlumberger (2000). For a range of different NaCl concentrations both values show a good similarity.

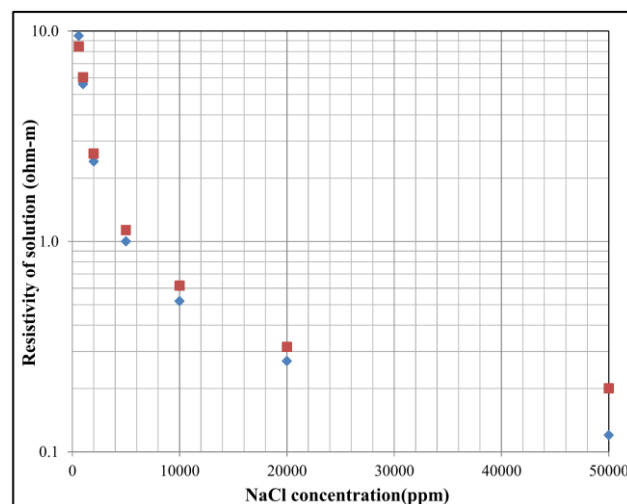


Figure 2.17 Comparisons between resistivity from laboratory for a NaCl solution (red square) and resistivity from Schlumberger (2000) for a NaCl solution (blue diamond).

Sediment samples were compacted in the box with the weight recorded. Two voltage electrodes were connected to the sediment sample through electrically conductive aluminum foil at both ends of the box. Cables were connected with the sample, a power source and a current and voltage meter. Current and voltage were measured and converted into apparent resistivity shown in Figure 2.18, recorded value of current and calculated electrical resistivity from Equation 2.18. The electrical resistivity was determined under laboratory conditions at room temperature, around 28 °C, with increasing water saturation from 0 to 100% of the sample in several steps, around 14-15, as following

$$\rho = \left(\frac{V}{I} \right) \left(\frac{A}{s} \right) \quad (2.18)$$

where ρ is the electrical resistivity in Ohm-m, V is the electrical potential in volt, I is the electrical current in ampere, A is the cross sectional area in m^2 , and s is the length in m. For example, for sample KH_1_2, 0.078 m is the length, $0.003 m^2$ is the area, 0.0050 A of is the electrical current, and 10 volt was the electrical potential. Therefore, the resistivity is $(10/0.005) \times (0.003/0.078) = 86,499$ Ohm-m calculated from Equation 2.18.

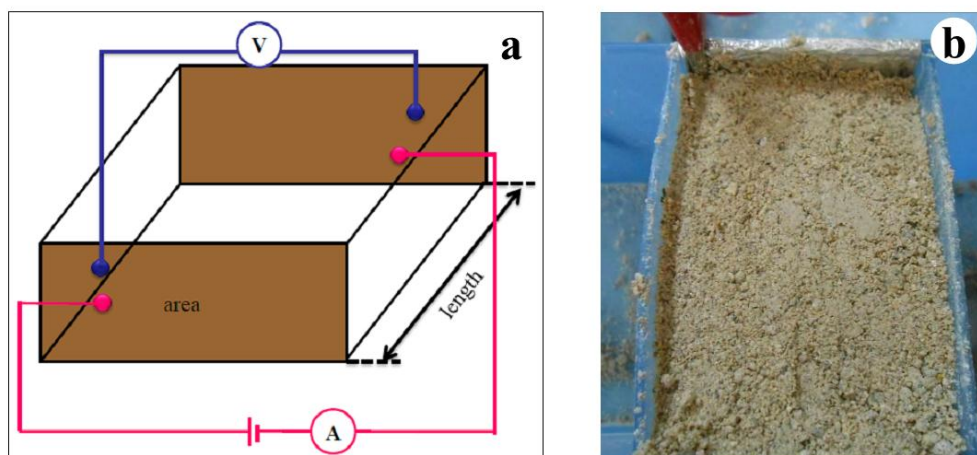


Figure 2.18 (a) Schematic diagram of the electrical laboratory measurements, (b) photo of the sediment samples in the box.

The results of the electrical resistivity were presented in a semi logarithmic plot, where the electrical resistivity was plotted on the log scale, and the water saturation was plotted in arithmetic scale as show in Figure 2.19.

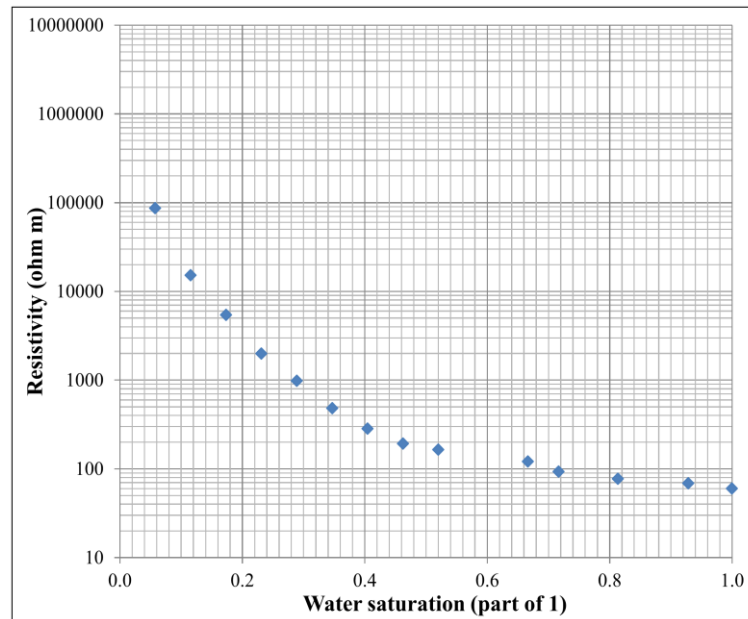


Figure 2.19 Correlation between electrical resistivity and water saturation of KH_1_2.

2.9.2 Electrical resistivity modeling

The resistivity of a saturated porous rock can be expressed by Archie's law (Telford et al., 1990) as below

$$\rho = aS^{-n}\phi^{-m}\rho_w \quad (2.19)$$

where S is the degree of the water saturation, ϕ is the porosity, ρ_w is the resistivity of water, m is the tortuosity factor (m are used like porosity exponent, shape factor, or cementation degree), n is the saturation exponent, and a is the constant (reflects the influence of mineral grains on current flow) (Kirsch, 2006).

For the interpretation of the resistivity data the factors saturation, porosity and clay content (clayey material is characterized by low electrical resistivity) were identified as crucial. For the conductivity of clay bearing sandstones and sediments following model of Sen et al. (1988) has been used, with

$$\sigma = S^n \phi^m a^{-1} [\sigma_w + A Q_v / (1 + C Q_v / \sigma_w)] \quad (2.20)$$

where, σ is soil/sediment conductivity in S/m ($\sigma = 1/\rho$), S is the degree of the water saturation, ϕ is porosity (a porosity decrease with increasing water saturation was observed during the laboratory measurements due to swelling of clay minerals; porosity values are shown in Appendix A, Table A.5), σ_w is the conductivity of water,

m is the tortuosity factor, n is saturation exponent, a is the constant, $A=1.94 \times m$ in (S/m)/(mol/l) and $C = 0.7/Q_v$ in S/m, Q_v (in mol/l) is the concentration of Na-exchange cations relative to the water saturated pore space, which depends on the cation exchange capacity (C_{ex}) in mol/g and the matrix specific density ρ_m . Q_v replaced by $Q_v^* = Q_v/S$ (for partial saturation; see Günzel, 1994), with

$$Q_v = C_{ex} \rho_m \frac{1-\phi}{\phi} \quad (2.21)$$

The dependence of the exchange capacity C_{ex} on the relative clay and silt content (mineral composition of clay) P_{clay} and P_{silt} is estimated by a relationship found by Günzel (1994), with

$$C_{ex} = 0.47(P_{clay} + 0.2P_{silt}) \quad (2.22)$$

For example, Archie's law was used with sample KB_8_2, with 9% degree of the water saturation, 35% porosity, 0.02 Ohm-m resistivity of water, and a , m and n were changed, which moved up or down of the fitted curve. The constant a was kept at 1 if possible, with mainly n and m were changed until the laboratory data points and the modeled line overlapped. For this sample, finally, a was 1, m was 2.1 and n was 1.3, with 68,731 Ohm-m resistivity calculated from Equation 2.19 (see Figure 2.20).

For example, modified Archie's law was used for sample KH_1_2 with 6% degree of the water saturation, 44% porosity, 0.02 Ω m conductivity of water, A is $1.94 \times m$, 28.9 % P_{clay} , 18.6 % P_{silt} , 2.52 g/cm³ mineral density, C_{ex} is $0.47 (0.289 + 0.186) = 0.153$ calculated from Equation 2.22, Q_v is $0.153 \times 5.52 \times ((1 - 0.44)/0.44) = 0.485$ mol/l calculated from Equation 2.21. It was tried to keep a at 1 if possible, with m and n were changed moving up or down the curve until data points and modeled line overlapped (see Figure 2.22 and 2.23). For this this sample a is 1, m is 1.25 and n is 2.55, and with 63,261 Ohm-m of resistivity calculated from Equation 2.20 (see Figure 2.21).

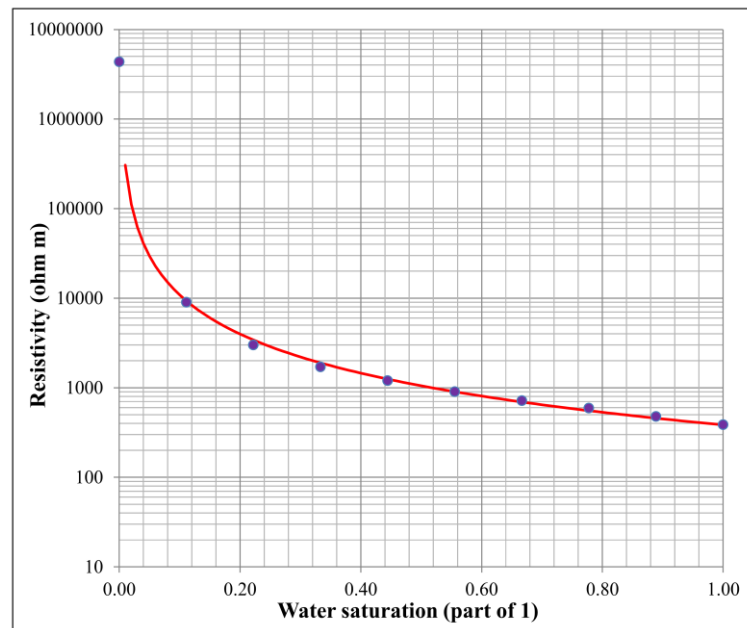


Figure 2.20 Correlation between electrical resistivity and water saturation of KB_8_2, blue circle is resistivity from laboratory and red line is resistivity model using Archie's law.

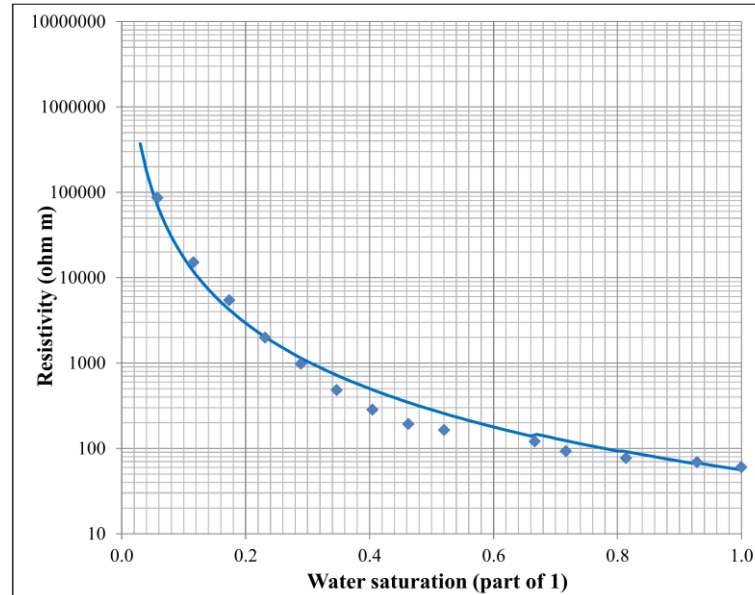


Figure 2.21 Correlation between electrical resistivity and water saturation of KH_1_2, blue circle is resistivity from laboratory and blue line is resistivity model calculated using modified Archie's law.

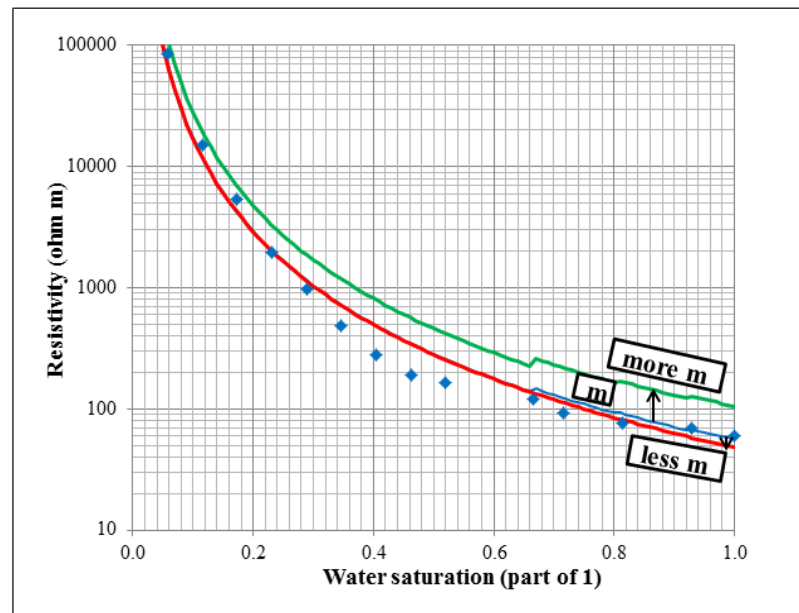


Figure 2.22 Correlation between electrical resistivity and water saturation of KH_1_2, blue circle is resistivity from laboratory, blue line is the resistivity calculated model with $m=1.25$, red line is the resistivity model when m is lower than 1.25 and the green line is the resistivity model when m is larger than 1.25.

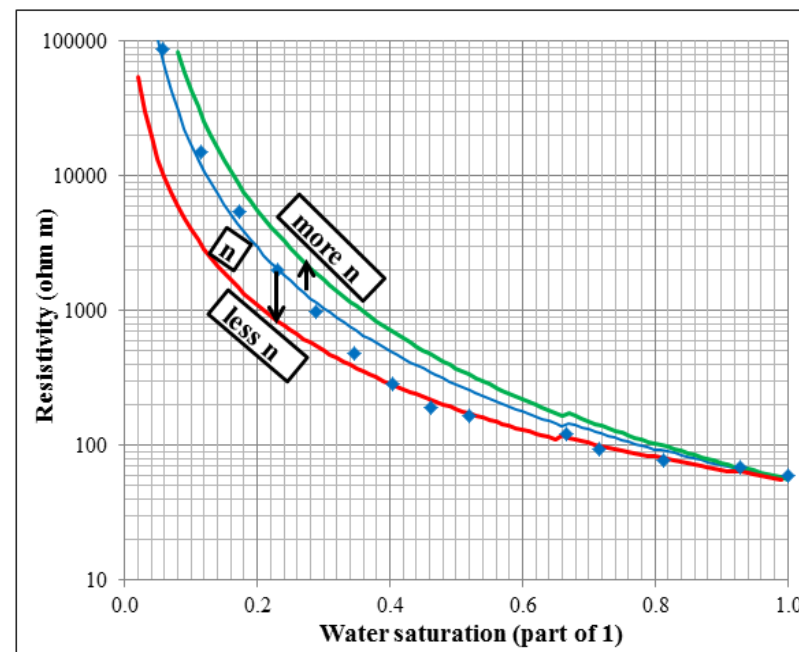


Figure 2.23 Correlation between electrical resistivity and water saturation of KH_1_2, black circle is resistivity from laboratory, red line is resistivity model with $n=2.55$, blue line is resistivity model when n is lower, and green line is resistivity model when n is higher than 2.55.

2.10 Ultrasonic velocity measurements

Theory

There are two groups of seismic waves, surface waves and body waves, with the latter ones being utilized in seismic surveys. The velocity of the propagation of body waves, compressional and shear wave velocity, in any solid earth material can be determined as a function of the density (ρ) and the elastic constants of the material. Compressional waves (the longitudinal, primary or P -wave) propagate in the medium in the same direction as the direction of wave propagation, P -wave velocity (V_p) is given by

$$V_p = \left[\left(k + \frac{4}{3} \mu \right) / \rho \right]^{\frac{1}{2}} \quad (2.23)$$

where κ is bulk modulus in Pa, μ is shear modulus in Pa, and ρ is density in kg/m^3 . Shear waves (transverse, secondary or S -wave) propagate in the medium in the direction perpendicular to the direction of wave travel, S -wave velocity (V_s) is given by

$$V_s = \left(\mu / \rho \right)^{\frac{1}{2}} \quad (2.24)$$

Compressional waves always travel faster than shear wave in the same medium and shear waves do not propagate through the liquids and gases because liquids and gases offer no resistance to shear deformation, so $\mu = 0$ (Sheriff and Geldart, 1995).

Ultrasonic velocity method is a non-destructive testing method based on measuring the travel time. The velocity of these waves traveling in a solid material depends on the density, porosity and elastic properties of the material. The ultrasonic system has two piezoelectric sensors coupled to the object with constant pressure. One of the transducers is stimulated using an ultrasonic pulser and the other is used as a receptor sensor. The transducers are in contact with the sample so that the vibrations are transferred to the sample. The waves travel through the sample and are picked up by the receiver show in Figure 2.24. From the travel time of each wave and the measured length of the sample the velocities can be determined (e.g. Siegesmund and Dürrast, 2011).

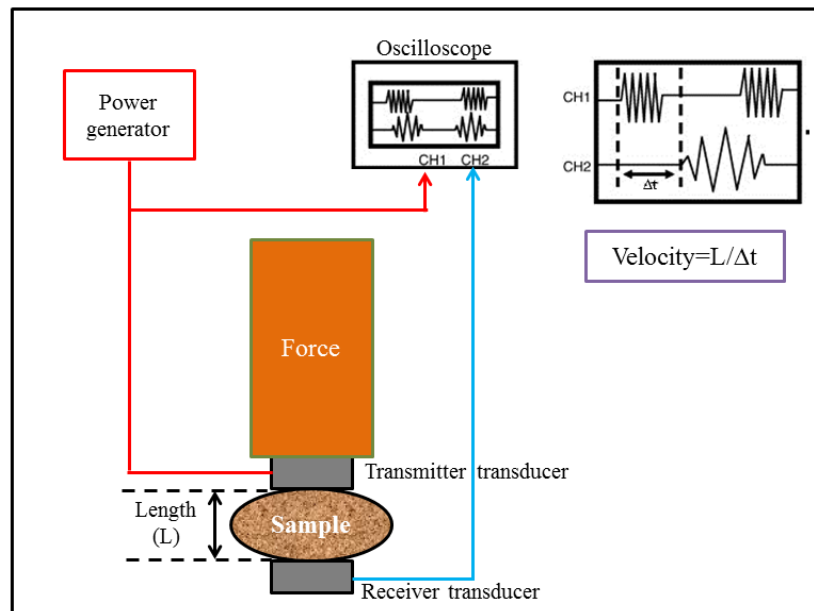


Figure 2.24 Schematic diagram of the seismic laboratory measurements.

Methodology

A complete description is provided in ASTM Test Designation C 597, Standard Test Method for Pulse Velocity through Concrete. For the seismic laboratory measurements transducers with 63 kHz for the P-wave and 33 kHz for the S-waves were used, together with Sonic Viewer-170, OYO. Uniaxial pressure of 0.122 MPa was applied for better contact as shown in Figure 2.25. First, the sediment sample was in a plastic bag which had holes so that any excessive air or water could flow out, by this avoiding any build-up of pore pressure. The sample as placed between the transducers and from this the sample length was determined. Weight was placed on the top transducers to increase the vertical pressure aiming to get clear signals.

Next, Sonic Viewer-170 was connected with power supply, set the power switch on, connected the Sonic Viewer-170 to P-wave transducer. The gain was set at 10-50, filter was set as high cut 1 MHz and low cut 30 KHz, no pre-trigger was used, the sampling range was 100-500 nanoseconds. Before the sample was set up the determination of the zero point is required. Here the transducers were set on each other, a measurement was taken and the cursor key was moved to the position of the first break and by this fixing the time as zero point. Then, the transducers were connected to the samples as illustrated in Figure 2.25 and the P-wave velocity was measured by identifying the first break. For S-wave transducer as similar procedure was carried out. Here the gain was 50-500, the filter a high cut 200 kHz and low cut 500 Hz, no pre-trigger, and a sampling range of 100-500 nanoseconds. The ultrasonic

velocity was determined under laboratory conditions with increasing water saturation from 0 to 100% of the sample in 6-12 steps.

The wave velocity is calculated by using the time taken by the pulse to travel the measured distance between the transmitter and the receiver. The pulse velocity is given by the formula

$$v = \frac{s}{t} \quad (2.25)$$

where v is the velocity (km/s), s is length of sample (cm) and t is delta time (μs). For example, V_P of KB_7_2, 35.36 mm distance, 72.50 μs time, 488 m/s of V_P . V_S of KB_7_2, 34.77 mm distance, 133.10 μs time, 261 m/s of V_S . This method was done at the School of Geotechnology, Institute of Engineering, Suranaree University of Technology, in Nakhon Ratchasima.

Uncertainties come with the identification of the first break by moving the cursor key in discrete steps. One step in the cursor results in different velocities. For example, V_P of KB_7_2, 80.0 μs time at the first break gives 516 m/s for V_P , whereas for the step 78.0 μs time 530 m/s of V_P will be calculated. However, the overall differences are small (see Figure 2.26.)

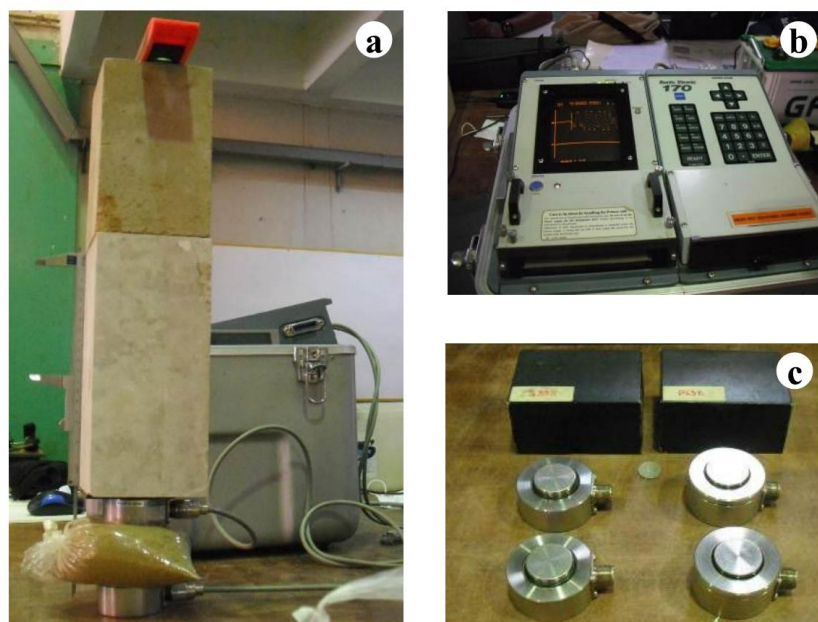


Figure 2.25 (a) Equipment set up in laboratory, (b) Sonic Viewer-170, (c) 63 kHz P-wave (right) and 33 kHz S-waves transducers (left).

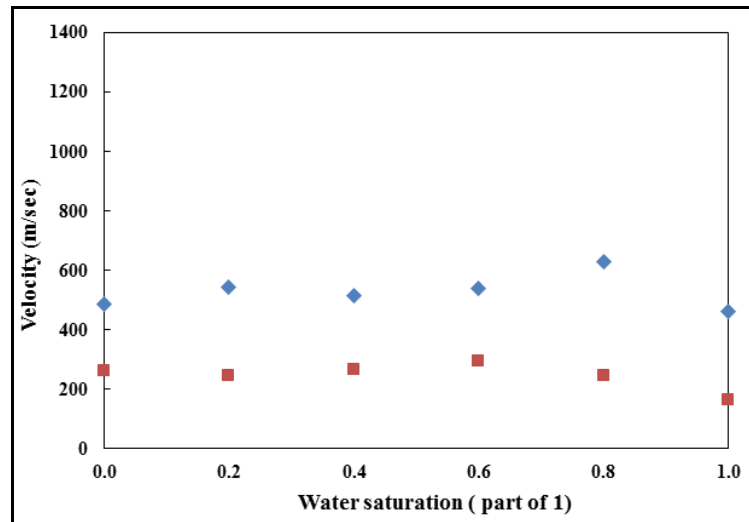


Figure 2.26 Velocity of KB_7_2, blue crystal is V_p , red square is V_s .

2.11 Elastic parameters

Theory

The elastic properties of substances are characterized by elastic modulus or constants which specify the relation between stress and strain. A stress is measured as force per unit area, a compressive stress if it acts perpendicular to the area and a shear stress if it acts parallel to it. A system of compressive stresses changes the volume but not the shape of a body; one of shear stresses changes the shape but not the volume. The strains in a body are deformations which produce restoring forces opposes to the stresses. Tensile and compressive stresses give rise to longitudinal and volume strains which are measured as angle of deformation. It is usually assumed that the strains are small and reversible, that is, a body resumes its original shape and size when the stresses are relieved. Hooke's law states that the stress is proportional to the strain, the constant of proportionality being known as the elastic modulus or elastic constant.

The main two elastic constants for studying elastic wave propagation in the earth are the bulk modulus (κ) and the shear modulus (μ). Shear modulus denoted by G , or S , or μ , is defined as the ratio of shear stress to the shear strain, unit is the Pascal (Pa).

$$\mu = \frac{F/A}{\Delta x/l} = \frac{Fl}{A\Delta x} \quad (2.26)$$

where F is the force which acts, A is area on which the force acts, Δx is transverse displacement, l is initial length. The bulk modulus B or k of a substance measures the substance's resistance to uniform compression. It is defined as the ratio of the infinitesimal pressure increase to the resulting relative decrease of the volume. Its SI unit is the Pascal,

$$k = \frac{\Delta P}{\Delta V/V} \quad (2.27)$$

where, ΔP is the pressure change, ΔV is the volume change, and V is the volume.

Methodology

From the velocity and bulk density the elastic moduli can be calculated, where V_P is the compressional (P) wave velocity in m/s, V_S is shear (S) wave velocity in m/s, and ρ is the density in kg/m^3 (Sheriff and Geldart, 1995), as following

$$\text{Young's modulus } (E) = \rho V_S^2 \left(\frac{3V_P^2 - 4V_S^2}{V_P^2 - V_S^2} \right) \quad (2.28)$$

$$\text{Poisson's ratio } (\sigma) = \frac{V_P^2 - 2V_S^2}{2(V_P^2 - V_S^2)} \quad (2.29)$$

$$\text{Bulk modulus } (k) = \rho \left(V_P^2 - \frac{4}{3} V_S^2 \right) \quad (2.30)$$

$$\text{Shear modulus } (\mu) = \rho V_S^2 \quad (2.31)$$

For example, the elastic modulus of KB_7_2 with 488 m/s P wave velocity, 261 m/s S wave velocity, 1.79 g/cm^3 bulk density at 0% water saturation, the Young's modulus is 0.32 GPa from Equation 2.28, the Poisson's ratio is 0.30 GPa from Equation 2.29, the bulk modulus is 0.26 GPa from Equation 2.30, and the shear modulus is 0.12 GPa from Equation 2.31. Figure 2.27 was shown elastic moduli of KB_7_2.

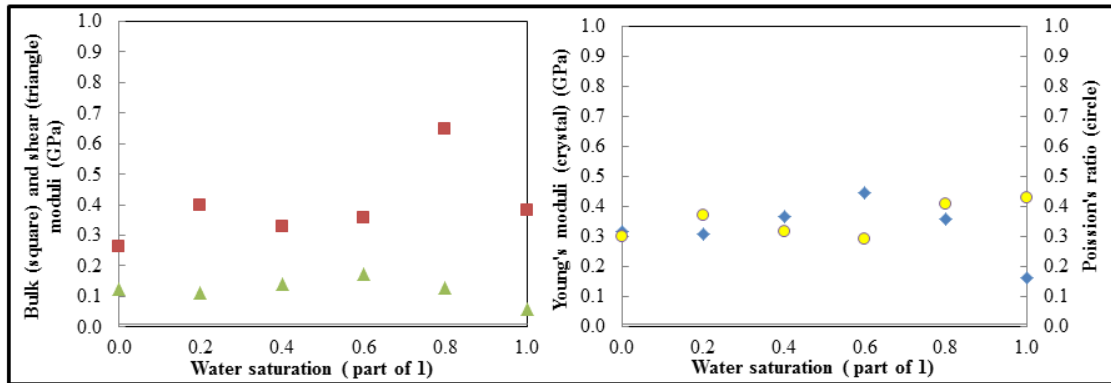


Figure 2.27 Elastic moduli of KB_7_2 , red square is bulk moduli, green triangle is shear moduli, blue crystal is Young's moduli, yellow circle is Poisson's ratio.

CHAPTER 3

RESULTS

3.1 Sample sites

The study area is located in Songkhla Province in Southern Thailand at the eastern boundary of the Hat Yai basin. Its eastern and western rims are bounded by north-south trending mountain ranges. It was previously thought that Gulf of Thailand and the Thailand-Malaysia border respectively bound the northern and southern boundaries of the basin (Lohawijarn, 2005). Generally, the landform features of Hat Yai District are divided into three zones namely hill, terrace and alluvial plain. Hill is comprised low lying hill trending north – south with an elevation of more than 50 meters above mean sea level. It is composed of sandstone, shale, mudstone, quartzite and granite such as Kho Hong Mountain. Terrace forms along Kho Hong Mountain which elevation is ranging from 10 to 50 meters. It is composed of white gravel, medium to coarse-grained clayey sand and silty sand. Alluvial plain is located mainly center and west of Hat Yai City. It is the flood plain of U-Tha Pao and Toey channel with a width ranging from 0.5 km to 3 km. The plain is relatively narrow in the upper part and wider with the shifting of main channel and its distributaries in the lower part. The elevation of this unit is not more than 10 meters above mean sea level (Chalermyanont, 1995).

Geologically, Hat Yai Basin is flanked to the east and west by granitic rocks intruding into Carboniferous and Triassic sedimentary and metamorphic rocks, which form the basement rock of the basin. Carboniferous rock comprises sandstone, siltstone, shale, mudstone, chert, and argillite, whereas Triassic rock is composed of sandstone, siltstone, mudstone, conglomerate, massive limestone and chert. The granites are Late Triassic to Early Jurassic and Late Cretaceous to Early Quaternary in age. They are mainly coarse-grained porphyritic biotite granites with some fine-to medium-grained, muscovite biotite granites and muscovite-garnet granites (Lohawijarn, 2005).

The subsoil in Hat Yai is alluvial and marine deposits. The alluvial deposit was originated from the sediment carried from Mountain such as Wang Pha, Kho Hong Mountain. Generally, the mountain consists of shale, mudstone, sandstone then the sediments are consisted of the product of erosion of these rocks. The alluvium consists of gravel, sand, silt, and clay. Gray to dark soft clay found along and in the vicinity area of Toey River may occur due to changing of its alignment or

abandoned swamp. The reddish to yellowish brown stiff to hard silty clay found at the area away from Toey River can be called as secondary deposit because it is modified in-situ after sedimentation due to weathering process. The marine terrace was formed by transgression and regression of the sea water. The transgression created sand to area whereas clay was formed by regression (Chalermmyanont, 1995).

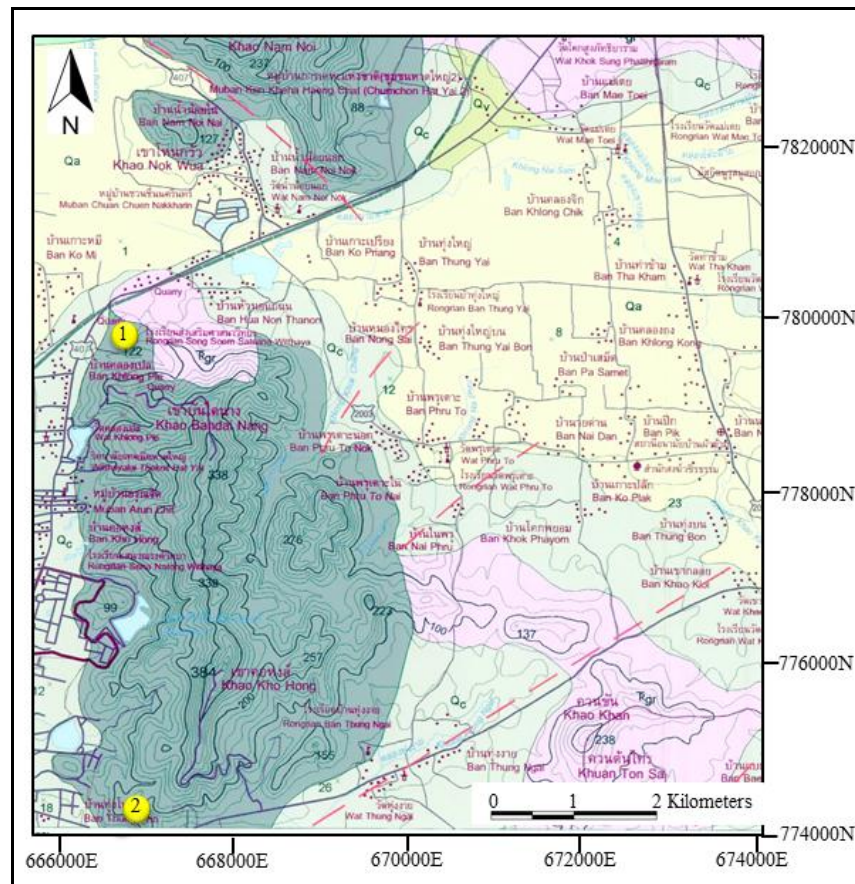


Figure 3.1 Geological map of study area in UTM grid (modified from Department of Mineral Resources, Thailand, sheet 5123 III, Changwat Songkhla, 2006), 1 is granite site, 2 is sandstone site, C is quartzitic sandstone, Tr_{gr} is biotite – muscovite – grained, Q_c is colluvium deposits, Q_a is alluvial deposits.

For this study unconsolidated sediments were taken from the Kho Hong Mountain range, which is trending North–South and underlain by sedimentary rocks ranging in age from Carboniferous to Triassic to Early Jurassic age (Pungrassmi, 1983). The geological map of study area was shown in Figure 3.1. Carboniferous (C) rocks which are the predominant rock type of quartzitic sandstone, bedded chert, siltstone, and shale, grayish white to deep red with fossil of brachiopods, bivalve, trilobite, and conodont. Quaternary deposit covers most of

colluvium deposits (Q_c) and alluvial deposits (Q_a). Colluvium deposits is sand, gravel, slightly clay and slightly, light brown to yellow, moderately coarse- to very coarse – grained, very poorly sorted, sub angular, abundant mottles and small amount iron concretion. Alluvial deposits is sand, silt, and clay, brownish gray to gray, fine – to medium – grained, moderately sorted, sub angular, small amount plant remains, rare iron concretion at low part. Igneous rock is Triassic age, biotite-muscovite-grained, porphyritic biotite granite, adamellite, and quartz veins (DMR, 2006).

Hat Yai city is under the influence of the southwest and northeast monsoon climate, northeast monsoon from October to mid-January and southwest monsoon from mid-May to mid-October. The climate is divided into two seasons including summer from February to July, after end of the northeast monsoon. The weather is getting hot, and the temperature is highest in April. For rainy season from August to January, there will be more rain when northeast monsoon blew through the Gulf of Thailand.

3.2 Outcrops

The two sample sites comprise different bedrock lithology; the first site is mainly granite at a mountain site in different states of weathering show in Figure 3.2. Granite intrusion in local rock, some area is hornfels and some area is granite. The granite has crumbled into a pile of decomposing igneous minerals, and their weathering products - clay, and other new sedimentary minerals. Weathering granite found at the base of granite slopes. Hornfels is a contact metamorphic rock that has been baked and indurated by the heat of igneous intrusions (granite) and have been rendered massive, hard and splinter.

The second site is mainly sandstone with different layers from bedrock to top soil show in Figure 3.3; this area is east of Prince of Songkla University. The outcrop has three main layers, top layer is topsoil, and they are organic matter giving them a darker color. Second layer is unconsolidated sediments, they are clay, silt, sand, gravel and rock fragment, and bottom layer is bedrock, sandstone and red mudstone.

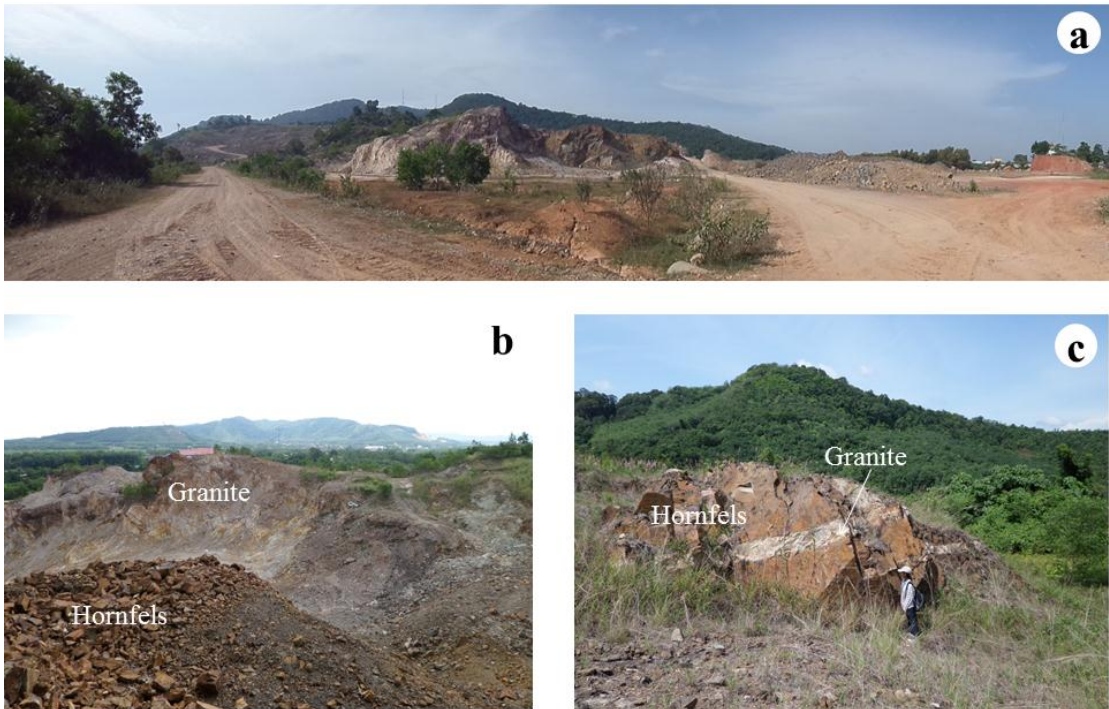


Figure 3.2 (a) Granite site, view to east (b) outcrop of granite and hornfels, (c) granite intrusion in hornfels.



Figure 3.3 Sandstone site, view to north.

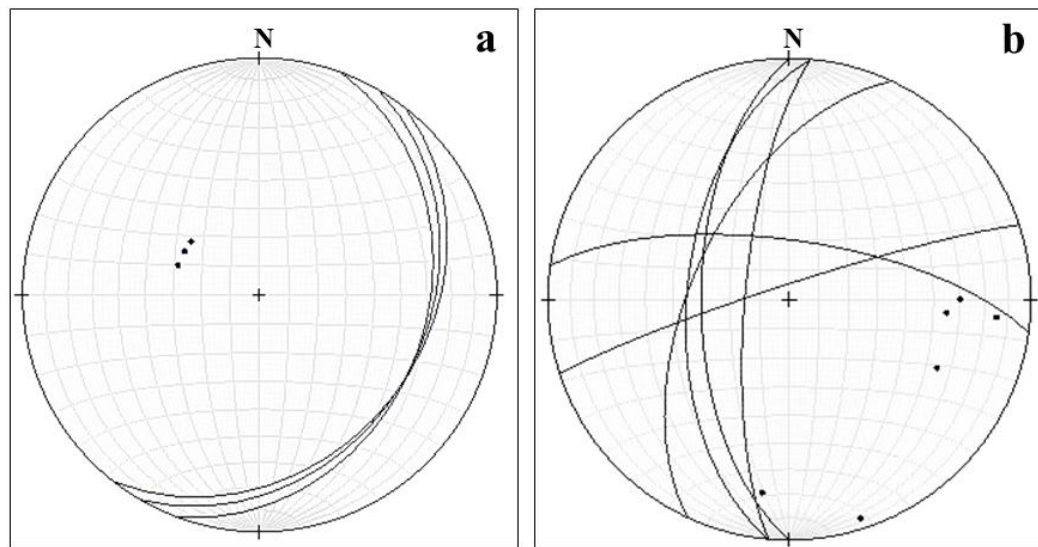


Figure 3.4 Stereo Net plots of (a) layering, (b) fault and joint of the sandstone site. Planes are shown as great circles and as poles.

The sedimentary layering of the area is dipping to the east to southeast from field measurements with 120/30P (dip direction/dip angle P=plane), 110/30P, and 128/30P. Faults and joints are dipping to the north and to the west with 270/60P, 275/75P, 270/55P, 008/70P, 295/57P, and 342/85P. Stereo net plots, lower hemisphere, of both structural elements are shown in Figure 3.4.

3.3 Sample description

Several sediment samples were collected from both sites. From the granite site six samples were collected during the first visit and nine samples during the second as shown in Figure 3.5. Collected samples are from different layers, from the top of the mountain, foothill, below the mountain, and from the nearby surface as shown in Table 3.1. Samples of the granite site were subject to different weathering, with samples near the top of the mountain showing less weathering, near the foothill and below the mountain more weathering; additionally also erosion and transport related phenomena as the later samples were transported and deposited farther away from the mountain.

Sample description comprising color, grain size, grain shape, structure and composition is shown in Table 3.2 and photos of the samples are shown in Figure 3.6.

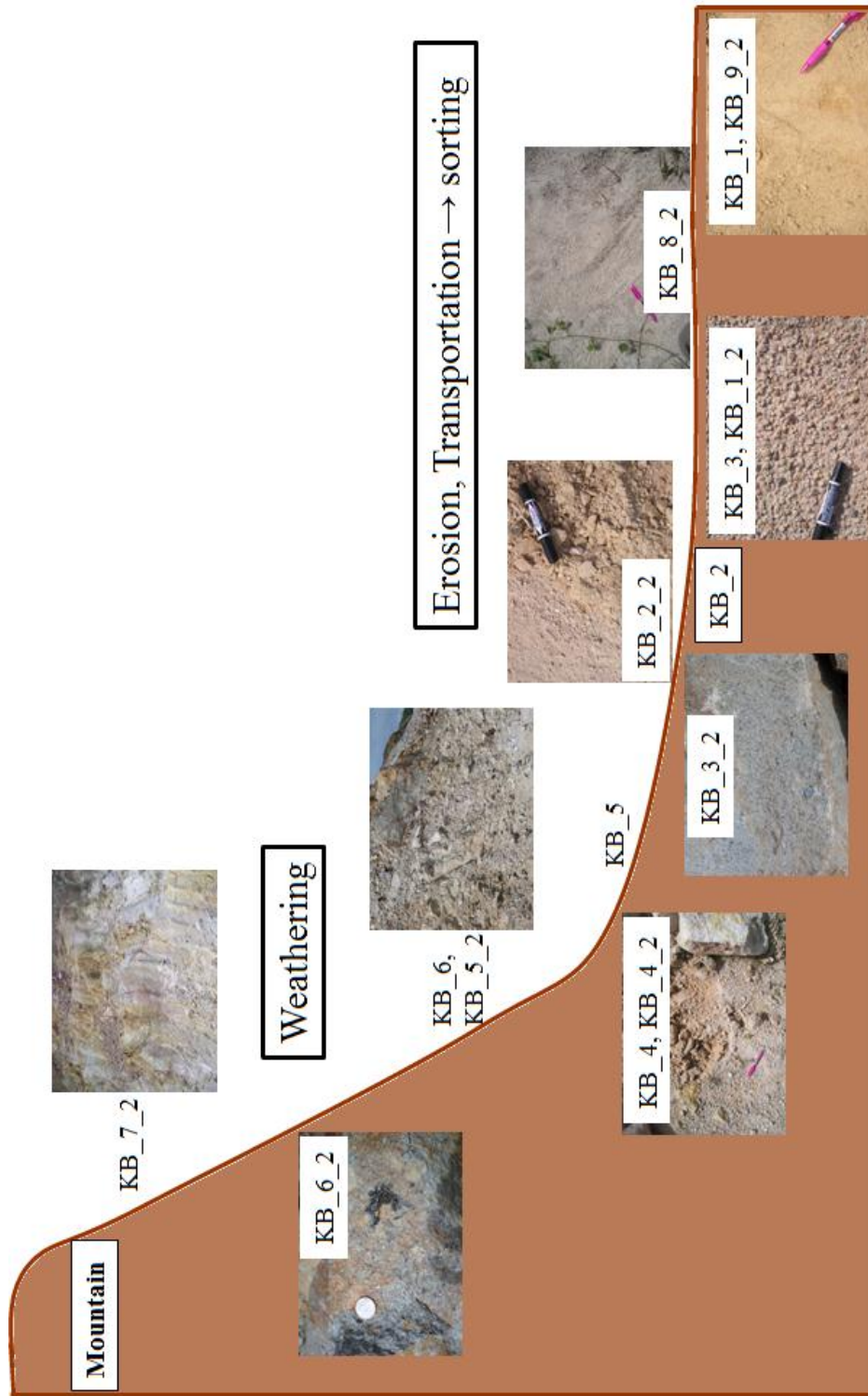


Figure 3.5 Photos and relative location of the sediment samples from the granite site.

Table 3.1 Sediment samples from the granite site.

UTM	Location	Sample name		Type
		29-May-13	20-Jul-13	
0666806 0779853	Mountain		KB_7_2	sediment
	Foothill	KB_6	KB_5_2	sediment
			KB_6_2	rock
0666802 0779972	Below the mountain	KB_2		sediment
		KB_4	KB_4_2	sediment
		KB_5		sediment
			KB_2_2	sediment
			KB_3-2	weathered granite
0667044 0780058 0666795 0779991	Surface	KB_1	KB_9_2	soil
		KB_3	KB_1_2	sediment
			KB_8_2	sediment

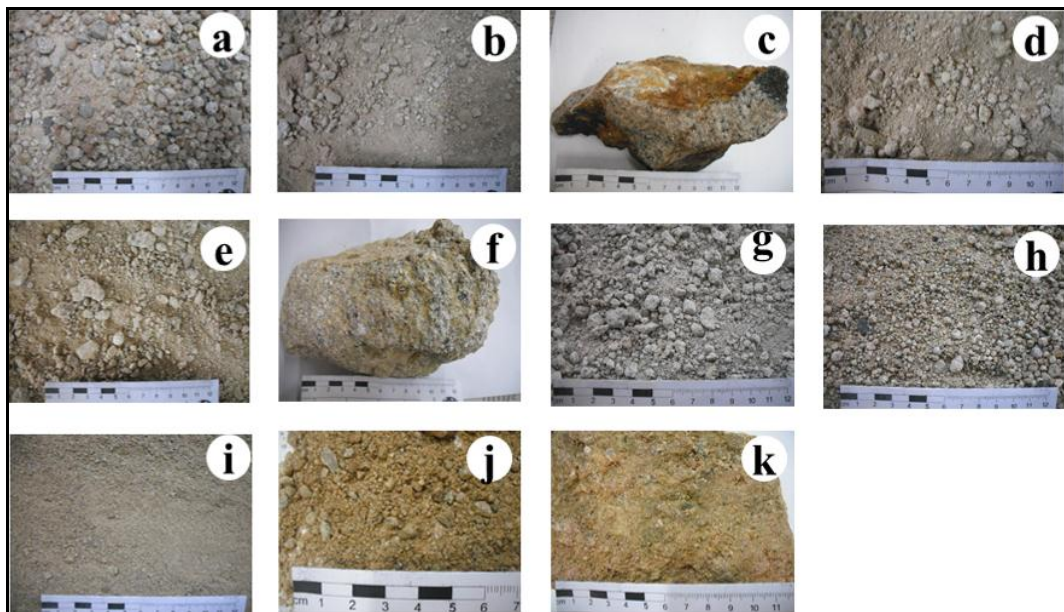


Figure 3.6 Photos of the sediment samples from the granite site; sample (a) KB_1_2, (b) KB_2_2, (c) KB_3_2, (d) KB_4_2, (e) KB_5_2, (f) KB_6_2, (g) KB_7_2, (h) KB_8_2, (i) KB_9_2, (j) KB_2, and (k) KB_5.

Table 3.2 Description of sediment samples from the granite site.

Sample name	Description
KB_1_2	Light brown and grey color, clay to gravel grain size, sub round particles, high sphericity, quartz and fragment, moderately sorted.
KB_2_2	Light brown and grey color, clay to gravel grain size, angular particles, low sphericity, quartz and clay, moderately sorted.
KB_3_2	White, light grey and brown color, coarse sand grain size, quartz, feldspar and hornblende.
KB_4_2	Light brown and light grey color, clay to gravel grain size, angular particles, low sphericity, quartz, clay and rock fragment, moderately sorted.
KB_5_2	Light brown and light grey color, clay to gravel grain size, angular particles, low sphericity, quartz, clay and rock fragment, moderately sorted.
KB_6_2	White, light grey and brown coarse sand grain size, quartz, feldspar and hornblende.
KB_7_2	Light grey color, clay to gravel grain size, angular particles, high sphericity, quartz, clay and rock fragment, well sorted.
KB_8_2	Light brown and light grey color, clay to sand grain size, sub round particles, high sphericity, quartz and clay, well sorted.
KB_9_2	Brown color, clay to gravel grain size, sub angular to sub rounded particles, low sphericity quartz, clay and rock fragment and well sorted.
KB_2	Yellow brown and light grey color, clay to gravel grain size, angular to sub angular shape, quartz and fragment, well sorted.
KB_5	Yellow and light grey color, phaneritic texture, quartz and feldspar.

At the sandstone site thirteen samples were collected during the first visit and twelve samples during the second visit as shown in Figure 3.7. Collected samples were from different layers and different vertical profiles as shown in Table 3.3. The descriptions of the samples are shown in Table 3.4 and in Figure 3.8 photos of the samples are shown.

Table 3.3 Sediment samples from the sandstone site.

Location		Sample name		Type
		29-May-13	20-Jul-13	
Northern profile	Top soil	KH_10	KH_1_2	soil
	Yellow gravel layer	KH_11	KH_2_2	sediment
	Sediment layer	KH_12	KH_3_2	sediment
	Soft rock	KH_13		sediment
	Hard rock		KH_4_2	rock
Central profile	Top soil		KH_5_2	soil
	Yellow gravel layer	KH_6	KH_6_2	sediment
	Sediment layer	KH_7	KH_7_2	sediment
	Soft rock	KH_8		sediment
	Hard rock		KH_8_2	rock
Southern profile	Top soil		KH_9_2	soil
	Yellow gravel layer	KH_5	KH_10_2	sediment
	Sediment layer		KH_11_2	sediment
	Hard rock		KH_12_2	rock
Deeper part	Left of hard rock	KH_1		red mudstone
	Right of hard rock	KH_2		sandstone
	Right of hard rock	KH_3		sandstone
	Next to KH_2,3	KH_4		sandstone

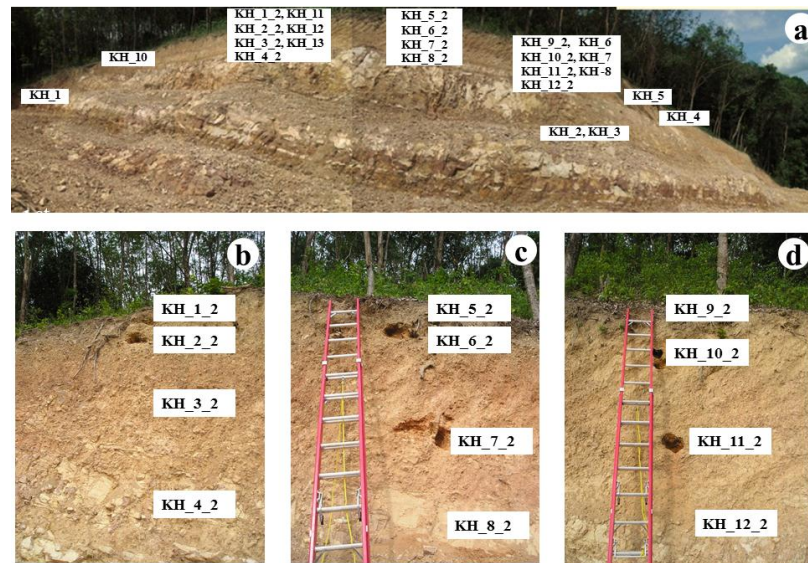


Figure 3.7 Photos of the sediment samples from sandstone site, (a) sandstone site, view to East, (b) northern profile, (b) central profile, and (d) southern profile.

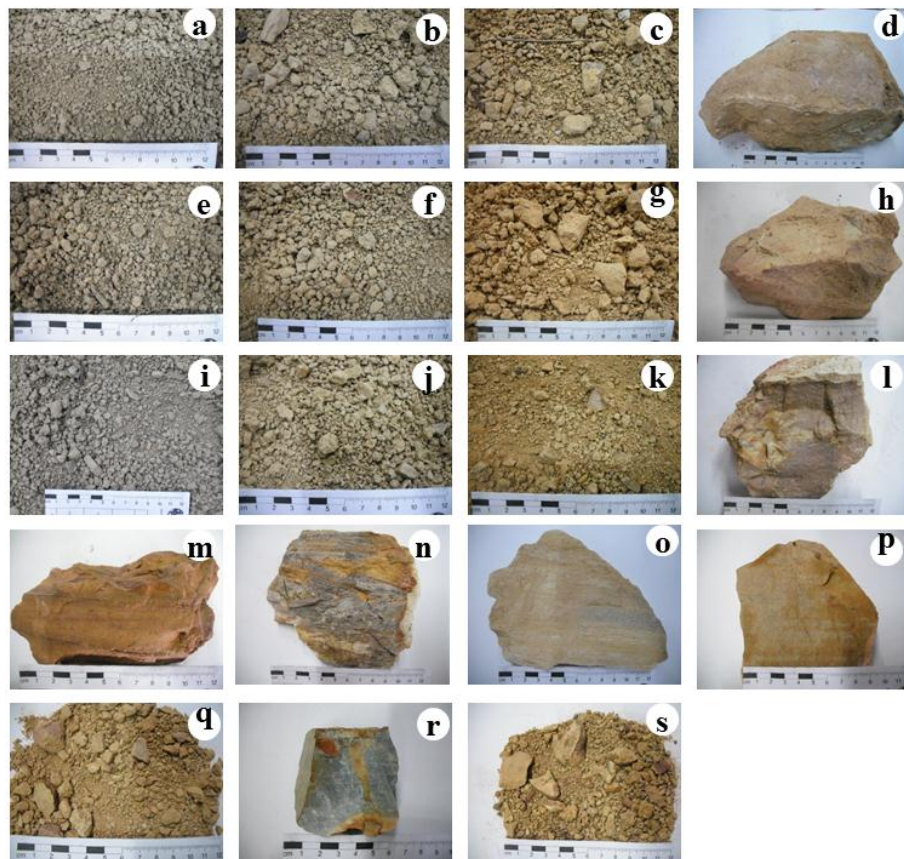


Figure 3.8 Photos of the sediment samples from the sandstone site; sample (a) KH_1_2, (b) KH_2_2, (c) KH_3_2, (d) KH_4_2, (e) KH_5_2, (f) KH_6_2, (g) KH_7_2, (h) KH_8_2, (i) KH_9_2, (j) KH_10_2, (k) KH_11_2, (l) KH_12_2, (m) KH_1, (n) KH_2, (o) KH_3, (p) KH_4, (q) KH_8, (r) KH_9, and (s) KH_13.

Table 3.4 Description of sediment samples from the sandstone site.

Sample name	Description
KH_1_2	Dark grey color, clay to gravel grain size, sub round to sub angle particles, low sphericity, quartz, clay and rock fragment, poorly sorted, more roots.
KH_2_2	Light brown color, clay to gravel grain size, and sub round to sub angle particles, low sphericity, quartz, clay and rock fragment, poorly sorted.
KH_3_2	Yellowish brown color, clay to gravel grain size, sub round to sub angle particles, low sphericity, quartz, clay and rock fragment, poorly sorted.
KH_4_2	Yellowish brown, white, and brown color, very fine to fine sand grain size, clay, very soft and smooth to touch, and well sorted.
KH_5_2	Dark grey color, clay to gravel grain size, sub round to sub angle particles, low sphericity, quartz, clay and rock fragment, poorly sorted, more roots.
KH_6_2	Light brown color, fine to clay to gravel grain size, sub round to sub angle particles, low sphericity, quartz, clay and rock fragment, very poorly sorted, and roots.
KH_7_2	Yellowish brown color, clay to gravel grain size, sub angle particles, low sphericity, quartz, clay and rock fragment, poorly sorted.
KH_8_2	Red purple, white, and brown color, very fine to fine sand grain size, clay, very soft and smooth to touch, well sorted.
KH_9_2	Dark grey color, clay to gravel grain size, sub round to sub angle particles, low sphericity, quartz, clay and rock fragment, poorly sorted, more roots.
KH_10_2	Light brown color, clay to gravel grain size, sub round to sub angle particles, low sphericity, quartz, clay and rock fragment, poorly sorted.
KH_11_2	Yellowish brown color, clay to gravel grain size, sub round to sub angle particles, high sphericity, quartz, clay and rock fragment, poorly sorted.
KH_12_2	Yellowish brown, white, and brown color, very fine to fine sand grain size, clay, very soft and smooth to touch, well sorted.
KH_1	Reddish brown color, very fine sand grain sizes, clay, very soft and smooth to touch, well sorted.
KH_2	Black, white and yellow color, fine sand grain size, clay and quartz, small layering.
KH_3	Black, white and yellow color, fine sand grain size, clay and quartz, small layering.
KH_4	Yellowish brown color, fine sand grain size, clay and quartz, small layering.
KH_8	Brown color, clay to gravel grain size, rounded particles, quartz, clay and rock fragment, high sphericity, moderately sorted.
KH_13	Reddish brown color, clay to gravel grain size, sub round particles, high sphericity, quartz, clay and rock fragment.

3.4 Density and Porosity

For the density determination samples of the two sites were chosen. The different bulk density values of the samples depend on the mineral density and porosity (pores, fractures). Mineral density, bulk density, and porosity shown in Figure 3.9 for samples from the granite site and Figure 3.10 for the sandstone site, with further details given in Appendix A, Table A.1.

The mineral density values do not depend on the degree of compaction of the sediments but on the mineralogical composition (see Section 3.5). The main components of the samples are quartz and kaolinite. The mineral density of samples from the granite site and granite site are 2.55 to 2.68 g/cm³ and 2.44 to 2.69 g/cm³ respectively.

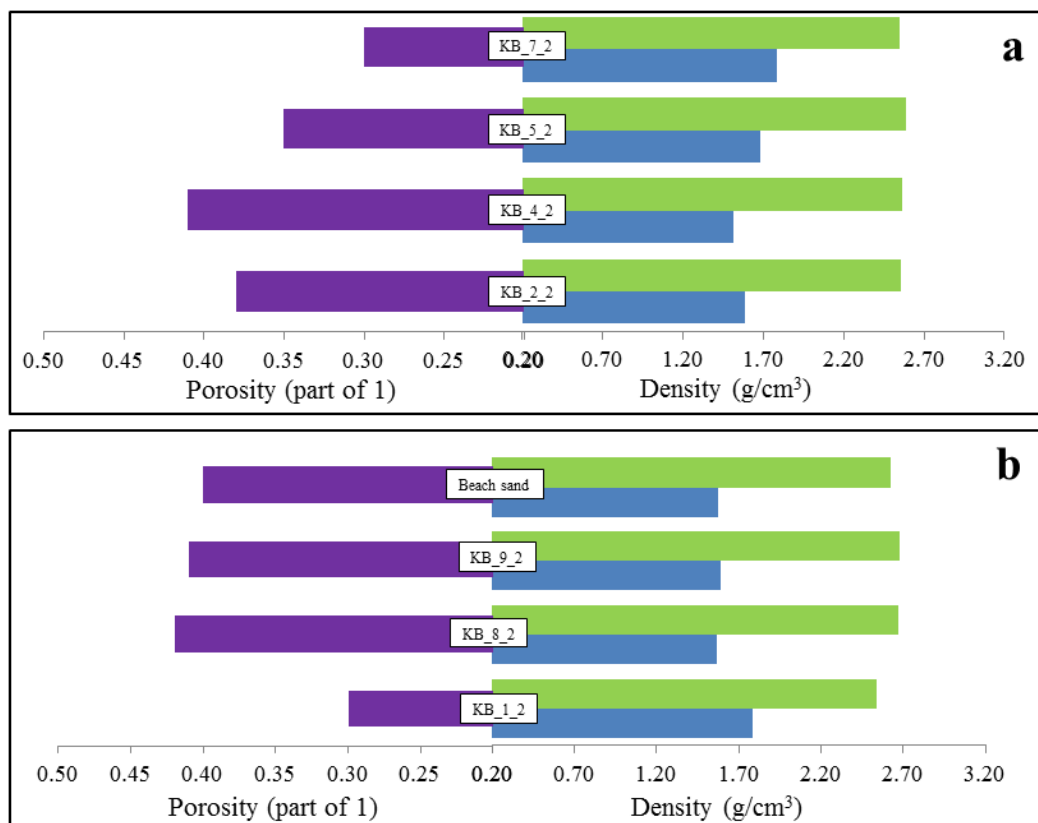


Figure 3.9 Density and porosity of samples from the granite site, green histogram is mineral density, blue histogram is bulk density, purple histogram is porosity, (a) samples KB_2_2, KB_4_2, KB_5_2, and KB_7_2, (b) samples KB_1_2, KB_8_2, KB_9_2, and beach sand.

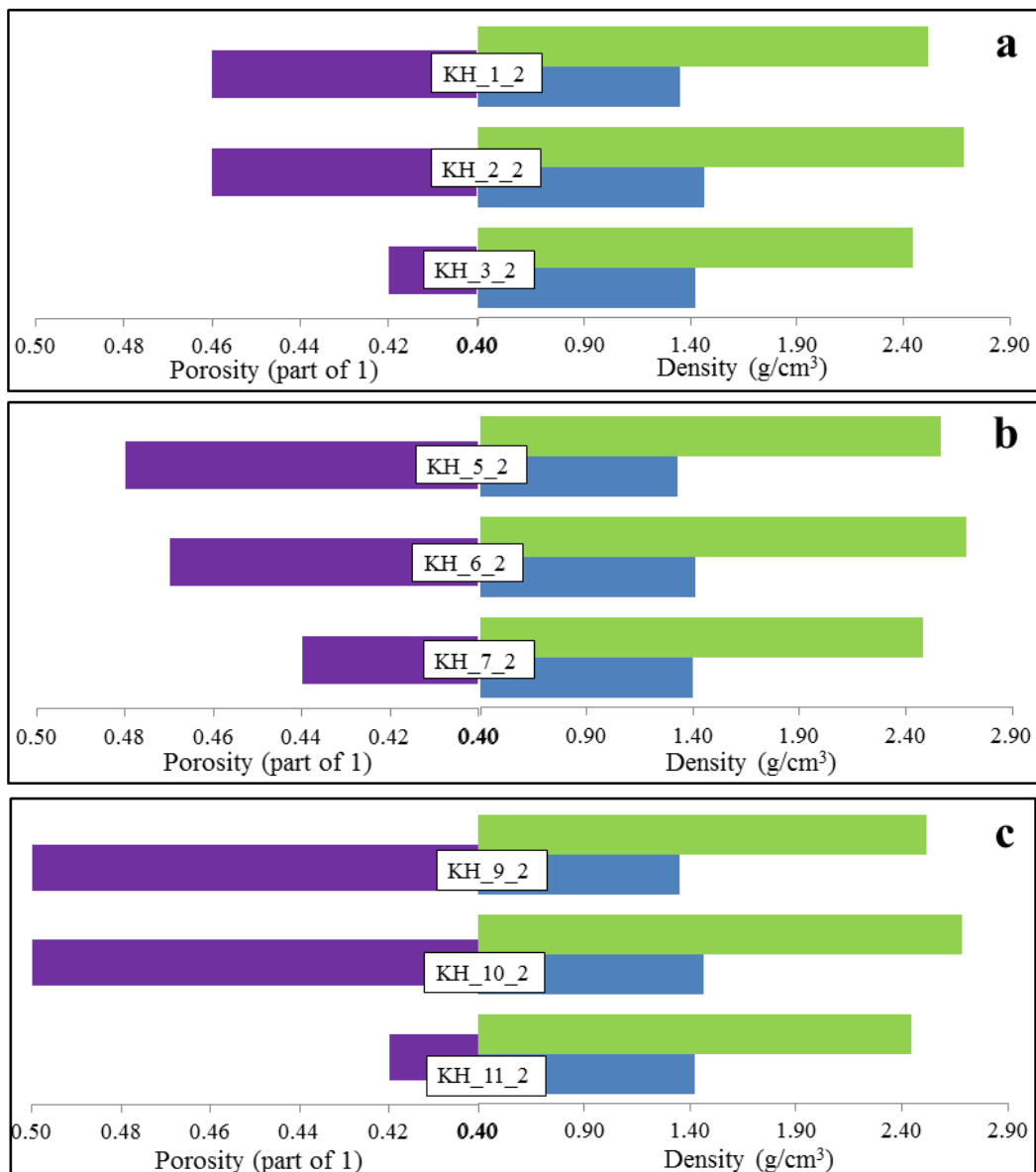


Figure 3.10 Density and porosity of samples from sandstone site, green histogram is mineral density, blue histogram is bulk density, purple histogram is porosity, (a) northern profile, (b) central profile, and (c) southern profile.

The bulk density increased when the porosity decreased because less pores and grains closer connected. The bulk density values of samples from the granite site vary from 1.51 to 1.79 g/cm³ and for the sandstone site from 1.28 to 1.42 g/cm³. Figure 3.9 (a) shows that the bulk density at the mountains (KB_7_2) is the highest compare to other samples from the site because it has less porosity; the lower density is found with KB_4_2 (high porosity). Figure 3.9 (b) also reveals that the bulk density of KB_1_2 is the highest compared to other samples and KB_8_2 has the

lowest value. The bulk density of the top soil (KH_1_2, KH_5_2, and KH_9_2) is the lowest because of higher porosity (Figure 3.10). The highest bulk density found in the middle layer of the northern profile and central profile, and the bottom layer of southern profile as these samples show low porosity.

Porosity of unconsolidated sediments depends on grain size, sorting and clay content (Kirsch et al, 2006), with lower porosity when having more gravel, mainly sand, and poor sorting (see Figure 3.11). For the granite site the porosity was 30-42% and for the sandstone site 42-50%. The results show that the samples from the sandstone site have higher porosity than the granite site because the samples at the granite site contain more gravel grain size (see Section 3.5) and are well sorted.

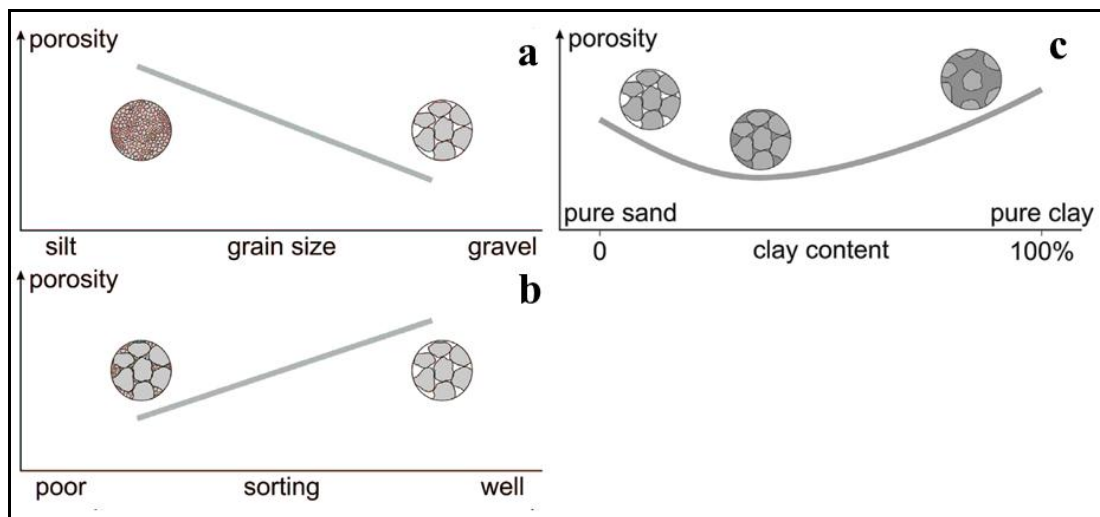


Figure 3.11 Influence of (a) grain size, (b) sorting and (c) clay content on the porosity of sediment material (Kirsch et al., 2006).

3.5 Grain size distribution

3.5.1 Grain size distribution

The grain size distributions of three of the unconsolidated sediment samples are shown in Figure 3.12 to Figure 3.16, with their frequency and cumulative curves based on the logarithmic particle size method. The grain size distributions of the samples show gravel (2.00–256 mm), sand (0.063–2.00 mm), silt (0.004–0.063 mm), and clay (less 0.004 mm) with further details are given in Appendix A, Table A2.

From Figure 3.12 it can be seen that KB_5_2 contained more coarse particles (gravel) than KB_2_2, KB_4_2, and KB_7_2 as it was near the foothill and

because of weathering, erosion, and transportation of particles, smaller particles were farther transported. KB_2_2, KB_4_2, and KB_7_2 have a higher content of coarser particles (sand) than other particles. KB_5_2 contained less clay and silt particles than other samples.

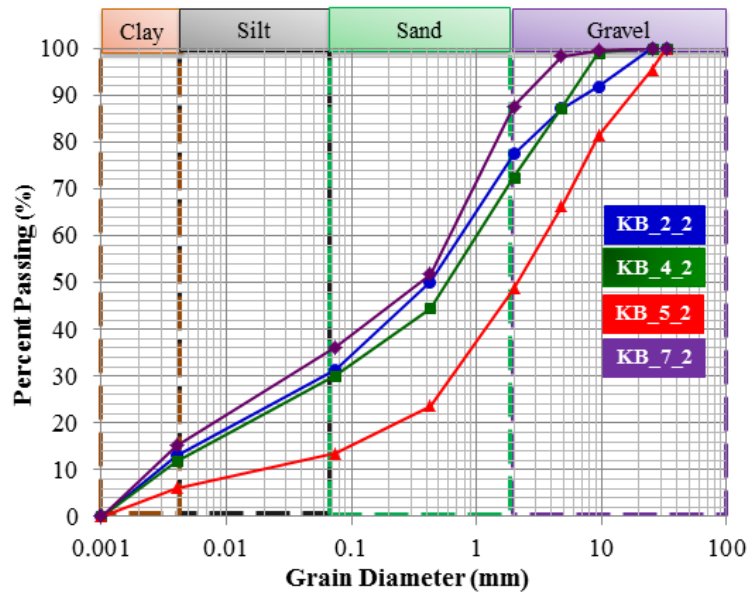


Figure 3.12 Grain size distribution of samples from the granite site; blue line - KB_2_2, green line - KB_4_2, red line - KB_5_2, purple line - KB_7_2.

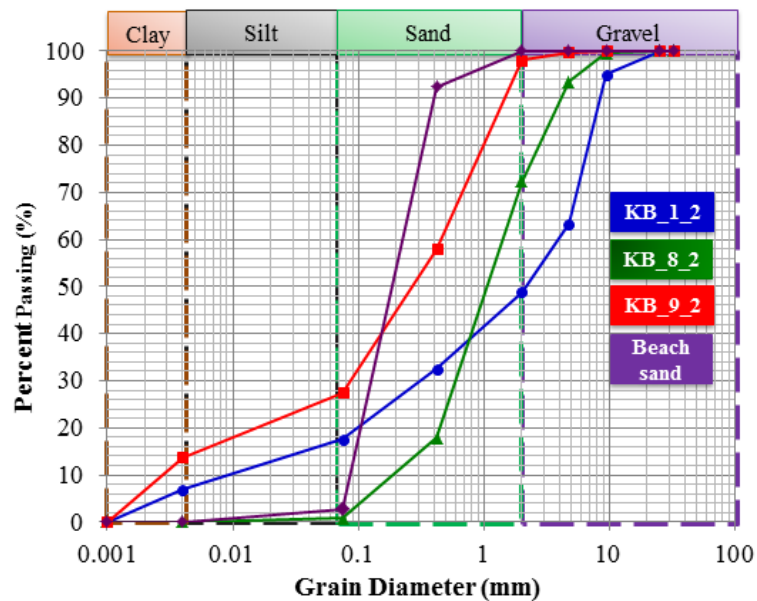


Figure 3.13 Grain size distribution of samples from the granite site and beach sand, blue line - KB_1_2, green line - KB_8_2, red line - KB_9_2, violet line - beach sand.

From Figure 3.13 it can be seen that KB_8_2 and KB_9_2 have more medium sized particles (sand) than KB_1_2 with more than 70%. KB_1_2 contained more coarse particles (gravel) than other samples and KB_9_2 has very less gravel particles than other samples. KB_8_2 contains smaller portions of clay and silt. Beach sand comprises only of sand grains. Beach sand is used here as natural clean (no clay containing) sand sample and was collected from a beach in Songkhla City.

Sample KH_1_2 contains less coarse particles (gravel) than KH_2_2 and KH_3_2 as it is the top soil (KH_1_2) and because of this subject to weathering, erosion, and transportation of particles (Figure 3.14). But KH_1_2 has a higher sand content than the other two samples, whereas KH_3_2 has the highest clay and gravel particles.

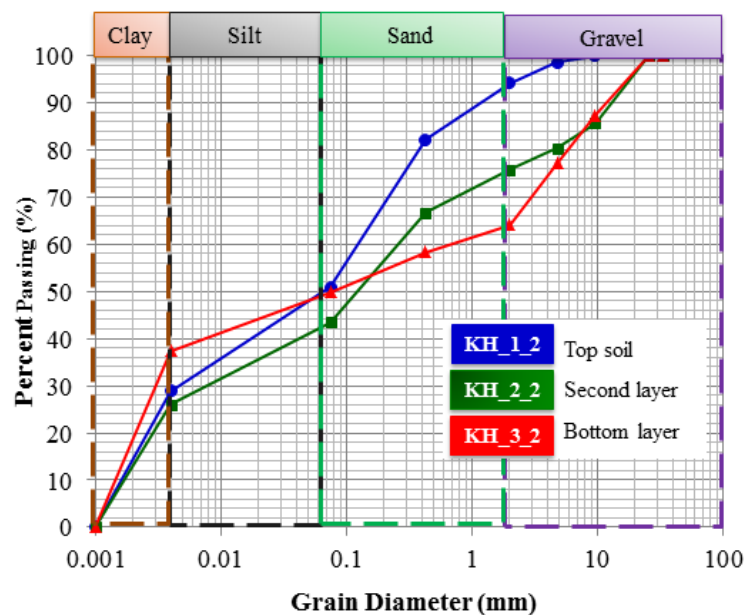


Figure 3.14 Grain size distribution of sandstone site, blue line - KH_1_2, green line - KH_2_2, red line - KH_3_2.

KH_5_2 contains less coarse particles (gravel) than KH_6_2 and KH_7_2 as it is the top soil (KH_5_2) but KH_5_2 has a higher silt and clay content than the other two samples, whereas KH_6_2 has the highest gravel content and KH_7_2 has the highest sand content (Figure 3.15). KH_10_2 contains less coarse particles (gravel) than KH_9_2 and KH_11_2 and it has the highest clay content, more than 50% (Figure 3.16). KH_9_2 has a higher sand content than the other two samples, whereas KH_11_2 has the highest gravel content.

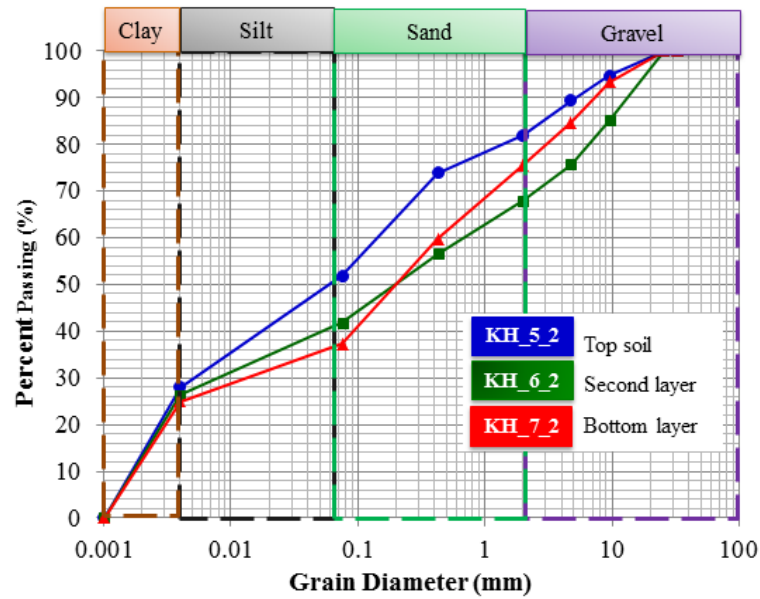


Figure 3.15 Grain size distribution of sandstone site, blue line - KH_5_2, green line - KH_6_2, red line - KH_7_2.

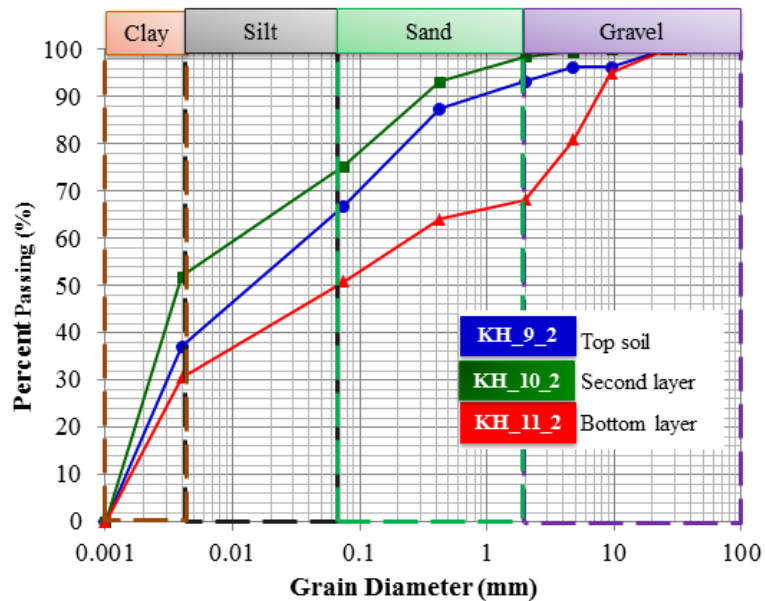


Figure 3.16 Grain size distribution of sandstone site, blue line - KH_9_2, green line - KH_10_2, red line - KH_11_2.

3.4.2 Texture

The content of sand, clay and silt were determined for the unconsolidated sediment samples and the obtained results were placed in the textural triangle shown in Figure 3.17 and Figure 3.18 with further details given in Appendix A Table A3. At the granite site, KB_8_2 is sand, and KB_1_2, KB_2_2, KB_4_2,

KB_5_2, KB_7_2, and KB_9_2 are sandy loam. Sand was loose and single grained, individual grains could be seen and felt. Squeezed in the hand when dried, it would fall apart when the pressure was released. When moisten, it would form a cast, but would crumble when touched. Sandy loam formed weak aggregates; it contained 45–85% sand, but has significant silt content and up to 20% clay. Squeezed when dried it forms a cast that readily fall apart, but when moisten it forms a cast that bear careful handling without breaking (Russell, 2005).

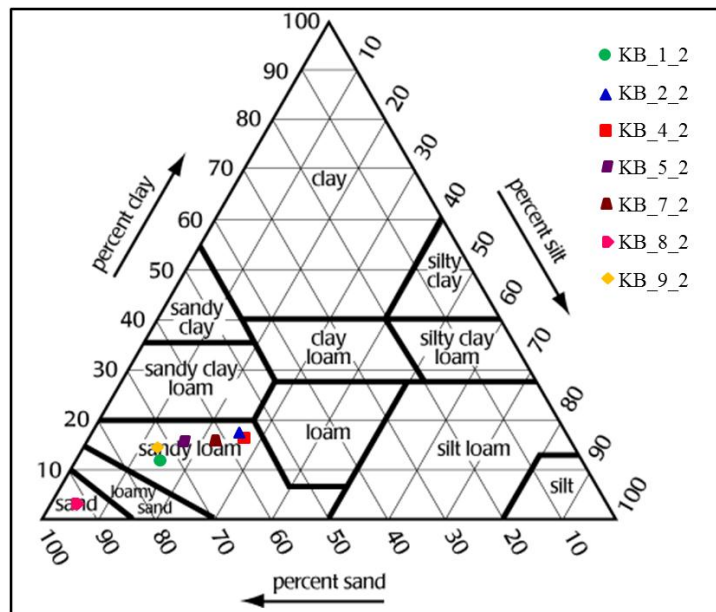


Figure 3.17 Triangle with the textural classification of samples from granite site.

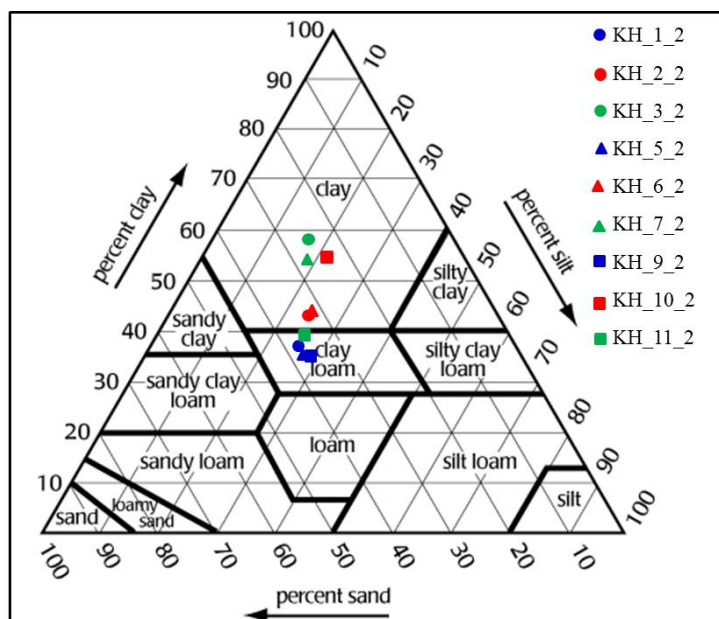


Figure 3.18 Triangle with the textural classification of samples from sandstone site.

Sandstone site, KH_1_2, KH_5_2, KH_9_2 and KH_11_2 are clay loam, and KH_2_2, KH_3_2, KH_6_2, KH_7_2 and KH_10_2 are clay. Clay loam was moderately fine-textured, hard when dried, friable or firm when moist, sticky and plastic and formed a cast that could bear handling. Clay was fine-textured, very sticky and very plastic when moist. It ribbons very well and forms a very good fingerprint; some clay was very firm or extremely firm when moist (Russell, 2005).

3.6 Composition

The qualitative mineralogical composition of the unconsolidated sediments was determined using X-ray diffraction patterns recorded with a Cu-K α , and results were shown Table 3.5. High quartz (SiO₂) content is recorded mainly in the granite site, with some variations depending on weathering. Feldspar-alkali minerals such as microcline (KAlSi₃O₈) are abundant after quartz. Clay minerals such as kaolinite (Al₂(Si₂O₅)(OH)₄), montmorillonite (Na_{0.3}(Al, Mg)₂Si₄O₁₀(OH)₂·xH₂O), and illite ((K,H₃O)Al₂Si₃AlO₁₀(OH)₂) are usually contained in sediments. Mica mineral such as muscovite (KAl₂(Si, Al)₄O₁₀(OH)₂) could also be found. The main mineral contained in the unconsolidated sediments of the sandstone sites is quartz and the minor ones are clay minerals with kaolinite (Al₂(Si₂O₅)(OH)₄) and illite ((K,H₃O)Al₂Si₃AlO₁₀(OH)₂). Further details are given in Appendix B.

Table 3.5 XRD results of unconsolidated sediment samples.

Sample name	JCPDF No.	Chemical Name	Chemical Formula
KB_1_2, KB_3	01-085-0798 01-078-1996 00-026-0911	Quartz Kaolinite 1\ITA\RG Illite-2\ITM\RG#1[NR]	SiO ₂ Al ₂ (Si ₂ O ₅)(OH) ₄ (K,H ₃ O)Al ₂ Si ₃ AlO ₁₀ (OH) ₂
KB_2_2	01-087-2096 01-078-1996 00-058-2035 00-058-2010	Quartz low, syn Kaolinite -1A Muscovite-2M1 Montmorillonite	SiO ₂ Al ₂ (Si ₂ O ₅)(OH) ₄ KAl ₂ (Si, Al) ₄ O ₁₀ (OH) ₂ Na _{0.3} (Al, Mg) ₂ Si ₄ O ₁₀ (OH) ₂ ·xH ₂ O
KB_3_2	01-087-2096 00-058-2035 01-078-1996 00-058-2010	Quartz low, syn Muscovite-2M1 Kaolinite -1A Montmorillonite	SiO ₂ KAl ₂ (Si, Al) ₄ O ₁₀ (OH) ₂ Al ₂ (Si ₂ O ₅)(OH) ₄ Na _{0.3} (Al, Mg) ₂ Si ₄ O ₁₀ (OH) ₂ ·xH ₂ O
KB_4_2, KB_4	01-085-0504 01-080-0885 00-026-0911 00-007-0330	Quartz Kaolinite 1\ITA\RG Illite-2\ITM\RG#1[NR] Illite-Momtmorillonite, regular	SiO ₂ Al ₂ (Si ₂ O ₅)(OH) ₄ (K,H ₃ O)Al ₂ Si ₃ AlO ₁₀ (OH) ₂ K-Al ₄ (SiAl) ₈ O ₂₀ (OH) ₄ ·xH ₂ O

Table 3.5 XRD results of unconsolidated sediment samples (continued).

Sample name	JCPDF No.	Chemical Name	Chemical Formula
KB_5_2, KB_6	03-065-0466 01-080-0886 00-026-0911	Quartz low, syn Kaolinite 1\ITA\RG Illite-2\ITM\RG#1[NR]	SiO ₂ Al ₂ (Si ₂ O ₅)(OH) ₄ (K,H ₃ O)Al ₂ Si ₃ AlO ₁₀ (OH) ₂
KB_6_2	01-087-2096 00-058-2035 00-058-2028	Quartz low, syn Muscovite-2M1 Kaolinite -1A	SiO ₂ KAl ₂ (Si, Al) ₄ O ₁₀ (OH) ₂ Al ₂ (Si ₂ O ₅)(OH) ₄
KB_7_2	01-087-2096 01-078-1996 00-058-2035	Quartz low, syn Kaolinite -1A Muscovite-2M1	SiO ₂ Al ₂ (Si ₂ O ₅)(OH) ₄ KAl ₂ (Si, Al) ₄ O ₁₀ (OH) ₂
KB_8_2	01-087-2096 00-058-2035 01-058-2028 00-019-0932	Quartz low, syn Muscovite-2M1 Kaolinite -1A Microcline, intermediate	SiO ₂ KAl ₂ (Si, Al) ₄ O ₁₀ (OH) ₂ Al ₂ (Si ₂ O ₅)(OH) ₄ KAlSi ₃ O ₈
KB_9_2, KB_1	01-085-0796 01-076-0918 00-026-0911	Quartz Microcline maximum Illite-2\ITM\RG#1[NR]	SiO ₂ KAlSi ₃ O ₈ (K,H ₃ O)Al ₂ Si ₃ AlO ₁₀ (OH) ₂
KB_2	01-085-0796 01-089-6538 00-026-0911	Quartz Kaolinite Illite- 2\ITM\RG#1[NR]	SiO ₂ Al ₂ (Si ₂ O ₅)(OH) ₄ (K,H ₃ O)Al ₂ Si ₃ AlO ₁₀ (OH) ₂
KB_5	03-065-0466 01-080-0886 00-026-0911	Quartz low, syn Kaolinite 1\ITA\RG Illite-2\ITM\RG#1[NR]	SiO ₂ Al ₂ (Si ₂ O ₅)(OH) ₄ (K,H ₃ O)Al ₂ Si ₃ AlO ₁₀ (OH) ₂
KH_1_2, KH_10	01-085-1053 01-080-0886	Quartz, syn Kaolinite 1\ITA\RG	SiO ₂ Al ₂ (Si ₂ O ₅)(OH) ₄
KH_2_2, KH_11	01-078-2315 01-080-0886 00-026-0911	Quartz Kaolinite 1\ITA\RG Illite-2\ITM\RG#1[NR]	SiO ₂ Al ₂ (Si ₂ O ₅)(OH) ₄ (K,H ₃ O)Al ₂ Si ₃ AlO ₁₀ (OH) ₂
KH_3_2, KH_12	01-085-0504 00-026-0911 01-080-0886	Quartz Illite-2\ITM\RG#1[NR] Kaolinite 1\ITA\RG	SiO ₂ (K,H ₃ O)Al ₂ Si ₃ AlO ₁₀ (OH) ₂ Al ₂ (Si ₂ O ₅)(OH) ₄
KH_4_2	01-087-2096 00-026-0911 01-078-1996	Quartz low, syn Illite -2M1(NR) Kaolinite -1A	SiO ₂ (K,H ₃ O)Al ₂ Si ₃ AlO ₁₀ (OH) ₂ Al ₂ (Si ₂ O ₅)(OH) ₄
KH_5_2	01-087-2096 01-078-1996 00-026-0911	Quartz low, syn Kaolinite -1A Illite -2M1(NR)	SiO ₂ Al ₂ (Si ₂ O ₅)(OH) ₄ (K,H ₃ O)Al ₂ Si ₃ AlO ₁₀ (OH) ₂
KH_6_2, KH_6	01-083-2565 01-080-0885 00-026-0911	Quartz, syn Kaolinite 1\ITA\RG Illite-2\ITM\RG#1[NR]	SiO ₂ Al ₂ (Si ₂ O ₅)(OH) ₄ (K,H ₃ O)Al ₂ Si ₃ AlO ₁₀ (OH) ₂
KH_7_2, KH_7	01-085-1053 01-080-0885	Quartz, syn Kaolinite 1\ITA\RG	SiO ₂ Al ₂ (Si ₂ O ₅)(OH) ₄
KH_8_2	01-087-2096 00-026-0911 01-078-1996	Quartz low, syn Illite -2M1(NR) Kaolinite -1A	SiO ₂ (K,H ₃ O)Al ₂ Si ₃ AlO ₁₀ (OH) ₂ Al ₂ (Si ₂ O ₅)(OH) ₄
KH_9_2	01-087-2096 01-078-1996 00-026-0911	Quartz low, syn Kaolinite -1A Illite -2M1(NR)	SiO ₂ Al ₂ (Si ₂ O ₅)(OH) ₄ (K,H ₃ O)Al ₂ Si ₃ AlO ₁₀ (OH) ₂

Table 3.5 XRD results of unconsolidated sediment samples (continued).

Sample name	JCPDF No.	Chemical Name	Chemical Formula
KH_10_2	01-085-0504	Quartz, syn	SiO ₂
KH_5	01-080-0885	Kaolinite 1\ITA\RG	Al ₂ (Si ₂ O ₅)(OH) ₄
KH_11_2	01-087-2096 01-078-1996	Quartz low, syn Kaolinite -1A	SiO ₂ Al ₂ (Si ₂ O ₅)(OH) ₄
KH_12_2	01-087-2096 01-078-1996 00-026-0911	Quartz low, syn Kaolinite -1A Illite -2M1(NR)	SiO ₂ Al ₂ (Si ₂ O ₅)(OH) ₄ (K,H ₃ O)Al ₂ Si ₃ AlO ₁₀ (OH) ₂
KH_1	01-083-2465 01-089-6538 00-026-0911	Quartz low, syn Kaolinite Illite-2\ITM\RG#1[NR]	SiO ₂ Al ₂ (Si ₂ O ₅)(OH) ₄ (K,H ₃ O)Al ₂ Si ₃ AlO ₁₀ (OH) ₂
KH_2	01-079-1910 01-080-0885	Quartz, syn Kaolinite 1\ITA\RG	SiO ₂ Al ₂ (Si ₂ O ₅)(OH) ₄
KH_3	01-086-1560 01-089-6538	Quartz low Kaolinite	SiO ₂ Al ₂ (Si ₂ O ₅)(OH) ₄
KH_4	01-087-2096 01-080-0886 00-026-0911	Quartz low Kaolinite 1\ITA\RG Illite-2\ITM\RG#1[NR]	SiO ₂ Al ₂ (Si ₂ O ₅)(OH) ₄ (K,H ₃ O)Al ₂ Si ₃ AlO ₁₀ (OH) ₂
KH_8	01-087-2096 01-080-0885	Quartz low Kaolinite 1\ITA\RG	SiO ₂ Al ₂ (Si ₂ O ₅)(OH) ₄
KH_9	01-083-2465	Quartz low, syn	SiO ₂
KH_13	01-085-0504 00-073-2234 01-080-0885	Quartz Hematite Kaolinite 1\ITA\RG	SiO ₂ Fe ₂ O ₃ Al ₂ (Si ₂ O ₅)(OH) ₄

3.7 Microstructures

SEM microphotographs of the samples showed differences in micro texture and morphology due to the mineral content and grain size distribution. Mineral constituents identified under SEM are clay and quartz, consistent with the XRD results. Further, details were given in Appendix C.

Figure 3.19 shown SEM microphotographs of samples granite site, Figure 3.19 (a, b, and c) shows pores and grains, which have a sub-rounded to rounded grain shape, a fine to coarse grain size ($\approx 0.1-2.5 \mu\text{m}$), massive and pseudo hexagonal grain of clay mineral (kaolinite), and micropore sizes. Figure 3.19 (d and e) shows pores and grains, sub-rounded to angular grain shape, a fine to very coarse grain size ($\approx 0.5-5 \mu\text{m}$), occurs as face to face stacks of pseudo hexagonal grain (clay: kaolinite), and macropores size ($\approx 0.1-4.0 \mu\text{m}$). Figure 3.19 (f) shows pores and grains, clay grains are a rounded grain shape, fine to coarse grain size ($\approx 0.1-2.5 \mu\text{m}$), pseudo hexagonal grain, quartz grains are well-rounded grain shape, medium to very coarse

grain size ($\approx 2\text{--}15\ \mu\text{m}$), on the surface of the grains is a small oval depressions fringed by clay, macropores size is $\approx 0.1\text{--}12\ \mu\text{m}$.

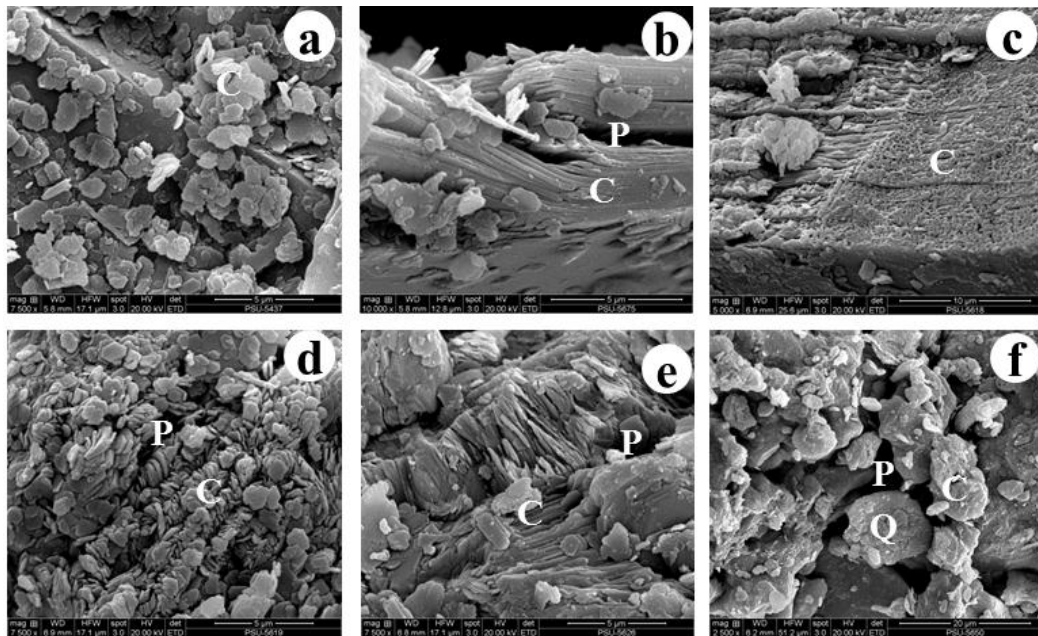


Figure 3.19 Micro structures of samples from the granite site, P is pore, Q is quartz, C is clay, (a)-(b) sample KB_1_2, (c)-(d) sample KB_4_2, (e) sample KB_5_2, and (f) sample KB_9_2,

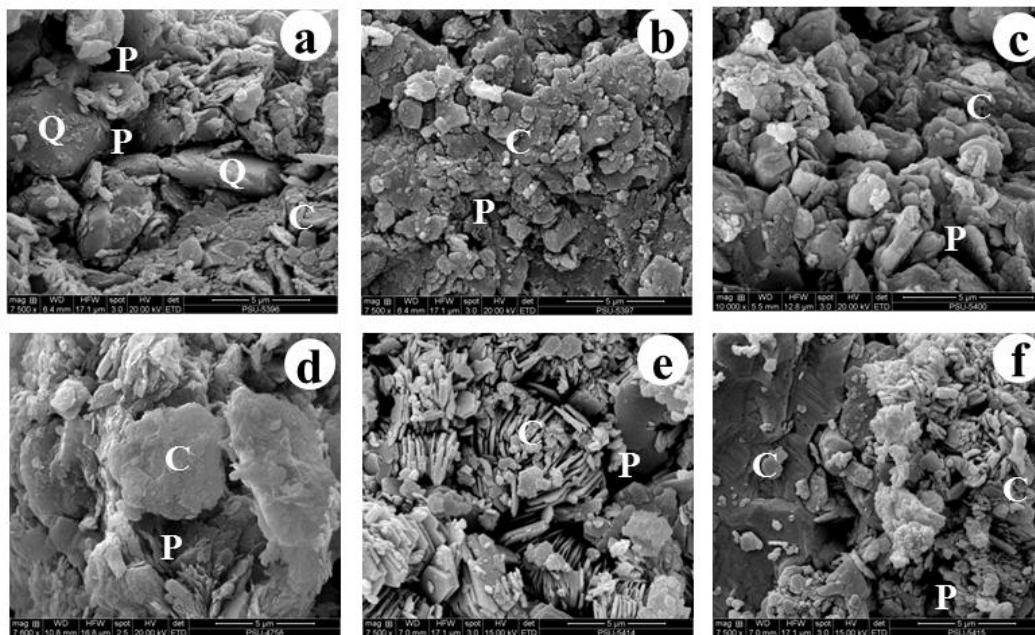


Figure 3.20 Micro structures of samples from the sandstone site, P is pore, Q is quartz, C is clay, (a)-(c) sample KH_1_2, (d) sample KH_2_2 and (e) – (f) sample KH_4_2.

Figure 3.20 shows SEM microphotographs of samples from the granite site. Figure 3.20 (c and d) shows SEM microphotographs with pores and grains, which have a sub-rounded to sub angular grain shape, a fine to coarse grain size ($\approx 0.5\text{-}3.0\ \mu\text{m}$), pseudo hexagonal grain, separated and linked by sheet of filamentous, and macropores size ($\approx 0.1\text{-}5.0\ \mu\text{m}$). Figure 3.20 (b and f) shows pores and grains with sub-rounded grain shape, a fine to coarse grain size ($\approx 0.1\text{-}2.5\ \mu\text{m}$), massive and pseudo hexagonal grains, and macropores with a size of $\approx 0.05\text{-}2.5\ \mu\text{m}$. Figure 3.20 (e) shows pores and grains, sub rounded to sub angular grain shape, a fine to coarse grain size ($\approx 0.1\text{-}2.5\ \mu\text{m}$), occurs as face to face stacks of pseudo hexagonal grain, and macropores size ($\approx 0.1\text{-}3.0\ \mu\text{m}$). Figure 3.20 (a) shows pores and grains; clay grains have a sub-rounded grain shape, a fine to coarse grain size ($\approx 0.5\text{-}1.5\ \mu\text{m}$) pseudo hexagonal grain, kaolinite composition, quartz grains have well-rounded grain shape, very coarse grain size ($\approx 6\ \mu\text{m}$); on the surface of the grains there a small oval depressions fringed by clay; macropores size is $\approx 0.1\text{-}2.5\ \mu\text{m}$.

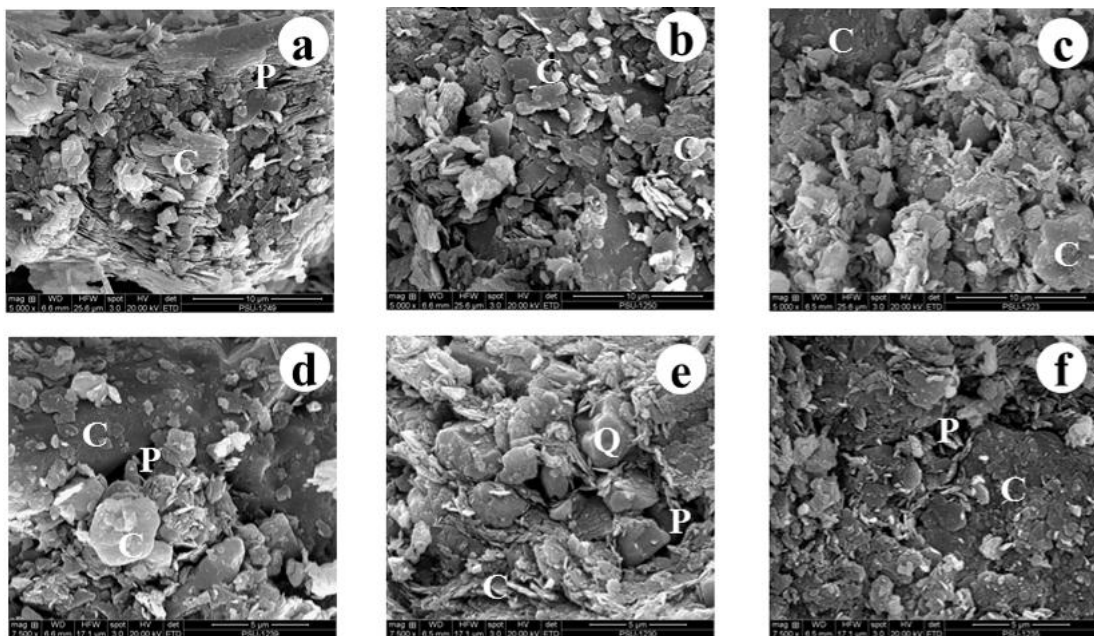


Figure 3.21 Micro structures and composition of sample after water saturation, P is pore, Q is quartz, C is clay, (a)-(b) sample KB_4_2, (c) sample KH_1_2, (d) sample KH_5_2, (e) sample KH_6_2, and (f) sample KH_7_2.

Figure 3.21 shows SEM microphotographs of sample after 100% water saturation and subsequent drying under air. Smaller pores are seen than in the SEM microphotographs of Figure 3.19 and Figure 3.20 because the grains are arranged closer together than before due to the saturation. From Figure 3.19 KB_4_2, the pore

size is about 0.1–4.0 μm , but the pore size of KB_4_2 in Figure 3.21 is less than 0.8 μm . The porosity decreased with increasing water saturation due to swelling of clay minerals; values are shown in Appendix A, Table A.5.

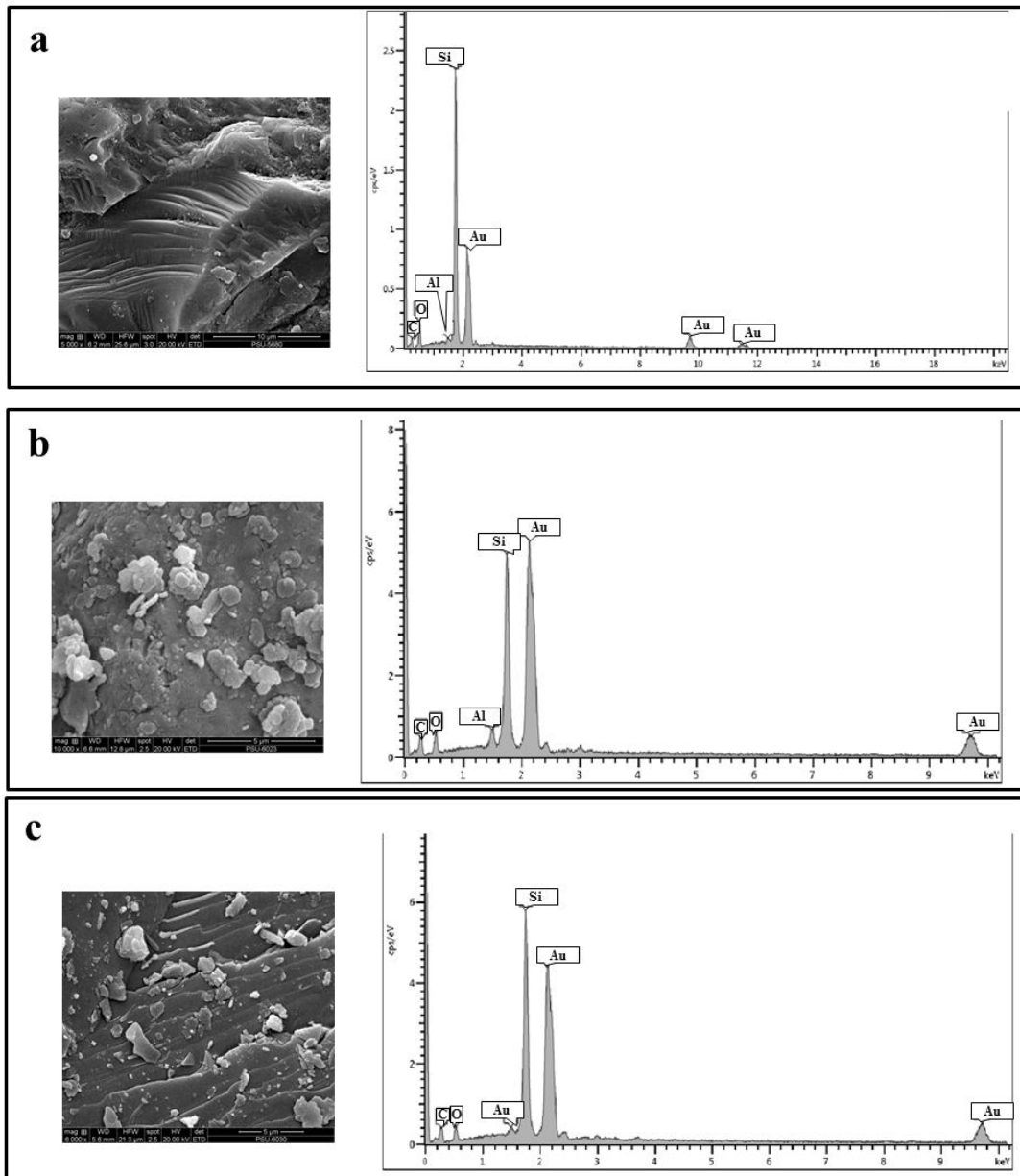


Figure 3.22 Composition of samples by EDS, sample (a) beach sand, (b) KB_1_2, and (c) KB_6_2. Au is from the sample coating.

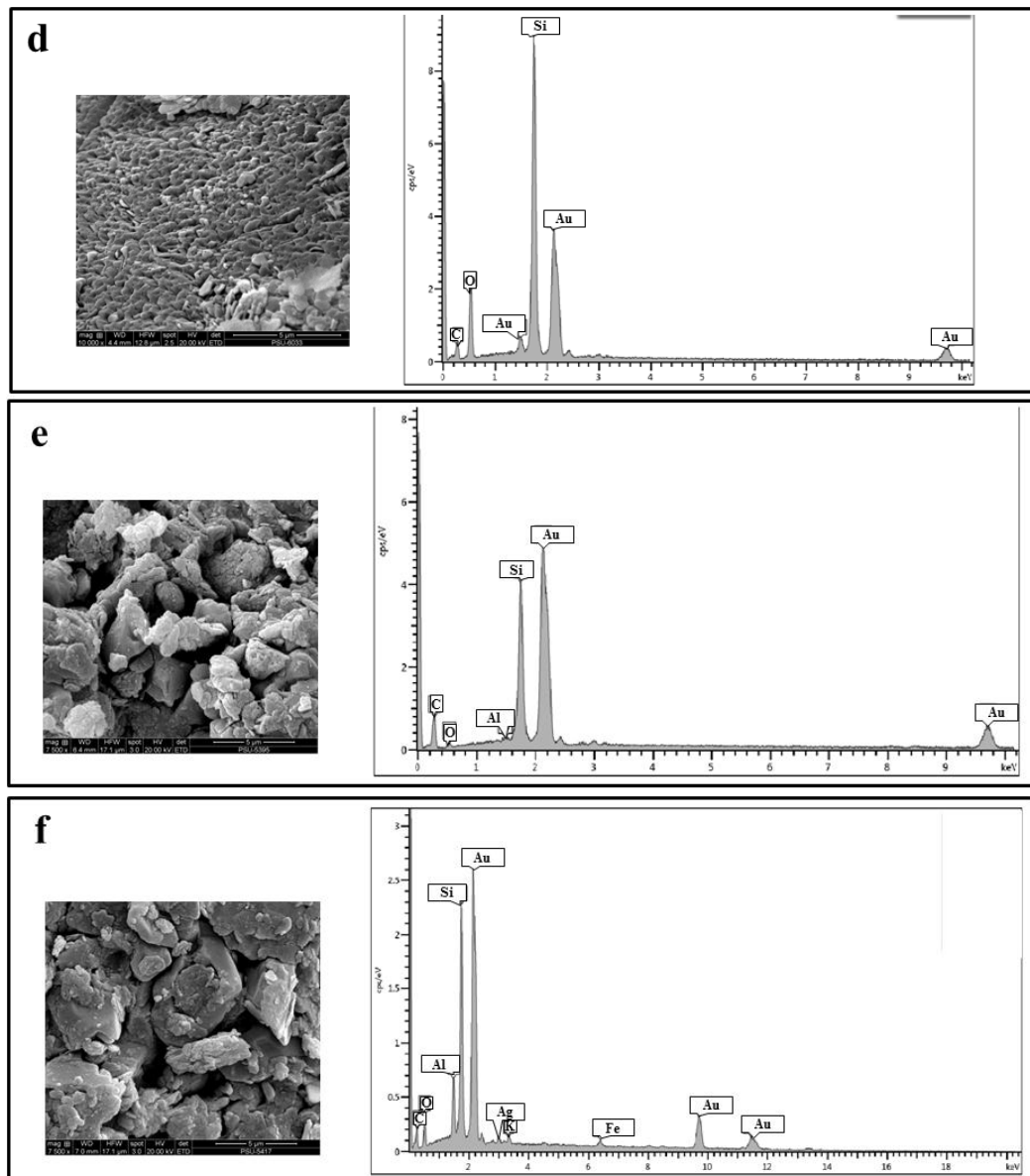


Figure 3.22 Composition of sample by EDS, sample (d) KB_7_2, (e) KH_1_2, and (f) KH_5_2. Au is from the sample coating.

From Figure 3.22, the EDS analysis of the unconsolidated sediment samples shows the presence of silicon (Si), aluminum (Al), oxygen (O), carbon (C), potassium (K), silver (Ag), iron (Fe), and gold (Au). The gold peak is high because of the thin gold coating. High peaks of Si and Al are identified as kaolinite, high peaks of Si, K, Al (K less than Al) and minor Mg, Ca and Fe are identified as illite, high peaks of Si and O are identified as quartz. Figure 3.21 (a, c, and d) identified quartz because it is high Si and O. Figure 3.22 (b, e, and f) shows kaolinite because of its high peak of Si and Al.

3.8 Hydraulic conductivity

Hydraulic conductivity values are related to the properties of the porous sediments (grain size distribution, grain shape, and porosity) and the properties of the fluid (temperature dependent fluid density and viscosity), here water. The results with water at a temperature of 26-29 °C are shown in Figure 3.23 and Figure 3.24.

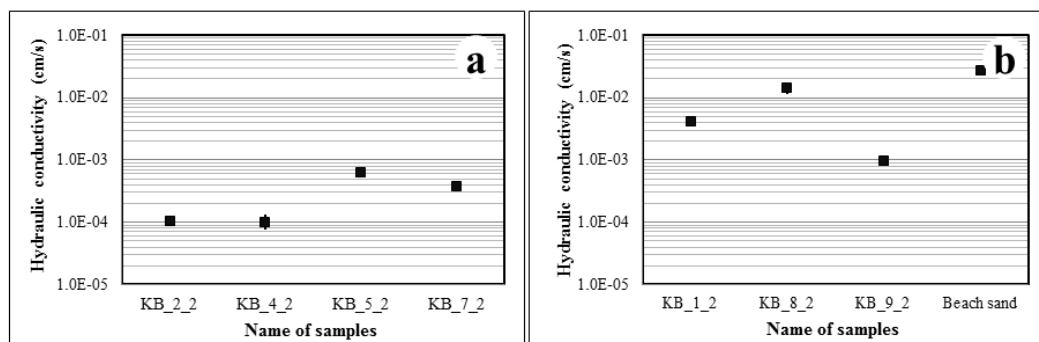


Figure 3.23 Hydraulic conductivity of samples from the granite site, (a) samples KB_2_2, KB_4_2, KB_5_2, and KB_7_2, (b) samples KB_1_2, KB_8_2 and KB_9_2, and beach sand.

The hydraulic conductivity of samples from the granite site are shown in Figure 3.23(a) where sample KB_5_2 has a higher hydraulic conductivity than KB_1_2, KB_4_2 and KB_7_2 because it contains more coarser grains (gravel and sand particles) than other samples. In Figure 3.23(b) sample KB_8_2 shows a high hydraulic conductivity; it also has a higher content of gravel and sand grain size (very few silt and clay). KB_1_2 and KB_9_2 show higher hydraulic conductivity as they have more gravel and sand particles as shown in Figure 3.22(a). Beach sand has the highest hydraulic conductivity; as it only contains of sand grain size.

For the hydraulic conductivity of samples from the sandstone site as shown in Figure 3.24(a) sample KH_3_2 has the highest hydraulic conductivity when compared to sample KH_1_2, and KH_3_2. Figure 3.24(b) shows that sample KH_6_2 has the highest hydraulic conductivity in the central profile. Figure 3.24(c) shows the southern profile with KH_9_2 having the highest hydraulic conductivity because it contains more sand and gravel sized material. However, the overall values of the hydraulic conductivity for the samples from the sandstone site vary less than an order of magnitude, whereas for the samples from the granite site the variation is larger, with more than two magnitudes. This is due to the heterogeneity in the grain

size distribution of the samples from the granite site, as well as differences in porosity.

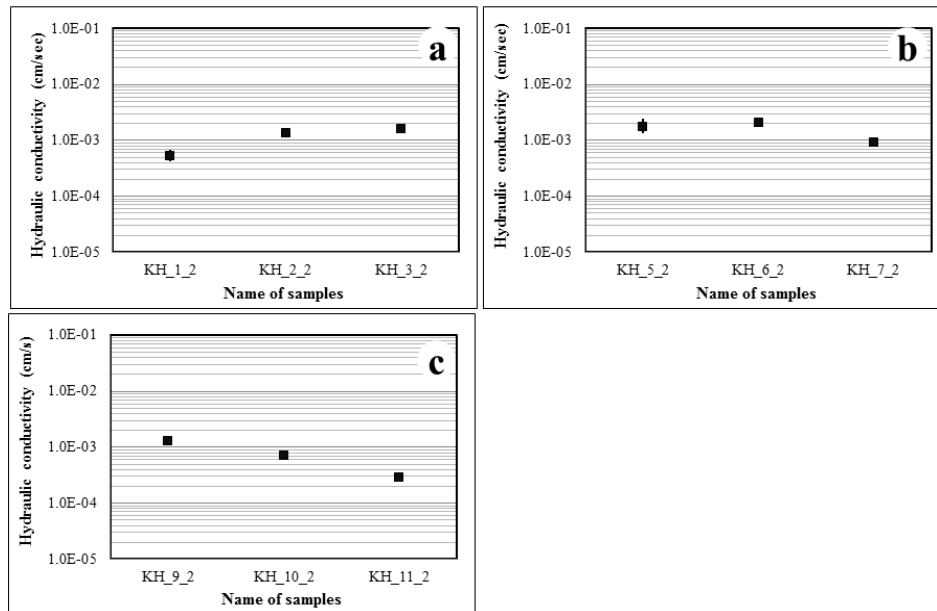


Figure 3.24 Hydraulic conductivity of samples form the sandstone site, (a) northern profile, (b) central profile, and (c) southern profile.

3.9 Electrical resistivity and water saturation

Result from the resistivity measurements versus increasing water saturation (0-100%) are shown in Figure 3.25 and Figure 3.26 in semi-log graphs. Measured resistivity decreases logarithmically with increasing water saturation. It can be seen that for a water content of 0-40% there is a larger gradient for the decrease of the electrical resistivity.

The lines in the figures represent the calculations of the electrical resistivity using Equation 2.20, and using average parameters from the laboratory measurements, clay content (percent of clay and silt), porosity, matrix density, and conductivity of the water used. In order to fit a curve with the experimental values from the electrical resistivity measurements, the values m , n , and a were changed; but it was tried not to change the values significantly. The shape of the curve for all four samples from the granite site is similar, but the absolute values are different, with the resistivity values showing following order: $KB_{5_2} > KB_{4_2} > KB_{2_2} > KB_{7_2}$ (Figure 3.25). However, samples in Figure 3.25 show significant difference in the gravel and sand grain size distribution. Sample KB_{5_2} has a gravel content of 51%

and a sand content of 36%, sample KB_4_2 has 28% and 43%, sample KB_2_2 has 23% and 47%, and sample KB_7_2 has 12% and 52%, respectively. A higher resistivity correlates with a higher content in gravel and vice versa. The larger gravel grains might obstruct the electrical pathway more than the sand grains and might also have an effect on the clay distribution in the sample. This would explain that the differences are more or less independent from the degree of saturation.

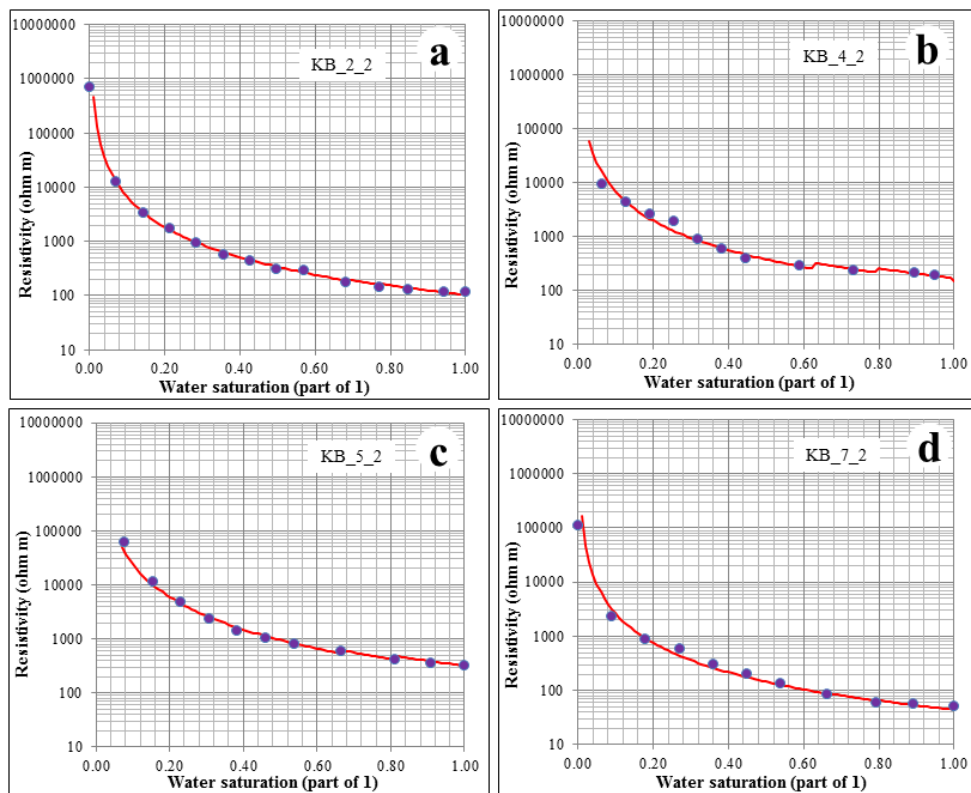


Figure 3.25 Resistivity of samples from the granite site with increasing water saturation, (a) sample KB_2_2, (b) sample KB_4_2, (c) sample KB_5_2, and (d) sample KB_7_2.

Figure 3.26 shows that the shape of the resistivity curves is similar, with the absolute resistivity values showing following order, KB_8_2 > KB_1_2 > beach sand > KB_9_2. Samples show a significant difference in the gravel and sand grain size distribution. Sample KB_8_2 has a gravel content of 28 % and a sand content of 72%, sample KB_9_2 has 2% and 73 %, sample KB_1_2 has 51% and 33%, sample KB_2_2 has 23% and 47%, respectively, and beach sand has a sand content of 100%. KB_1_2 shows the lower resistivity because it has a higher density (1.78 g/cm^3), related to a higher compaction. Compaction affects mainly the inter aggregate pores or macropores, and most of the electrical carriers involved in the

electrical measurements were located in the intra aggregate pores often associated with the clay phase (Seladji et al, 2010).

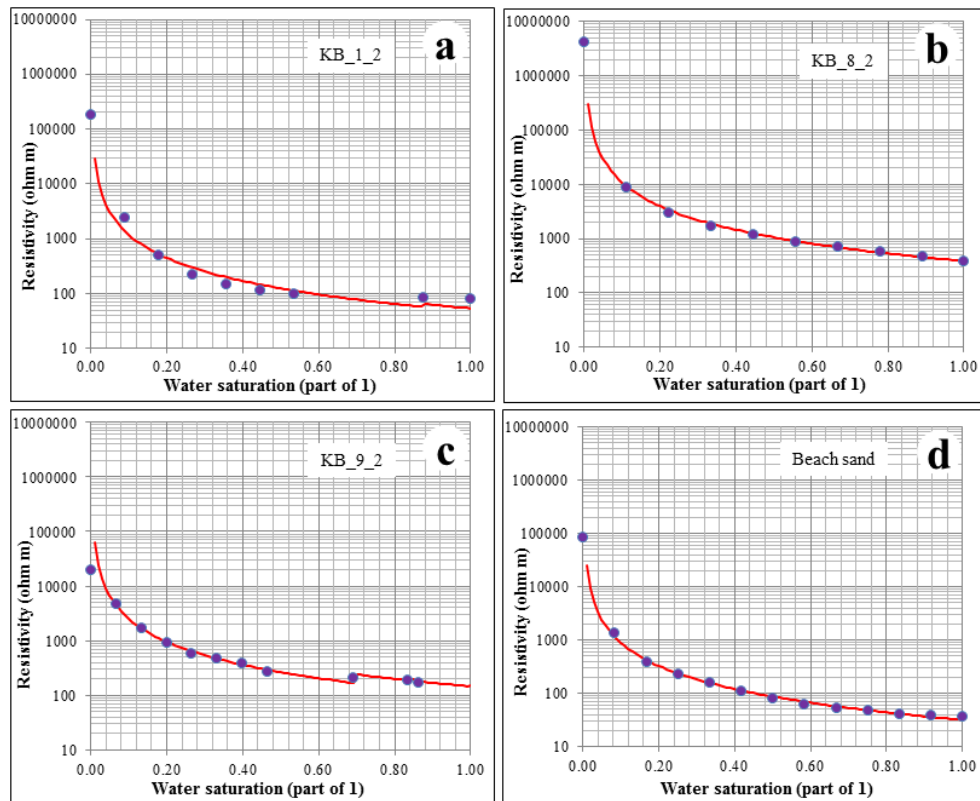


Figure 3.26 Resistivity of samples from the granite site with increasing water saturation, (a) sample KB_1_2, (b) sample KB_8_2, (c) sample KB_9_2, and (d) sample beach sand.

For the samples from the sandstone site also the measured resistivity decreases logarithmically with increasing water saturation. The shape of the curve for all three samples is similar and similar to the samples from the granite site, but the absolute values are different, with the resistivity values showing following order, top soil < second layer < bottom layer (see Figure 3.27). However, for the samples here the clay content is relatively similar, which might not explain the differences in the absolute resistivity values. These samples in Figure 3.27 show significant difference in the gravel and sand grain size distribution.

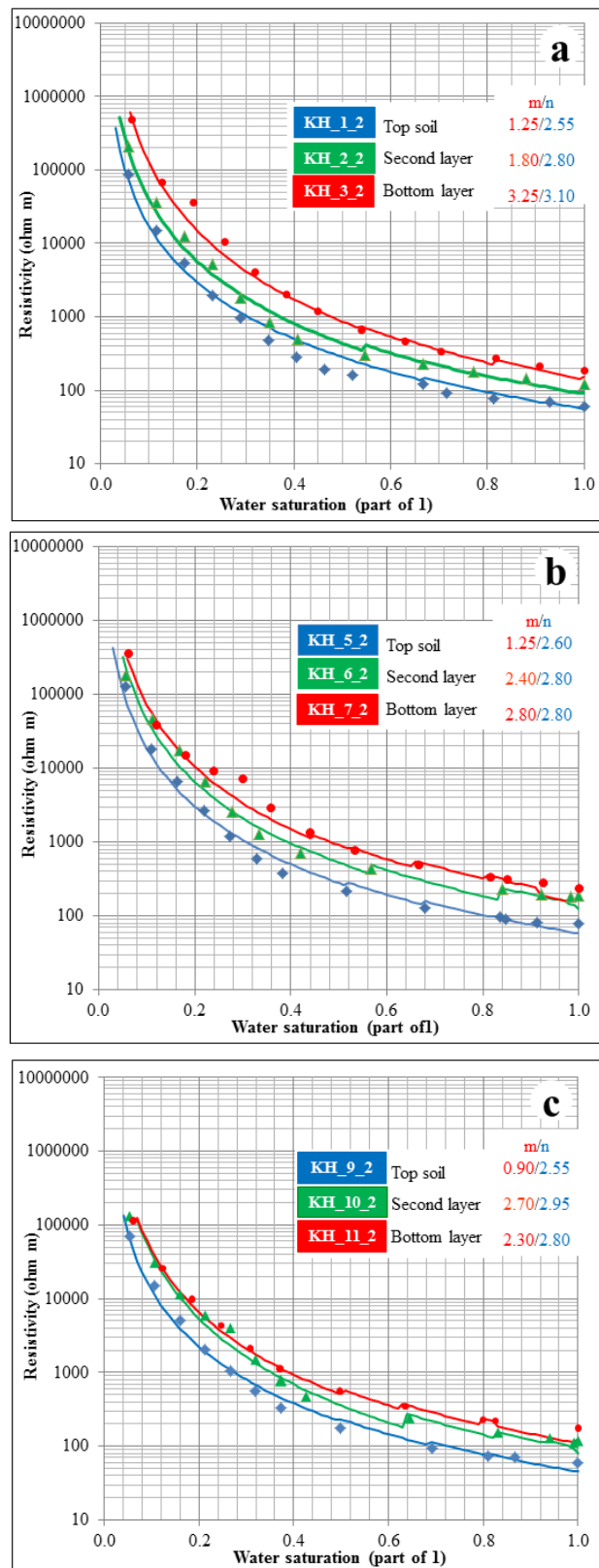


Figure 3.27 Resistivity of samples from the sandstone site with increasing water saturation (a) northern profile, (b) central profile, and (c) southern profile.

Figure 3.27(a) shows the resistivity values for the northern vertical profile, with the absolute resistivity values showing following order, $KH_{3_2} > KH_{2_2} > KH_{1_2}$, because a higher resistivity correlates with a higher content in gravel and vice versa. Sample KH_{3_2} has a gravel content of 36% and a sand content of 15%, whereas sample KH_{2_2} has 24% and 36%, and sample KH_{1_2} has 6% and 47%, respectively. The resistivity values of the central profile show following order, $KH_{7_2} > KH_{6_2} > KH_{5_2}$. Sample KH_{7_2} has a gravel content of 24% and a sand content of 42 %, sample KH_{6_2} has 32 % and 28 %, and sample KH_{5_2} has 18 % and 33 %, respectively (Figure 3.27 (b)). In Figure 3.27 (c) the resistivity values of the southern profile are displayed showing following order, $KH_{11_2} > KH_{10_2} > KH_{9_2}$. Sample KH_{11_2} has a gravel content of 32% and a sand content of 18%, sample KH_{10_2} has 1% and 25%, and sample KH_{9_2} has 7% and 29%, respectively. KH_{10_2} has less gravel and sand content than KH_{9_2} , but KH_{10_2} shows a higher resistivity than it because KH_{10_2} has a higher density than sample KH_{9_2} . In Figure 3.27, the second and bottom layer show a similar curve shape because the value of m and n are not different, but the top layer shows a different curve because the value of m and n are different from the other layers.

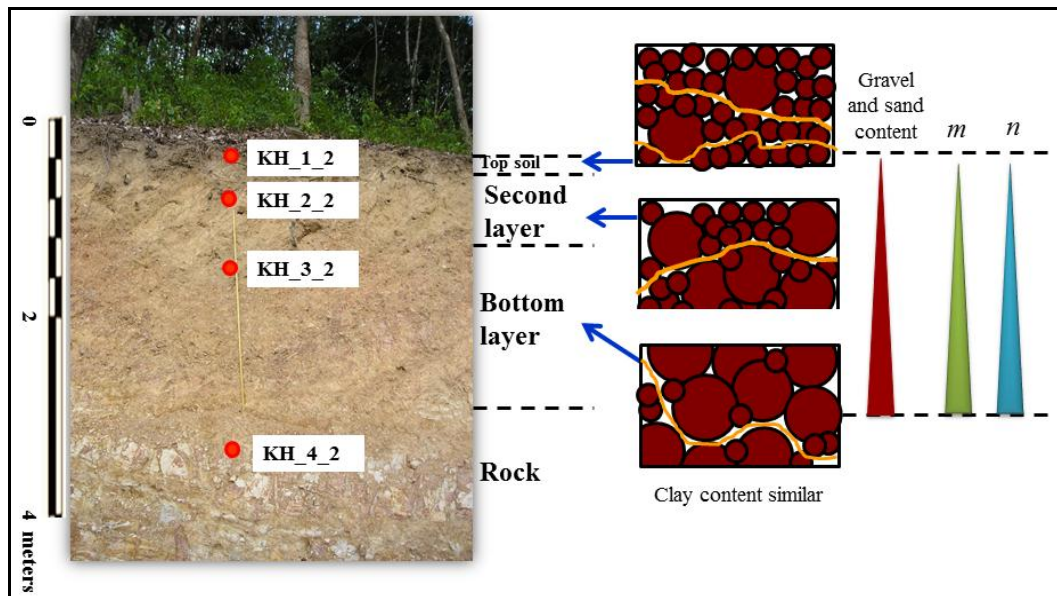


Figure 3.28 Relation between grain size distribution, m , and n .

The shape of the resistivity curve can be attributed to a combination of electrolytic conductivity of the pore fluid and colloidal conductivity processes related to the clay content. In Figure 3.28, the value of m and n increase with increasing depth although all samples have similar clay content (see Section 3.5). However, the grain

size distributions of the samples from the three layers are different, with an increase in grain size with depth. The electrical charges located at the surface of the clay grain size distribution lead to lower electrical resistivity than in coarse grain size distribution because the magnitude of the specific surface area was less, as shown in Figure 3.28 (Samouëlian et al., 2005). A large specific surface area supports the surface conductivity because a number of cations in clay minerals have a higher valence; electrical charge of the clay mineral surface is negative. It is compensated by the concentration of cations in the pore water in the mineral surface. This process is related to the cation exchange capacity (CEC). The calculation of the resistivity of clayey material is not trivial, since the electrical current flow is possible through clay minerals as well as through pore fluid (Kirsch, 2006).

3.10 Velocity and water saturation

Results from the ultrasonic velocity measurements versus increasing water saturation (0-100%) are shown in Figure 3.29, 3.30, and 3.31. The shape of the curve for V_P and V_S is similar; V_P shows higher velocity values than the V_S values. V_S shows a small decrease when the water content is increasing. Figure 3.28 shows the velocities of beach sand, where the shape of the curve for V_P and V_S is similar. V_P has higher velocities than V_S , and there is a small decrease of the P-wave velocity in at 0-40% water saturation. When the water saturation of the sample is higher than 40%, a small increase in the P-wave velocity can be observed.

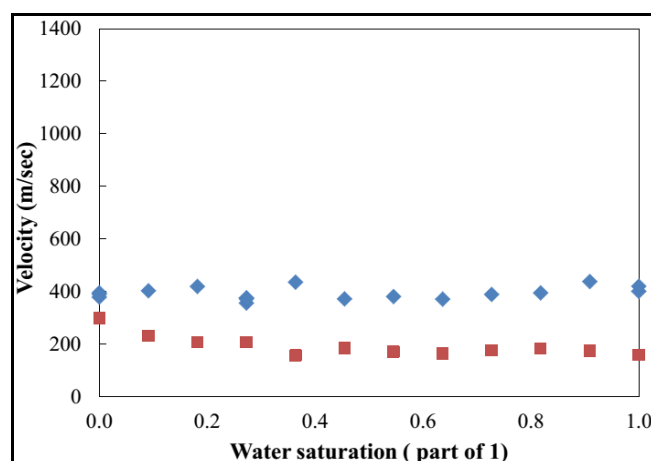


Figure 3.29 Velocity of beach sand, blue crystal is V_P , red square is V_S .

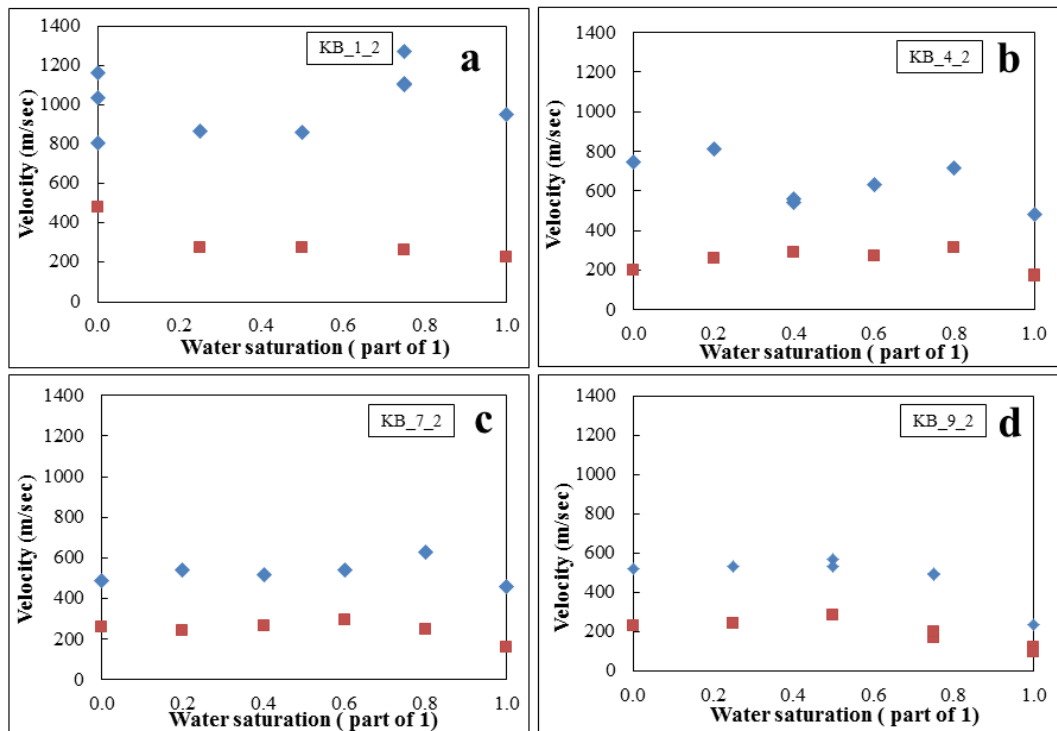


Figure 3.30 Velocity of samples from the granite site, blue crystal is V_p , red square is V_s , (a) KB_1_2, (b) KB_4_2, (c) KB_7_2, and (d) KB_9_2.

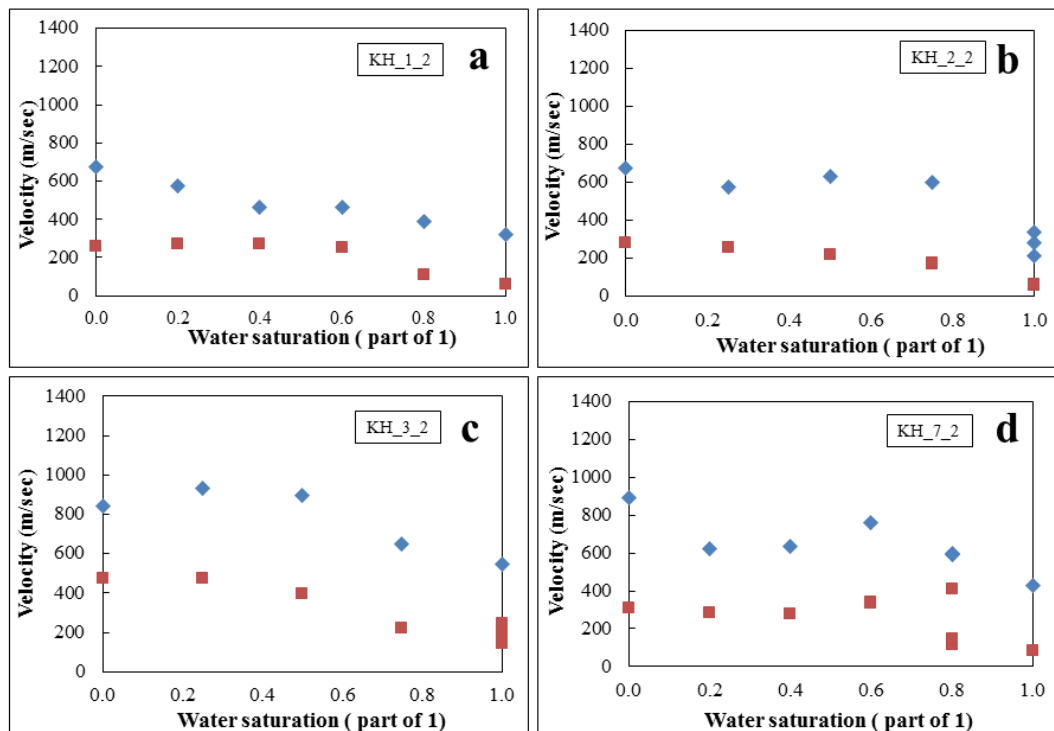


Figure 3.31 Velocity of samples from the sandstone site, blue crystal is V_p , red square is V_s , (a) KH_1_2, (b) KH_2_2, (c) KH_3_2, and (d) KH_7_2.

Figure 3.30 shows that V_P of sample KB_1_2, KB_4_2 and KB_7_2 decrease at lower values of water saturation. V_P increases when the water saturation is in the range of 50-80% and decreases at water saturation of more than 80%. V_P of sample KB_1_2 shows high values because it has a lower clay content, higher density, and lower porosity. V_S shows a small decrease with increasing water saturation and the values do not show much change. The seismic velocities of KB_9_2 do not much change at low water saturation but decrease at high water saturation (more than 80%).

Figure 3.31 shows the velocities of KH_1_2, KH_2_2, and KH_3_2. The shape of the velocity curves for V_P and V_S show a slow decrease when the water saturation increases. The velocity of sample KH_7_2 at a water saturation of 40-60% increases and then decreases at more than 60% water saturation due to the effect from clay content; this sample has lower clay content. Figure 3.29, 3.30, and 3.31 show a gradual decrease of V_S with increasing water saturation from 0 to approximately 1.0 because of a density effect. The density increases from 0-100% due to water saturation, replacing air in the pores. V_P of the sample increases slightly and then decreases with increasing water saturation. The mechanism of the velocity change at low water saturation is comparatively complex, because the dehydrating and solidification of the clay minerals between the unconsolidated sediment grains has to be taken into account. However, in clean sand that does not contain clay some researchers have observed the same velocity changes (Ge et al., 2003). This phenomenon is caused by the physical and chemical interaction between water and unconsolidated sediment skeleton and the uneven distribution of pore fluid at different locations of the sample. Interactions between the individual pore constituents and between pore constituents and solid skeleton (e.g., capillary tension, surface boundary effects) have an influence on the seismic velocities. The different influences on the elastic properties result in different types of velocity-saturation functions. Table 3.7 and 3.8 show descriptions of two sediment samples with increasing water saturation; Figure 3.32 and 3.33 show photos of the same samples for the same water saturation levels.

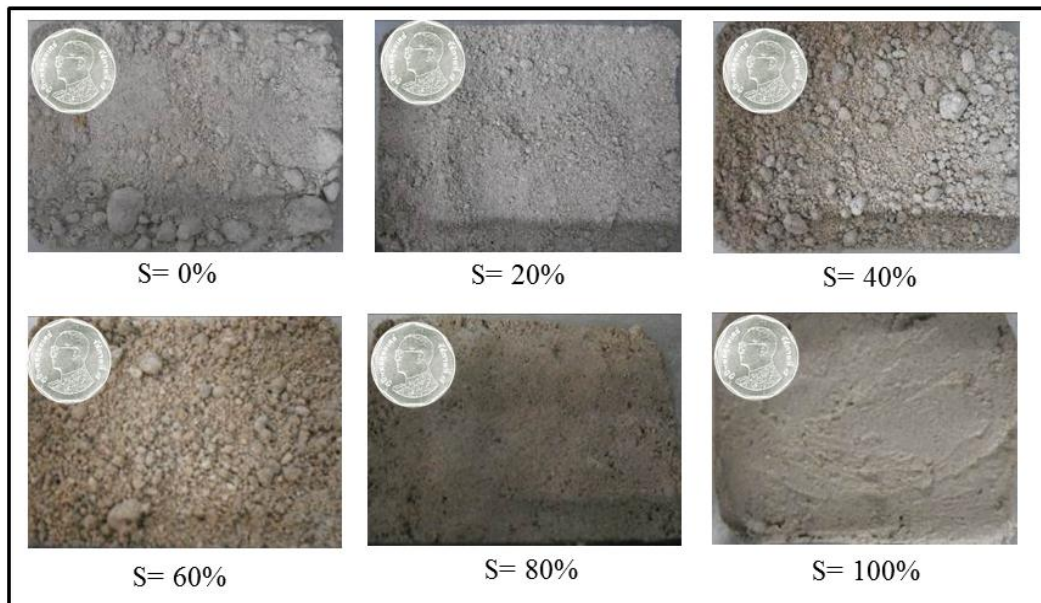


Figure 3.32 Photos of sample KB_7_2 with increasing water saturation.

Table 3.6 Comparison between seismic velocities and sediment characteristics at different levels of water saturation, here sample KB_7_2.

Water saturation (part of 1)	V_P (m/s)	V_S (m/s)	Macroscopic sample description
0.00	488	261	Crumbly, negligible connect between grains
0.20	542	246	Some grain with connect, small grain connect
0.40	516	268	More grain connect, small and big grain
0.60	542	294	Grain connect, early stick
0.80	627	247	Grain together, hard, very stick, tight
1.00	462	164	Plastic, water coming out, stick ,soft

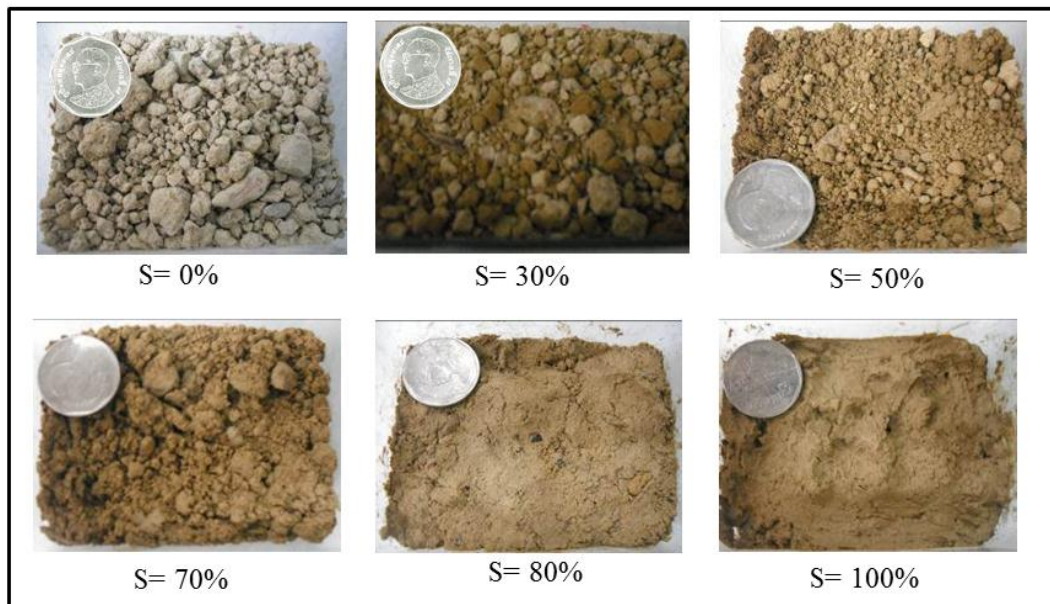


Figure 3.33 Photos of sample KH_2_2 with increasing water saturation.

Table 3.7 Comparison between seismic velocities and sediment characteristics at different levels of water saturation, here sample KH_2_2.

Water saturation (part of 1)	V_P (m/s)	V_S (m/s)	Macroscopic sample description
0.00	488	261	Crumbly, not agglomeration
0.20	542	246	Some grain with connect
0.50	516	268	More grain connect, small grain connect
0.70	542	294	Grain connect, early stick, big grain
0.80	627	247	Grain together, very stick, hard, tight
1.00	462	164	Plastic, water coming out, stick, soft

3.11 Elastic moduli

The elastic moduli, bulk and shear moduli, Young's moduli, and Poisson's ratio were calculated from the ultrasonic compression (V_P) and shear wave velocities (V_S) and density. Figures 3.34, 3.35, Figures 3.36 show relationships between bulk and shear moduli, Young's moduli Poisson's ratio and water saturation. From Figure 3.34 it can be seen that the values of the bulk moduli and shear moduli have a similar shape curve, whereas the Young's moduli did not change much. The shape curve of the Poisson's ratio shows a small increase.

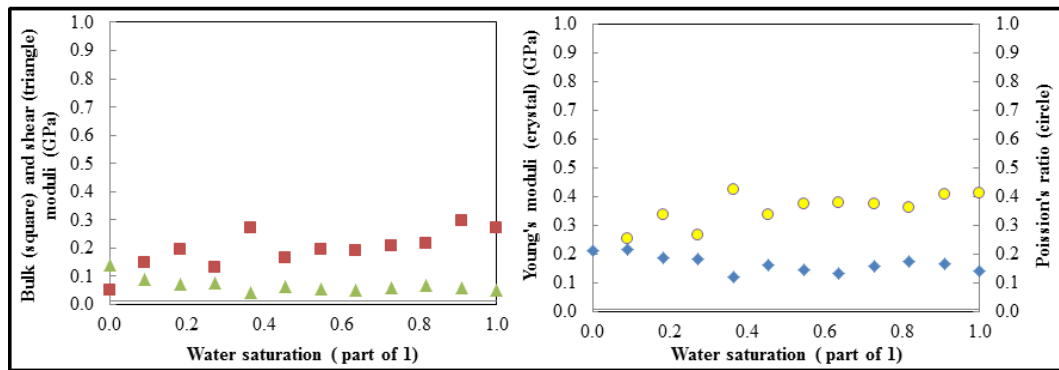


Figure 3.34 Elastic moduli of beach sand, red square is bulk moduli, green triangle is shear moduli, blue crystal is Young's moduli, yellow circle is Poisson's ratio.

Figures 3.35 shows sample KB_1_2 and that the bulk modulus is higher than the shear moduli; the shape of the curve shows a small change at low water saturation. The elastic moduli increase at 50-80% water saturation and decreases above 80% water saturation. The shear modulus decreases slowly, the Young's modulus shows a small increase but decreases at high water saturation (more than 80%); the Poisson's ratio shows a small increase. For Sample KB_4_2 the bulk moduli increases at 0-20% and 50-80% water saturation and decreases when the water saturation is more than 80%. The shear modulus and Young's modulus slowly increases with increasing water saturation but decreases at 80% water saturation. The Poisson's ratio decreases at lower and increases at higher water saturation. For sample KB_7_2 the bulk and shear moduli slowly increase but decrease at 80% water saturation. The Young's modulus decreases at high water saturation (more than 80%), and the Poisson's ratio decrease at lower water saturation and increases at higher water saturation. For Sample KB_9_2 the bulk and shear moduli slowly increase with increasing water saturation and decrease when the water saturation is more than 80%. The Young's modulus shows a small increase at lower values of water saturation but decreases at high water saturation (more than 80%). The Poisson's ratio decreases at low water saturation and increases at high water saturation.

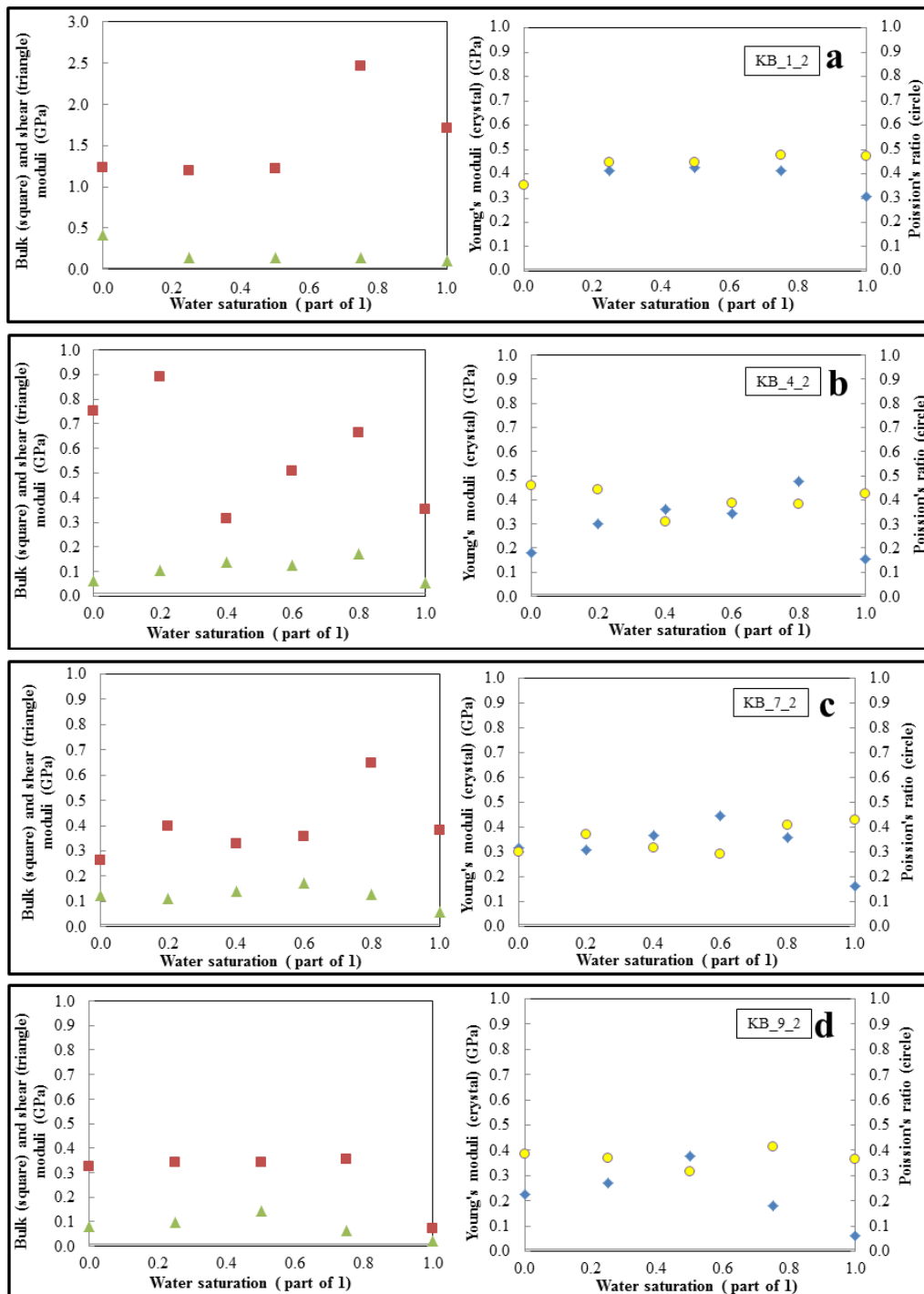


Figure 3.35 Elastic moduli of samples from the granite site (a) KB_1_2, (b) KB_4_2, (c) KB_7_2, (d) KB_9_2, red square is bulk moduli, green triangle is shear moduli, blue crystal is Young's moduli, yellow circle is Poisson's ratio.

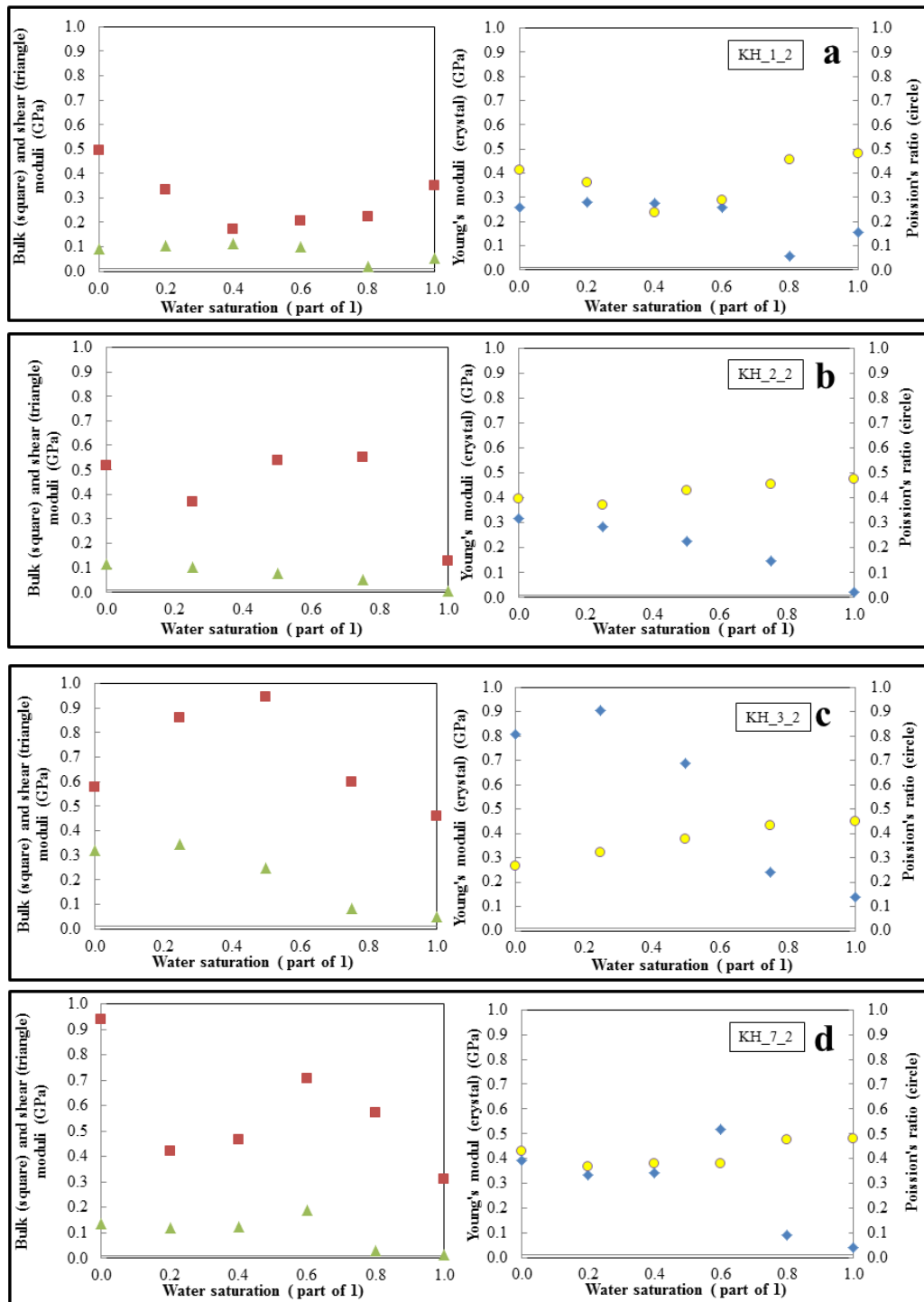


Figure 3.36 Elastic moduli of samples from the sandstone site (a) KH_1_2, (b) KH_2_2, (c) KH_3_2, (d) KH_7_2, red square is bulk moduli, green triangle is shear moduli, blue crystal is Young's moduli, yellow circle is Poisson's ratio.

Figures 3.36, sample KH_1_2 bulk modulus is decreasing at low water saturation and increased at high water saturation. The shear modulus slowly increased with increasing water saturation but decreases at more than 80% water saturation. The Young's modulus shows a small increase but decreases at high water saturation (more than 80%), and the Poisson's ratio decreases at low water saturation and increase at high water saturation. For Sample KH_2_2 and KH_7_2 the bulk modulus was higher at dry conditions but increased at low water saturation and decreases when the water saturation was higher. The shear moduli slowly decrease, as well as the Young's moduli, whereas the Poisson's ratios increase at high water saturation. For Sample KH_3_2 the bulk and shear moduli decreased at lower water saturation and increased when the water saturation was higher. The Young's modulus shows a small increase but decreases at high water saturation (more than 20%), and the Poisson's ratio increased at higher water saturation.

A change in the wave propagation from one lithology to another or from an unsaturated to a saturated medium leads to variations in the value of Poisson's ratio from 0 (indicating a considerable change in volume) to 0.5 (indicating no volumetric change, corresponding to fluids). Also, Poisson's ratio can have negative values, and these indicate certain properties (Salem, 2000). The Poisson's ratio of a stable, isotropic, linear elastic material cannot be less than -1.0 nor greater than 0.5 due to the requirement that Young's modulus, the shear modulus and bulk modulus have positive values. Most materials have Poisson's ratio values ranging between 0.0 and 0.5, values range from 0.05 for very hard, rigid rocks (Sheriff and Geldart, 1995), between 0.2 and 0.35 for most consolidated rock, between 0.4 and 0.45 for unconsolidated materials (Ikelle and Amundsen, 2005). Poisson's ratio is higher when having a higher bulk modulus and lower compressibility, and the Poisson's ratio increases with increasing water saturation and with decreasing porosity.

CHAPTER 4 DISCUSSION AND CONCLUSION

4.1 Physical properties of sediments

All samples of this study were collected from the shallow subsurface comprising of unconsolidated sediments and soils above the bedrock. Overlying the bedrock is a zone of rock fragments, ranging in size from boulders to very fine particles. The top layer, or top soil, is where most of biological and chemical activities take place and can be enriched in organic matter, resulting in dark brown or black color. The middle and bottom layer is fragmented material, a weathering product from the underlying bedrock. Several samples were taken for this study from two sites, one with granite as bedrock and another with sandstone as bedrock. Various measurements on different samples were carried out, so that finally seven samples from the granite (KB) site and nine samples from the sandstone (KH) site will be used for further discussions. The minerals which make up the largest part of these rocks by volume are quartz, feldspar (microcline), and clay (kaolinite, montmorillonite, and illite) and mica (muscovite) in the granite site (see Table 4.1). The main mineral components of sandstone site are quartz, and clay (kaolinite and illite) (see Table 4.2).

Table 4.1 Composition of samples from the granite site.

Sample name	Quartz	Microcline	Kaolinite	Montmo-rillonite	Illite	Muscovite
KB_1_2	✓		✓		✓	
KB_2_2	✓		✓	✓		✓
KB_3_2	✓		✓	✓		✓
KB_4_2	✓		✓		✓	
KB_5_2	✓		✓		✓	
KB_6_2	✓		✓			✓
KB_7_2	✓		✓			✓
KB_8_2	✓	✓	✓			✓
KB_9_2	✓	✓			✓	

Table 4.2 Composition of samples from the sandstone site.

Sample name	Quartz	Kaolinite	Illite
KH_1_2	✓	✓	
KH_2_2	✓	✓	✓
KH_3_2	✓	✓	✓
KH_4_2	✓	✓	✓
KH_5_2	✓	✓	✓
KH_6_2	✓	✓	✓
KH_7_2	✓	✓	
KH_8_2	✓	✓	✓
KH_9_2	✓	✓	✓
KH_10_2	✓	✓	
KH_11_2	✓	✓	
KH_12_2	✓	✓	✓

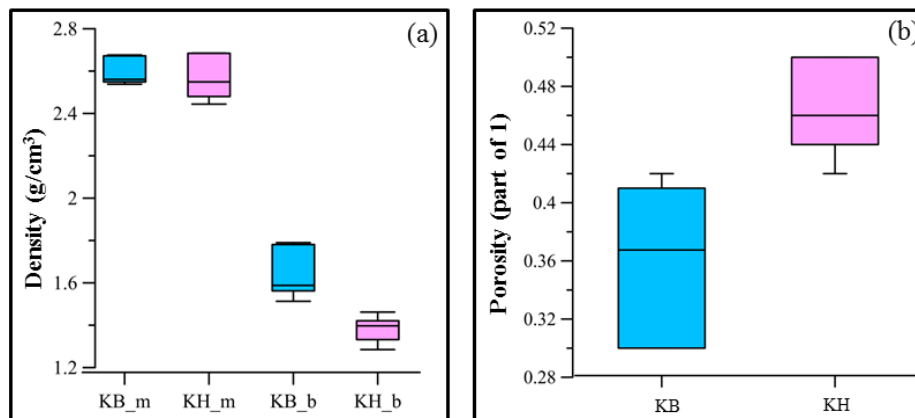


Figure 4.1(a) density, KB_m is mineral density of granite site, KH_m is mineral density of sandstone site, KB_b is bulk density of granite site, and KH_b is bulk density of sandstone site, (b) porosity, blue column is granite site and pink column is sandstone site.

Figure 4.1 shows a comparison of the porosity, mineral and bulk density of samples from both sites. At the granite site the mineral density is 2.55 to 2.68 g/cm³, 1.51 to 1.79 g/cm³ for the bulk density, and 30 to 42% porosity. At the sandstone site the mineral density is 2.44 to 2.69 g/cm³, with the middle layer having the highest mineral density, and 1.28 to 1.42 g/cm³ for the bulk density, and 42 to 50% porosity.

The main cause of the density differences is the porosity, as the density differences between the solid components and the air or the water is much greater than the density differences between typical solid components. Bulk density usually refers to the existing condition where the saturation can vary from 0 to 1 (0-100%). Bulk density decreases with a increase in porosity, and also a decrease in water saturation. Bulk density of the samples from the granite site is higher than for the sandstone site (see Figure 4.1) because the porosity of samples from the granite site is lower than from the sandstone site, and as the mineral densities are not really different.

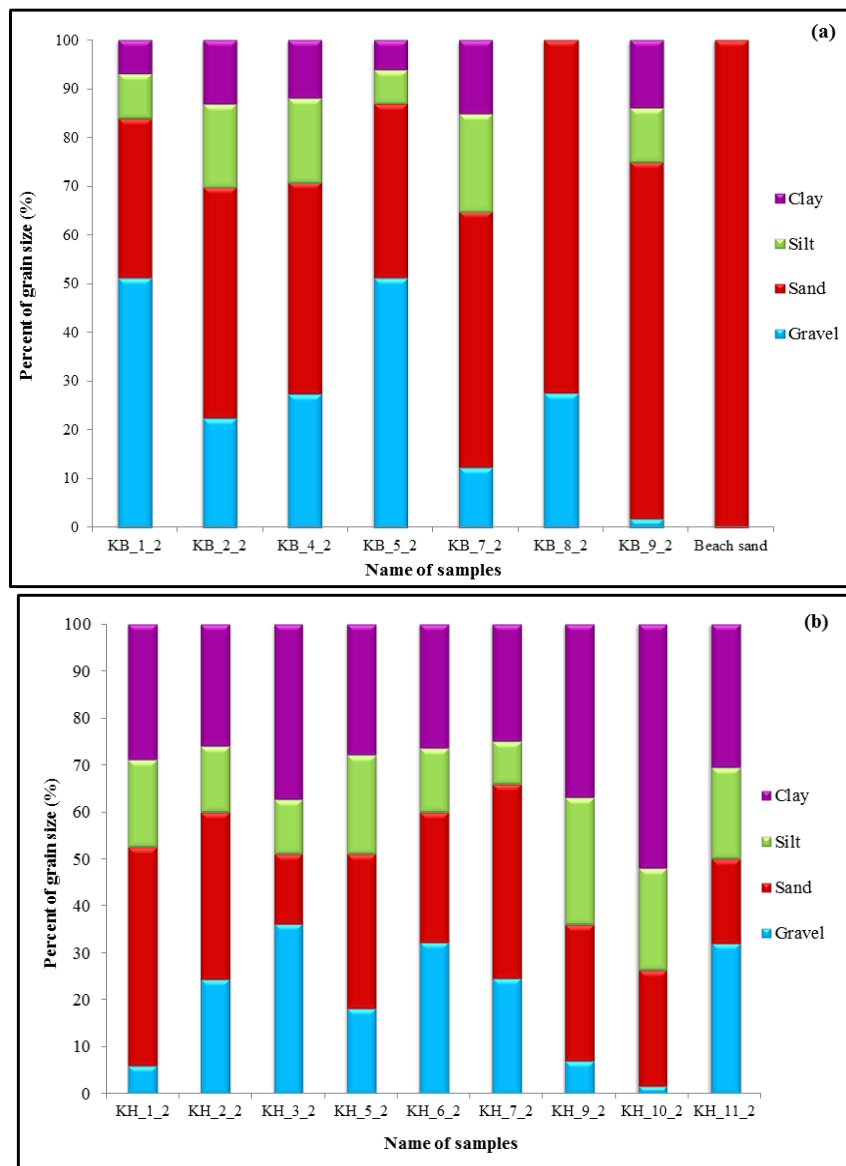


Figure 4.2 Percent of grain size, purple is clay, green is silt, red is sand, and blue is gravel (a) granite site and beach sand, and (b) sandstone site.

Materials from shallow sediments usually show a grain size distribution mainly from clay size to gravel size. The grain size distribution of the samples here show that more than 65% of the granite site and about 50% of the sandstone site of the unconsolidated sediment fraction exceeded a grain size of 0.063 mm (gravel and sand) as shown in Figure 4.2. The classification of samples from the granite site is sandy loam and sand, and sandstone site is clay and clay loam. Pore sizes range from less than 0.1 μm to 15 μm for the granite site, and less than 0.1 μm to 5 μm for the sandstone site. In Figure 4.3 (a), among all samples from the granite site KB_8_2 shows the highest value because it contains only sand and gravel. In Figure 4.3 (b), the values of the samples from the sandstone site are similar because of similar sample characteristics (see Chapter 3).

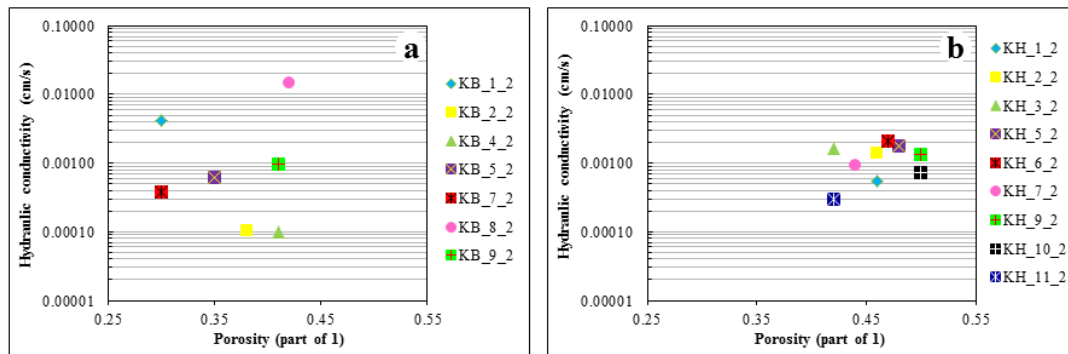


Figure 4.3 Relations between porosity and hydraulic conductivity, (a) granite site, and (b) sandstone site.

4.2 Parameters in resistivity modeling

Calculations of the electrical resistivity using the modified Archie's law are using average parameters from the laboratory measurement, clay content (percent of clay and silt), porosity, matrix density, and conductivity of the water used. Archie's law in clean sediments does not take into account the surface conduction because it is small compared with that provided by the pore fluid (Glover, 2010). In order to fit a curve with the experimental values from the electrical resistivity measurements, the values m , n , and a in the equation were changed; but it was attempted not to change parameter a significantly. The parameter a is related to the path length of the current flow. It depends on the compaction, pore structure, porosity, and grain size. The values of parameter a are in the range of 0.5-2.0.

The parameter n is referred to as the saturation exponent, and thought to account for the connectedness of the water in the partially saturated case. The value

of n is not really adequate to describe the relationship between resistivity and water saturation range of 0 to 100 % (Knight and Endres, 2005). The parameter n depends on the presence of the nature of the fluid in the pore space, wettability of the sediment surface, texture, and the presence of clay mineral. An increase of the n value decreases the connectedness of the pore fluid at low saturation state. The parameter n usually is fixed to values close to 2 (Knight and Endres, 2005).

The parameter m represents the connectedness of the pore network usually for the fully water saturation case. The parameter m depends on the degree of cementation, type of pore, tortuosity, constriction in porous network, and shape, as well as sorting and packing of grains. The cementation factor m increases with decreases connectedness of pore space at higher saturation. For most sediments a value of m between 1.5 and 2.5 is used (Glover, 2010). When m was increased, the curve changed to higher resistivity values at higher degrees of saturation and the curve changed to much higher resistivity values at lower degrees of saturation when n was increased.

The resistivity modeling for samples from the granite site the curve fit is quite good. For example, a higher resistivity comes with a higher content in coarser material, such as KB_8_2, which has a larger portion of sand grain size. The resistivity model curves for samples from the sandstone site show a similar shape, with the absolute resistivity values showing following order: top soil < middle layer < bottom layer.

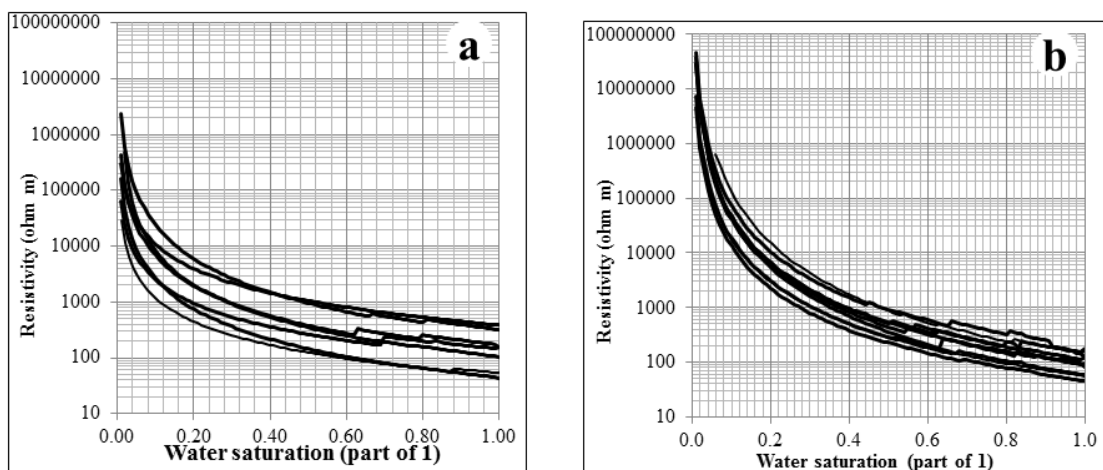


Figure 4.4 Resistivity modeling (a) granite site, and (b) sandstone site.

In Figure 4.4, resistivity values and curves are similar for each site because of similar composition and grain size, but both sites are different because of

different sample composition and grain size. Samples from the granite site show a higher range in the absolute resistivity values because of a higher range in composition and grain size. Samples from the sandstone site have higher clay content. A summary of all m , n , and a values for seven samples from the granite site and nine samples from the sandstone site give following values, $m=0.50-2.40$, $n=1.40-2.00$, $a=0.80-1.00$ for sediments from the granite site, and $m=0.90-3.25$, $n=2.55-3.10$, $a=1.0$ for the sandstone site as shown in Figure 4.5. Values of m for samples from the granite and sandstone site are overlapping, with the values of m of the sandstone site slightly higher because the connectedness of the pore space lower due to higher clay content. Values of n for samples from the granite site are significant lower than for the sandstone site. Values of n of the sandstone site are higher because of higher clay content. The clay minerals lower the connectedness especially at lower water saturation levels.

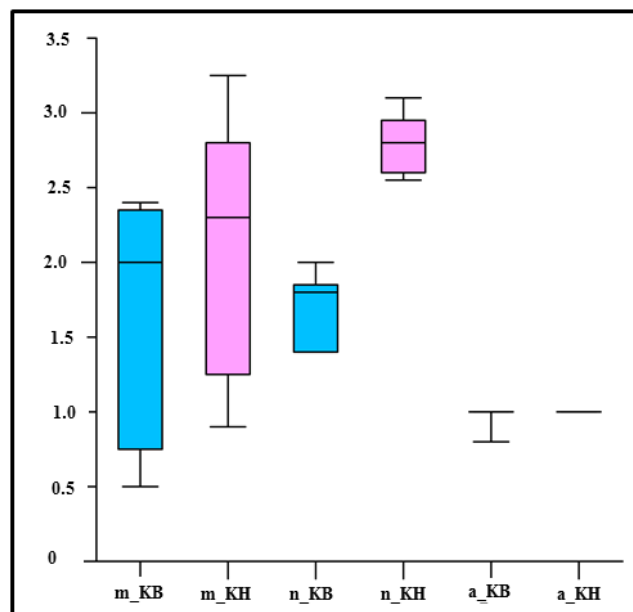


Figure 4.5 Box plot of resistivity modeling parameter: m is cementation factor, n is saturation exponent, and a is a constant, blue column is granite site and pink column is sandstone site.

The electrical resistivity of clay bearing unconsolidated sediments is a complex phenomenon. Laboratory measurements have shown that the electrical resistivity decreases when the water content increases because of a combined effect from the electrolytic conductivity of the pore fluid and the colloidal conductivity from the clay mineral, and that the data follow current theory. The high clay content in sediments with the relatively fresh water in area means that conduction due to ionic

conductivity in pore fluid can be small relative to surface conduction. The very low clay content with the fresh water, surface conduction can be the dominant form of electrical conduction (Knight and Endres, 2005). However, the fitting parameter, m , n , and a , vary with different sediment type. Even with limited data the differences are clear. Further, the results of this study suggest that the grain size distribution has a significant effect on the absolute resistivity, independent from the water saturation.

4.3 Parameters in velocity modeling

As shown in Chapter 3 (Figure 3.31, 3.32; Table 3.7, 3.8) the change of the P-wave velocity correlates with the macroscopic visible change of the sediment with increasing water saturation. With increasing water saturation first some grains stick together, and at about 80% water saturation almost all grains stick together correlating with increased V_P values. V_S decreases when the water saturation increases because fluids have no shear resistance; there is no influence on the unconsolidated sediments bulk shear modulus but the density increases from 0-100% of water saturation. V_S is at a minimum (mass density is largest), the material begins drying, the velocity increases primarily because of the decrease in mass density. With a further increase in the saturation the sediments exhibit a state closer to liquid behavior which correlates with a sharp drop in the P-wave and S-wave velocities, and values of the Poisson's ratio are reaching 0.48, which is almost 0.5 representing fully elastic state.

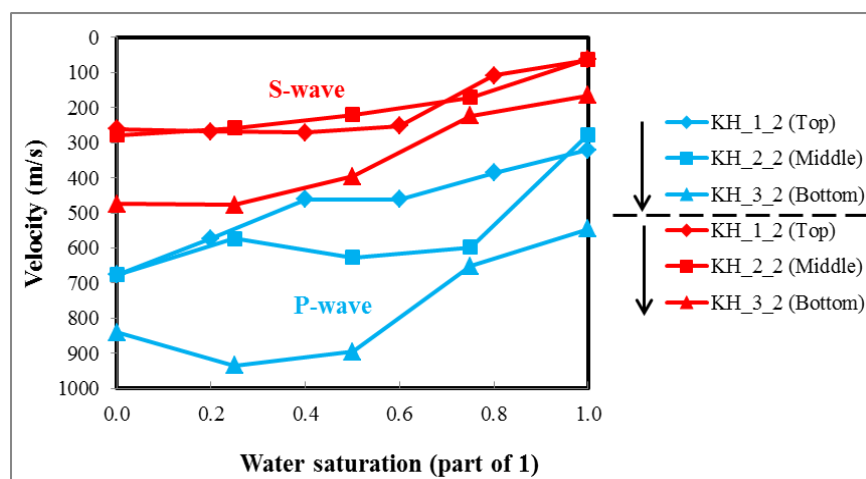


Figure 4.6 Velocities of KH samples (sandstone site) with increasing water saturation, red line is V_S and blue line is V_P .

As shown in Figure 3.29 for the velocities of samples from the granite site the shape of the curve of V_p and V_s is similar. For the samples from the sandstone site Figure 4.4 reveals that the velocity of the bottom layers are higher than the other two layers above. This can be mainly attributed to the lower porosity of this layer (see Figure 3.10). The differences in the porosity of the upper to layers are not so significant than comparing these layers to the bottom layer.

The decrease of the P- and S-wave velocities with increasing water saturation can be explained by the Biot-Gassmann effect, as the increase in the bulk density due to water replacing air in the pores is larger than the increase in the effective bulk moduli of the overall granular material (Wulff and Burkhardt, 1997). But the large change in the velocity values, especially with higher saturation values can be not fully explained by this.

4.3.1 Total and effective stress

There is an extensive literature on the behavior of soils and unlithified sediments as a function of stress conditions (Knight and Endres, 2005). For unconsolidated sediments, the dependence on stress conditions is primarily due to induced changes in pore structure and grain-grain interaction as the physical properties of solid and fluid components are essentially independent of pressure under these conditions. However, due to experimental challenges, there is general lack of laboratory measurements that detail the effects of pressure on geophysical properties at very shallow depths, i.e., less than 20 m below the surface (Knight and Endres, 2005).

Crane (2013) shows that for shallow sediments the added effect of the interparticle stress can suppress the Biot-Gassmann effect, which means that the seismic velocities can be higher than predicted; for clayey sediments the seismic velocities still decrease with increasing saturation. Interparticle stress is a combination of soil suction stress and the apparent tensile stress at saturated state of the sediment as a result of cohesive and physiochemical forces (Bishop et al., 1960), which combine van der Waals attractions, electrical double layer repulsion, and chemical cementation effects (Lu and Likos, 2006).

Stresses in the shallow subsurface are effective stress, the average stress carried by the granular matrix. Effective stress was equated to total stress minus pore pressure (Terzaghi, 1943). In the shallow subsurface interparticle stress can be several orders of magnitude larger than the net overburden stress, which is the overburden pressure minus pore pressure (Ikari and Kopf, 2011). It is typically used

in granular contact models to represent stress at the grain contacts and is the weight of the sediment above the grain contact minus the local pore pressure. Velocities increase and decrease much more than can be explained by changes in net overburden stress. The definition was refined to fully explain stress in the unconsolidated sediments, with

$$P = (\sigma - \mu_a) + \sigma'_s + \sigma_{CO} \quad (4.1)$$

where P is the total effective stress, σ is the total stress, μ_a is pore air pressure, $\sigma - \mu_a$ is the net overburden stress, σ'_s is soil suction stress (Lu and Likos, 2006), and σ_{CO} is apparent tensile stress at the saturated state caused by cohesive or physiochemical forces (Bishop et al., 1960). Physiochemical forces are local forces arising from individual contributions from van der Waals attractions, electrical double layer repulsion, and chemical cementation effects (Lu and Likos, 2006).

Cohesion is a term used in describing the shear strength soils. In natural soils, cohesion results from electrostatic bonds between clay and silt particles. Soils devoid of clay or silt are not cohesive except for capillary forces arising when little water forms bridges between sand grains, resulting in negative pore pressure or suction (De Blasio, 2011). Saturated cohesion (σ_{CO}) is constant for different soil types ($\sigma_{CO} = 300$ Pa for sand (Krantz, 1991), $\sigma_{CO} = 16,000$ Pa for clay (Bishop, 1960)).

Pressure conditions are determined by overburden and fluid pressure. Overburden (also call confining or lithostatic) pressure is due to the weight of the overlying mass supported by the solid grains (Knight and Endres, 2005) shown in Figure 4.5. When the weight of the sediment is much larger than horizontal stresses, the difference ($\sigma - \mu_a$) becomes net overburden stress and can be calculated using the following formula,

$$\sigma - \mu_a = \rho_{bulk}gh_1 + (\rho_{bulk} - \rho_{water})gh_2 \quad (4.2)$$

where ρ_{matrix} is the density of the solid matrix, ρ_{water} is the density of water ($\rho_{water} = 1,000$ kg/m³), g is gravitational acceleration ($g = 9.81$ m/s²), h_1 is the height of the sediment column not influenced by buoyancy ($h_1 = 0.01$ m), and h_2 is the height of the sediment column supported by buoyancy ($h_2 = 8.20$ m; this value is derived from the vertical load onto the sample during laboratory measurements). Under normal pore pressure conditions, pore-pressure is calculated $\mu_a = \rho_{water}g h_2$.

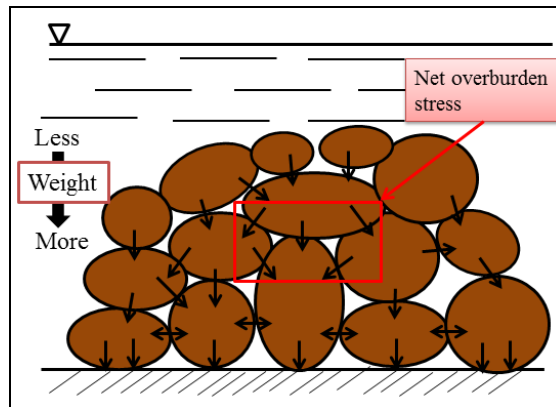


Figure 4.7 Schematic drawing of net overburden stress for a sediment with grain to grain contacts.

Suction stress provides a framework for the examination of the state of stress in unsaturated soil that differs radically from the more commonly known two independent stress state variable approaches, the total stress and matrix suction are hypothesized to be the necessary and sufficient stress variables for describing the mechanical behavior of unsaturated soil. Matrix suction is a function of many soil properties such as the grain size and the geometry of the pores constrained between the soil particles, and matrix suction depends on the pore fluid properties such as the interfacial forces, density, and the degree of saturation (Farouk et al., 2004). Matrix suction is defined as the difference between the pore-air pressure (μ_a) and the pore-water pressure (μ_w), $\mu_a - \mu_w$ is the matrix suction. The matrix suctions generated by the surface tension acting on the meniscus are the effect of the grain sizes, the water content, and the specific gravity of the particles. The meniscus formed between adjacent particles of soil by the soil suction creates a normal force between the particles, which bonds them in a temporary way (see Figure 46).

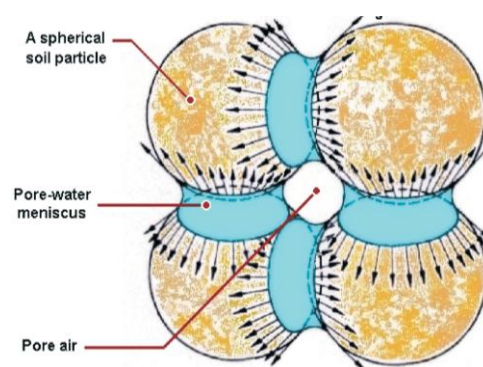


Figure 4.8 Water meniscuses at one point of contact between two soil particles (Farouk et al., 2004).

The suction stress can be used as an index that assesses the state of stress for unsaturated soil because of the close relationship between matrix suction and the degree of saturation, follow

$$\sigma'_s = -(\mu_a - \mu_w)S_e \quad (4.3)$$

where μ_w is the pore water pressure, μ_a is the pore-air pressure, S_e is the effective saturation. If van Genuchten's (1980) soil-water characteristic curves (SWCC) are used, the normalized degree of saturation can be expressed as

$$S_e = \left\{ \frac{1}{1 + [\alpha(\mu_a - \mu_w)]^n} \right\}^{\frac{n-1}{n}} \quad (4.4)$$

where n and α are empirical fitting parameters of unsaturated soil properties, with α being the inverse of air entry pressure for water saturated soil and n being the pore size distribution parameter. Figure D.1 in the Appendix shows the range of values of the α and n parameters for various soil types. The suction stress for the full range of saturation can be arrived at by substituting Equation (4.4) into Equation (4.3) and eliminating matrix suction

$$\sigma'_s = -\frac{S_e}{\alpha} \left(S_e^{\frac{n}{1-n}} - 1 \right)^{1/n} \quad (4.5)$$

For the beach sand and KB_7_2 sample the seismic velocities were calculated using either total effective stress or net overburden as shown in Table 4.1. Figure 4.9 and Figure 4.10 shows velocities with the total effective stress are higher than velocities with the net overburden, but total effective stress are similar the net overburden for beach sand. The total effective stress has significant effect on velocities for clay more than for sand. Over a range of 10-95% water saturation the predicted seismic velocity in sand increases with water saturation, destructively interfering with the Biot-Gassmann effect. In clays, velocity decreases as water saturation increases, but when interparticle stresses are considered the difference between the fastest and slowest velocities is twice as large (Crane, 2013). In clays, the variation of seismic velocity with water saturation is almost double the range

predicted when only net overburden stress is considered to influence stress at the grain contacts.

Table 4.3 Physical and theoretical properties and model parameters of sands and clays for seismic velocity calculations.

Model Parameters	Beach sand	KB_7_2 (sandy loam)
Grain Shear Modulus (GPa)	45 (Mavko et al., 2009)	21 (modified after Mavko et al., 2009)
Grain Bulk Modulus (GPa)	37 (Mavko et al., 2009)	25 (Mavko et al., 2009)
Grain Density (kg/m ³)	2,650	2,550
Grain Poisson's Ratio	0.14	0.43
Porosity	0.40	0.35
Water Density (kg/m ³)	1,000	1,000
Air Density (kg/m ³)	1.22	1.22
Gravitational Acceleration (m/s ²)	9.81	9.81
Coordination Number	1	1
Van Genuchten n Fitting Parameter	5	2
Van Genuchten α Fitting Parameter (kPa ⁻¹)	0.5	0.01
Matrix Cohesion (Pa)	300 (Krantz, 1991)	16,000 (Bishop, 1960)

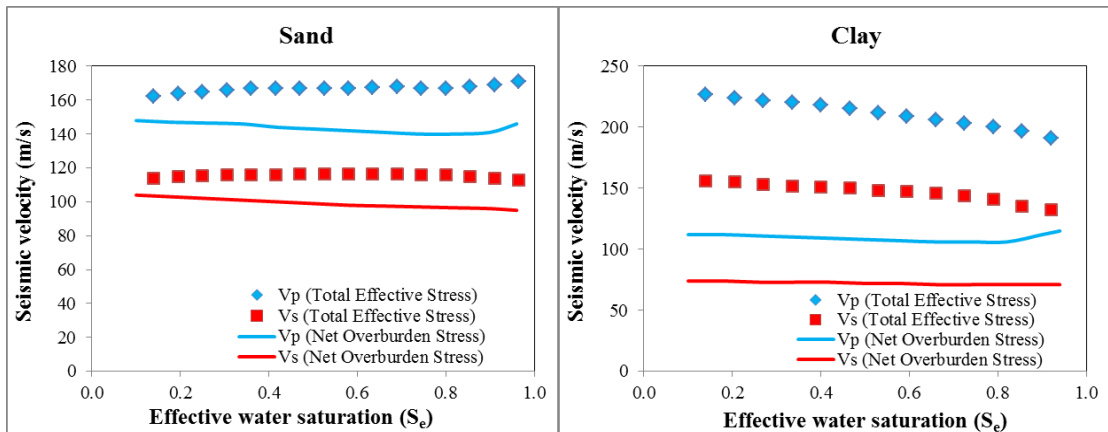


Figure 4.9 V_P and V_S calculated over a range of water saturation for sand at 10 cm depth and clay at 1 m depth to emphasize the contribution of interparticle stresses (Crane, 2013) using the parameter shown in Appendix, Table D1.

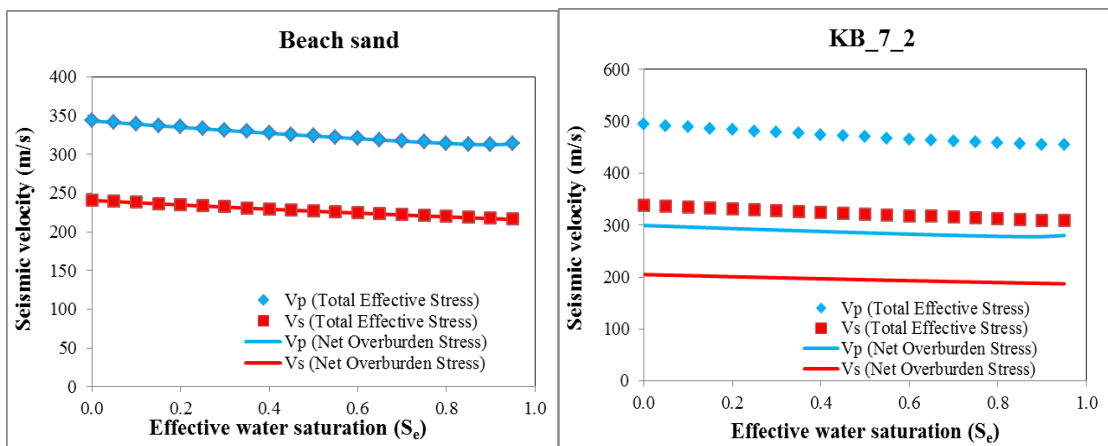


Figure 4.10 V_P and V_S calculated over a range of water saturation for beach sand and sample KB_7_2 using the parameter shown in Table 4.1.

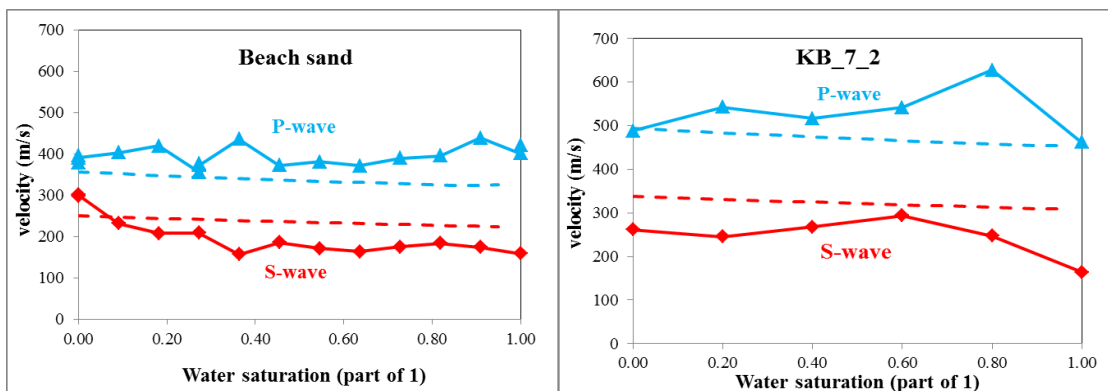


Figure 4.11 V_P and V_S are calculated over a range of water saturation for sand and clay, the blue line is V_P , and the red line is V_S .

From Figure 4.11 it can be seen that the data from the calculation with total effective stress and the data from laboratory measurements are in relatively good agreement; the model parameters however might need to be refined. Especially the absolute velocity values are relatively good determined by the model with the total effective stress. This emphasizes the need to incorporate the total effective stress for shallow subsurface investigations. In sands, calculations of seismic velocity that include interparticle stresses predict an increase in seismic velocity with increasing water saturation, and a decrease in velocity caused decrease in the net overburden stress gradient with the addition of water, due to buoyancy. The water saturation decreases in clays, calculated velocities have twice the range predicted by effective bulk modulus and density changes of the pore space. This greater sensitivity of velocity to water saturation makes clays more suitable for water saturation modeling. However, at higher values of the water saturation of sample KB_7_2 (clay) the seismic velocities decrease because the sample tends to more plastic behavior, also indicated by the Poisson's ratio. This might not be well refined by the model calculations.

In summary, understanding seismic velocities of clay bearing unconsolidated sediments is challenging due to complex phenomena in the sediment. Laboratory measurements have shown that the seismic velocities decreases when water saturation increase because of the Biot-Gassmann effect. However, the absolute changes are better explained when taken into account the interparticle stress, and here also the vertical loading. With a water saturation of more than 80% the seismic velocities decrease dramatically as the sediment samples approaching a state closer to plastic behavior. In Figure 4.12, the velocity values are similar because porosities are similar; but resistivities are different because of different clay content (see above).

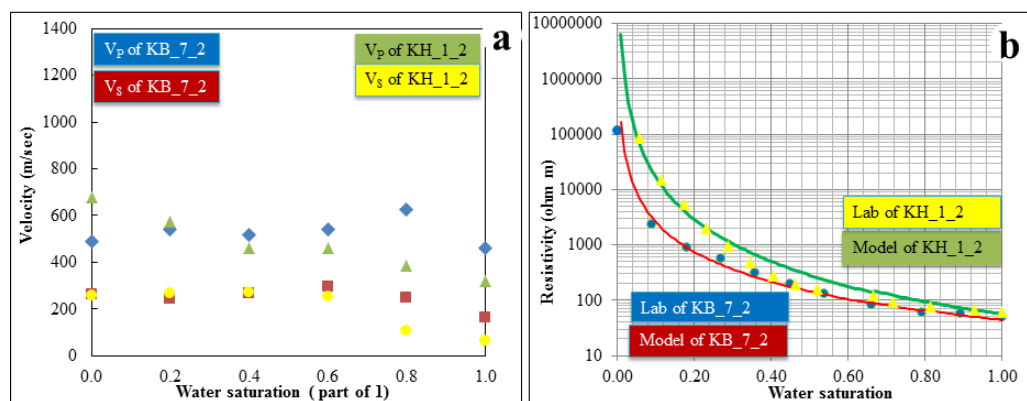


Figure 4.12 Comparisons between granite site and sandstone site, (a) velocity, and (b) resistivity.

4.4 Applicability of work

The objective of this study was to understand the changes of properties of clay bearing unconsolidated sediments through investigations of the physical properties (porosity, density, hydraulic conductivity, and water saturation), geophysical (seismic velocities and electrical conductivity) and related geomechanical properties (elastic moduli) with increasing water saturation. Such an enhanced understanding can have application in various fields, for example in understanding landslide mechanisms, using electrical resistivity sensors in landslide early warning systems, or in modern agriculture, which is using resistivity measurements for soil moisture determination.

BIBLIOGRAPHY

- Alden, A. (2013). Sediment Grain Size Categories. http://geology.about.com/od/sediment_soil/a/sedimentsizes.htm (Oct. 8, 2013).
- American Society for Testing and Materials (ASTM). (1998). ASTM D 422- Standard Test Method for Particle-Size Analysis of Soils. In Annual Book of ASTM Standards. ASTM International, United States.
- American Society for Testing and Materials (ASTM). (2005). ASTM G187 - Standard Test Method for Measurement of Soil Resistivity Using the Two-Electrode Soil Box Method. In Annual Book of ASTM Standards. ASTM International, United States.
- American Society for Testing and Materials (ASTM). (2010). ASTM D854 - Standard Test Methods for Specific Gravity of Soil Solids by Water Pycnometer. In Annual Book of ASTM Standards. ASTM International, United States.
- American Society for Testing and Materials (ASTM). (2010). ASTM D5084-03 Standard Test Methods for Measurement of Hydraulic Conductivity of Saturated Porous Materials Using a Flexible Wall Permeameter. ASTM International, United States.
- American Society for Testing and Materials (ASTM). 2001. ASTM C136 - Standard Test Method for Sieve Analysis of Fine and Coarse Aggregates. In Annual Book of ASTM Standards. ASTM International, United States.
- American Society for Testing and Materials (ASTM). 2003. ASTM Test Designation C 597-02, Standard Test Method for Pulse Velocity through Concrete, In Annual Book of ASTM Standards. ASTM International, United States.
- Atlas, B. (1985). Log Interpretation Charts. Baker Hughes Inc., Houston, TX.
- Bai, W., Kong, L. and Guo, A. (2013). Effects of physical properties on electrical conductivity of compacted lateritic. *Journal of Rock Mechanics and Geotechnical Engineering* 5, 406–411.
- Barends, F.B.J. (2013). Permeability. <http://geo.citg.tudelft.nl/~uffink/syllabus/CT3320/part1/0a/0a.html> (Oct. 1, 2013).
- Beven, K. and German, P. (1982). Macropores and water flow in soils. *Water Resources Research* 18(5), 1311–1325.
- Biot, M.A. (1956). Theory of elastic waves in a fluid-saturated porous solid. 1. Low frequency range. *Journal of the Acoustical of the Society of America*. Vol. 28, 168-178.

- Bishop, A.W. (1959). The principle of effective stress. *Teknish Ukeblad*, 106: 859-863.
- Bishop, A.W., Alpan, I., Blight, G., and Donald, I. (1960). Factors controlling the strength of partly saturated cohesive soils. Imperial College of Science and Technology, University of London, 503-532.
- Blott, S. J. and Pye, K. (2001). Gradistat: a grain size distribution and statistics package for the analysis unconsolidated sediment. *Earth Surface Processes and Landforms* 26: 1237–1248.
- Brovelli A. and Cassiani G. (2010). A combination of the Hashin-Shtrikman bounds aimed at modeling electrical conductivity and permittivity of variably saturated porous media. *Geophys. Journal. Int.* Vol. 180, 225-237.
- Brovelli A. and Cassiani G. (2011). Combined estimation of effective electrical conductivity and permittivity for soil monitoring. *Water Resources Research*, Vol. 47, W08510.
- Brown, G. (2013). Darcy's Law Basics and More. <http://biosystems.okstate.edu/~darcy/laloi/basics.htm> (Oct. 1, 2013).
- Bryson, L. S. (2005). Evaluation of geotechnical parameters using electrical resistivity measurements. *Proc., Earthquake Engineering and Soil Dynamics*, GSP 133, Geo-Frontiers 2005, ASCE, Reston, VA.
- Chalermmyanont, T. (1995). Engineering properties of Hat Yai subsoils. Mater degree thesis School of Civi Engineering, Asain Institute of Technology, Thailand.
- Chen, P., Wei, C., Liu, J. and Ma, T. (2013). Strength theory model of unsaturated soils with suction Stress concept. *Journal of Applied Mathematics*.
- Chik, Z. and Islam, S.M.T. (2012). Finding Soil Particle Size through Electrical Resistivity in Soil Site Investigations. *The Electronic Journal of Geotechnical Engineering*, Vol. 17, 1867-1876.
- Citizendium. (2007). Geotechnical investigation. http://en.citizendium.org/wiki/Geotechnical_investigation, (April 9, 2015).
- Clapp, R. B. and Hornberger, G. M. (1978). Empirical equations for some soil hydraulic properties. *Water Resources Research*, Vol. 14, 601-604.
- Crane, J. M., 2013. Effects of stress and water saturation on seismic velocity and attenuation in near surface sediments. PhD Thesis, Louisiana State University U.S.A. [Online]. Available: <http://etd.lsu.edu/docs/available/etd-08132013-190600/>
- Das, B.M. (2006). *Principles of Geotechnical Engineering*. Thomson Canada Limited, Canada.

- Davis, S.N. and De Wiest, R.J.M. (1966). *Hydrogeology*. John Wiley, New York, 463 pp.
- De Blasio, F.V. (2011). *Introduction to the physics of landslide: lecture notes on the dynamics of mass wasting (Chapter 2 friction, cohesion, and slope stability)*. Springer Science Business Media, 23-52.
- DMR. (2006). *Geological map of Thailand 1:50,000, sheet 5123 III, Changwat Songkhla*.
- Dobrin M. B. and Savit C. H. (1988). *Introduction to geophysical prospecting*. McGraw Hill, New York, U.S.A., 752 pp.
- Driscoll, F.G. (1986). *Groundwater and Wells*. 2nd edition. Johnson Division, St Paul, Minnesota, 1089 pp.
- Farouk, A. Lamboj, L. and Kos, J. (2004). A Numerical Model to Predict Matrix Suction Inside Unsaturated Soils. *Acta Polytechnica* Vol. 44(4), 3-10.
- Fitzner, B., and Basten, D. (1994). *Gesteinsporosität – Klassifizierung, meßtechnische Erfassung und Bewertung ihrer Verwitterungsrelevanz – Jahresberichte aus dem Forschungsprogramm “Steinzerfall-Steinkonservierung” 1992, Förderprojekt des Bundesministers für Forschung und Technologie*. Verlag Ernst & Sohn, Berlin.
- Fratta, D., Fernández A.L. and Santamarina, J.C. (2001). Geo-materials: Non-destructive evaluation in geo-system. In Thompson & Chimenti (Eds.), *AIP Conference Proceedings*, American Institute of Physics, 1148–1155.
- Fredlund, D. G. and Rahardjo, H. (1993). *Soil Mechanics for Unsaturated Soils*. John Wiley & Sons, Inc., U.S.A.
- Friedel, S., Thielen, A. and Springman, S.M. (2006). Investigation of a slope endangered by rainfall-induced landslides using 3D resistivity tomography and geotechnical testing. *Journal of Applied Geophysics* 60, 100–114.
- Friedman, S. P. (2005). Soil properties influencing apparent electrical conductivity: a review. *Computers and Electronics in Agriculture* 46, 45–70.
- Fukue, M., Minatoa, T., Horibe, H., and Taya, N. (1999). The micro-structure of clay given by resistivity measurement. *Engineering Geology* 54. 43–53.
- Gassmann, F. (1951). Über die Elastizität poröser Medien. *Vierteljahrsschrift der Naturforschenden Gesellschaft in Zürich* 96, 1-23.
- Ge, S., Wenlue, S. and Dongquan, Y. (2003). Elastic wave velocity versus saturation and pore fluid distribution relationship. *Chinese Journal of Geophysics*, Vol. 46, 192-198.

- Gee, G. W. and Bauder, J. W. (1987). Particle – size Analysis. In Klute, A. (eds) Methods of Soil analysis Part 1- Physical and Mineralogical methods 2nd Edition, Soil Science Society of America and American Society of Agronomy, USA, 383-412.
- Geotechnical Observations Limited. (2000). What is soil suction? www.geo-observations.com/Information/Whatissoilsuction.html, (March 1, 2015).
- Glover, P.W.J. (2010). A generalized Archie’s law for n phases. *Geophysics*, Vol.75 (6), E247–E265.
- Günzel, F. (1994). Geoelektrische Untersuchung von Grundwasserkontaminationen unter Berücksichtigung von Ton- und Wassergehalt auf die elektrische Leitfähigkeit des Untergrundes, PhD thesis Ludwig-Maximilians-Universität, München.
- Harris, W. and White, G.N. (2008). X-ray Diffraction Techniques for Soil Mineral Identification. In Ulery, A.L. and Drees, L.R. (eds) Methods of Soil Analysis Part 5—Mineralogical Methods, Soil Science Society of America, Wisconsin, 81-116.
- Hartge, K.H and Horn, R. (1999). Einführung in die Bodenphysik. Enke, Stuttgart, German.
- Herod, M. (2011). Groundwater Flow. <http://globalgeology.blogspot.com/2011/06/back-to-basics-on-groundwater.html> (Oct. 1, 2013).
- Hossain, Md. K. (2010). Effect of Rainfall on Matric Suction and Stability of a Residual Granite Soil Slope. *Dhaka University of Engineering & Technology Journal*. Vol.1(1), 37-41.
- IHRD. (2014). The role of clays and shales in low resistivity log response. http://www.ihrdc.com/els/ipimsdemo/t26/offline_IPIMS_s23560/resources/data/G4105.htm. (Dec. 19, 2014).
- Ikari, M.J. and Kopf, A.J. (2011). Cohesive strength of clay-rich sediment. *Geophysical Research Letters* 38, L16309.
- Ikelle, L.T and Amundsen, L. (2005). Introduction to Petroleum Seismology. Society of Exploration Geophysicists, U.S.A.
- Immoor, L. (2006). Permeability, porosity and capillarity. <http://jroberson.mssd14.wikispaces.net/file/view/Permeability,porosity,capilarity.pdf> (Sep. 14, 2013).
- Jarvis, N. (2007). A review of non–equilibrium water flow in solute transport in soil macropores; principles, controlling factors and consequences for water quality. *European Journal of Soil Sciences* 58(3), 523–546.

- Kibria, G. (2011). Determination of geotechnical properties of clayey soil from resistivity imaging (RI). Mater degree thesis of Science in Civi Engineering, University of Texas at Arlington, Partial Fulfillment.
- Kirsch, R. (2006). Groundwater Geophysics – a Tool for Hydrogeology. Springer-Verlag Berlin Heidelberg, Germany.
- Kirsch, R., Rumpel, H., Scheer, W. and Wiederhold, H. (2006). Groundwater Resources in Buried Valleys. Leibniz Institute for Applied, Germany.
- Knight, R.J. and Endres, A. (2005). An introduction to rock physics principles for near- surface geophysics. In Butler, D. K. (eds) Near- surface geophysics, Society of Exploration Geophysicists, U.S.A., 31-70.
- Lewis, D.W. and McConchie, D. (1994). Analytical sedimentology. Chapman & Hall, New York.
- Lohawijarn, W. (2005). Potential ground water resources of Hat Yai Basin in Peninsular Thailand by gravity study. Songklanakarin Journal of Science and Technology. Vol 27(3), 633-647.
- Lu, N., Likos, W. J. (2004). Unsaturated soil mechanics. John Wiley & Sons, U.S.A.
- Lu, N., Likos, W. J. (2006). Suction stress characteristic curve for unsaturated soil. Journal of Geotechnical and Geoenvironmental Engineering, Vol. 132, 131-142.
- Mavko, G., Mukerji, T., and Dvorkin, J. (2009). The Rock Physics Handbook, Tools for Seismic Analysis of Porous Media. Cambridge University Pres, New York.
- Mindlin, R. D., and Deresiewicz, H. (1953). Elastic spheres in contact under varying oblique forces. Journal of Applied Mechanics. Vol.20, 327-344.
- Morris, D. A. and A. I. Johnson, A.I., (1967). Summary of hydrologic and physical properties of rock and soil materials as analyzed by the Hydrologic Laboratory of the U.S. Geological Survey, U.S. Geological Survey Water-Supply Paper 1839-D, 42p.
- Natural Resources Conservation Service Michigan, United States Department of Agriculture. Section 3 Sedimentation Chapter2 Sediment Properties. In National Engineering Handbook. http://www.nrcs.usda.gov/wps/portal/nrcs/detail/mi/technical/engineering/?cid=nrcs141p2_024573. (Dec. 19, 2014).
- Pagano, L., Picarelli, L., Rianna, G. and Urciuoli, G. (2010). A simple numerical procedure for timely prediction of precipitation-induced landslides in unsaturated pyroclastic soils. Landslides 7, 273–289.
- Price, D.G. (2009). Chapter 2 Geological Materials. In Freitas, M. H. de (eds) Engineering Geology Principles and Practice, Springer – Verlag Berlin Heidelberg, Germany, 21-61.

- Pungrassami, T., (1983). Geology and mineral Resources of Songkhla Province, Thailand. Proc. of the Workshop on Stratigraphic Correlation of Thailand and Malaysia. Vol 1, Technical Papers, GST and GSM, Hat Yai, Thailand.
- QAQC LAB. (2012). Equipment for quality control and R&D: sieve shaker. QAQC Lab. www.qclabequipment.com/efl230.jpg (Aug 11, 2014).
- Revil A. and Glover P.W.J. (1997). Theory of ionic-surface electrical conduction in porous media. *Physical Review B -Condensed Matter and Materials Physics*, Vol. 55, 1757-1773.
- Revil A. and Glover P.W.J. (1998). Nature of surface electrical conductivity in natural sands, sandstones, and clays. *Geophysical Research Letters*, Vol. 25, 691-694.
- Revil A., Cathles L. M., Losh S. and Nunn J.A. (1998). Electrical conductivity in shaly sands with geophysical applications. *Journal of Geophysical Research: Solid Earth*, Vol. 103, 23925-23936.
- Russell, E. (2005). Unit 2.1 Soils and Soil Physical Properties. In Miles, A. and Brown, M. (eds) *Teaching Organic Farming and Gardening*, Center for Agroecology & Sustainable Food Systems, University of California, Santa Cruz, 28-29.
- Salem, H.S. (2000). Poisson's ratio and the porosity of surface soils and shallow sediments, determined from seismic compressional and shear wave velocities. *Géotechnique*, Vol 50 (4), 461-463.
- Samouëlian, A., Cousin, I., Tabbagh, A., Bruand, A. and Richard, G., (2005). Electrical resistivity survey in soil science: a review. *Soil & Tillage Research*, Vol. 83, pp.173–193.
- Sassa, K., Nagai, O., Solidum, R., Yamazaki, Y. and Ohta, H. (2010). An integrated model simulating the initiation and motion of earthquake and rain induced rapid landslides and its application to the 2006 Leyte landslide. *Landslides*, Vol. 7, 219–236.
- Schlumberger. (1987). *Log Interpretation Principle / Application*, New York.
- Schlumberger. (2000). *Log Interpretation Charts*. Schlumberger Ed. Schlumberger, Texas.
- Schön, J. H. (2011). *Physical Properties of Rocks*. Oxford, United Kingdom.
- Schweitzer, J. (2010). Scanning Electron Microscope. <http://www.purdue.edu/rem/rs/sem.html> (Oct. 1, 2013).
- Seladji, S., Cosenza, P., Tabbagh, A., Ranger, J. and Richard, G. (2010). The effect of compaction on soil electrical resistivity: a laboratory investigation. *European Journal of Soil Science*, Vol.61, 1043-1055.

- Sen, P.N., Goode, P.A. and Sibbit, A. (1988). Electrical conduction in clay bearing sandstones at low and high salinities. *Journal of Applied Physics*, Vol. 63, 4832-4840.
- Sheriff, R.E and Geldart, L.P. (1995). *Exploration Seismology*. Press Syndicate of University Cambridge, United Kingdom.
- Siegesmund, S. and Dürrast, H. (2011). Physical and mechanical properties of rocks. In: Siegesmund, S. and Snethlage, R. (eds) *Stone in Architecture*, 4th Edition, Springer-Verlag Berlin Heidelberg, Germany, 97-225.
- Solids Wiki. (2012). Analyzing sieves. http://solidswiki.com/images/1/1b/Analysis_sieve.gif (Aug 11, 2014).
- Song, Y.-S., Hwang, W. K., Jung, S. J. and Kim, T. H. (2012). A comparative study of suction stress between sand and silt under unsaturated conditions. *Engineering Geology*, Vol.124, 90-97.
- Springman, S., Jommi, C. and Teyssere, P. (2003). Instabilities on moraine slopes induced by loss of suction: a case history. *Geotechnique*, Vol. 53(1), 3–10.
- Stadler, L., Hinkelmann, R. and Zehe, E. (2009). Two-phase flow simulation of water infiltration into layered natural slopes inducing soil deformation. *Proceedings of the International Conference ‘Landslide Processes’*, held in Strasbourg, France, from February 6 to 7, 2009. 197–201.
- Substect. (2013). Stabilization of colloids. http://www.substech.com/dokuwiki/doku.php?id=stabilization_of_colloids. (Jan. 19, 2015).
- Swapp, S. (2013). Scanning Electron Microscopy (SEM). http://serc.carleton.edu/research_education/geochemsheets/techniques/SEM.html (Sep. 4, 2014).
- Telford, W.M., Geldart, L.P. and Sheriff, R.E. (1990). *Applied Geophysics*. Press Syndicate of University Cambridge, United Kingdom.
- Terzaghi, K., Peck, R. B., and Mesri, G. (1996). *Soil mechanics in engineering practice*. John Wiley & Sons, Inc., Canada.
- The Nation. (2011). Land encroachers blamed. *Nation Multimedia*, 4 April 2011.
- Todd, D. K. (1980). *Groundwater Hydrology*. 2nd edition, John Wiley, New York.
- Uchida, T., Kosugi, K. and Mizuyama, T. (2001). Effects of pipe flow on hydrological processes and its relation to landslide: a review of pipe flow studies in forested head-water catchments. *Hydrological Processes* 15(11), 2151–2174.
- USGS. (2013). Pore Water. http://toxics.usgs.gov/definitions/pore_water.html (Sep. 14, 2013).

- van Genuchten, M.T. (1980). A closed-form equation for predicting the hydraulic conductivity of unsaturated soils. *Soil Sci. Soc. Am. J.* 44, 892-898.
- Welton, J. E. (2003). *SEM Petrology Atlas*. The American Association of Petroleum Geologists, U.S.A.
- Wentworth, C.K.A (1922). Scale of grade and class terms for clastic sediments, *The Journal of Geology*, Vol.30, 377-392.
- Wulff, A.M. and Burkhardt, H. (1997). Dependence of seismic wave attenuations and velocities in rock on pore fluid properties. *Physics and Chemistry of the Earth*, Vol.22, 69-73.

APPENDIX

APPENDIX A
OBSERVED AND CALULATED DATA

Table A.1 Density and porosity

Sample name	Mineral Density (g/cm³)	Bulk Density (g/cm³)	Porosity (part of 1)
KH_1_2	2.52	1.35	0.46
KH_2_2	2.68	1.46	0.46
KH_3_2	2.44	1.42	0.42
KH_5_2	2.57	1.33	0.48
KH_6_2	2.69	1.41	0.47
KH_7_2	2.48	1.40	0.44
KH_9_2	2.55	1.29	0.50
KH_10_2	2.65	1.33	0.50
KH_11_2	2.45	1.42	0.42
KB_1_2	2.54	1.78	0.30
KB_2_2	2.56	1.58	0.38
KB_4_2	2.56	1.51	0.41
KB_5_2	2.59	1.68	0.35
KB_7_2	2.55	1.79	0.30
KB_8_2	2.67	1.56	0.42
KB_9_2	2.68	1.59	0.41

Table A.2 Grain size distribution

Sample name	Grain size (%)								
	33.10	25.40	9.52	4.75	2.00	0.42	0.075	0.004	0.001
KB_1_2	100	100	95	63	49	33	18	7	0
KB_2_2	100	100	92	87	77	50	31	13	0
KB_4_2	100	100	99	87	72	44	30	12	0
KB_5_2	100	96	81	66	49	24	13	6	0
KB_7_2	100	100	100	98	88	52	36	15	0
KB_8_2	100	100	100	94	72	18	1	0	0
KB_9_2	100	100	100	100	98	58	27	14	0
KB_2	100	100	93	79	62	23	2	0	0
KB_5	100	100	96	83	60	29	17	5	0
KH_1_2	100	100	100	99	94	82	51	29	0
KH_2_2	100	100	86	80	76	67	43	26	0
KH_3_2	100	100	87	77	64	58	50	37	0
KH_5_2	100	100	95	89	82	74	52	28	0
KH_6_2	100	100	85	76	68	57	42	26	0
KH_7_2	100	100	93	85	76	60	37	25	0
KH_9_2	100	100	96	96	93	87	67	37	0
KH_10_2	100	100	100	100	99	93	75	52	0
KH_11_2	100	100	95	81	68	64	51	31	0
KH_8	100	100	90	80	75	67	44	25	0
KH_13	100	100	79	68	59	43	26	16	0
beach sand	100	100	100	100	100	92	3	0	0

Table A.3 Soil texture

Sample name	Soil texture (%)		
	Sand	Clay	Silt
KB_1_2	0.73	0.12	0.16
KB_2_2	0.56	0.19	0.25
KB_4_2	0.55	0.18	0.27
KB_5_2	0.69	0.15	0.17
KB_7_2	0.60	0.17	0.23
KB_8_2	0.93	0.04	0.04
KB_9_2	0.73	0.15	0.12
KH_1_2	0.38	0.38	0.24
KH_2_2	0.31	0.45	0.24
KH_3_2	0.24	0.58	0.18
KH_5_2	0.38	0.35	0.27
KH_6_2	0.31	0.46	0.24
KH_7_2	0.29	0.53	0.19
KH_9_2	0.39	0.36	0.26
KH_10_2	0.26	0.52	0.22
KH_11_2	0.35	0.40	0.25

Table A.4 Hydraulic conductivity

Name	h_1 (cm)	h_2 (cm)	Time (s)	Temp (°C)	K_T (cm/s)	h_T/h_{20}	k_{20} (cm/s)	Average (cm/s)
Beach sand	120	4	4.00	29.0	0.035	0.8139	0.02870	0.0276
	121	4	4.44	29.0	0.032	0.8139	0.02592	
	123	4	4.47	29.0	0.032	0.8139	0.02587	
	121	4	3.80	29.0	0.037	0.8139	0.03025	
	125	4	4.24	29.0	0.034	0.8139	0.02740	
KB_1_2	120	4	24.50	26.0	0.006	0.8694	0.00501	0.0042
	120	4	25.40	26.0	0.006	0.8694	0.00483	
	120	4	28.24	26.0	0.005	0.8694	0.00434	
	120	4	31.73	26.0	0.004	0.8694	0.00387	
	120	4	34.31	26.0	0.004	0.8694	0.00357	
	121	6	25.23	29.0	0.005	0.8139	0.00402	
	121	6	28.73	29.0	0.004	0.8139	0.00353	
KB_2_2	80	4	994.11	27.5	0.000	0.8410	0.00011	0.0001
	80	4	1000.30	27.0	0.000	0.8502	0.00011	
	80	4	893.60	27.0	0.000	0.8502	0.00012	
	80	4	894.60	27.5	0.000	0.8410	0.00012	
	80	4	869.50	29.0	0.000	0.8139	0.00012	
	80	4	864.42	29.0	0.000	0.8139	0.00012	
	80	4	955.41	29.0	0.000	0.8139	0.00011	
KB_4_2	120	4	1304.23	27.0	0.000	0.8502	0.00009	0.0001
	80	4	817.59	27.0	0.000	0.8502	0.00013	
	80	4	792.44	28.0	0.000	0.8598	0.00013	
	80	4	922.65	28.0	0.000	0.8598	0.00012	
	80	6	1085.53	29.0	0.000	0.8139	0.00008	
	80	6	1124.40	29.0	0.000	0.8139	0.00008	
	80	6	1137.66	29.0	0.000	0.8139	0.00008	
	121	6	1152.41	29.0	0.000	0.8139	0.00009	
KB_5_2	80	4	194.48	28.0	0.001	0.8598	0.00055	0.0006
	80	4	166.52	28.0	0.001	0.8598	0.00064	
	80	4	155.91	28.0	0.001	0.8598	0.00069	
	80	4	169.72	28.0	0.001	0.8598	0.00063	
	80	4	163.44	28.0	0.001	0.8598	0.00065	
	80	4	189.68	28.0	0.001	0.8598	0.00056	
KB_7_2	60	4	238.24	29.0	0.000	0.8139	0.00038	0.0004
	60	4	269.42	29.0	0.000	0.8139	0.00034	
	67	4	299.47	29.0	0.000	0.8139	0.00032	
	60	4	227.61	29.0	0.000	0.8139	0.00040	
	60	4	203.06	29.0	0.001	0.8139	0.00045	
KB_8_2	120	4	6.62	29.0	0.021	0.8139	0.01734	0.0145
	120	4	7.70	29.0	0.018	0.8139	0.01491	
	120	4	8.11	29.0	0.017	0.8139	0.01416	
	120	4	7.91	29.0	0.018	0.8139	0.01451	
	120	4	9.97	29.0	0.014	0.8139	0.01152	

Table A.4 Hydraulic conductivity (continued)

Name	h_1 (cm)	h_2 (cm)	Time (s)	Temp (°C)	K_T (cm/s)	h_T/h_{20}	k_{20} (cm/s)	Average (cm/s)
KB_9_2	120	4	102.57	29.0	0.001	0.8139	0.00112	0.0010
	120	4	118.74	29.0	0.001	0.8139	0.00097	
	120	4	123.49	29.0	0.001	0.8139	0.00093	
	120	4	123.89	29.0	0.001	0.8139	0.00093	
	120	4	127.05	29.0	0.001	0.8139	0.00090	
KH_1_2	120	4	208.13	28.5	0.001	0.8229	0.00056	0.0005
	120	4	194.81	28.0	0.001	0.8318	0.00060	
	120	4	274.36	28.0	0.001	0.8318	0.00043	
	120	4	170.97	28.0	0.001	0.8318	0.00069	
	120	4	173.37	28.0	0.001	0.8318	0.00068	
	120	4	242.67	28.0	0.001	0.8318	0.00048	
	120	4	238.94	28.0	0.001	0.8318	0.00049	
	120	4	276.12	28.0	0.001	0.8318	0.00042	
	KH_2_2	120	4	89.72	28.0	0.002	0.8318	
120		4	83.81	28.0	0.002	0.8318	0.00140	
120		4	90.09	27.5	0.002	0.8410	0.00132	
120		4	86.98	27.5	0.002	0.8410	0.00136	
120		4	78.97	28.0	0.002	0.8318	0.00149	
120		4	80.64	28.0	0.002	0.8318	0.00146	
KH_3_2		121	6	53.18	27.0	0.002	0.8502	0.00199
	121	6	57.32	27.0	0.002	0.8502	0.00185	
	121	6	58.81	27.0	0.002	0.8502	0.00180	
	121	6	62.66	27.0	0.002	0.8502	0.00169	
	121	6	70.32	27.0	0.002	0.8502	0.00151	
	120	4	71.18	26.5	0.002	0.8598	0.00170	
	120	4	77.27	26.5	0.002	0.8598	0.00157	
	120	4	82.35	26.5	0.002	0.8598	0.00147	
	120	4	89.00	26.5	0.002	0.8598	0.00136	
KH_5_2	120	4	56.55	27.0	0.002	0.8502	0.00212	0.0018
	120	4	48.68	26.5	0.003	0.8598	0.00249	
	120	4	62.15	26.5	0.002	0.8598	0.00195	
	120	4	65.02	26.5	0.002	0.8598	0.00187	
	120	4	80.30	26.5	0.002	0.8598	0.00151	
	120	4	86.43	26.5	0.002	0.8598	0.00140	
	120	4	85.66	28.0	0.002	0.8598	0.00142	
	120	4	91.16	28.0	0.002	0.8598	0.00133	
KH_6_2	120	4	56.08	27.0	0.003	0.8502	0.00214	0.0021
	120	4	55.97	27.0	0.003	0.8502	0.00214	
	120	4	57.48	27.0	0.002	0.8502	0.00209	
	120	4	58.04	27.0	0.002	0.8502	0.00207	

Table A.4 Hydraulic conductivity (continued)

Name	h_1 (cm)	h_2 (cm)	Time (s)	Temp (°C)	K_T (cm/s)	h_T/h_{20}	k_{20} (cm/s)	Average (cm/s)
KH_7_2	121	6	106.80	28.0	0.001	0.8598	0.00100	0.0009
	121	6	115.25	27.5	0.001	0.8410	0.00091	
	121	6	115.54	27.0	0.001	0.8502	0.00092	
	121	6	117.82	27.0	0.001	0.8502	0.00090	
KH_9_2	120	4	85.70	29.0	0.002	0.8139	0.00134	0.0013
	119	4	90.39	29.0	0.002	0.8139	0.00127	
	119	4	85.81	29.0	0.002	0.8139	0.00133	
	118	4	82.18	29.0	0.002	0.8139	0.00139	
	118	4	85.85	29.0	0.002	0.8139	0.00133	
	119	4	85.73	29.0	0.002	0.8139	0.00134	
KH_10_2	120	4	157.61	27.0	0.001	0.8502	0.00076	0.0007
	120	4	150.04	27.0	0.001	0.8502	0.00080	
	120	4	166.39	27.0	0.001	0.8502	0.00072	
	120	4	170.06	27.0	0.001	0.8502	0.00071	
	120	4	170.00	27.0	0.001	0.8502	0.00071	
	120	4	176.87	27.0	0.001	0.8502	0.00068	
KH_11_2	123	6	357.14	27.0	0.000	0.8502	0.00030	0.0003
	121	6	355.73	27.0	0.000	0.8502	0.00030	
	121	6	333.56	27.0	0.000	0.8502	0.00032	
	117	6	344.30	27.0	0.000	0.8502	0.00030	
	121	6	383.34	27.0	0.000	0.8502	0.00028	

Table A.5 Resistivity from measurement

Sample name	Saturation (part of 1)	Resistivity (ohm m)	Porosity (part of 1)
KB_1_2	0.00	188405.80	0.30
	0.13	2435.83	0.30
	0.25	512.21	0.30
	0.38	223.25	0.30
	0.50	150.99	0.30
	0.63	117.43	0.30
	0.75	101.72	0.30
	0.88	80.67	0.23
	1.00	77.97	0.23
KB_2_2	0.00	707426.38	0.38
	0.08	12670.32	0.38
	0.15	3392.93	0.38
	0.23	1783.43	0.38
	0.31	966.87	0.38
	0.38	572.04	0.38
	0.46	438.03	0.38
	0.54	308.02	0.38
	0.62	300.82	0.38
	0.69	190.86	0.37
	0.77	164.74	0.36
	0.85	148.26	0.36
	0.92	135.46	0.36
	1.00	133.29	0.36
KB_4_2	0.00		0.41
	0.08		0.41
	0.17	9357.34	0.41
	0.25	4372.94	0.41
	0.33	2722.98	0.41
	0.42	1937.13	0.41
	0.50	895.88	0.41
	0.58	616.85	0.41
	0.67	410.91	0.37
	0.75	313.17	0.35
	0.83	245.79	0.33
	0.92	223.64	0.34
	1.00	206.18	0.35

Table A.5 Resistivity from measurement (continued)

Sample name	Saturation (part of 1)	Resistivity (ohm m)	Porosity (part of 1)
KB_5_2	0.00		0.35
	0.09	62439.61	0.35
	0.18	11458.33	0.35
	0.27	4857.20	0.35
	0.36	2439.60	0.35
	0.45	1436.11	0.35
	0.55	1069.07	0.35
	0.64	836.57	0.35
	0.73	624.37	0.33
	0.82	471.28	0.31
	0.91	401.45	0.31
	1.00	365.74	0.31
KB_7_2	0.00	116216.22	0.30
	0.10	2344.60	0.30
	0.20	922.75	0.30
	0.30	586.63	0.30
	0.40	312.05	0.30
	0.50	203.79	0.30
	0.60	133.96	0.30
	0.70	92.06	0.29
	0.80	71.40	0.28
	0.90	66.85	0.28
	1.00	59.93	0.28
KB_8_2	0.00	4350000.00	0.42
	0.11	8969.07	0.42
	0.22	3002.07	0.42
	0.33	1705.88	0.42
	0.44	1201.66	0.42
	0.56	904.37	0.42
	0.67	716.64	0.42
	0.78	591.03	0.42
	0.89	475.93	0.42
	1.00	387.01	0.42

Table A.5 Resistivity from measurement (continued)

Sample name	Saturation (part of 1)	Resistivity (ohm m)	Porosity (part of 1)
KB_9_2	0.00	-	0.41
	0.09	20165.09	0.41
	0.18	4702.97	0.41
	0.27	1730.77	0.41
	0.36	913.46	0.41
	0.45	585.62	0.41
	0.55	473.95	0.41
	0.64	387.93	0.41
	0.73	267.07	0.34
	0.82	206.56	0.33
	0.91	195.15	0.34
	1.00	172.05	0.33
beach sand	0.00	85500.00	0.40
	0.08	1379.03	0.40
	0.17	389.34	0.40
	0.25	232.46	0.40
	0.33	157.75	0.40
	0.42	109.34	0.40
	0.50	79.91	0.40
	0.58	62.14	0.40
	0.67	53.37	0.40
	0.75	47.08	0.40
	0.83	40.71	0.40
	0.92	38.24	0.40
	1.00	36.57	0.40
KH_1_2	0.00	-	0.46
	0.07	86499.36	0.46
	0.14	15122.27	0.46
	0.21	5426.56	0.46
	0.29	1983.93	0.46
	0.36	978.50	0.46
	0.43	481.62	0.46
	0.50	282.86	0.46
	0.57	192.22	0.46
	0.64	163.82	0.46
	0.71	120.44	0.43
	0.79	97.60	0.43

Table A.5 Resistivity from measurement (continued)

Sample name	Saturation (part of 1)	Resistivity (ohm m)	Porosity (part of 1)
KH_1_2	0.86	82.41	0.42
	0.93	75.39	0.41
	1.00	65.83	0.41
KH_2_2	0.00		0.46
	0.08	205558.60	0.46
	0.17	36582.46	0.46
	0.25	12512.26	0.46
	0.33	5245.12	0.46
	0.42	1806.16	0.46
	0.50	844.76	0.46
	0.58	490.54	0.46
	0.67	316.48	0.41
	0.75	247.26	0.40
	0.83	192.97	0.39
	0.92	158.70	0.38
	1.00	134.85	0.37
KH_3_2	0.00		0.42
	0.08	476851.85	0.42
	0.15	67057.29	0.42
	0.23	36370.06	0.42
	0.31	10596.71	0.42
	0.38	4010.90	0.42
	0.46	2024.37	0.42
	0.54	1172.59	0.42
	0.62	684.98	0.41
	0.69	494.18	0.40
	0.77	367.15	0.40
	0.85	318.96	0.38
	0.92	249.57	0.38
	1.00	225.47	0.37
KH_5_2	0.00		0.48
	0.08	128186.27	0.48
	0.15	17935.53	0.48
	0.23	6544.04	0.48
	0.31	2660.77	0.48
	0.38	1197.34	0.48

Table A.5 Resistivity from measurement (continued)

Sample name	Saturation (part of 1)	Resistivity (ohm m)	Porosity (part of 1)
KH_5_2	0.46	602.81	0.48
	0.54	374.11	0.48
	0.62	226.57	0.44
	0.69	140.52	0.40
	0.77	107.55	0.38
	0.85	98.76	0.40
	0.92	89.15	0.40
	1.00	85.10	0.40
KH_6_2	0.00		0.47
	0.08	181597.22	0.47
	0.17	46365.25	0.47
	0.25	17294.97	0.47
	0.33	6553.88	0.47
	0.42	2563.73	0.47
	0.50	1285.64	0.47
	0.58	724.87	0.46
	0.67	455.89	0.41
	0.75	254.61	0.35
	0.83	210.89	0.35
	0.92	194.34	0.36
	1.00	200.45	0.38
KH_7_2	0.00		0.44
	0.08	368055.56	0.44
	0.15	39434.52	0.44
	0.23	15389.08	0.44
	0.31	9317.86	0.44
	0.38	7252.33	0.44
	0.46	2938.57	0.44
	0.54	1409.15	0.42
	0.62	812.92	0.41
	0.69	524.79	0.38
	0.77	379.58	0.36
	0.85	347.62	0.37
	0.92	288.75	0.37
	1.00	255.08	0.38

Table A.5 Resistivity from measurement (continued)

Sample name	Saturation (part of 1)	Resistivity (ohm m)	Porosity (part of 1)
KH_9_2	0.08	70675.81	0.50
	0.17	14764.47	0.50
	0.25	5120.22	0.50
	0.33	2052.96	0.50
	0.42	1054.09	0.50
	0.50	556.29	0.50
	0.58	333.43	0.50
	0.67	183.61	0.46
	0.75	109.12	0.41
	0.83	86.02	0.39
	0.92	80.92	0.40
	1.00	69.82	0.39
	KH_10_2	0.08	132103.69
0.15		30763.87	0.50
0.23		11487.28	0.50
0.31		5933.32	0.50
0.38		4003.14	0.50
0.46		1492.20	0.50
0.54		775.74	0.50
0.62		472.29	0.50
0.69		246.56	0.42
0.77		160.36	0.39
0.85		134.62	0.38
0.92		119.25	0.39
1.00		122.68	0.41
KH_11_2	0.00		0.42
	0.09	115635.07	0.42
	0.18	25847.84	0.42
	0.27	9764.74	0.42
	0.36	4329.19	0.42
	0.45	2112.56	0.42
	0.55	1112.44	0.42
	0.64	579.93	0.39
	0.73	369.79	0.36
	0.82	251.80	0.33
	0.91	237.17	0.35
	1.00	193.69	0.33

Table A.6 Velocity from measurement

Name	V _P				V _S			
	Water (cm ³)	Distance (mm)	Time (μsec)	Velocity (m/s)	Water (cm ³)	Distance (mm)	Time (μsec)	Velocity (m/s)
beach sand	0	40.61	107.40	378	0	34.22	114.70	298
	0	39.31	99.40	395	0	34.47	114.70	300
	0	40.31	103.40	390	25	36.87	159.50	231
	25	39.36	97.70	403	50	39.07	188.30	207
	50	47.01	112.10	419	75	34.87	167.50	208
	75	38.21	107.30	356	100	52.27	333.10	157
	75	42.76	113.70	376	125	46.12	249.10	185
	75	42.91	115.30	372	150	44.57	261.10	171
	100	48.86	112.10	436	175	43.87	269.10	163
	125	49.46	132.90	372	200	42.92	245.10	175
	150	48.81	128.10	381	225	44.22	241.10	183
	175	46.31	124.90	371	250	41.92	241.10	174
	200	49.86	128.10	389	275	36.97	233.10	159
	225	39.21	99.30	395				
	250	46.31	105.70	438				
	275	43.01	107.30	401				
	275	38.36	91.30	420				
KB_1_2	0	25.31	24.50	1033	0	21.77	45.10	483
	0	22.71	19.50	1165	35	26.42	95.10	278
	0	21.41	26.50	808	70	24.67	89.10	277
	35	26.51	30.50	869	105	27.37	103.10	265
	70	29.71	34.50	861	140	20.77	92.10	225
	105	29.41	26.50	1110				

Table A.6 Velocity from measurement (continued)

Name	V _P				V _S			
	Water (cm ³)	Distance (mm)	Time (μsec)	Velocity (m/s)	Water (cm ³)	Distance (mm)	Time (μsec)	Velocity (m/s)
KB_2_2	105	27.31	21.50	1270				
	105	27.01	24.50	1103				
	140	24.31	25.50	953				
KB_4_2	0	47.71	64.10	744	0	40.67	201.10	202
	40	22.11	27.30	810	40	22.97	89.10	258
	80	42.76	78.50	545	80	32.77	113.10	290
	80	39.51	70.50	560	120	38.17	141.10	270
	120	35.41	56.10	631	160	31.97	101.90	314
	160	37.81	52.90	715	200	17.27	97.10	178
	200	14.26	29.50	483	200	23.57	141.10	167
	240	4.96	3.30	1504				
KB_7_2	0	35.36	72.50	488	0	34.77	133.10	261
	40	40.41	74.50	542	40	40.07	163.10	246
	80	40.51	78.50	516	80	30.32	113.10	268
	120	32.76	60.50	542	120	32.07	109.10	294
	160	29.16	46.50	627	160	25.02	101.10	247
	200	6.51	14.10	462	200	16.87	103.10	164
KB_9_2	0	42.11	80.50	523	0	34.32	151.10	227
	50	33.26	62.50	532	50	42.02	173.10	243
	100	33.21	58.50	568	50	36.87	151.10	244
	100	31.86	59.50	536	100	28.87	101.10	286

Table A.6 Velocity from measurement (continued)

Name	V _P				V _S			
	Water (cm ³)	Distance (mm)	Time (μsec)	Velocity (m/s)	Water (cm ³)	Distance (mm)	Time (μsec)	Velocity (m/s)
KB_9_2	150	29.91	60.50	494	150	28.32	165.10	172
	150	29.01	59.50	488	150	28.37	141.10	201
	200	3.61	15.50	233	200	5.02	42.10	119
					200	4.22	44.10	96
KH_1_2	0	39.56	58.50	676	0	29.47	113.10	261
	60	35.81	62.50	573	60	44.77	167.10	268
	120	37.11	80.50	461	120	31.77	117.10	271
	180	31.61	68.50	461	180	33.02	131.10	252
	240	29.56	76.50	386	240	18.27	167.10	109
	300	7.01	21.90	320	300	7.87	125.10	63
KH_2_2	0	41.56	37.50	1108	0	34.32	123.10	279
	0	37.51	55.50	676	60	36.47	141.10	258
	60	36.41	63.50	573	120	37.72	171.10	220
	120	37.96	60.50	627	180	30.67	181.10	169
	180	27.81	46.50	598	180	31.12	181.10	172
	240	11.01	32.50	339	240	6.87	116.10	59
	240	9.41	33.50	281	240	6.87	106.10	65
	240	6.01	28.50	211				

Table A.6 Velocity from measurement (continued)

Name	V _P				V _S			
	Water (cm ³)	Distance (mm)	Time (μsec)	Velocity (m/s)	Water (cm ³)	Distance (mm)	Time (μsec)	Velocity (m/s)
KH_3_2	0	34.61	23.50	1473	0	31.82	67.10	474
	0	27.31	32.50	840	60	32.02	67.10	477
	60	31.31	33.50	935	120	21.02	53.10	396
	120	30.01	33.50	896	180	16.37	73.10	224
	180	15.96	24.50	652	240	17.97	36.10	498
	240	13.91	25.50	546	240	25.77	48.10	536
		34.61	23.50	1473	240	23.97	42.10	569
					240	19.72	80.10	246
					240	6.77	48.10	141
					240	11.77	62.10	189
KH_7_2	0	41.61	46.50	895	0	41.52	133.10	312
	60	37.11	59.30	626	60	36.87	129.10	286
	120	39.61	62.50	634	120	36.27	129.10	281
	180	23.91	31.40	762	180	26.17	77.10	339
	240	23.96	40.10	598	180	24.52	73.10	335
	240	19.91	33.70	591	240	10.72	93.10	115
	300	16.41	38.50	426	240	14.37	35.10	409
					240	16.57	111.10	149
					300	17.77	209.10	85

Table A.7 Elastic moduli

Name	Water (cm ³)	Water Saturation (part of 1)	Vp (cm/s)	Vs (cm/s)	Density (g/cm ³)	Young's moduli (GPa)	Bulk moduli (GPa)	Shear moduli (GPa)	Poisson's Ration
Sand	0	0.0	388	299	1.57	0.21	0.05	0.14	0.24
	25	0.1	403	231	1.61	0.22	0.15	0.09	0.25
	50	0.2	419	207	1.65	0.19	0.20	0.07	0.34
	75	0.3	368	208	1.69	0.19	0.13	0.07	0.27
	100	0.4	436	157	1.73	0.12	0.27	0.04	0.43
	125	0.5	372	185	1.77	0.16	0.16	0.06	0.34
	150	0.5	381	171	1.81	0.14	0.19	0.05	0.37
	175	0.6	371	163	1.84	0.14	0.19	0.05	0.38
	200	0.7	389	175	1.88	0.16	0.21	0.06	0.37
	225	0.8	395	183	1.92	0.18	0.21	0.06	0.36
	250	0.9	438	174	1.96	0.17	0.30	0.06	0.41
	275	1.0	411	159	2.00	0.14	0.27	0.05	0.41
KB_1_2	0	0.0	1002	483	1.78	1.12	1.23	0.41	0.35
	35	0.3	869	278	1.84	0.41	1.20	0.14	0.44
	70	0.5	861	277	1.90	0.42	1.22	0.15	0.44
	105	0.8	1161	265	1.97	0.41	2.47	0.14	0.47
	140	1.0	953	225	2.03	0.30	1.71	0.10	0.47
KB_4_2	0	0.0	744	202	1.51	0.18	0.75	0.06	0.46
	40	0.2	810	258	1.57	0.30	0.89	0.10	0.44
	80	0.4	553	290	1.63	0.36	0.32	0.14	0.31
	120	0.6	631	270	1.69	0.34	0.51	0.12	0.39

Table A.7 Elastic moduli (continued)

Name	Water (cm ³)	Water Saturation (part of 1)	Vp (cm/s)	Vs (cm/s)	Density (g/cm ³)	Young's moduli (GPa)	Bulk moduli (GPa)	Shear moduli (GPa)	Poisson's Ration
KB_4_2	160	0.8	715	314	1.75	0.48	0.67	0.17	0.38
	200	1.0	483	172	1.81	0.15	0.35	0.05	0.43
KB_7_2	0	0.0	488	261	1.79	0.32	0.26	0.12	0.30
	40	0.2	542	246	1.86	0.31	0.40	0.11	0.37
	80	0.4	516	268	1.93	0.37	0.33	0.14	0.32
	120	0.6	542	294	2.00	0.45	0.36	0.17	0.29
	160	0.8	627	247	2.08	0.36	0.65	0.13	0.41
	200	1.0	462	164	2.15	0.16	0.38	0.06	0.43
KB_9_2	0	0.0	523	227	1.59	0.23	0.33	0.08	0.38
	50	0.3	532	243	1.67	0.27	0.34	0.10	0.37
	100	0.5	552	286	1.75	0.38	0.34	0.14	0.32
	150	0.8	491	186	1.83	0.18	0.36	0.06	0.42
	200	1.0	233	107	1.91	0.06	0.07	0.02	0.37
KH_1_2	0	0.0	676	261	1.35	0.26	0.50	0.09	0.41
	60	0.2	573	268	1.43	0.28	0.33	0.10	0.36
	120	0.4	461	271	1.51	0.27	0.17	0.11	0.24
	180	0.6	461	252	1.59	0.26	0.20	0.10	0.29
	240	0.8	386	109	1.67	0.06	0.22	0.02	0.46
	300	1.0	320	63	1.76	0.15	0.35	0.05	0.48

Table A.7 Elastic moduli (continued)

Name	Water (cm ³)	Water Saturation (part of 1)	Vp (cm/s)	Vs (cm/s)	Density (g/cm ³)	Young's moduli (GPa)	Bulk moduli (GPa)	Shear moduli (GPa)	Poisson's Ration
KH_2_2	0	0.0	676	279	1.46	0.32	0.52	0.11	0.40
	60	0.3	573	258	1.55	0.28	0.37	0.10	0.37
	120	0.5	627	220	1.64	0.23	0.54	0.08	0.43
	180	0.8	598	171	1.72	0.15	0.55	0.05	0.46
	240	1.0	277	62	1.81	0.02	0.13	0.01	0.47
KH_3_2	0	0.0	840	474	1.42	0.81	0.58	0.32	0.27
	60	0.3	935	477	1.51	0.91	0.86	0.34	0.32
	120	0.5	896	396	1.59	0.69	0.94	0.25	0.38
	180	0.8	652	224	1.68	0.24	0.60	0.08	0.43
	240	1.0	546	165	1.76	0.14	0.46	0.05	0.45
KH_7_2	0	0.0	895	312	1.40	0.39	0.94	0.14	0.43
	60	0.2	626	286	1.48	0.33	0.42	0.12	0.37
	120	0.4	634	281	1.57	0.34	0.46	0.12	0.38
	180	0.6	762	337	1.65	0.52	0.71	0.19	0.38
	240	0.8	594	132	1.74	0.09	0.57	0.03	0.47
	300	1.0	426	85	1.82	0.04	0.31	0.01	0.48



Scientific Equipment Center, Prince of Songkla University

Central Academic Administrator Bld. Hat-Yai Campus, Songkhla 90110

Tel.0 7428 6904-7 Fax.0 7421 2813

F-RES-003 Rev. 7 10/09/55

No. 2219/56 Page 2/3

No.	Sample Name	JCPDF No.	Chemical Name	Chemical Formula
2557-5	KB5	03-065-0466	Quartz low, syn	SiO ₂
		01-080-0886	Kaolinite 1\TA\RG	Al ₂ (Si ₂ O ₃)(OH) ₄
		00-026-0911	Illite-2\ITM\RG#1 [NR]	(K, H ₃ O)Al ₂ Si ₃ AlO ₁₀ (OH) ₂
2557-6	KB6	03-065-0466	Quartz low, syn	SiO ₂
		01-080-0886	Kaolinite 1\TA\RG	Al ₂ (Si ₂ O ₃)(OH) ₄
		00-026-0911	Illite-2\ITM\RG#1 [NR]	(K, H ₃ O)Al ₂ Si ₃ AlO ₁₀ (OH) ₂
2557-7	KH1	01-083-2465	Quartz low, syn	SiO ₂
		01-089-6538	Kaolinite	Al ₂ (Si ₂ O ₃)(OH) ₄
		00-026-0911	Illite-2\ITM\RG#1 [NR]	(K, H ₃ O)Al ₂ Si ₃ AlO ₁₀ (OH) ₂
2557-8	KH2	01-079-1910	Quartz	SiO ₂
		01-080-0885	Kaolinite 1\TA\RG	Al ₂ (Si ₂ O ₃)(OH) ₄
2557-9	KH3	01-086-1560	Quartz low	SiO ₂
		01-089-6538	Kaolinite	Al ₂ (Si ₂ O ₃)(OH) ₄
2557-10	KH4	01-087-2096	Quartz low	SiO ₂
		01-080-0886	Kaolinite 1\TA\RG	Al ₂ (Si ₂ O ₃)(OH) ₄
		00-026-0911	Illite-2\ITM\RG#1 [NR]	(K, H ₃ O)Al ₂ Si ₃ AlO ₁₀ (OH) ₂
2557-11	KH5	01-085-0504	Quartz	SiO ₂
		01-080-0885	Kaolinite 1\TA\RG	Al ₂ (Si ₂ O ₃)(OH) ₄
2557-12	KH6	01-083-2465	Quartz low, syn	SiO ₂
		01-080-0885	Kaolinite 1\TA\RG	Al ₂ (Si ₂ O ₃)(OH) ₄
		00-026-0911	Illite-2\ITM\RG#1 [NR]	(K, H ₃ O)Al ₂ Si ₃ AlO ₁₀ (OH) ₂
2557-13	KH7	01-085-1053	Quartz, syn	SiO ₂
		01-080-0885	Kaolinite 1\TA\RG	Al ₂ (Si ₂ O ₃)(OH) ₄
2557-14	KH8	01-087-2096	Quartz low	SiO ₂
		01-080-0885	Kaolinite 1\TA\RG	Al ₂ (Si ₂ O ₃)(OH) ₄
2557-15	KH9	01-083-2465	Quartz low, syn	SiO ₂


Scientific Equipment Center, Prince of Songkla University

Central Academic Administrator Bld. Hat-Yai Campus, Songkhla 90110

Tel.0 7428 6904-7 Fax.0 7421 2813

F-RES-003 Rev. 7 10/09/55

No. 2219/56 Page 3/3

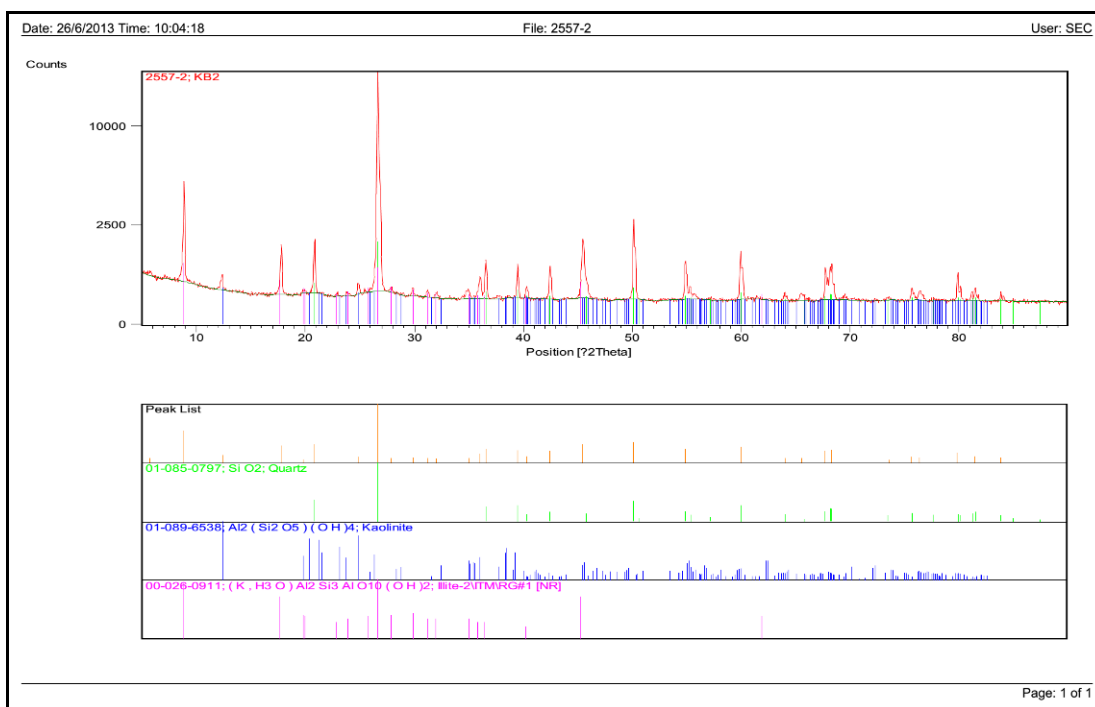
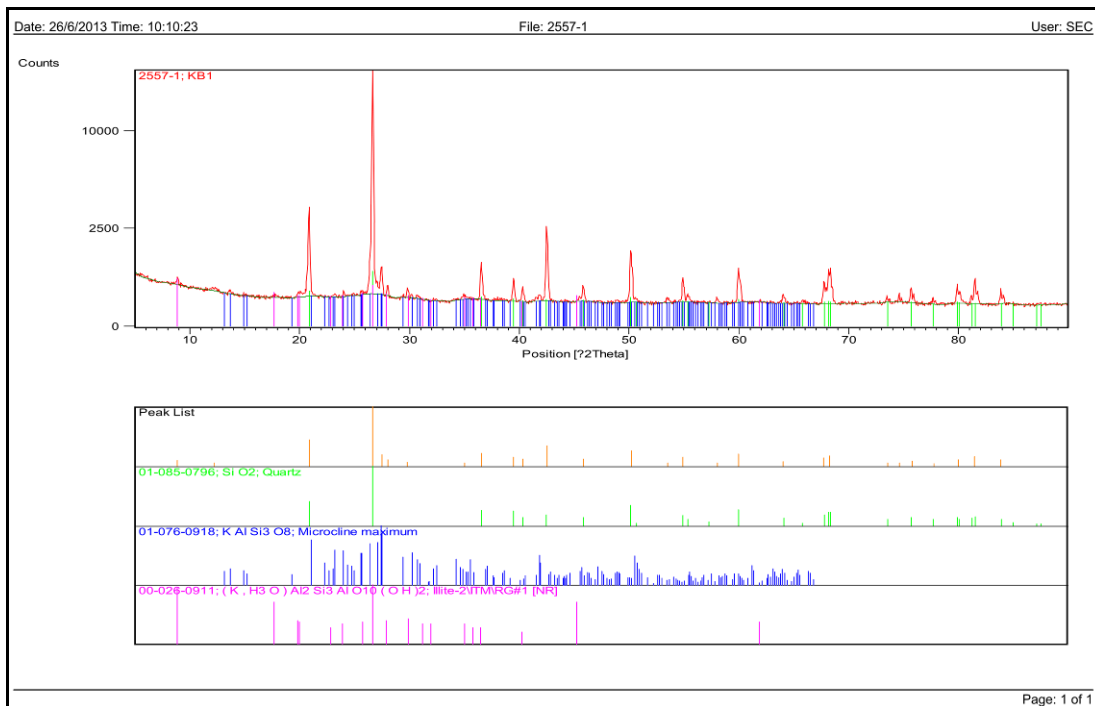
No.	Sample Name	JCPDF No.	Chemical Name	Chemical Formula
2557-16	KH10	01-085-1053	Quartz, syn	SiO ₂
		01-080-0886	Kaolinite 1\ITARG	Al ₂ (Si ₂ O ₅)(OH) ₄
2557-17	KH11	01-078-2315	Quartz	SiO ₂
		01-080-0886	Kaolinite 1\ITARG	Al ₂ (Si ₂ O ₅)(OH) ₄
		00-026-0911	Illite-2\ITM\RG#1 [NR]	(K, H ₃ O)Al ₂ Si ₃ AlO ₁₀ (OH) ₂
2557-18	KH12	01-085-0504	Quartz	SiO ₂
		00-026-0911	Illite-2\ITM\RG#1 [NR]	(K, H ₃ O)Al ₂ Si ₃ AlO ₁₀ (OH) ₂
		01-080-0886	Kaolinite 1\ITARG	Al ₂ (Si ₂ O ₅)(OH) ₄
2557-19	KH13	01-085-1054	Quartz	SiO ₂
		01-073-2234	Hematite, syn	Fe ₂ O ₃
		01-080-0885	Kaolinite 1\ITARG	Al ₂ (Si ₂ O ₅)(OH) ₄

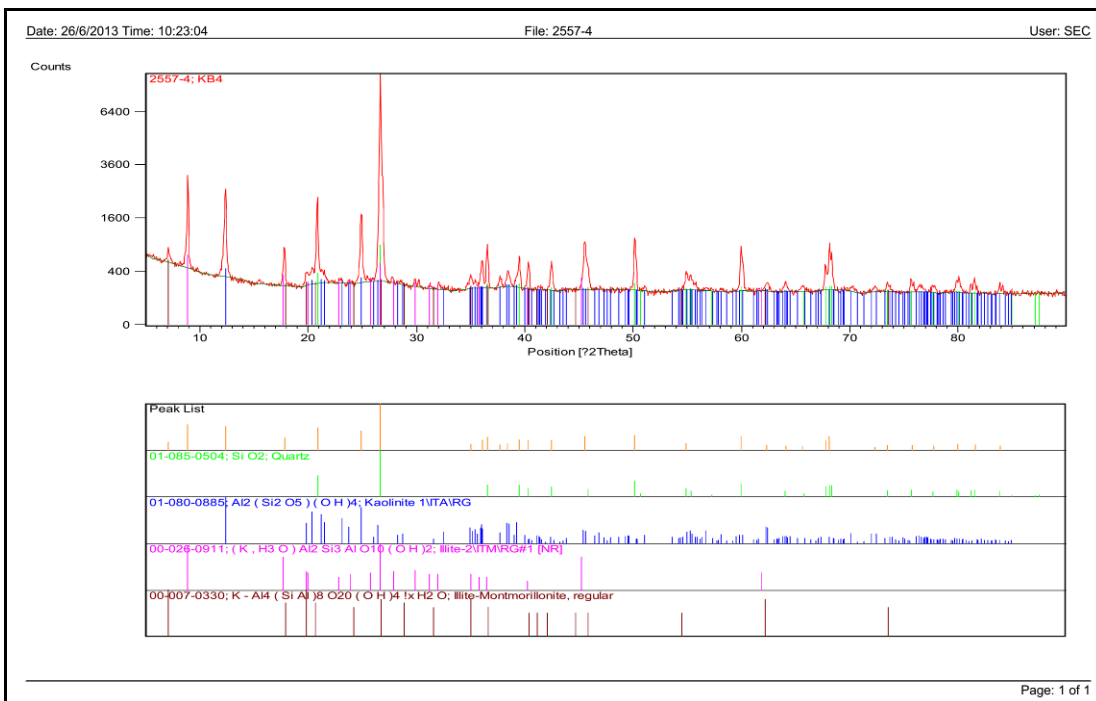
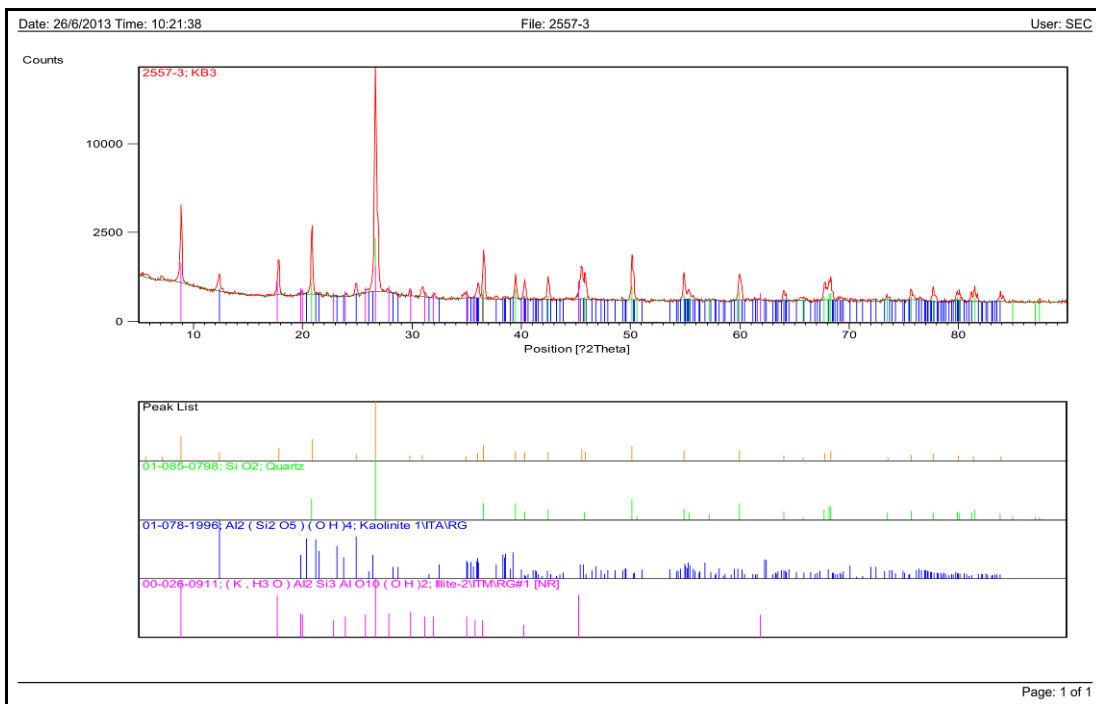
*As shown in attached diffractogram and refer to folder rawdata\XRD\Customer\56\2xxx\2557

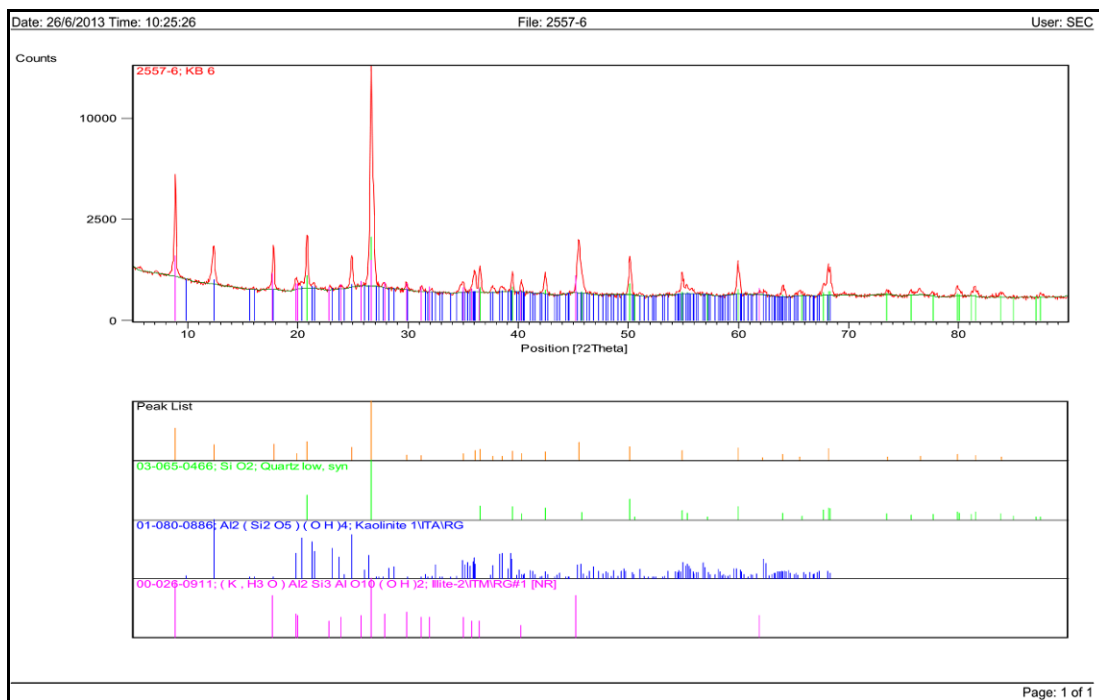
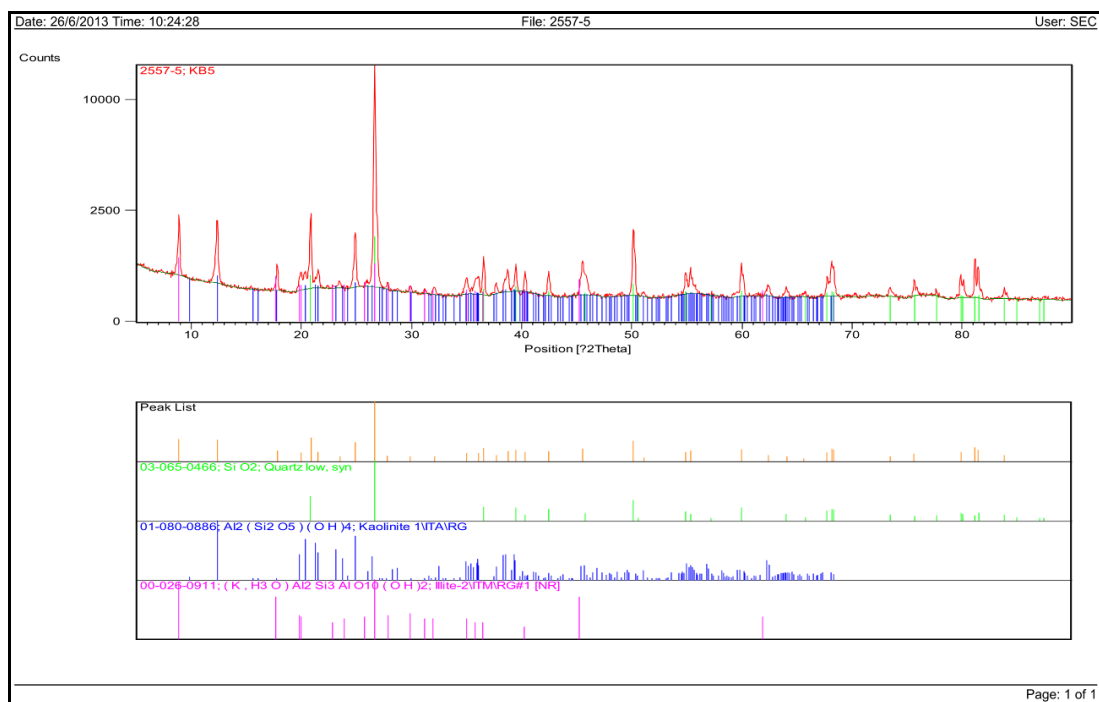
(Mrs. Roosanee Kulvijitra)

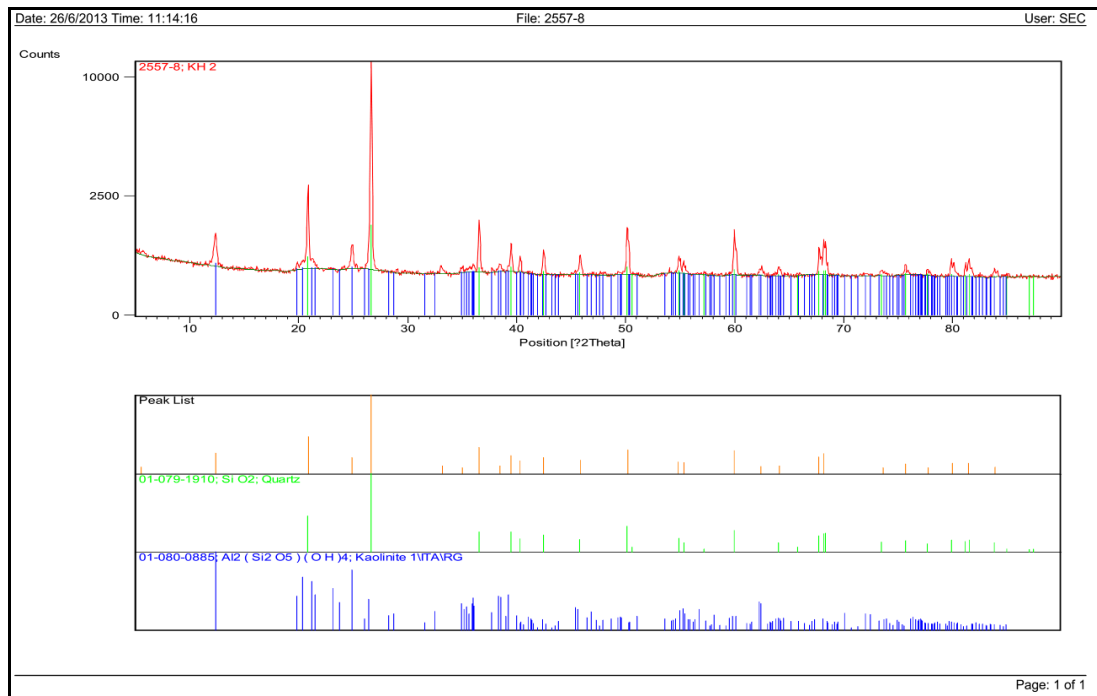
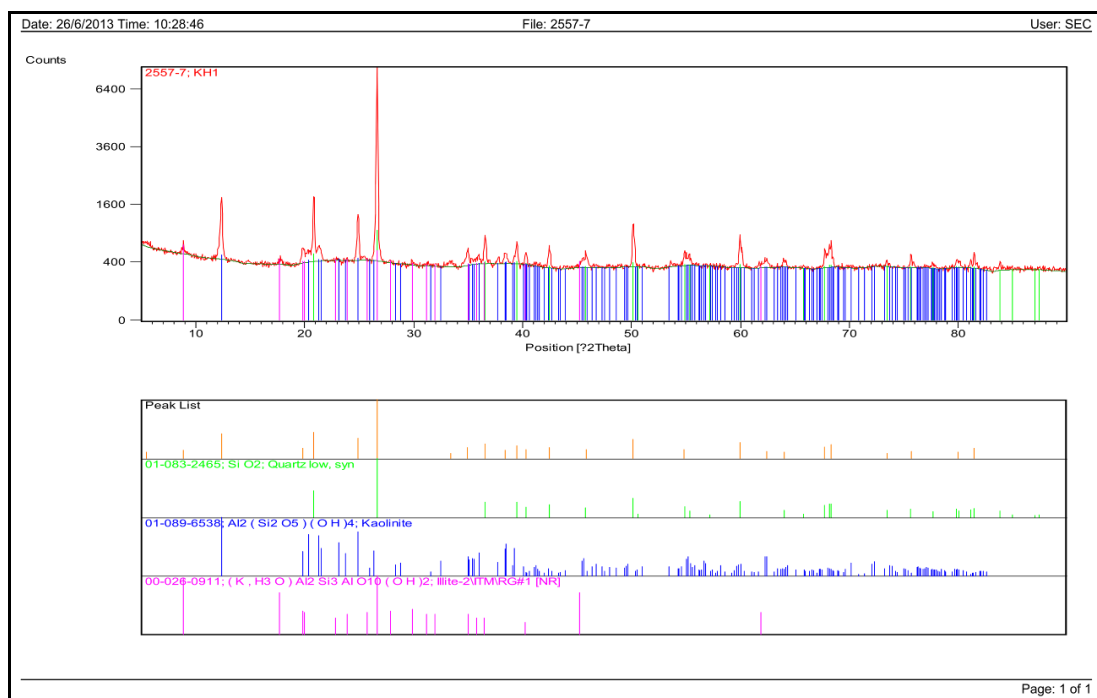
Head of Scientific Research Equipment Services

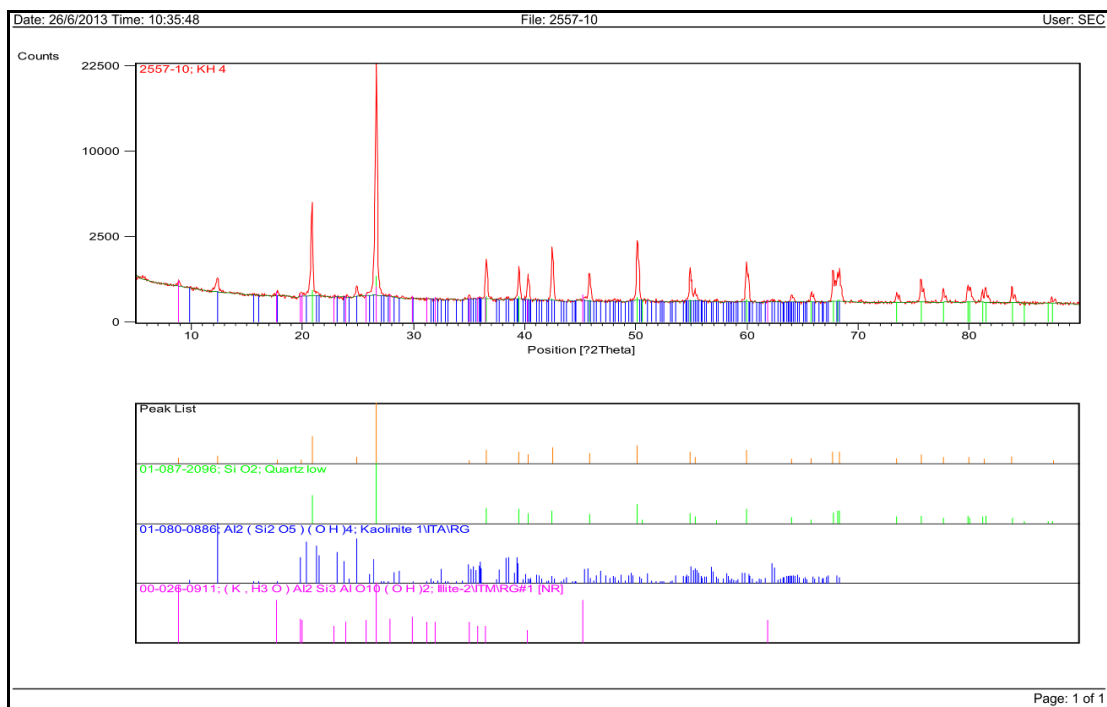
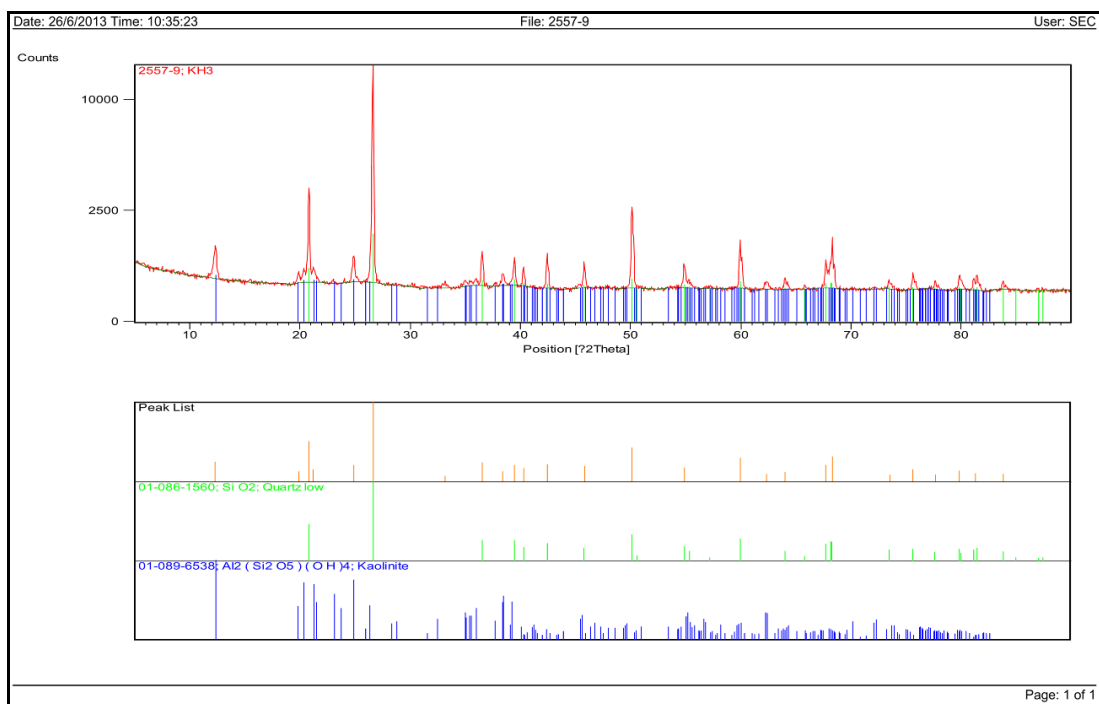
June 27, 2013

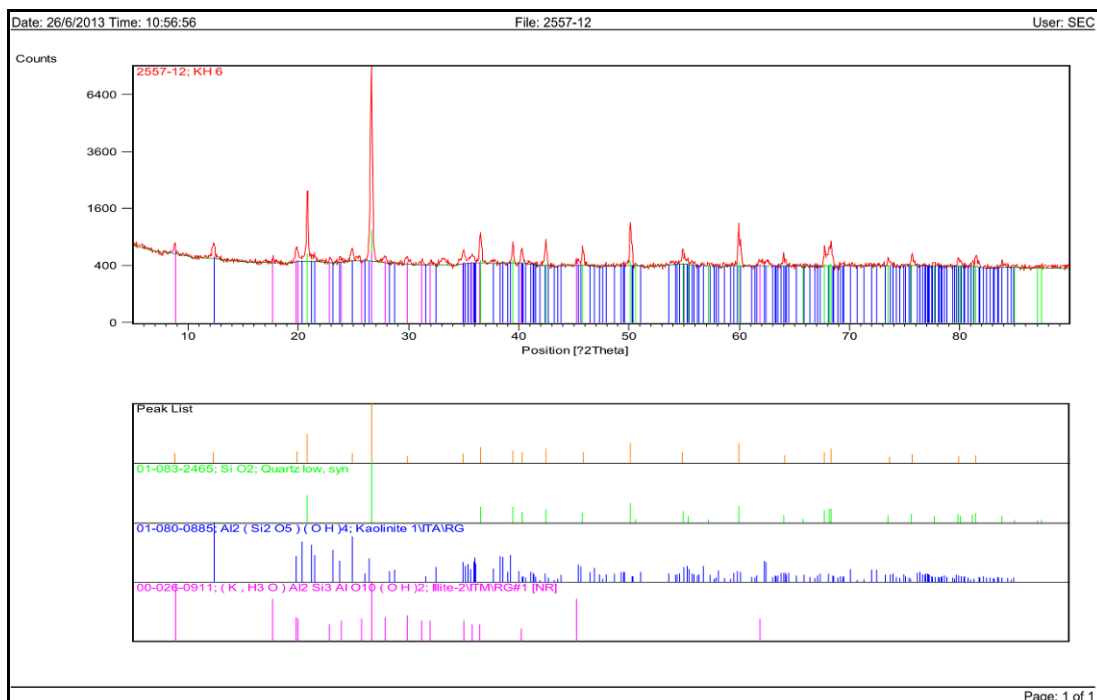
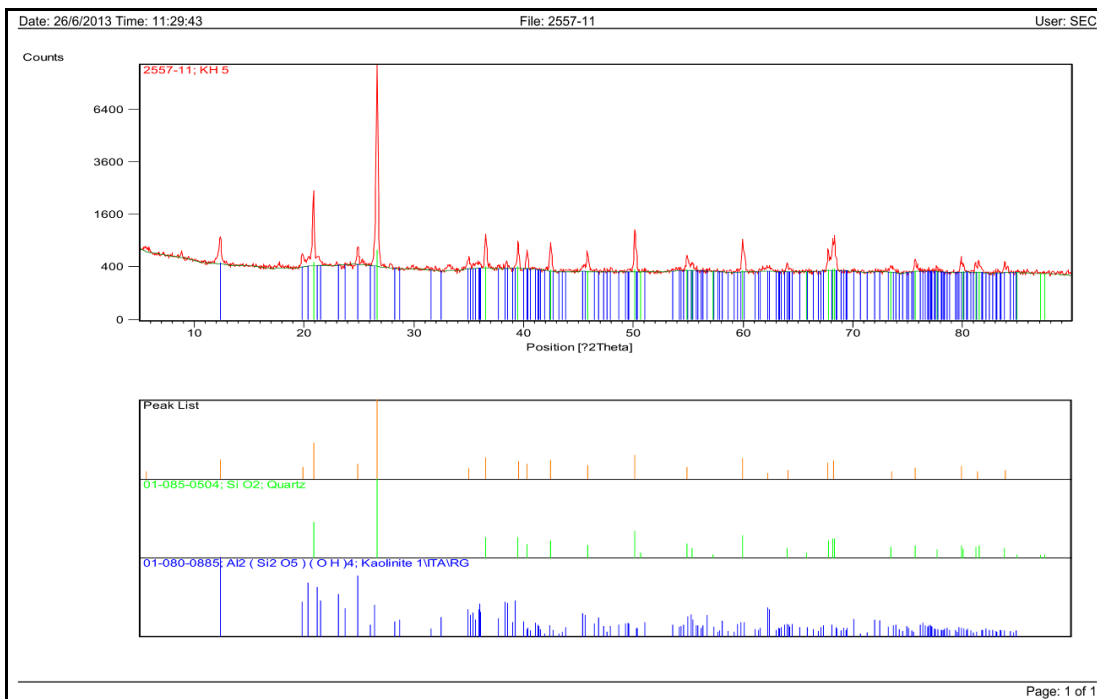


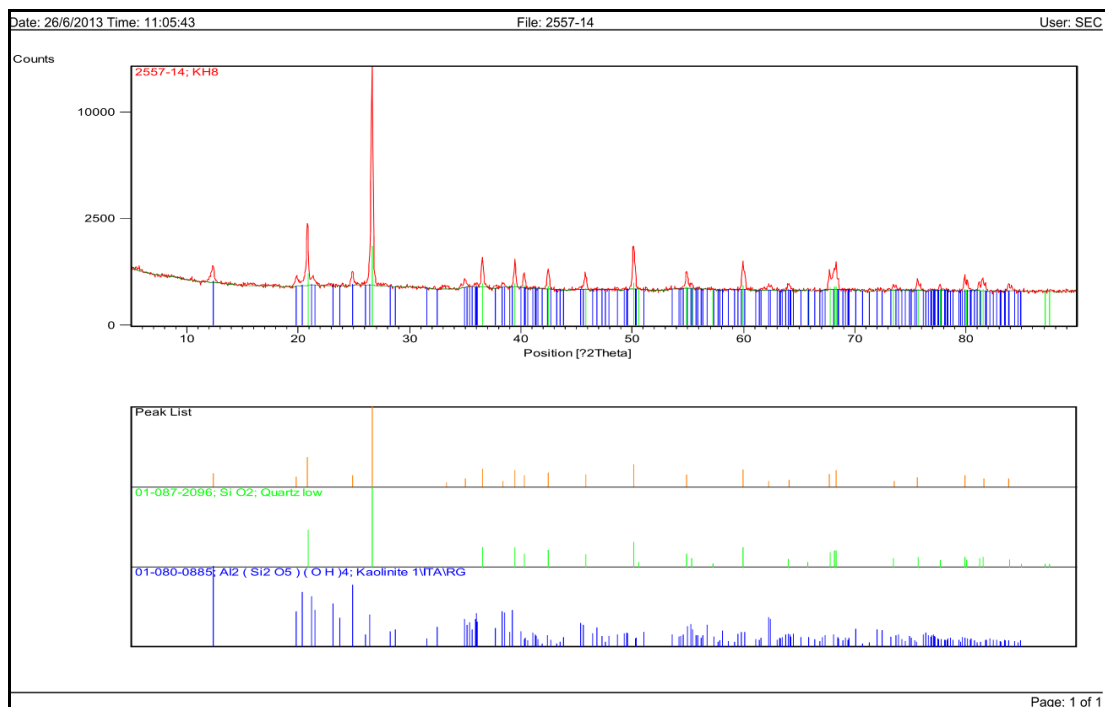
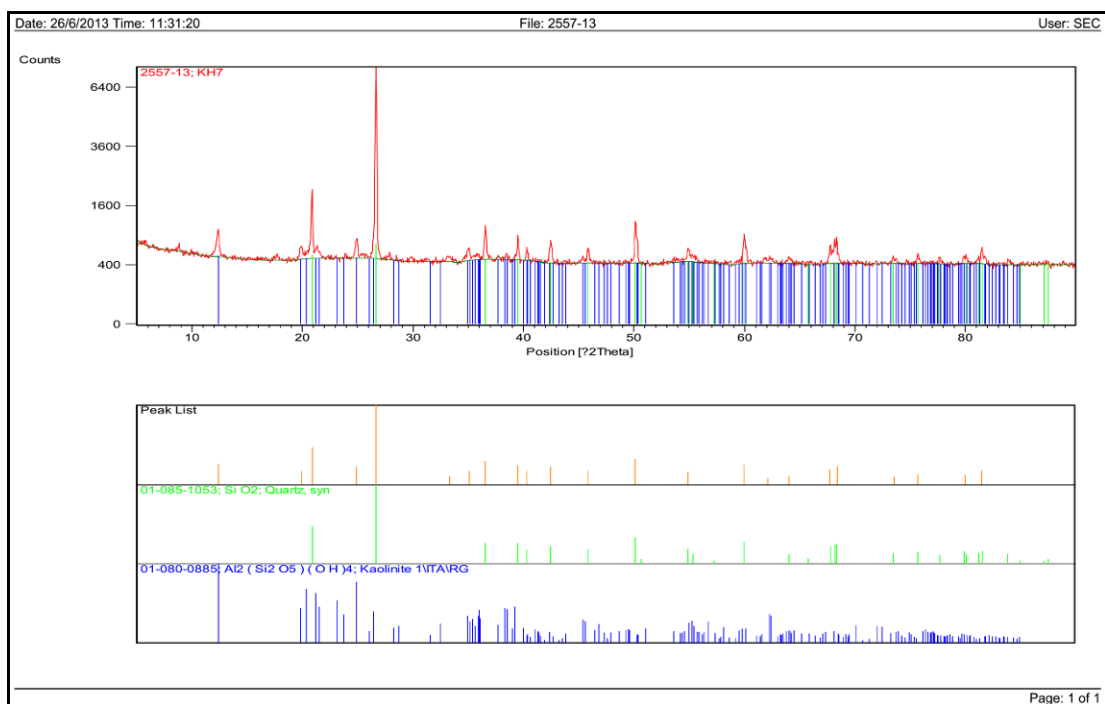


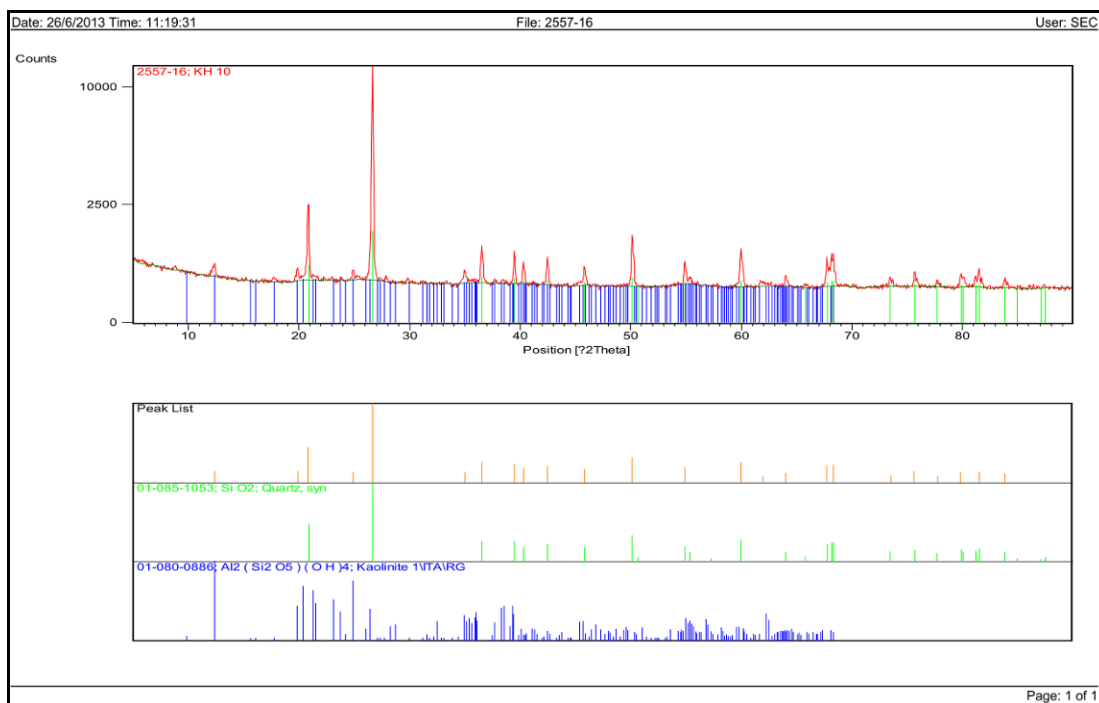
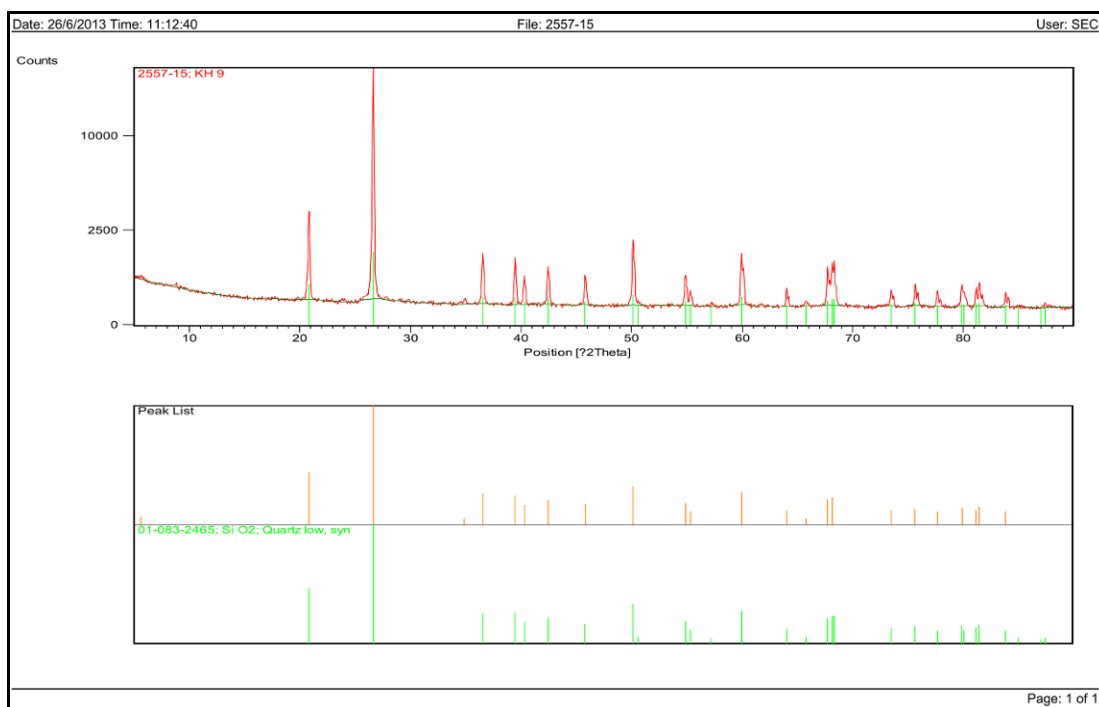


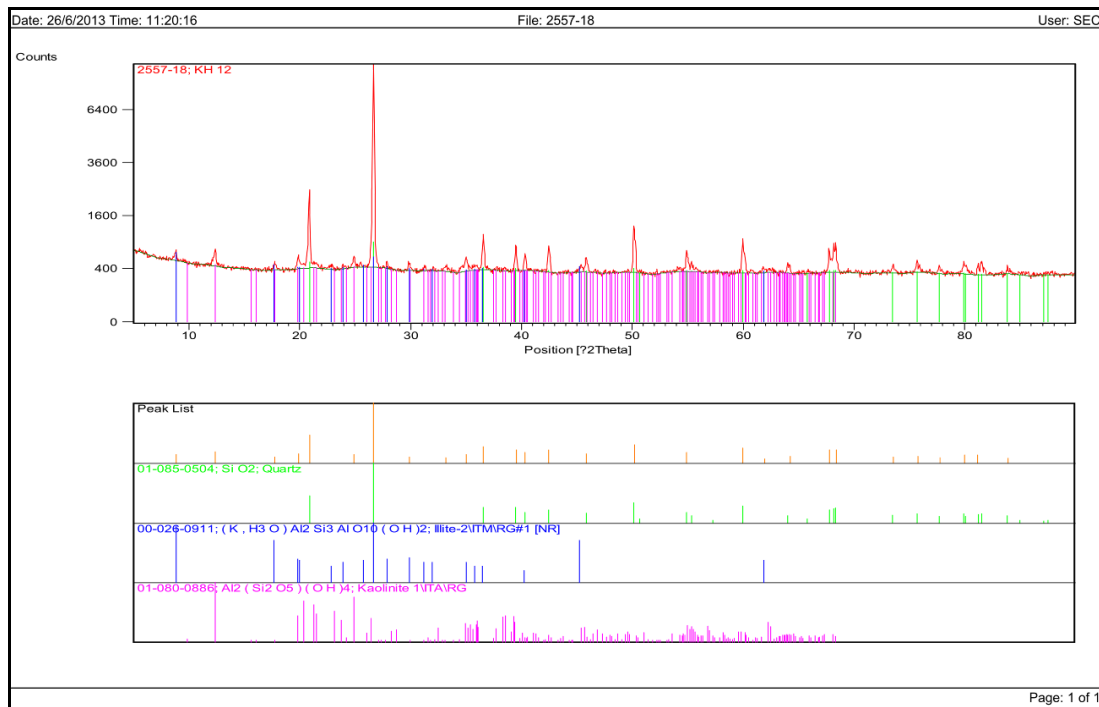
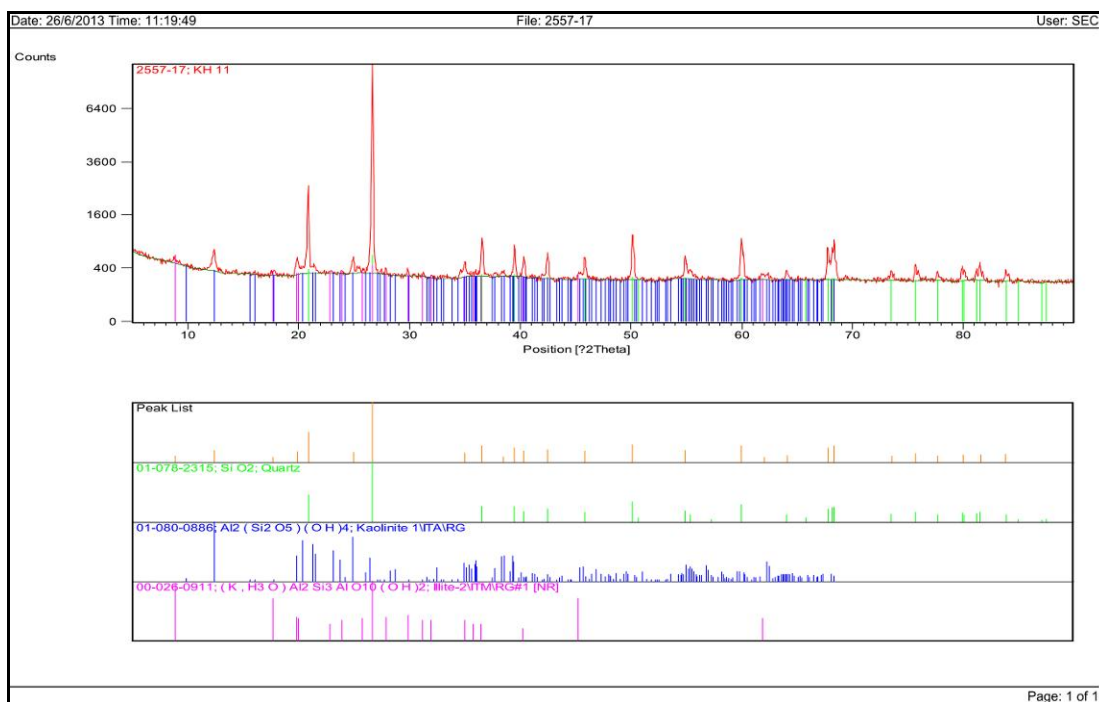


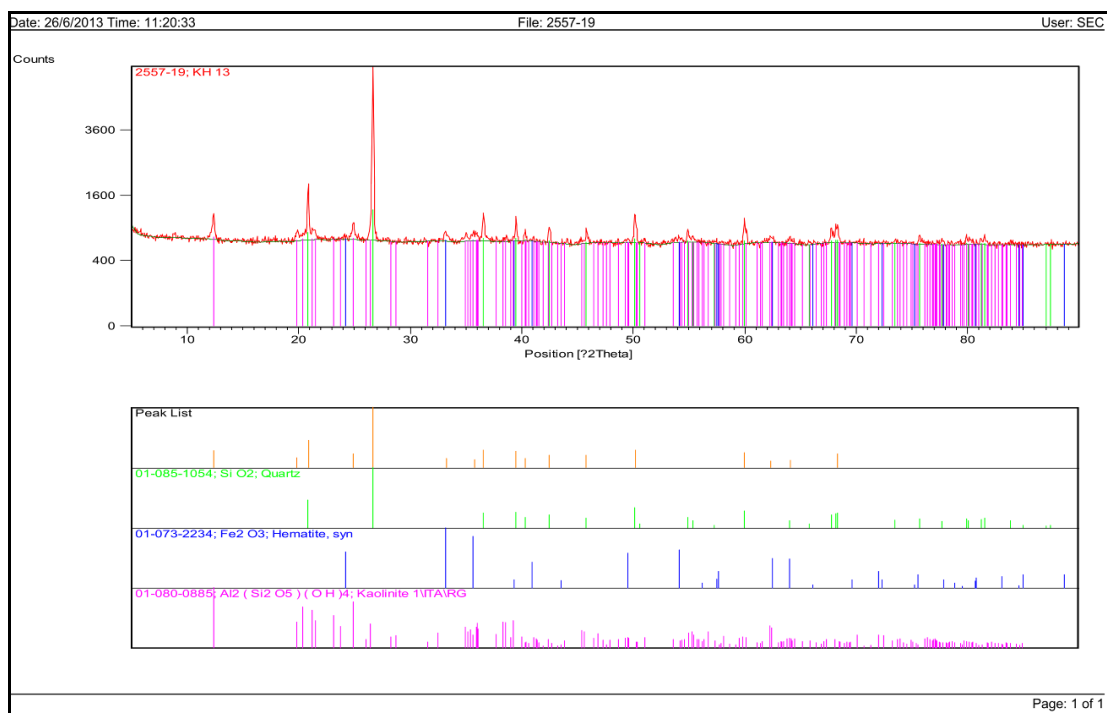














Scientific Equipment Center, Prince of Songkla University

Central Academic Administrator Bld. Hat-Yai Campus, Songkhla 90110

Tel.0 7428 6904-7 Fax.0 7421 2813

F-RES-003 Rev. 7 10/09/55

No. 2618/57 Page 1/2

TEST REPORT

Customer Name and Address: Miss Saowapa Suksawat
 Department of Physics, Faculty of Science, Prince of Songkla University

Test Request Form No.: 3473/57

Test Item(s) Received Date: August 26, 2014

Test Request Date: August 26, 2014

Analyst: Mr. Sukit Atiphan and Mr. Panupong Lim-u-sanno

Test Performed Date: August 29 and September 5, 2014

Test Method Used: Refer to WI-RES-XRD-001

Test Equipment: X-ray Diffractometer, X'Pert MPD, PHILIPS, Netherlands

Test Technique: X-ray Diffraction

Test Condition:

Objective	: Phase identify	Sample preparation	: Pressed powder
X-ray tube	: Cu tube	X-ray generator	: 40 kV & 30 mA
Wavelength	: 0.154 nm (CuK α)	Scan program	: geo new-0.4
Scan range (2 θ)	: 5-90 $^{\circ}$	Step size (2 θ)	: 0.05 $^{\circ}$
Time/step	: 1 sec	Scan speed	: 3 $^{\circ}$ /min

Test Item(s) Description: rocks and sediments **Quantity:** 12 samples

Test Result(s):

No.	Sample Name	JCPDF No.	Chemical Name	Chemical Formula
3473-1	KH_4_2	01-087-2096	Quartz low, syn	SiO ₂
		00-026-0911	Illite-2M1 (NR)	(K, H ₃ O)Al ₂ Si ₃ AlO ₁₀ (OH) ₂
		01-078-1996	Kaolinite-1A	Al ₂ (Si ₂ O ₅)(OH) ₄
3473-2	KH_5_2	01-087-2096	Quartz low, syn	SiO ₂
		01-078-1996	Kaolinite-1A	Al ₂ (Si ₂ O ₅)(OH) ₄
		00-026-0911	Illite-2M1 (NR)	(K, H ₃ O)Al ₂ Si ₃ AlO ₁₀ (OH) ₂
3473-3	KH_8_2	01-087-2096	Quartz low, syn	SiO ₂
		00-026-0911	Illite-2M1 (NR)	(K, H ₃ O)Al ₂ Si ₃ AlO ₁₀ (OH) ₂
		01-078-1996	Kaolinite-1A	Al ₂ (Si ₂ O ₅)(OH) ₄
3473-4	KH_9_2	01-087-2096	Quartz low, syn	SiO ₂
		01-078-1996	Kaolinite-1A	Al ₂ (Si ₂ O ₅)(OH) ₄
		00-026-0911	Illite-2M1 (NR)	(K, H ₃ O)Al ₂ Si ₃ AlO ₁₀ (OH) ₂


Scientific Equipment Center, Prince of Songkla University

Central Academic Administrator Bld. Hat-Yai Campus, Songkhla 90110

Tel.0 7428 6904-7 Fax.0 7421 2813

F-RES-003 Rev. 7 10/09/55

No. 2618/57 Page 2/2

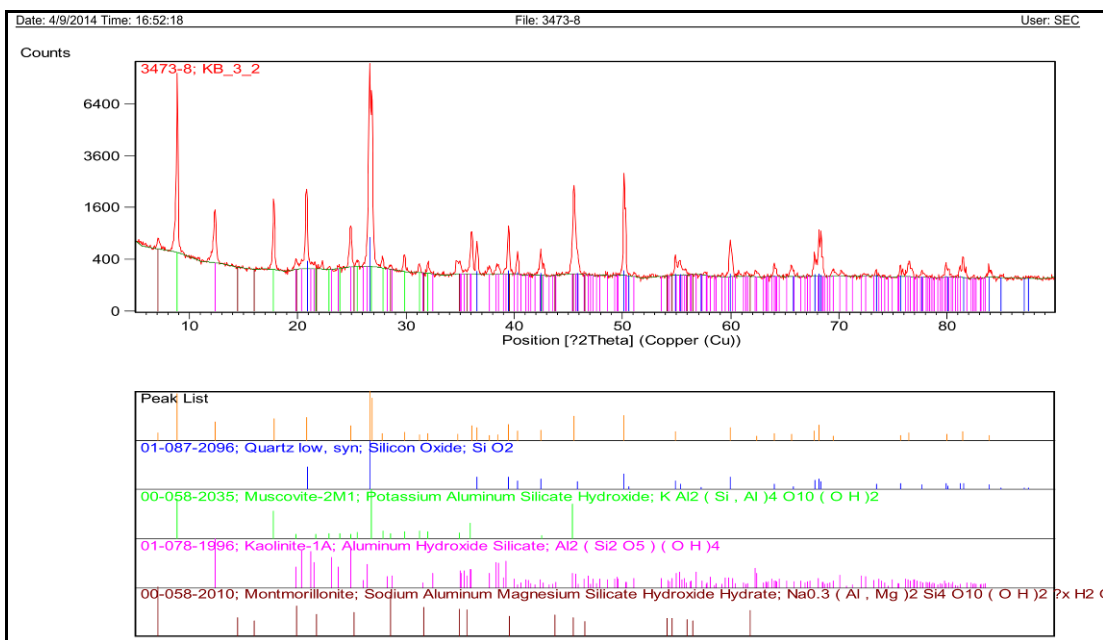
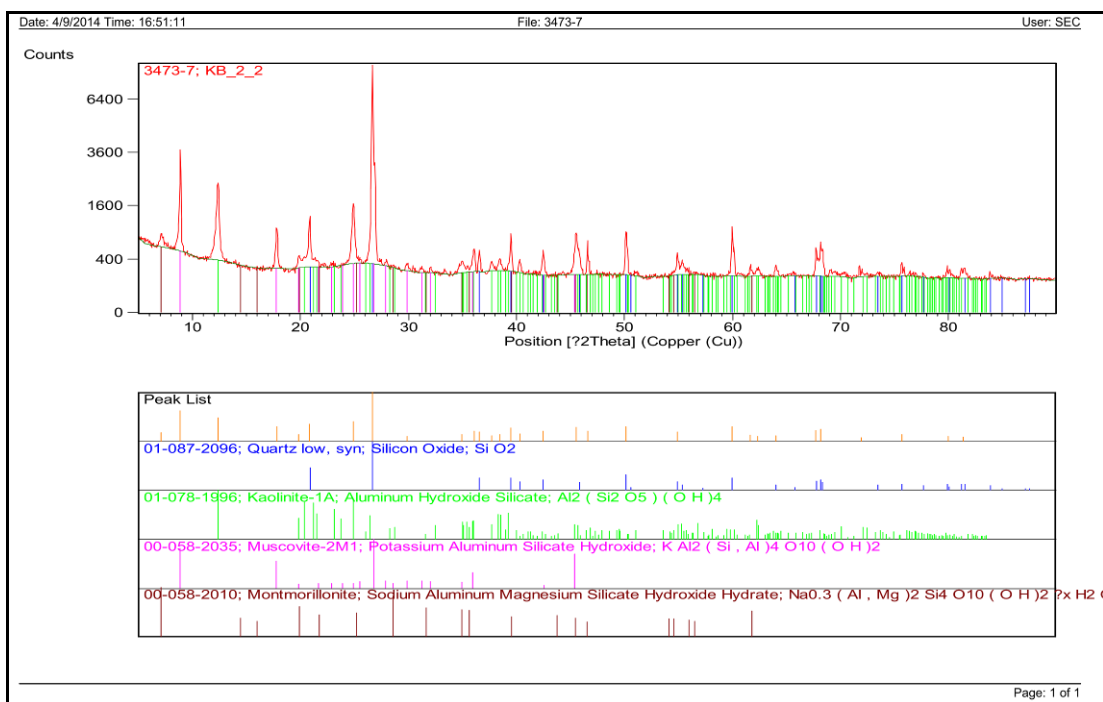
No.	Sample Name	JCPDF No.	Chemical Name	Chemical Formula
3473-5	KH_11_2	01-087-2096	Quartz low, syn	SiO ₂
		01-078-1996	Kaolinite-1A	Al ₂ (Si ₂ O ₅)(OH) ₄
3473-6	KH_12_2	01-087-2096	Quartz low, syn	SiO ₂
		01-078-1996	Kaolinite-1A	Al ₂ (Si ₂ O ₅)(OH) ₄
		00-026-0911	Illite-2M1 (NR)	(K, H ₃ O)Al ₂ Si ₃ AlO ₁₀ (OH) ₂
3473-7	KB_2_2	01-087-2096	Quartz low, syn	SiO ₂
		01-078-1996	Kaolinite-1A	Al ₂ (Si ₂ O ₅)(OH) ₄
		00-058-2035	Muscovite-2M1	KAl ₂ (Si, Al) ₄ O ₁₀ (OH) ₂
		00-058-2010	Montmorillonite	Na _{0.3} (Al, Mg) ₂ Si ₄ O ₁₀ (OH) ₂ ·xH ₂ O
3473-8	KB_3_2	01-087-2096	Quartz low, syn	SiO ₂
		00-058-2035	Muscovite-2M1	KAl ₂ (Si, Al) ₄ O ₁₀ (OH) ₂
		01-078-1996	Kaolinite-1A	Al ₂ (Si ₂ O ₅)(OH) ₄
		00-058-2010	Montmorillonite	Na _{0.3} (Al, Mg) ₂ Si ₄ O ₁₀ (OH) ₂ ·xH ₂ O
3473-9	KB_6_2	01-087-2096	Quartz low, syn	SiO ₂
		00-058-2035	Muscovite-2M1	KAl ₂ (Si, Al) ₄ O ₁₀ (OH) ₂
		00-058-2028	Kaolinite-1A	Al ₂ Si ₂ O ₅ (OH) ₄
3473-10	KB_7_2	01-087-2096	Quartz low, syn	SiO ₂
		01-078-1996	Kaolinite-1A	Al ₂ (Si ₂ O ₅)(OH) ₄
		00-058-2035	Muscovite-2M1	KAl ₂ (Si, Al) ₄ O ₁₀ (OH) ₂
3473-11	KB_8_2	01-087-2096	Quartz low, syn	SiO ₂
		00-058-2035	Muscovite-2M1	KAl ₂ (Si, Al) ₄ O ₁₀ (OH) ₂
		00-058-2028	Kaolinite-1A	Al ₂ Si ₂ O ₅ (OH) ₄
		00-019-0932	Microcline, intermediate	KAlSi ₃ O ₈
3473-12	A	01-085-1108	Calcite	Ca(CO ₃)
		01-085-0794	Quartz, syn	SiO ₂
		01-075-1655	Dolomite	CaMg(CO ₃) ₂

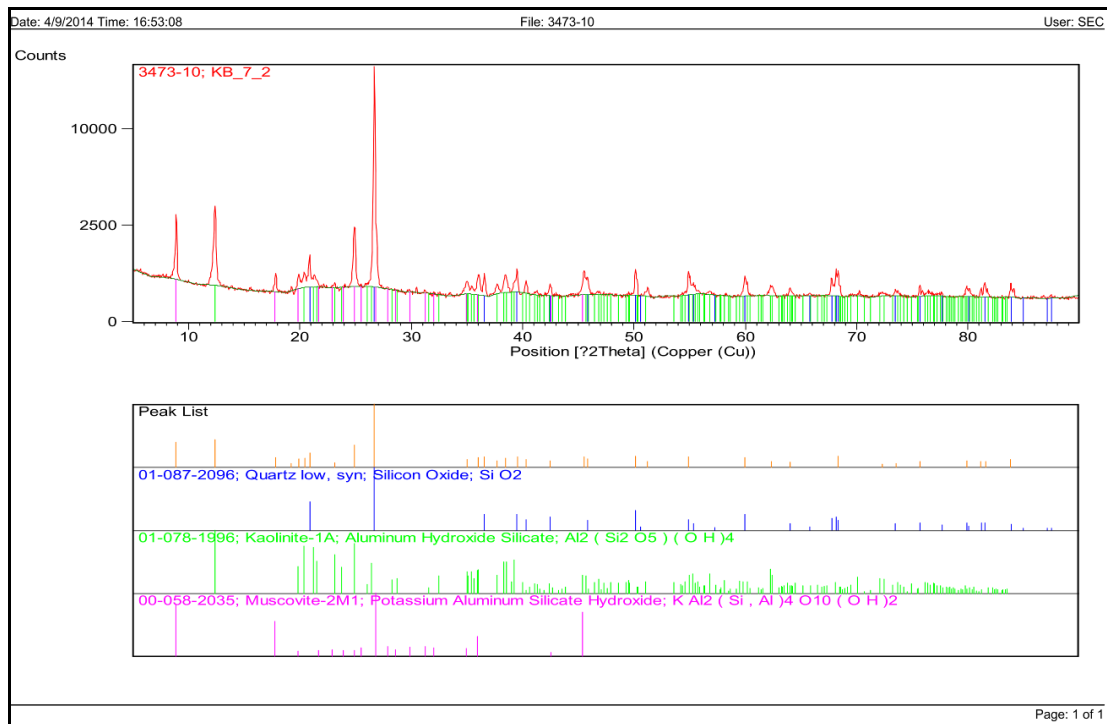
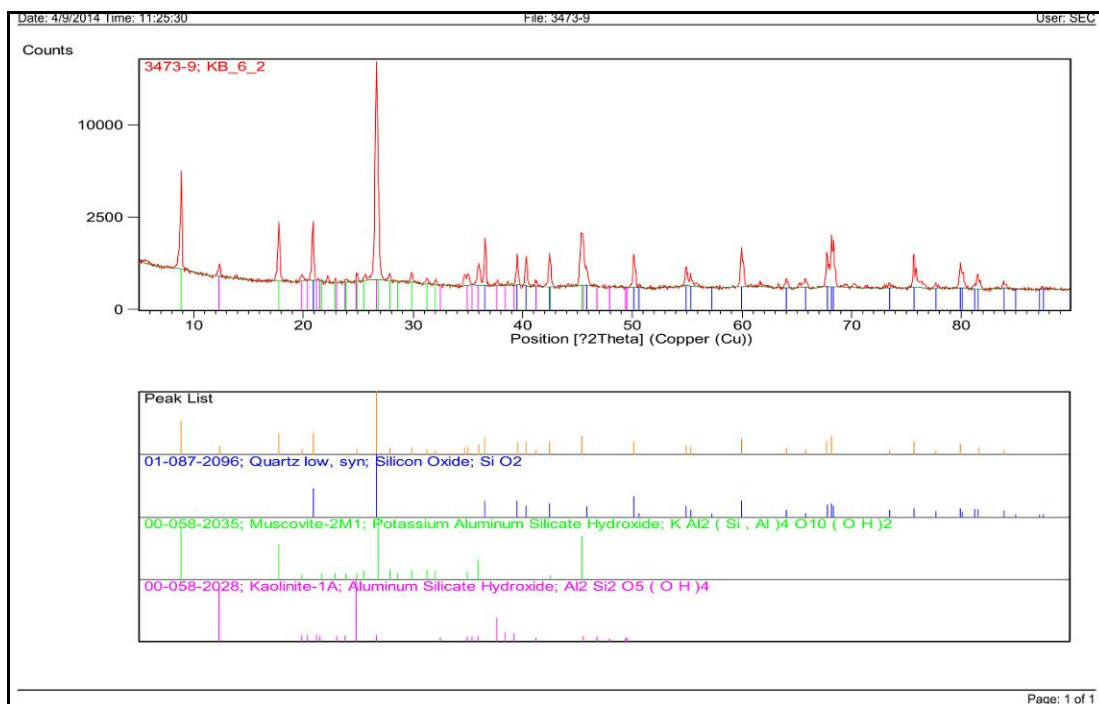
*As shown in attached diffractogram and refer to folder rawdata\XRD\Customer\573xxx\3473

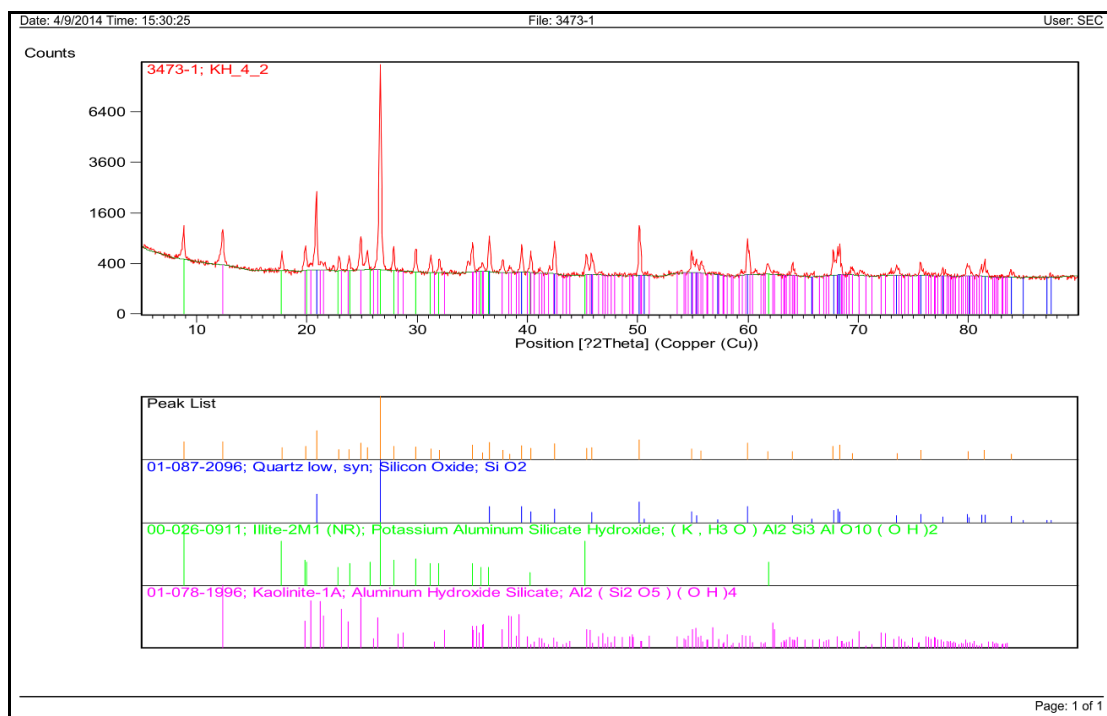
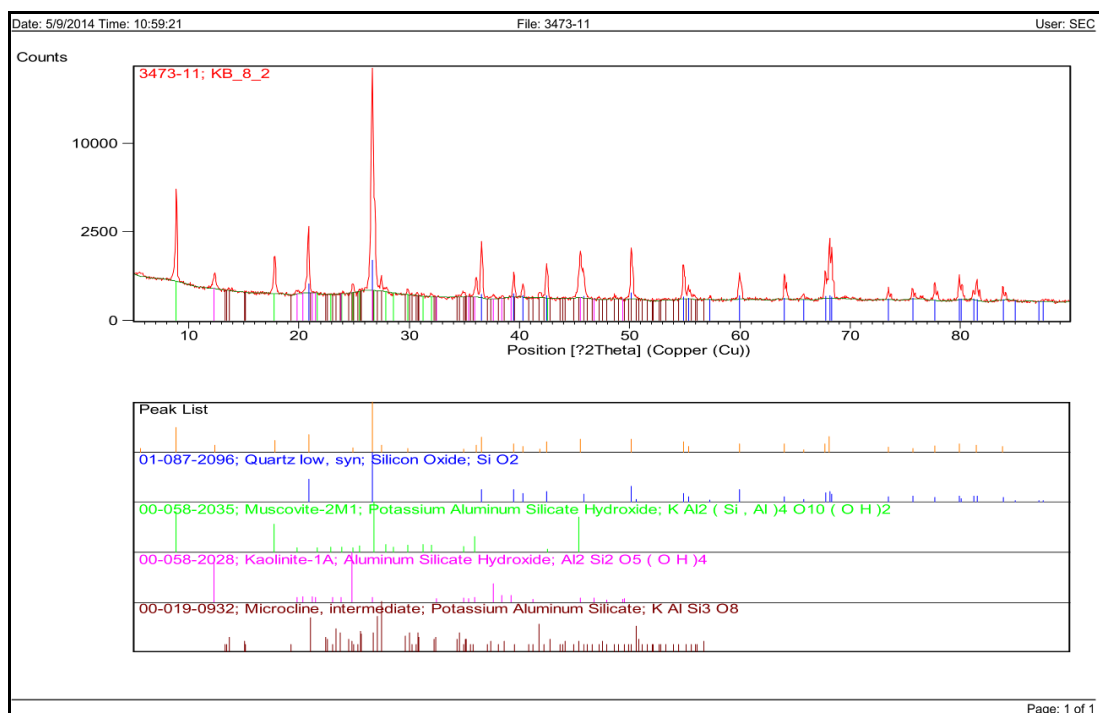
(Mrs. Roosanee Kulvijitra)

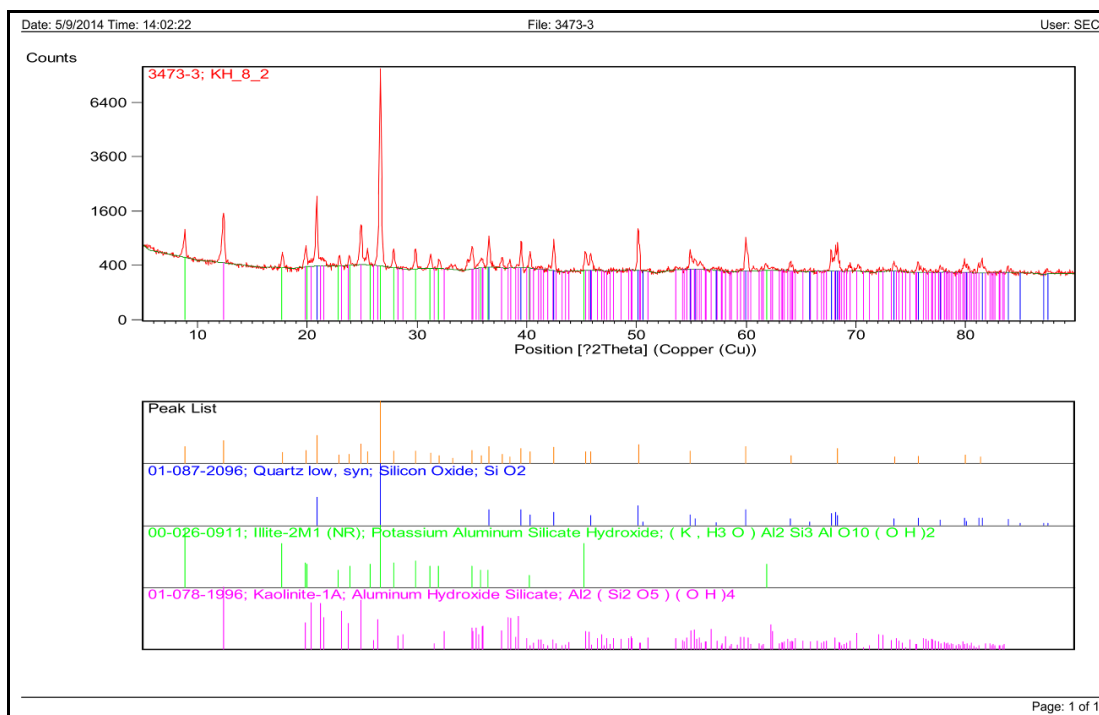
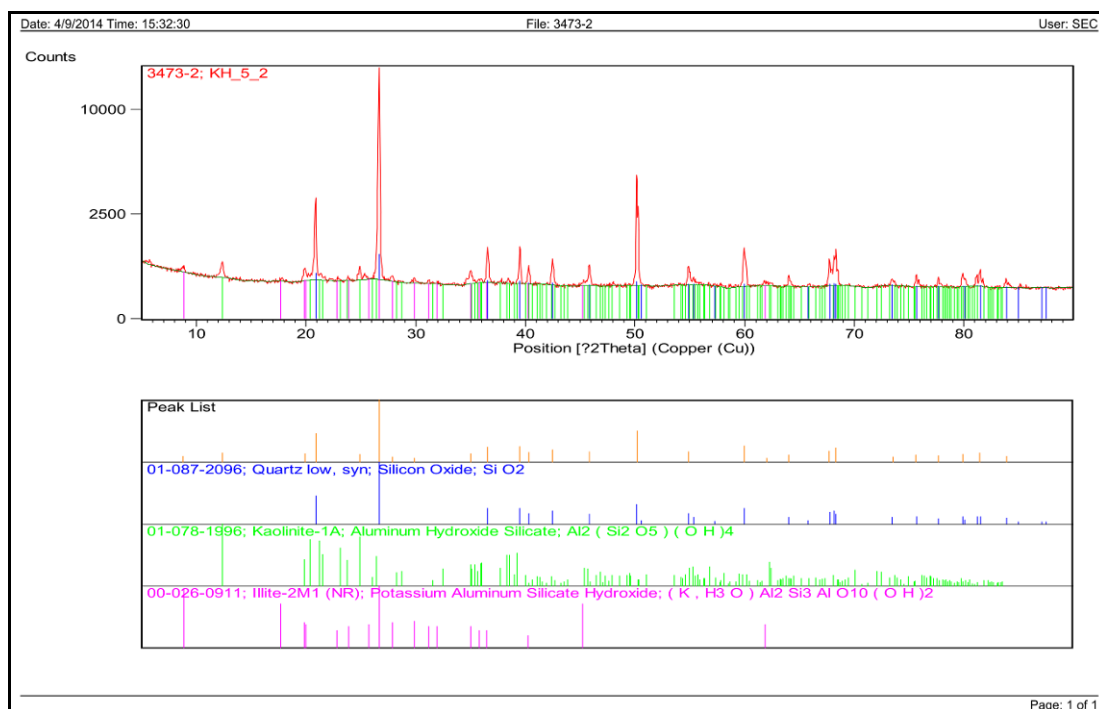
Head of Scientific Research Equipment Services

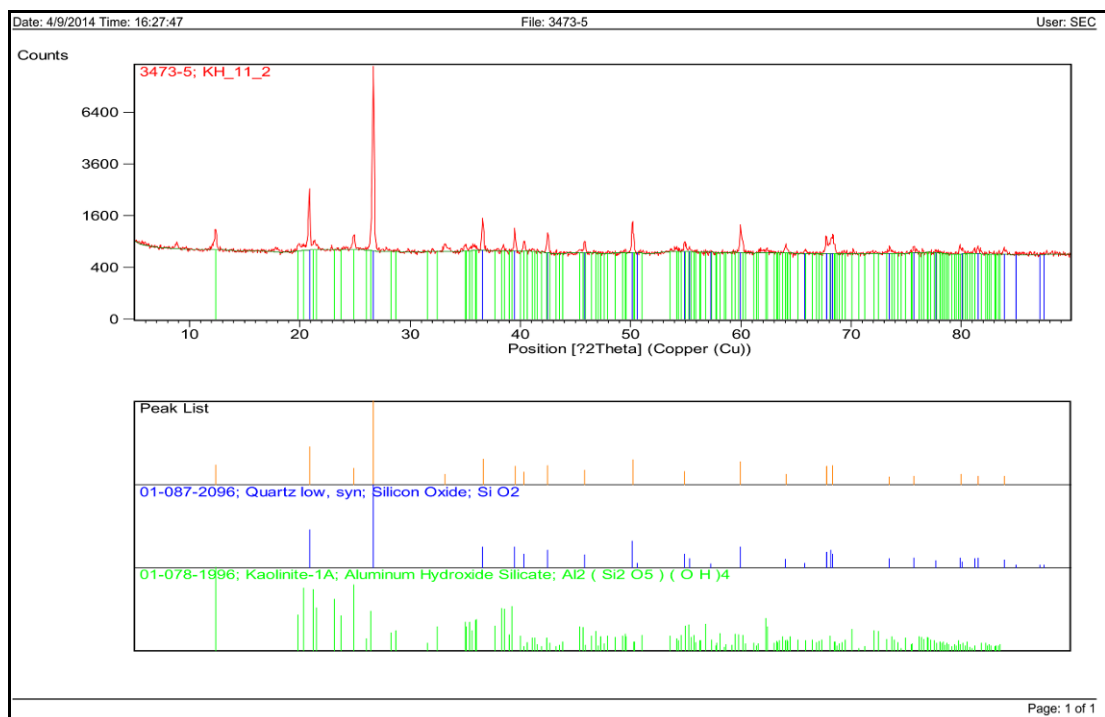
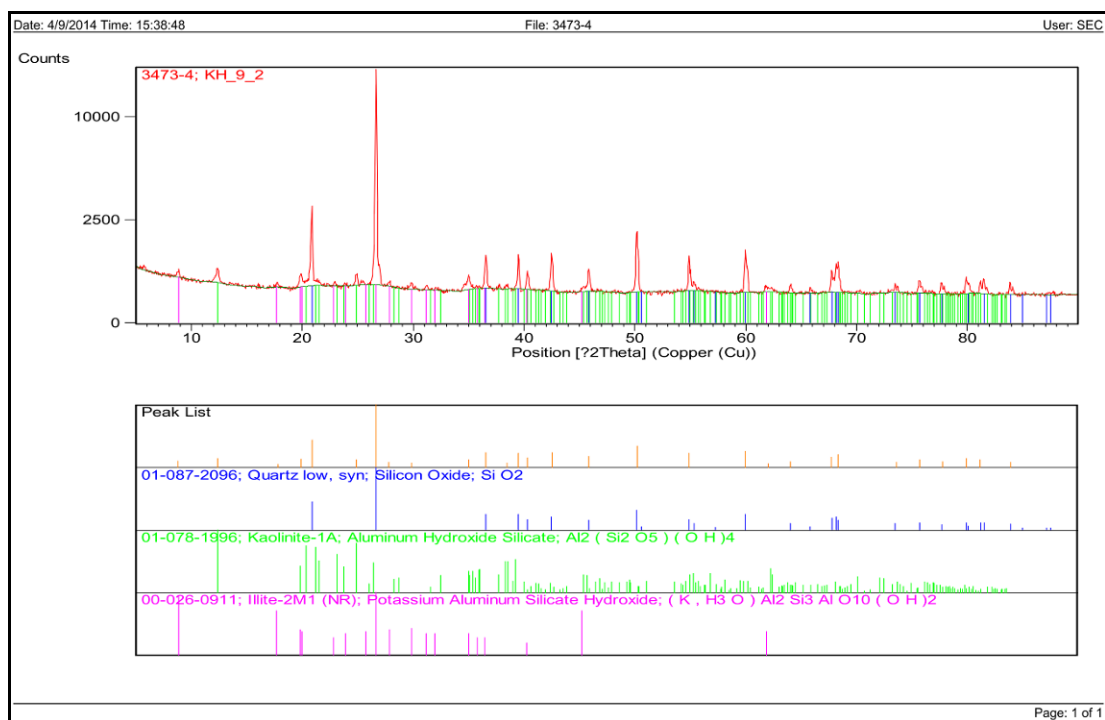
September 5, 2014







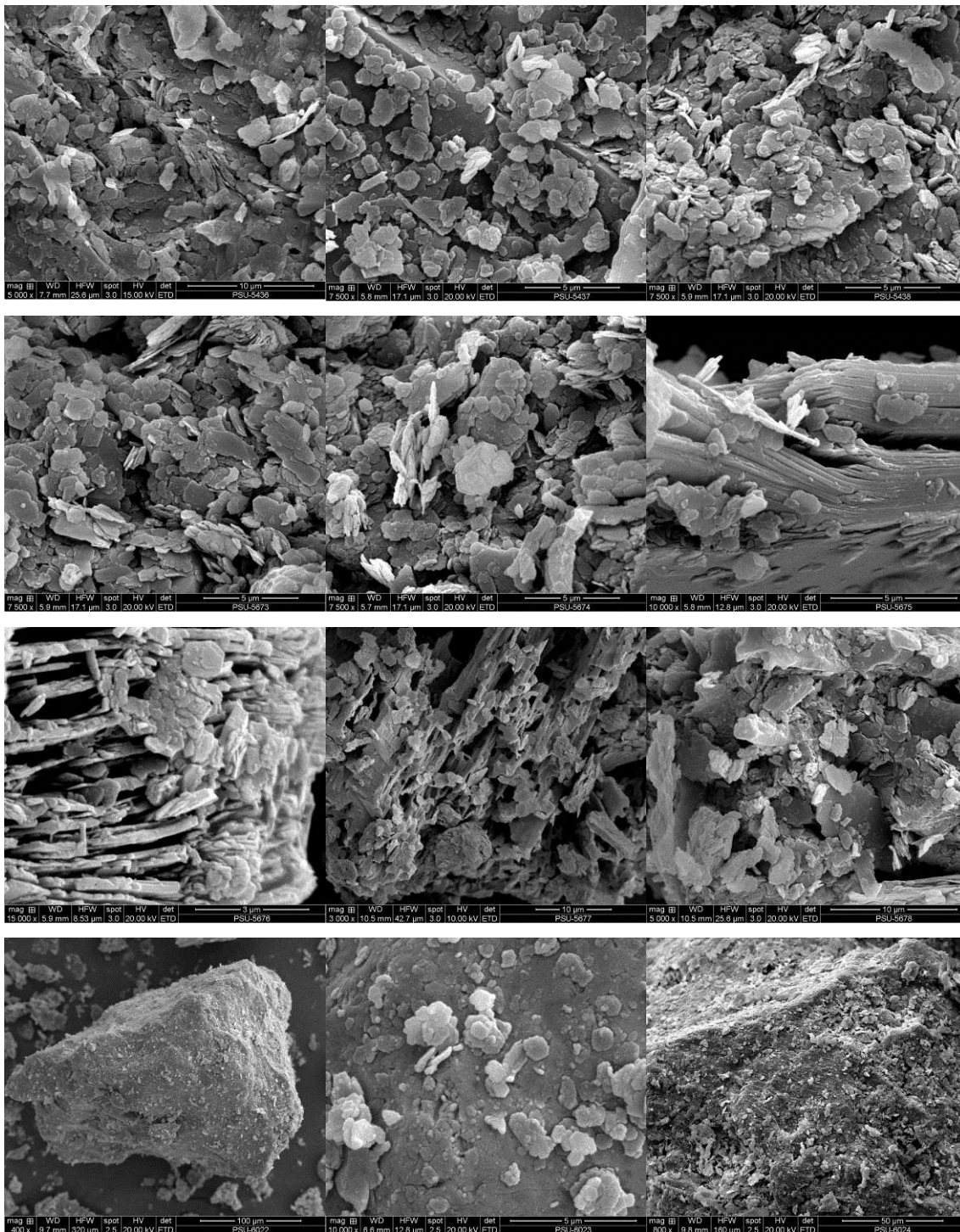




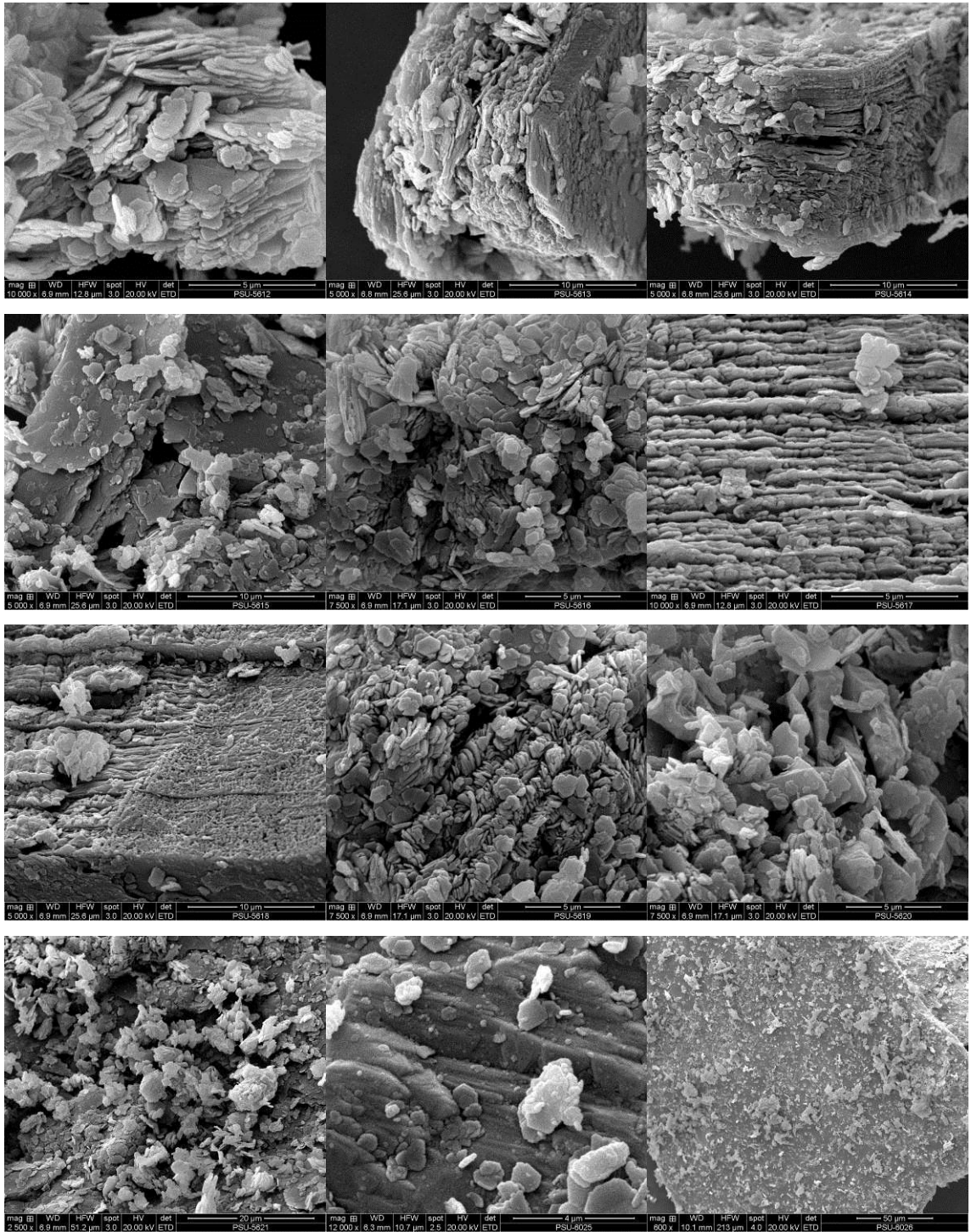
APPENDIX C

SEM OF SAMPLES

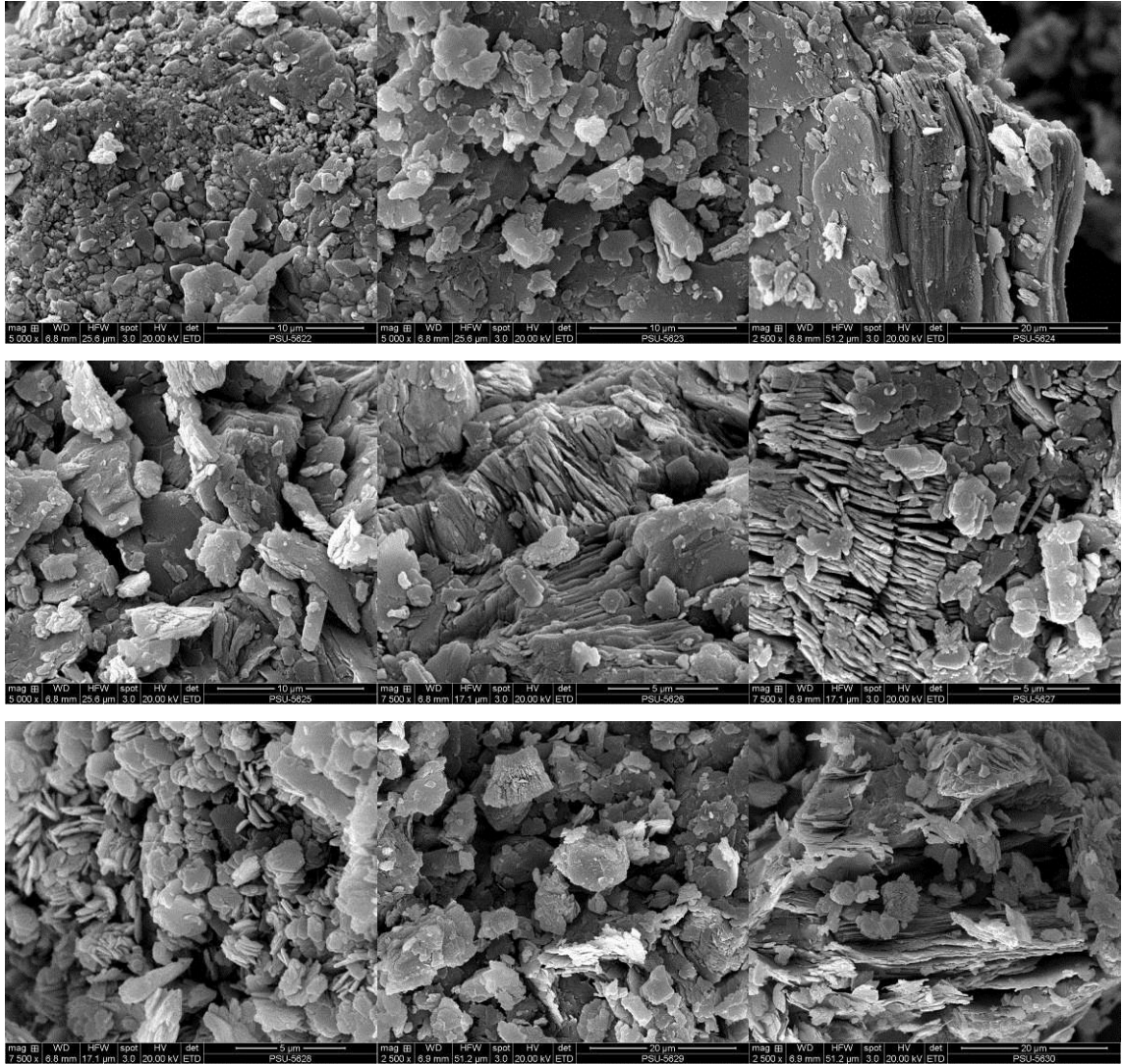
KB_1_2



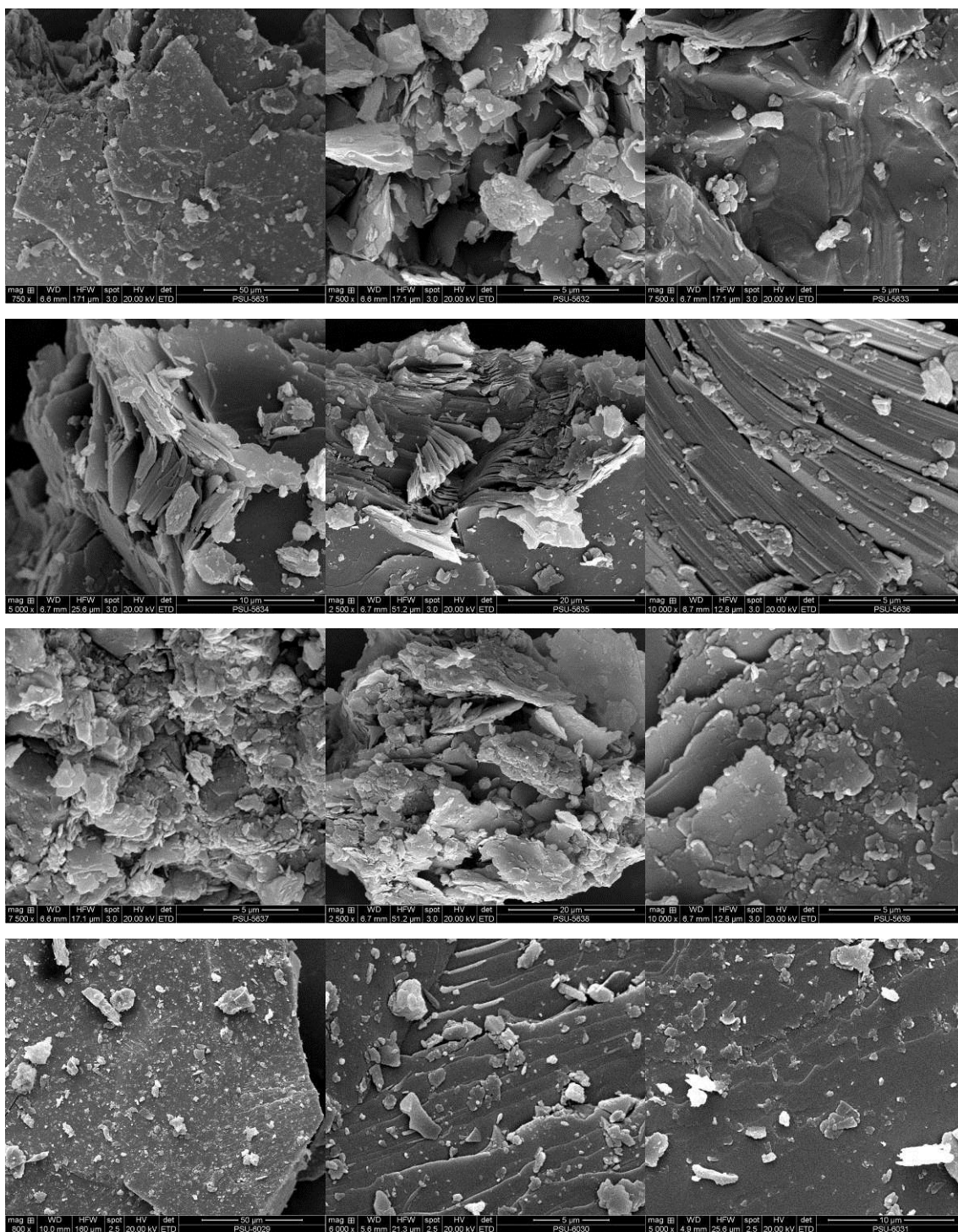
KB_4_2



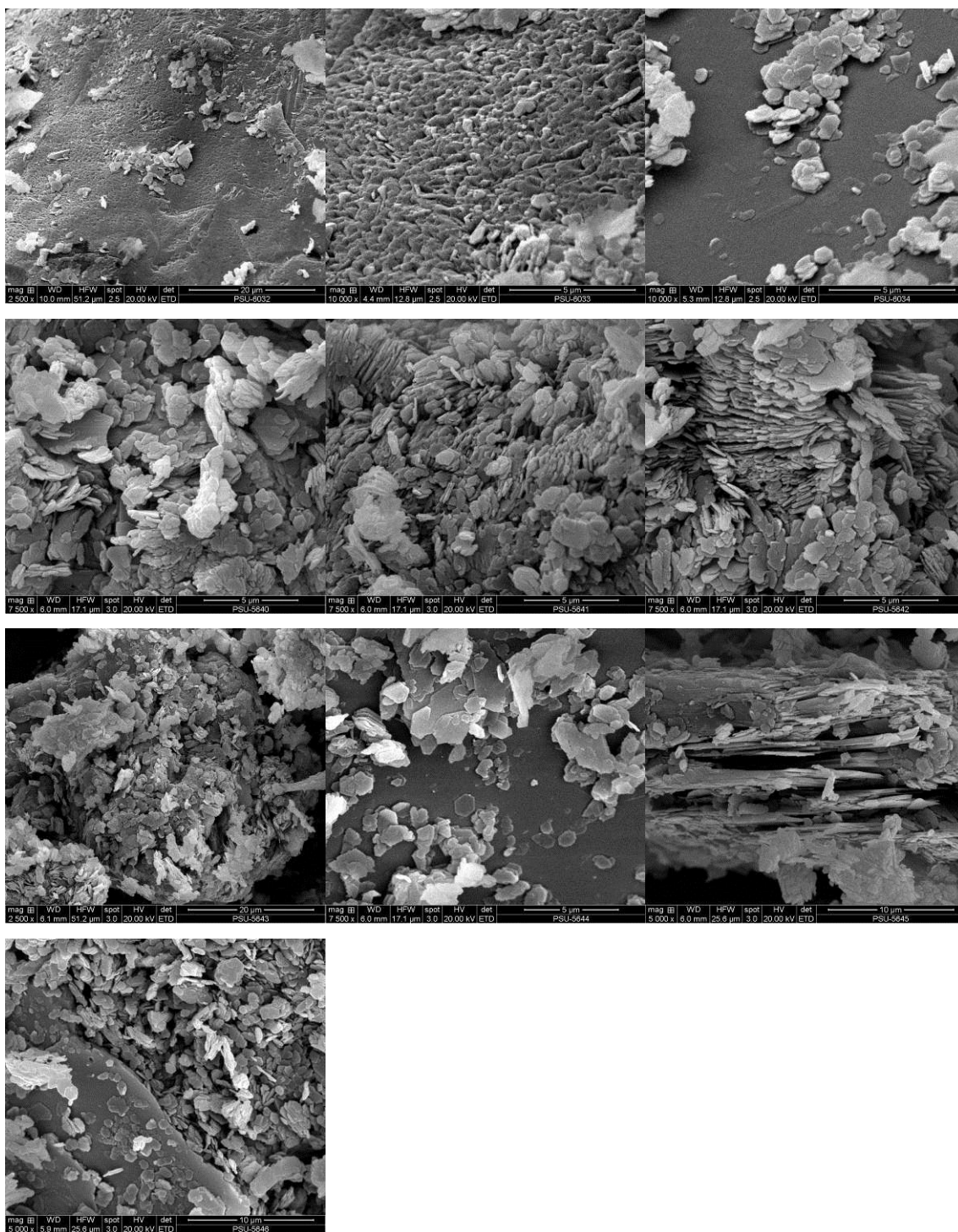
KB_5_2



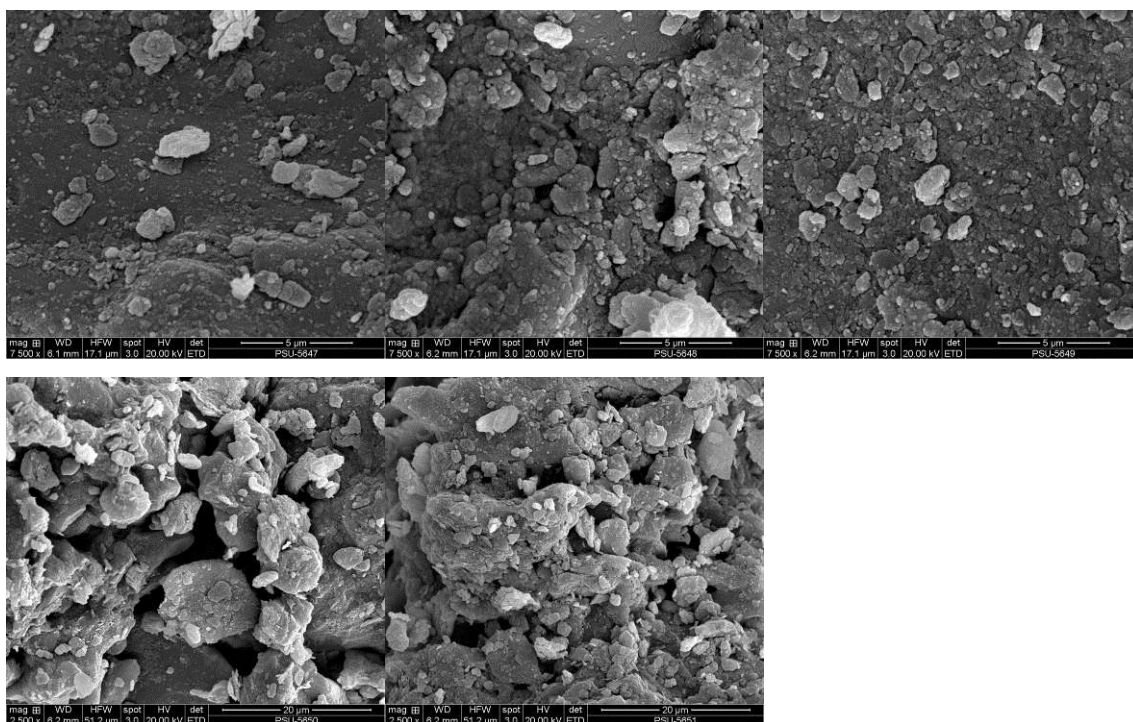
KB_6_2



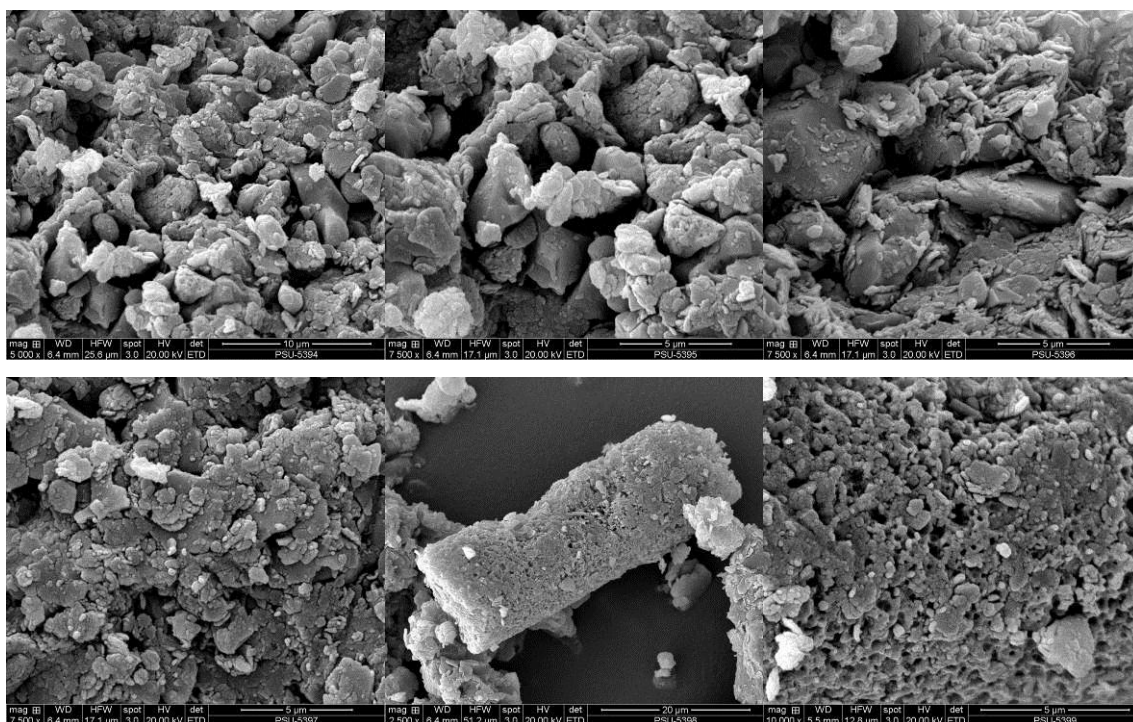
KB_7_2



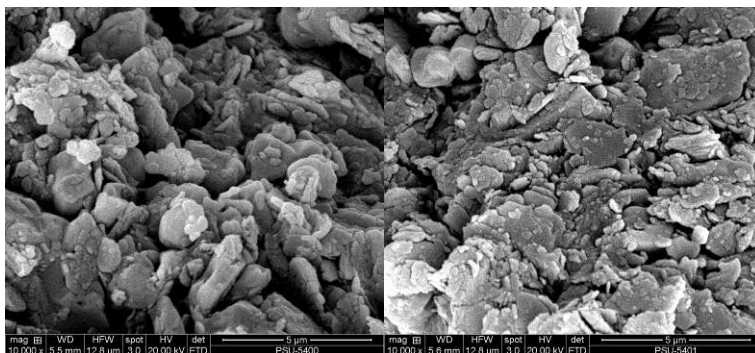
KB_9_2



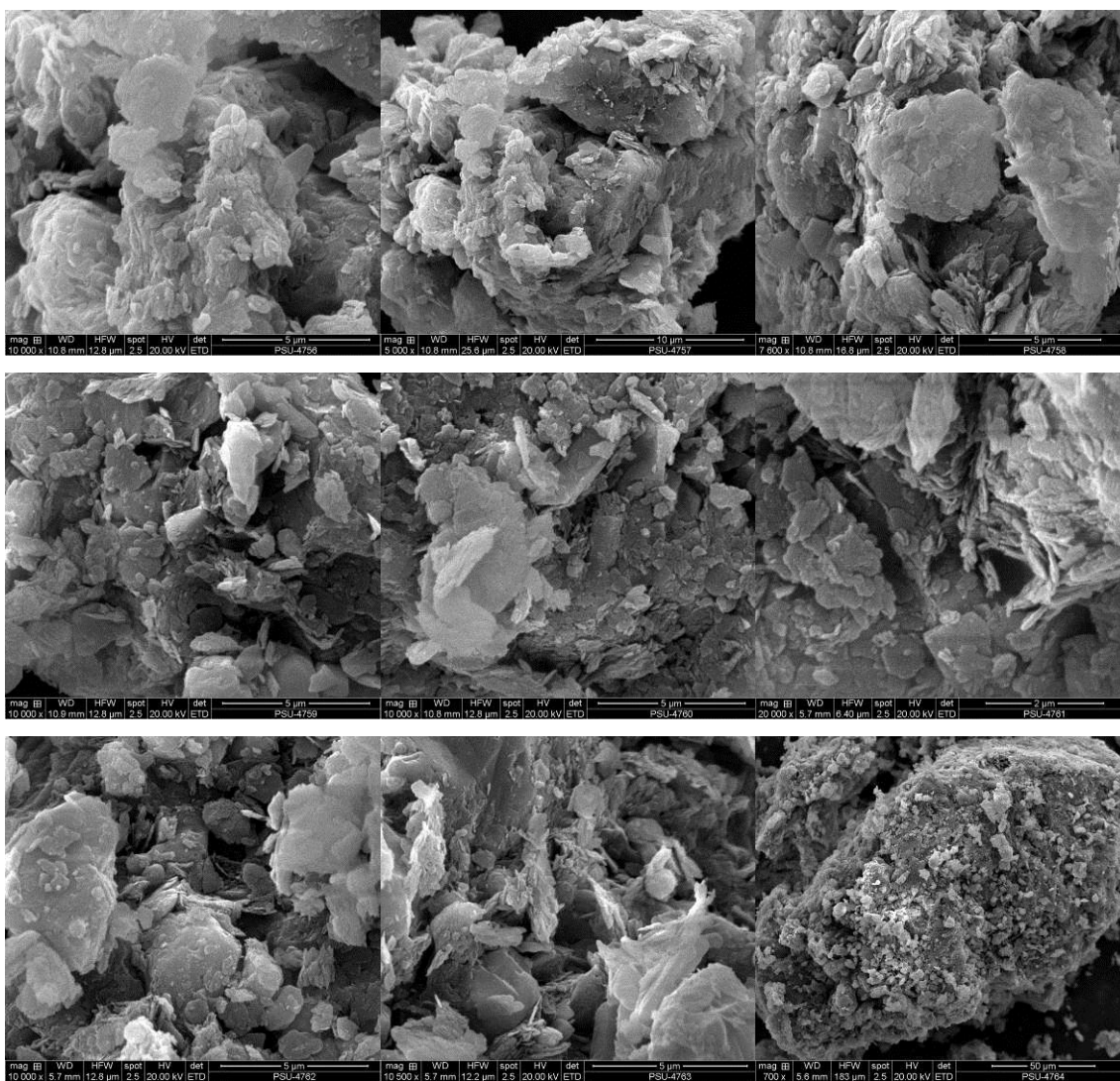
KH_1_2



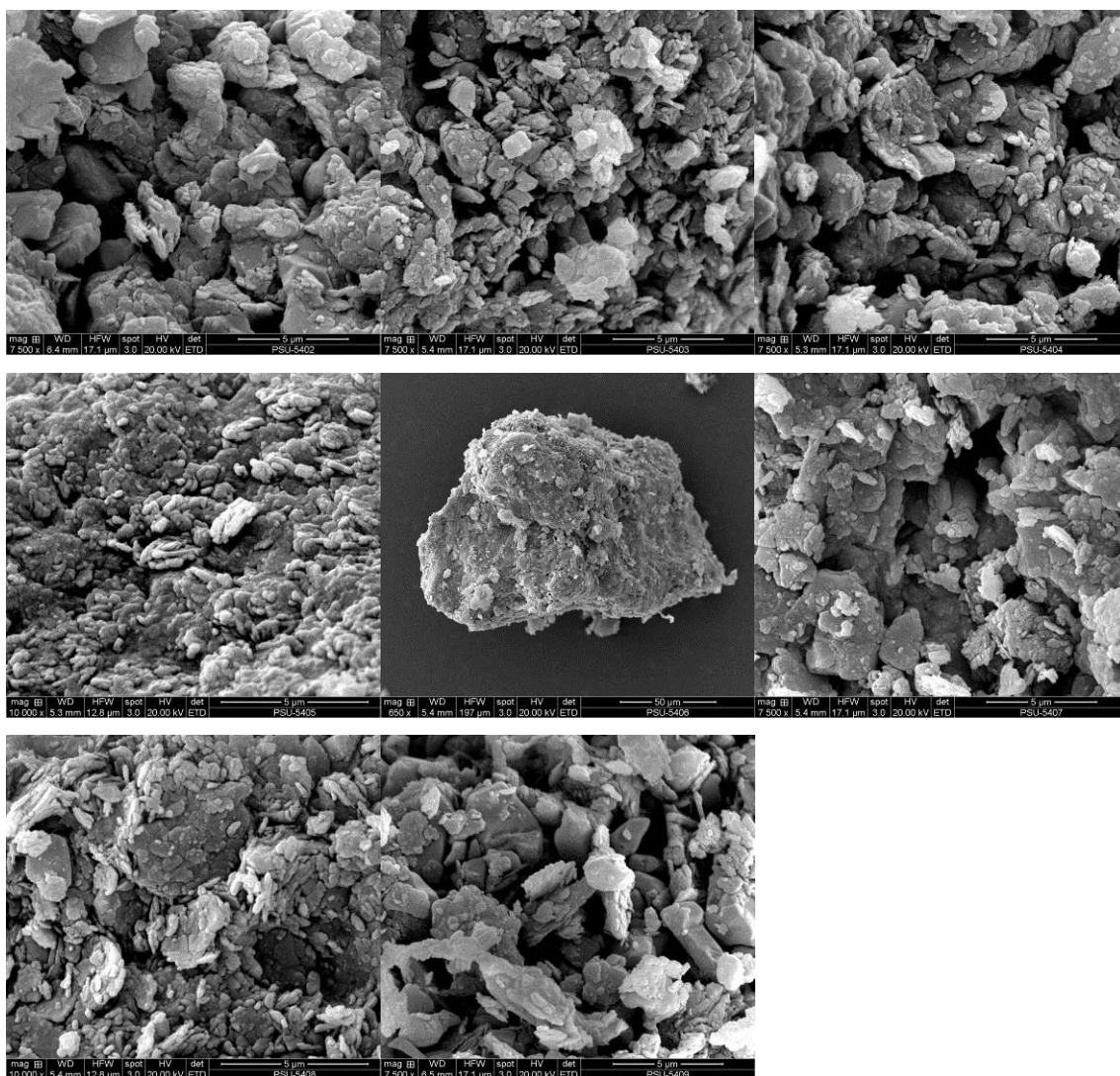
KH_1_2



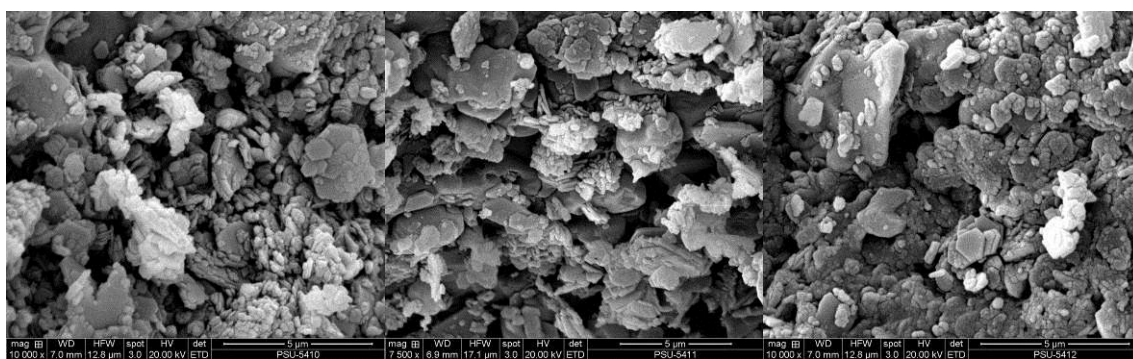
KH_2_2



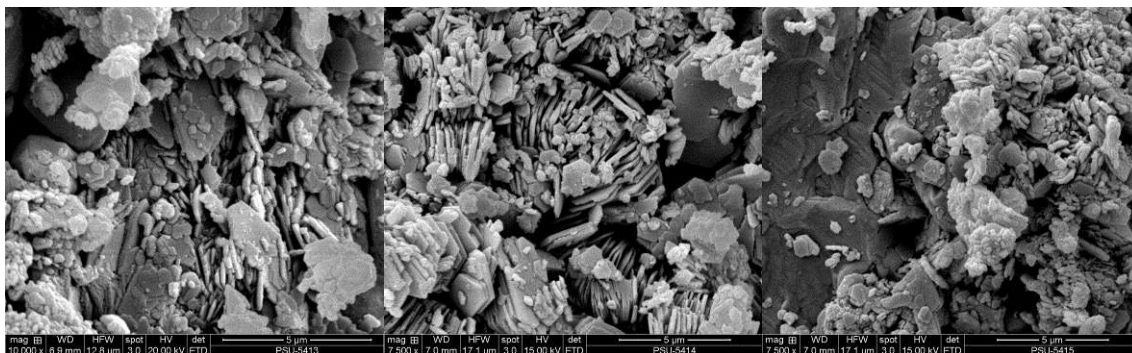
KH_3_2



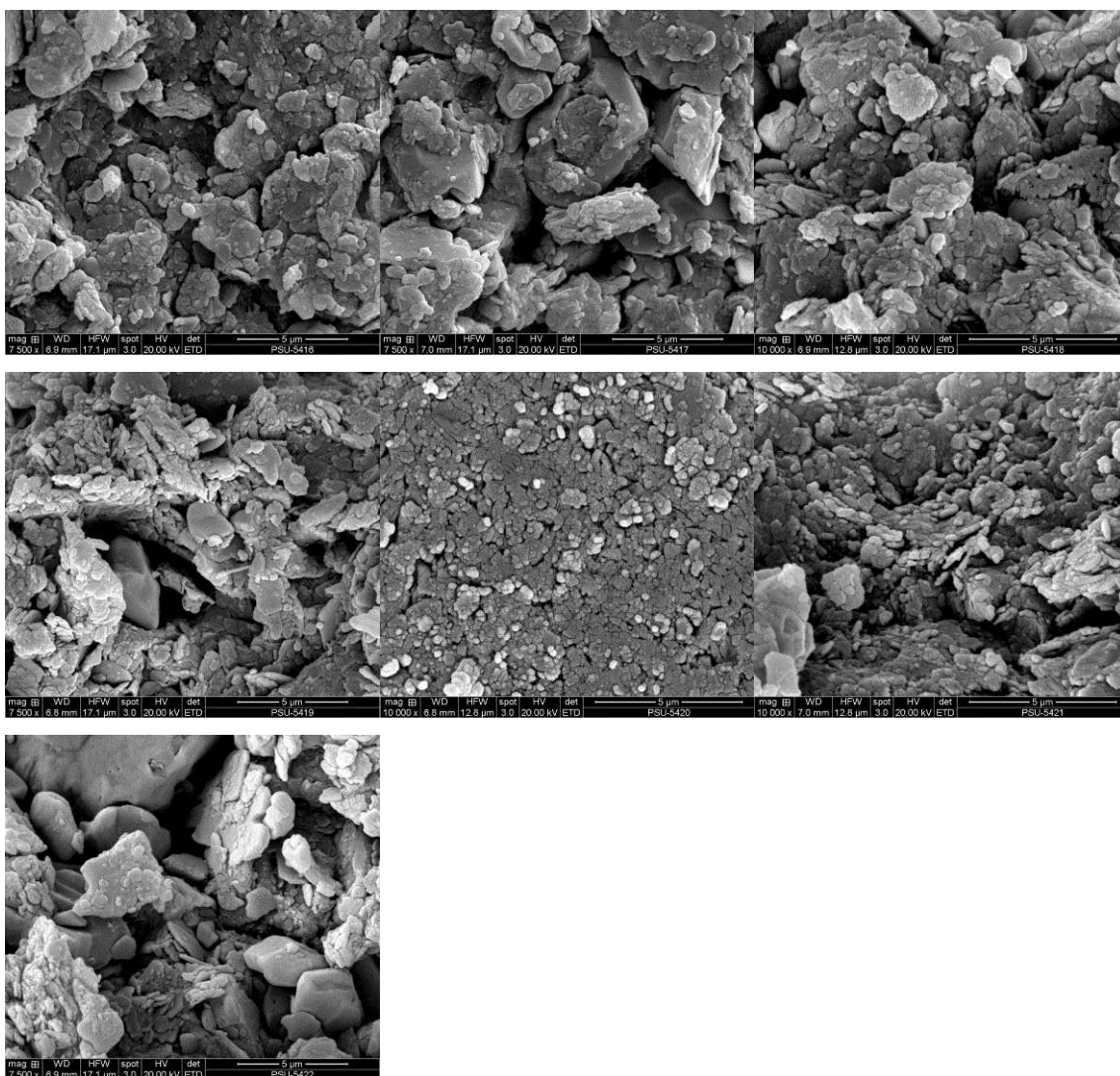
KH_4_2



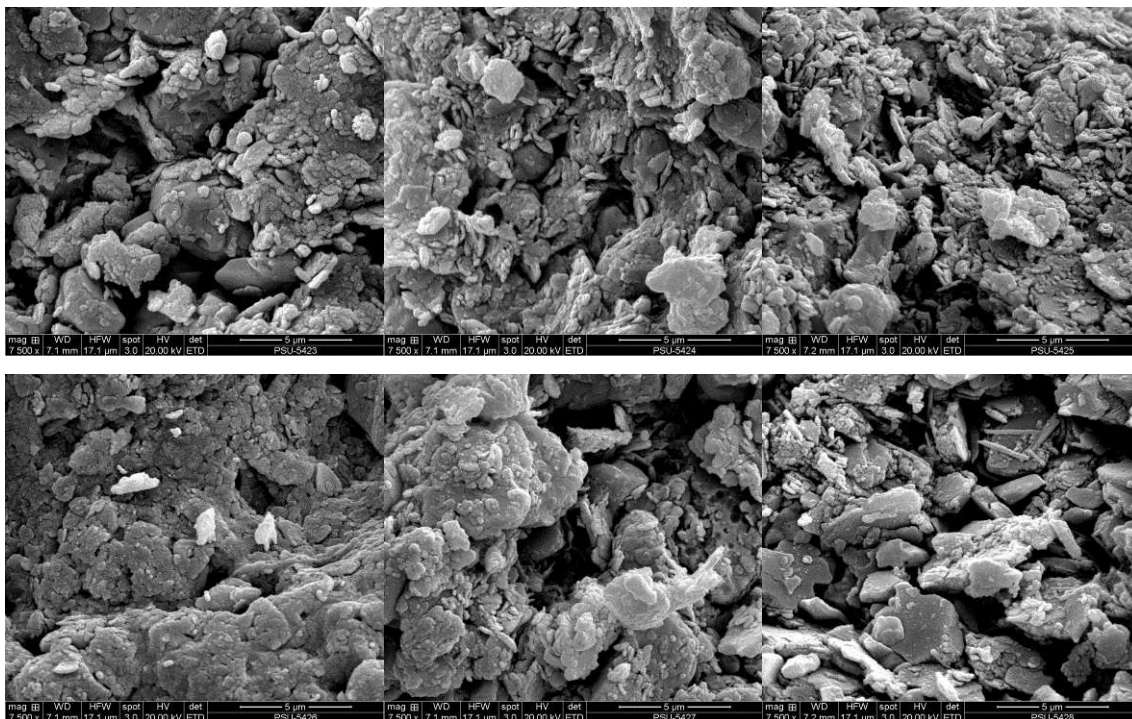
KH_4_2



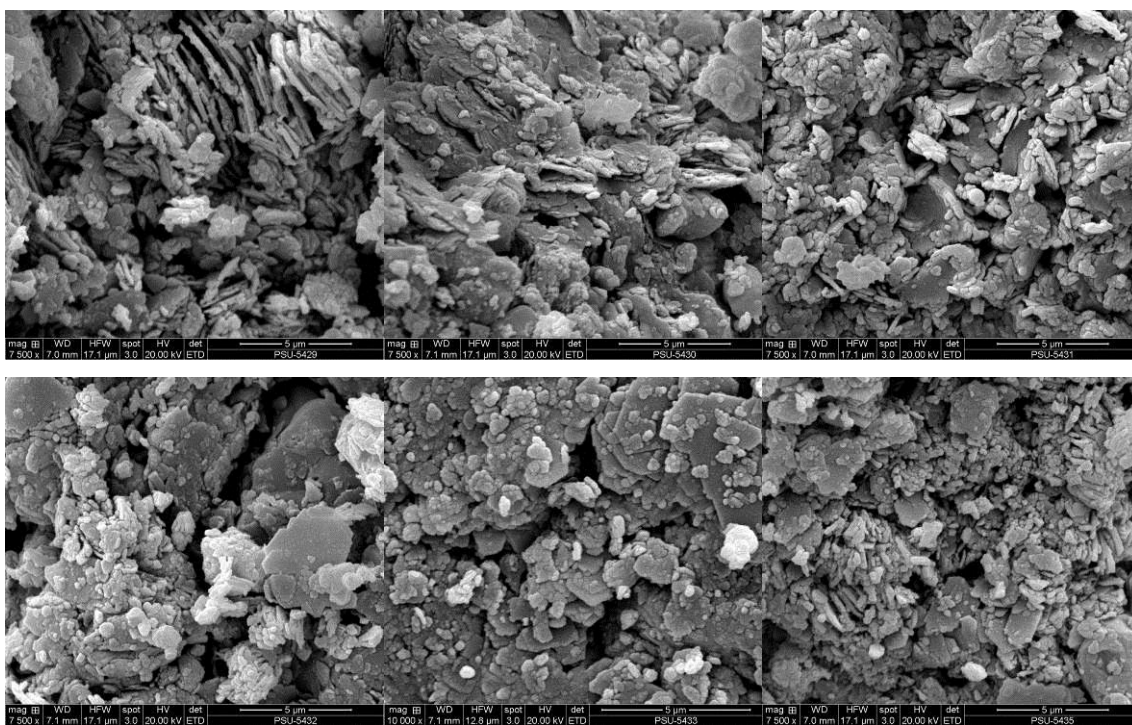
KH_5_2



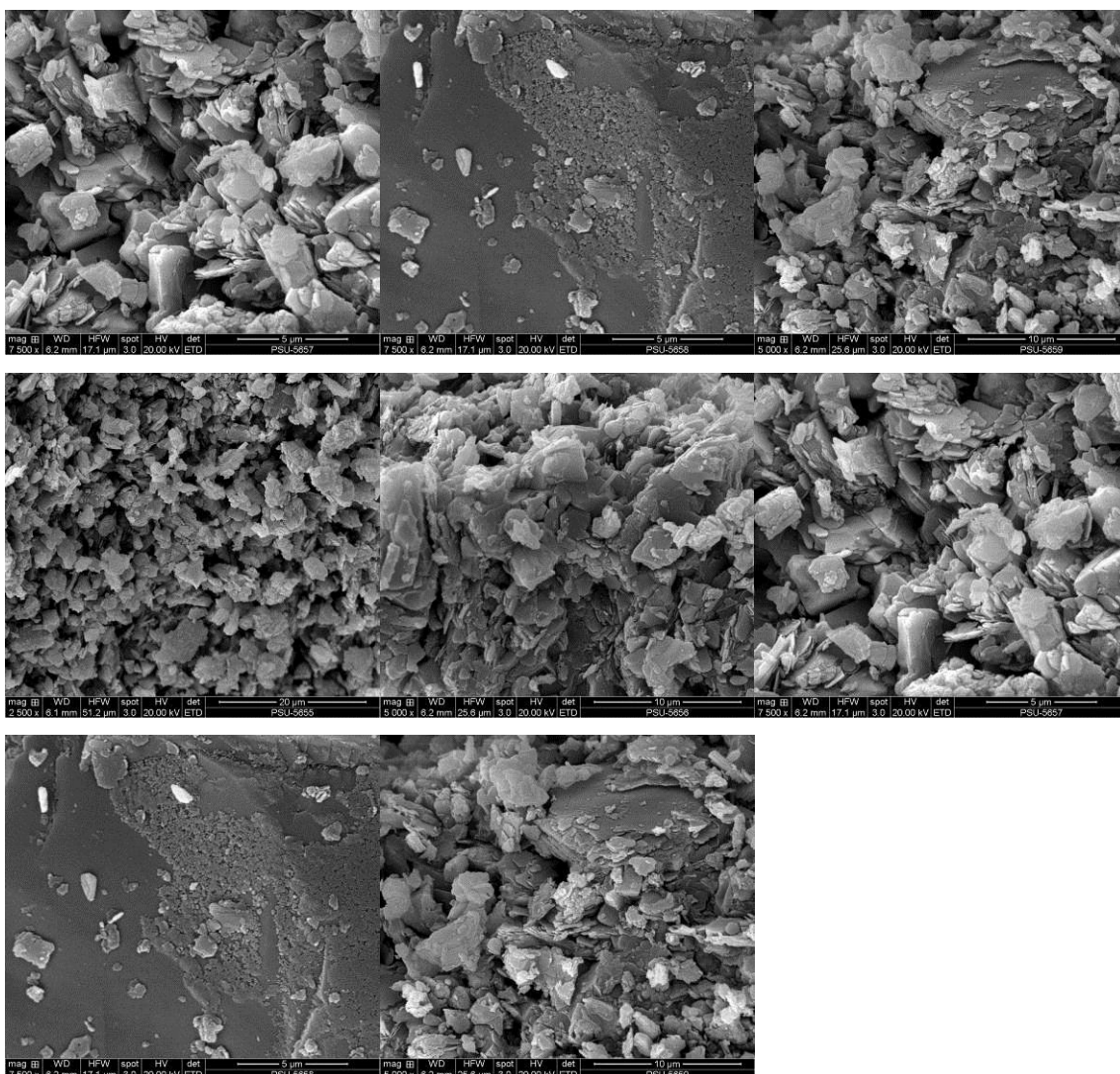
KH_6_2



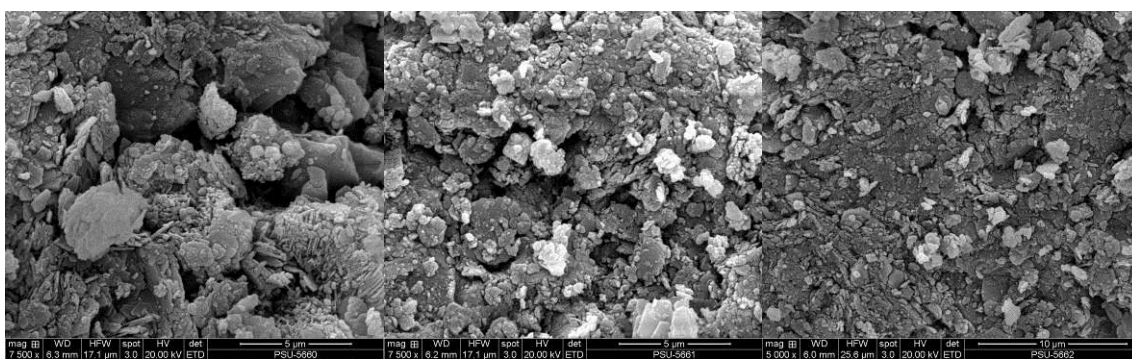
KH_7_2



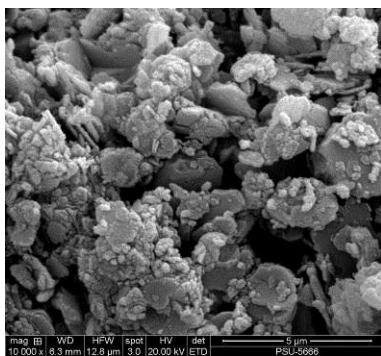
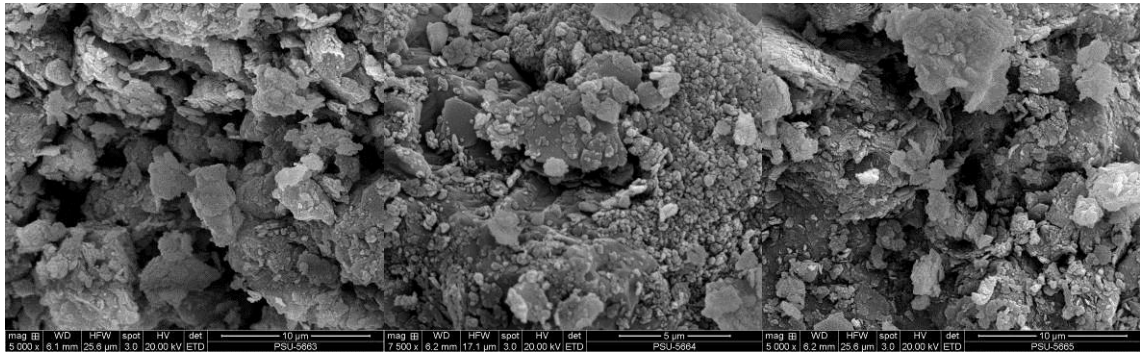
KH_8_2



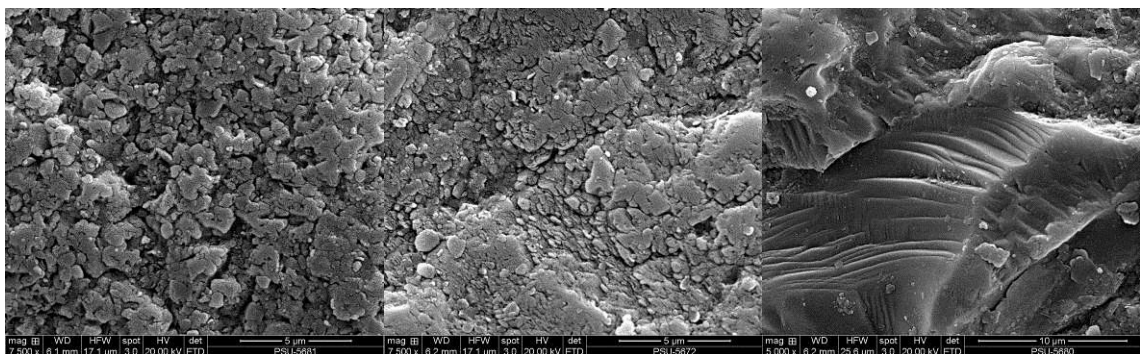
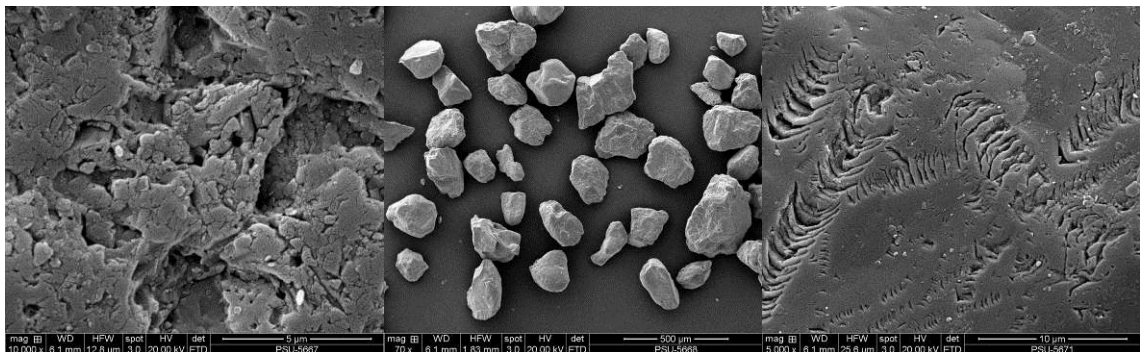
KH_13

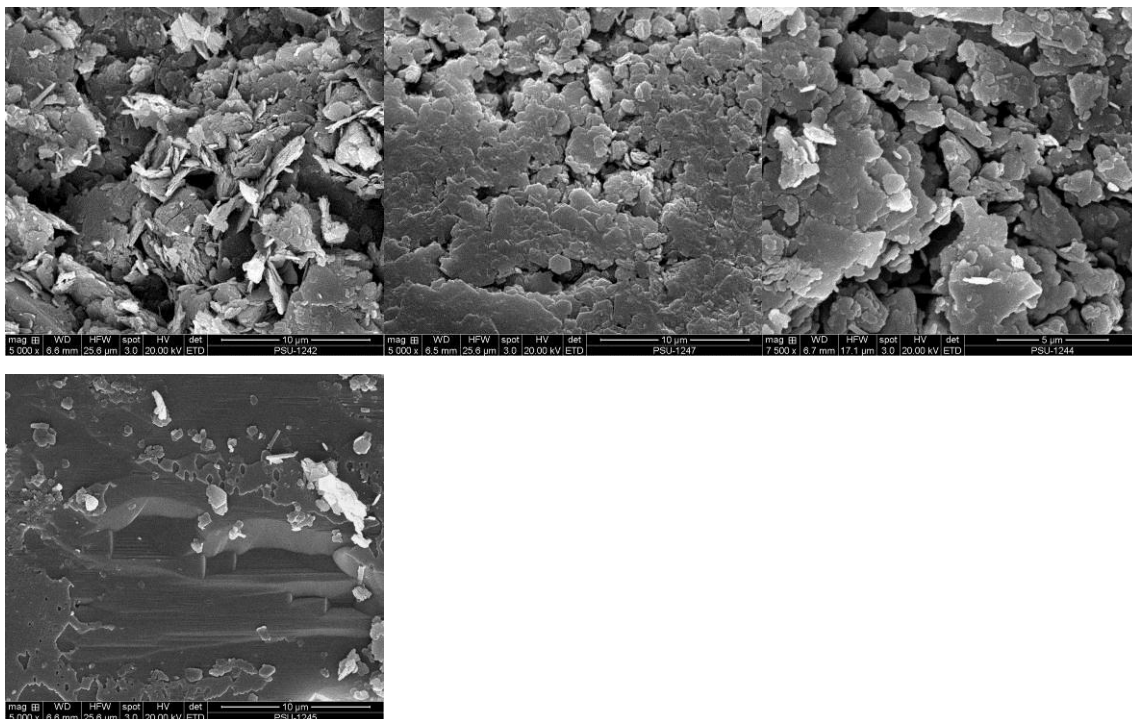
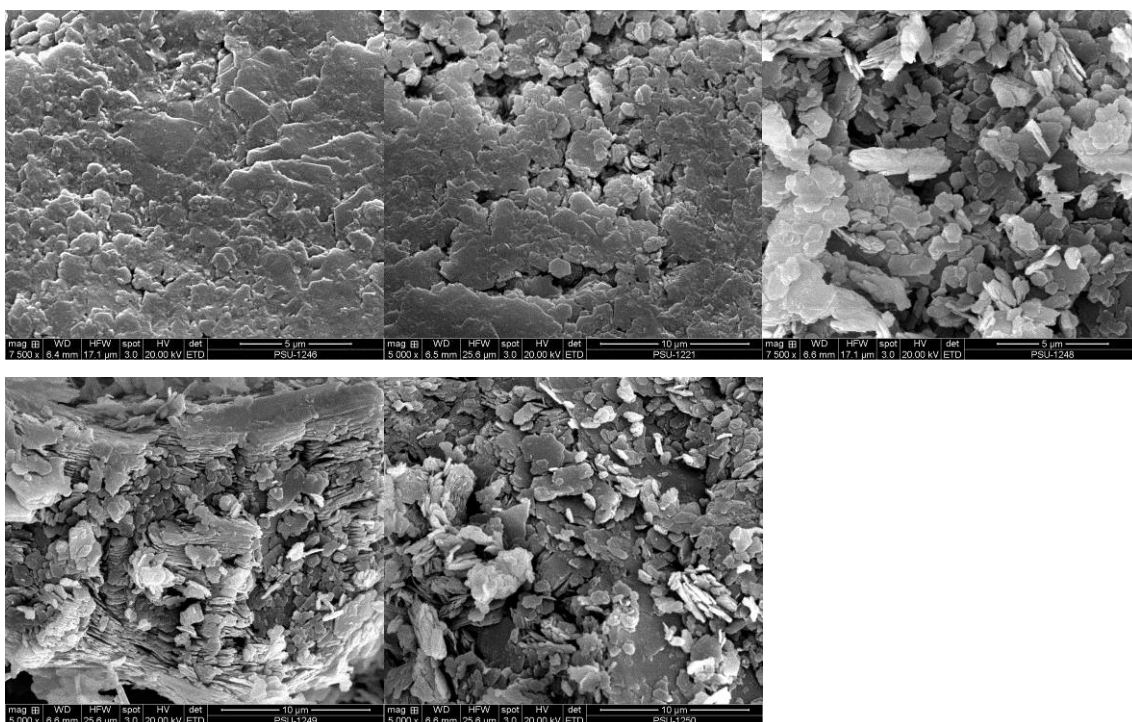


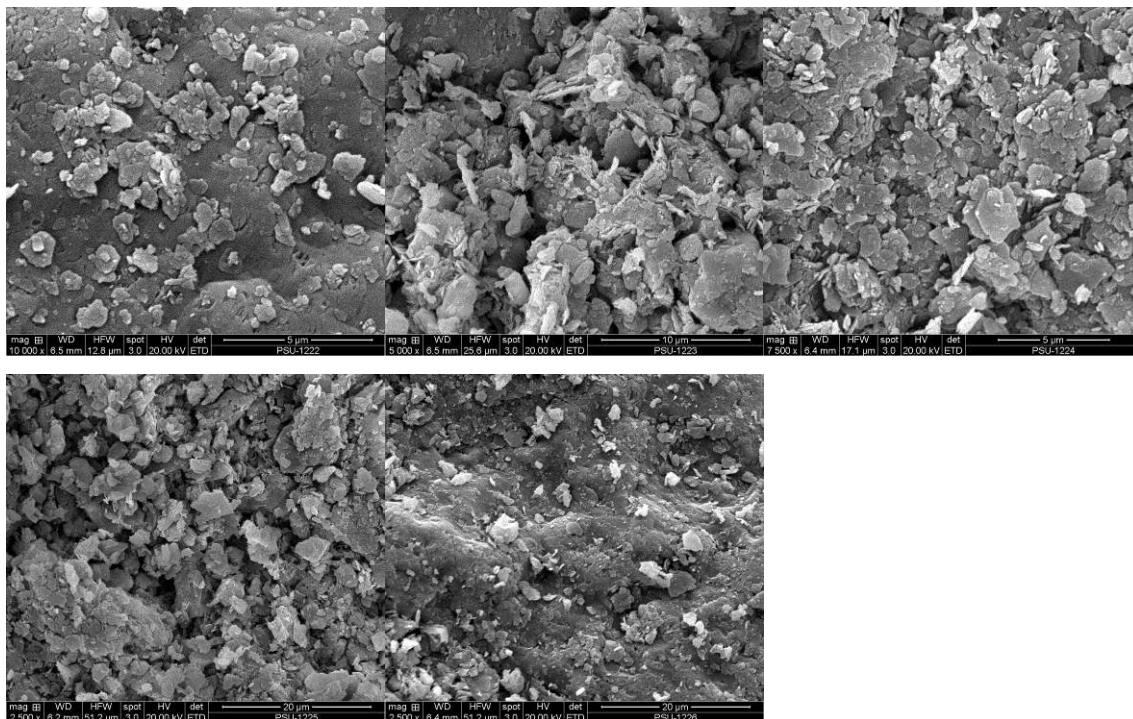
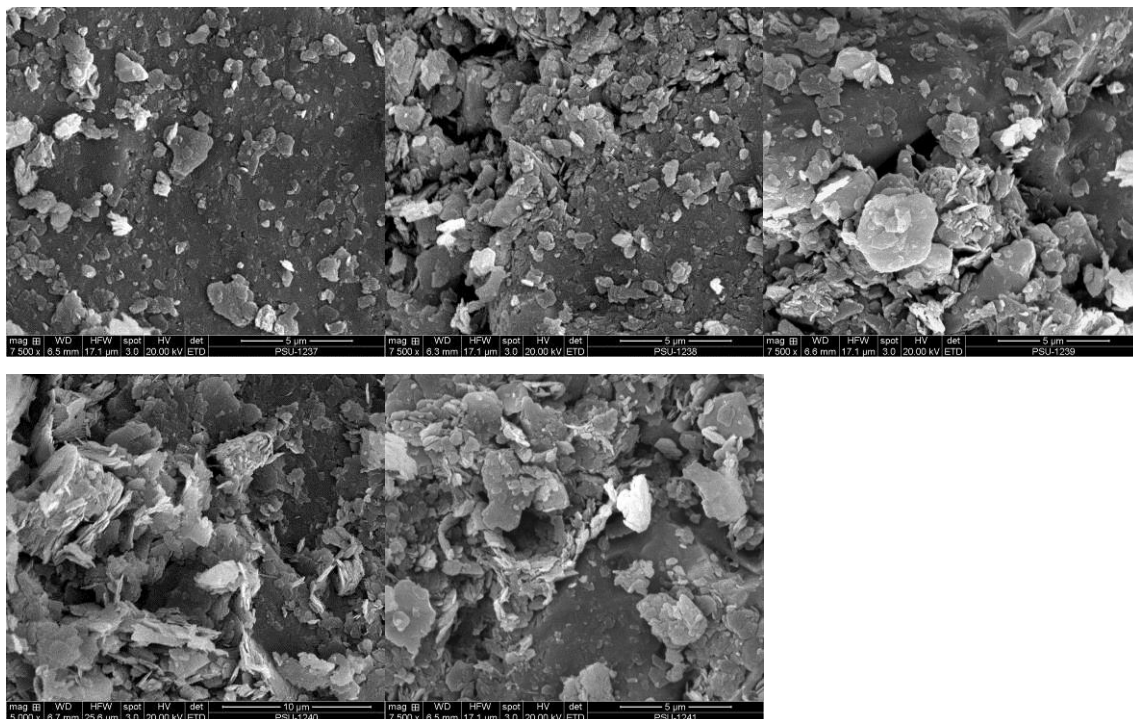
KH_13



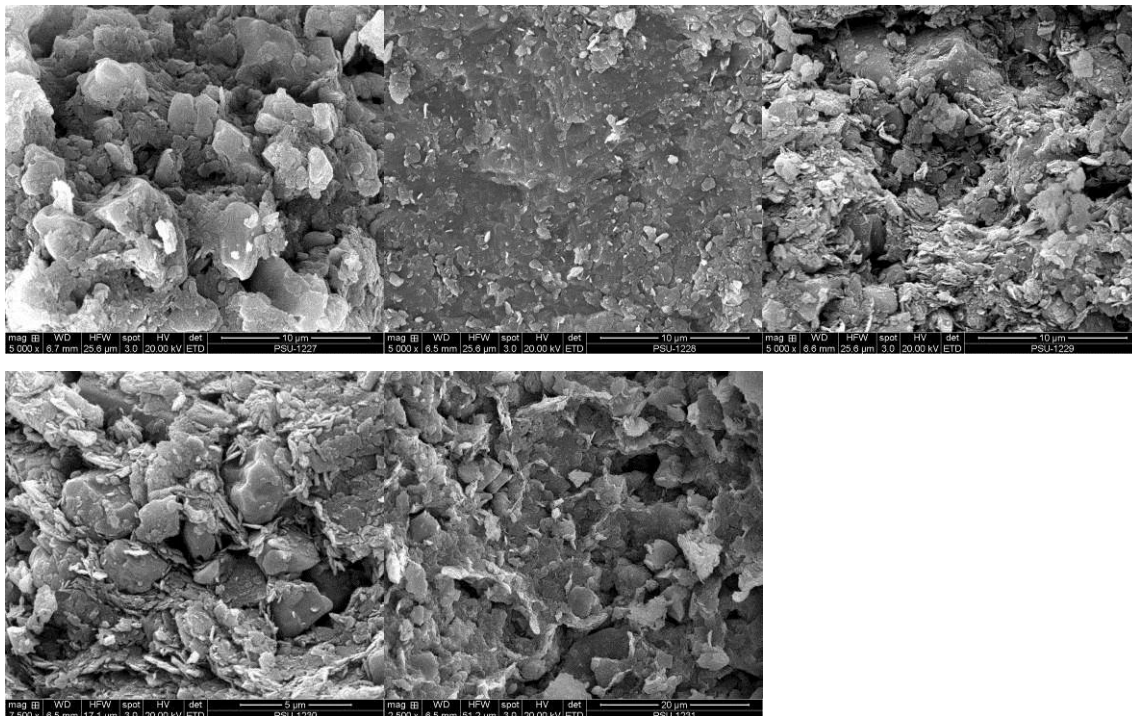
Beach sand



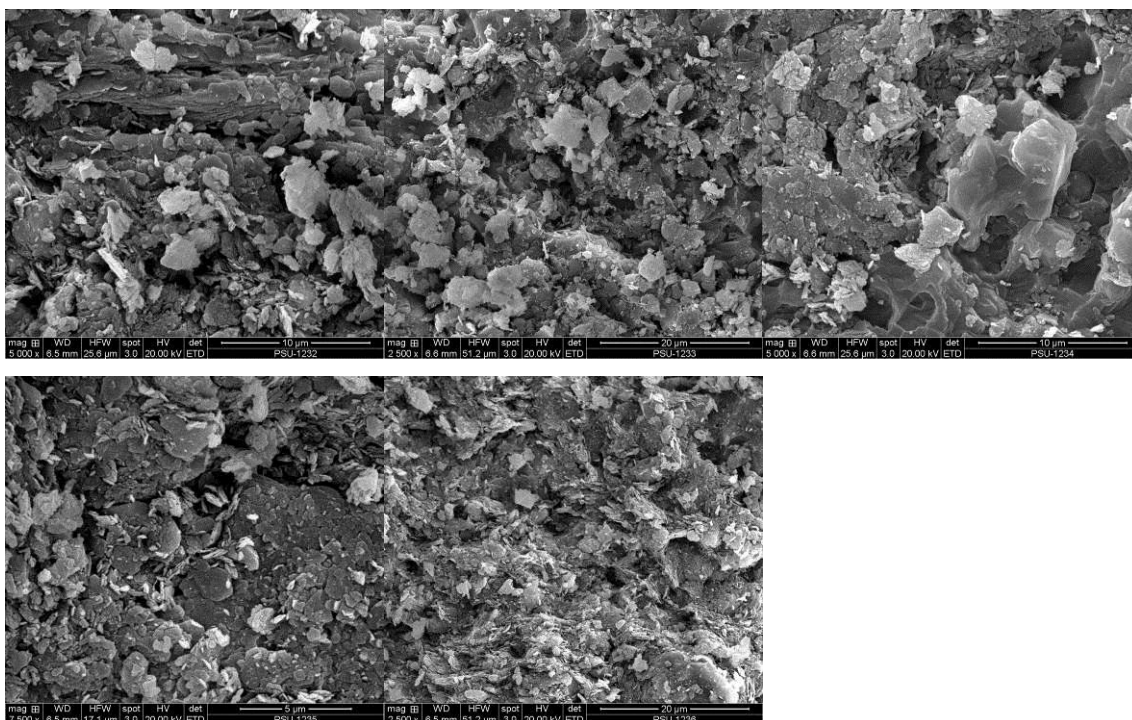
KB_2_2 (Resistivity)**KB_4_2 (Resistivity)**

KH_1_1 (Resistivity)**KH_5_1 (Resistivity)**

KH_6_1 (Resistivity)



KH_7_1 (Resistivity)



APPENDIX D
DATA FOR CALCULATION OF VELOCITY

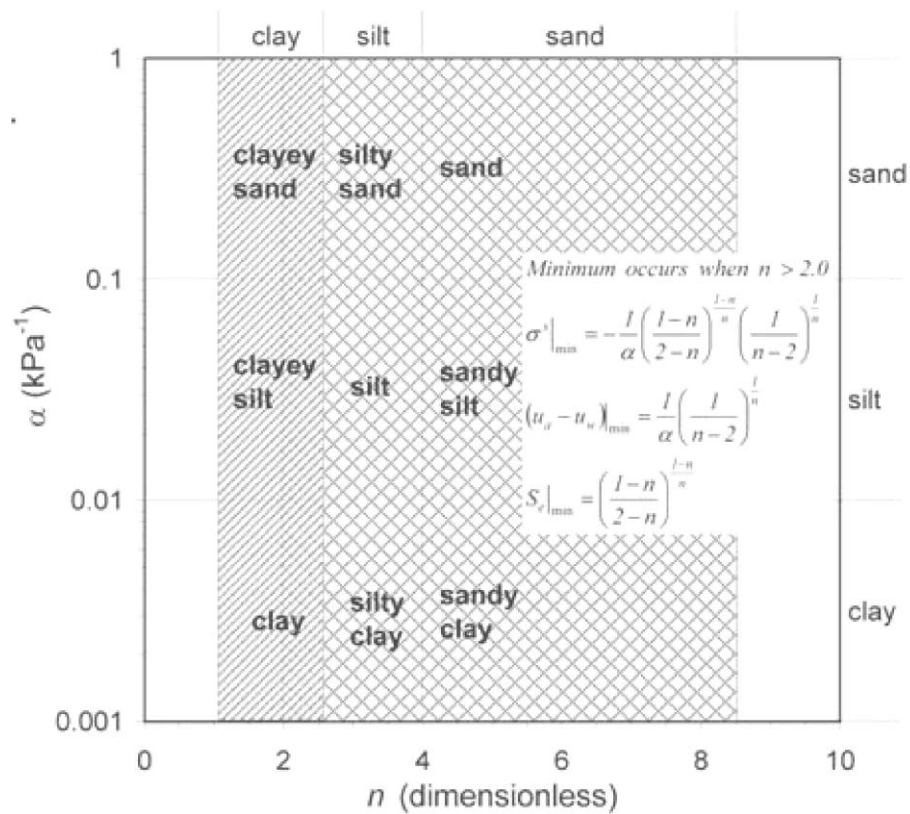


Figure D.1 The range of values α (the inverse of air entry pressure for water saturated soil) and n (the pore size distribution parameter) of the and parameters for various soil types (Lu et al., 2010).

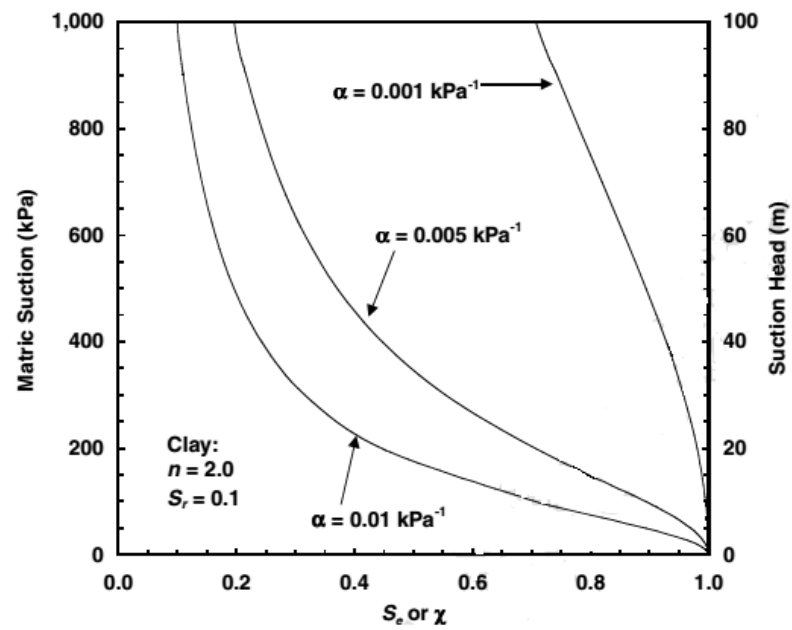


Figure D.2 Soil-water characteristic curves and corresponding effective stress parameter functions for clay (Lu and Likos, 2004).

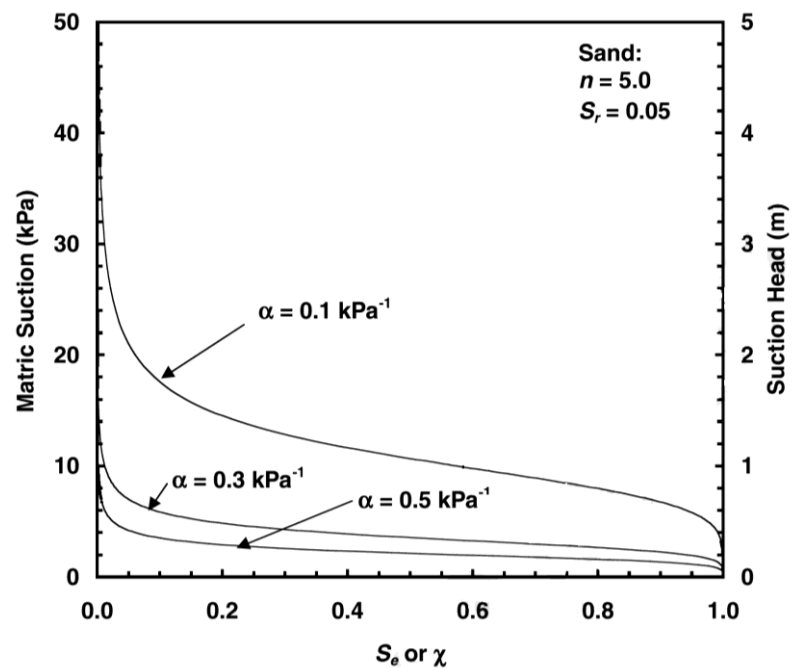


Figure D.3 Soil-water characteristic curves and corresponding effective stress parameter functions for sand (Lu and Likos, 2004).

Table D.1. Physical and theoretical properties and model parameters of sands and clays for seismic velocity calculations, sand at 10 cm and clay at 1 m depth to emphasize the contribution of interparticle stress (Crane, 2013).

Model Parameters	Sand	Reference	Clay	Reference
Grain Shear Modulus (Pa)	4.5×10^{10}		9.9×10^9	
Grain Bulk Modulus (Pa)	3.66×10^{10}		2.5×10^{10}	
Grain Density (kg/m^3)	2650	Mavko et al. (2003)	2550	Mavko et al. (2003)
Grain Poisson's Ratio	0.15		0.15	
Porosity	0.35		0.56	
Water Density (kg/m^3)	1000		1000	
Air Density (kg/m^3)	1.22		1.22	
Gravitational Acceleration (m/s^2)	9.81		9.81	
Coordination Number	1		1	
Van Genuchten n Fitting Parameter	5.69		2	
Van Genuchten α Fitting Parameter	4.56	Engel (2005)	0.01	Song et al. (2012)
Irreducible Water Content	0.024		0.10	
Matrix Cohesion (Pa)	300	Krantz, (1991)	16000	Bishop, (1960)

PUBLICATIONS



PROCEEDINGS OF THE
FIFTH THAILAND SYMPOSIUM ON

ROCK MECHANICS

K. Fuenkajorn
N. Phien-wej

EDITORS

Seismic velocities of unconsolidated sediments with clay

S. Suksawat

Department of Physics, Faculty of Science, Prince of Songkla University, HatYai 90112, Thailand

H. Dürrast

Department of Physics, Faculty of Science, Prince of Songkla University, HatYai 90112, Thailand

Geophysics Research Center (GRC), Prince of Songkla University, HatYai 90112, Thailand

Keywords: Unconsolidated sediments, ultrasonic velocity, clay, water saturation

ABSTRACT: Geophysical investigations are targeting the shallow subsurface, with velocity methods among the main ones used. One objective is the determination of velocities, compressional wave (V_p) and shear-wave velocities (V_s). For the interpretation of velocity data it is essential to know the influence of the sediment properties, e.g. composition, grain size, grain shape, porosity, bulk density, moduli, and water saturation. These relationships are obtained from laboratory measurements of P- and S-waves under controlled conditions (pulse transmission ultrasonic technique). The velocity was determined under laboratory conditions with increasing water saturation (0–100%). For this study disturbed samples of unconsolidated sediments from different layers from bedrock to the top soil layer were taken from two location of the Khao Khohong mountain range near Hat Yai District, Songkhla Province. The two sample locations comprise different bedrock lithologies, sandstone and granite.

1 INTRODUCTION

The seismic technique is one of the most used geophysical methods for shallow subsurface investigations. Seismic velocities are based on elastic constants and density of the material investigated (Telford et al., 1990). Seismic velocities are parameters that are exhibiting a large range of values sensitive to various factors like the nature of material, components (minerals, matrix components), porosity, density, water or fluid saturation, and others. The shallow subsurface is a few hundred meters in depth and comprises mainly of unconsolidated sediments, porous material, solid fragmental material from weathering of bedrocks, transported and deposited mainly by water that form layers on the Earth's surface at normal temperature and pressure conditions; near surface unconsolidated sediments, e.g., are sand, gravel, silt, mud, alluvium, and others (Immoor, 2006). The shallow subsurface is the source for groundwater as well as the region of landslide hazards, and the main resource in agriculture, soil. Characteristics of unconsolidated sediments are composition, grain size, grain shape, grain arrangement, as well as pore size and shape. Important physical properties used for various applications are density (bulk and mineral density), porosity, water saturation, electrical resistivity, and velocities (Schön, 2011).

1.1 Study area

For this study disturbed samples of unconsolidated sediments from different layers from bedrock to the top soil layer were taken from two location of the Khohong mountain range in Hat Yai District, Songkhla Province. The two sample locations comprise different bedrock lithology, first, mainly granite at a mountain site in different states of weathering and second, mainly sandstone with different layers from bedrock to top soil. From the later site samples have been collected as a profile from the top layer to the bottom layer. The top layer is top soil (KH_1_2), dark grey soil with roots, the second layer is yellowish brown unconsolidated sediment (KH_2_2), and bottom layer is brown unconsolidated sediment (KH_3_2). Below the last layer is bedrock, here a sand/siltstone (Figure1).

1.2 Material

All samples show macroscopically visible clay content after collected in the outcrops. The mineral analysis of the samples show that all of them mainly consist of quartz, kaolinite and illite, both clay minerals, and some minor phase like hematite. The mineral density of the samples from the granite site are around 2.5 to 2.6 g/cm³, which reflects the main minerals with quartz (2.648 g/cm³), kaolinite (2.594 g/cm³) and illite (2.660 g/cm³) (data from Schön, 2011). The bulk density values are much smaller, around 1.5-1.8 g/cm³, thus reflecting the porosity of the samples with 30 to 40%, which is common for such sediments (e.g. Schön, 2011). Higher bulk density correlates with lower porosity values and vice versa. The values of the mineral density of the samples from the sandstone site are around 2.45 to 2.68 g/cm³, which here also reflect the main minerals with quartz, kaolinite, and illite. The bulk density values are much smaller, around 1.3-1.5 g/cm³, thus reflecting the porosity of the samples with 42 to 50%, which is common for such sediments (e.g. Schön, 2011).

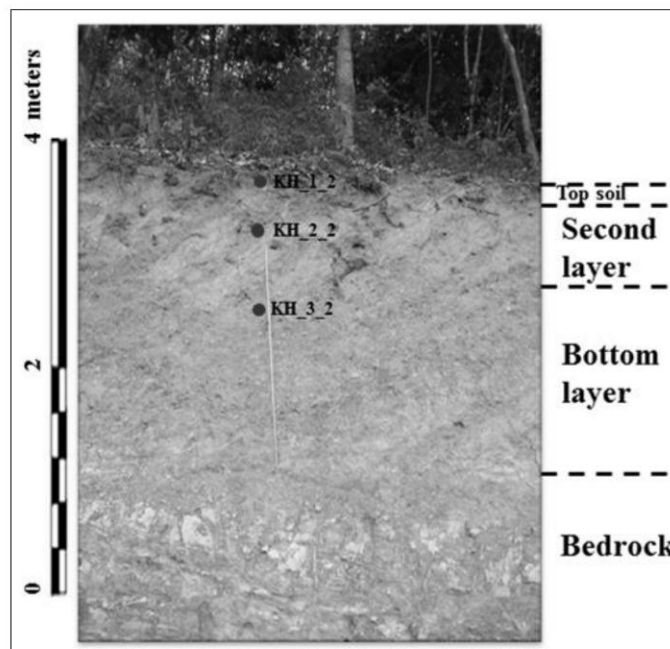


Figure 1. Sample locations of unconsolidated sediments from Khohong mountain range. Bedrock is a sand/siltstone, red point are sample locations with sample name.

1.3 Velocities

There are two groups of seismic waves, surface waves and body waves, with the latter ones being utilized in seismic surveys. The velocity of the propagation of body waves, compressional and shear wave velocity, in any solid earth material can be determined as a function of the density (ρ) and the elastic constants of the material.

Compressional waves (longitudinal, primary, or P-waves) propagate in the medium in the same direction as the direction of wave propagation, P-wave velocity (VP) is given by

$$V_p = \left[\left(\kappa + \frac{4}{3}\mu \right) / \rho \right]^{\frac{1}{2}} \quad (1)$$

where κ is the bulk modulus in Pa, μ is the shear modulus in Pa, and ρ is density in kg/m³.

The direction of the shear wave (transverse, secondary or S-wave) motion in a medium is perpendicular to the direction of the wave propagation direction, with the S-wave velocity (Vs) given by

$$V_s = \left(\mu / \rho \right)^{\frac{1}{2}} \quad (2)$$

Compressional waves always travel faster than shear waves in the same medium and shear waves do not propagate through the liquids and gases because liquids and gases offer no resistance to shear deformation, so $\mu = 0$ (Sheriff & Geldart, 1995).

2 EXPERIMENT

Ultrasonic velocity method is a non-destructive testing method widely used for laboratory investigations and also at outdoor conditions. Two piezoelectric sensors are coupled tightly to an object at constant pressure, one is a transducer emitting ultrasonic pulses and the other is the receiver. The transducer is contact with the sample so that the vibrations are transferred to the sample. The wave travel through the sample and are picked up by the receiver (Figure 2). After calibration of the system the travel time of the seismic waves are measured from the transmitting to the receiving sensor. With the measurement of the sample length the velocities can be calculated. A complete description of the method is provided in the ASTM Test Designation C 597, Standard Test Method for Pulse Velocity through Concrete (ASTM, 2003).

For the seismic laboratory measurements transducers with 63 kHz for the P-wave and 33 kHz for the S-waves were used, together with Sonic Viewer-170, OYO, using a uniaxial pressure of 122 kPa for ensure a good contact in order to get clear waveforms with clear first breaks. First, the sediment sample was put in a plastic bag which holes so that any excessive air or water could flow out, by this avoiding any build-up of pore pressure. The sample as placed between the transducers and from this the sample length was determined. Weight was placed on the top transducers to increase the pressure aiming to get clear signals.

For the measurements gain was set at 10-50, filter at high cut 1 MHz and low cut 30 KHz, and a sampling range of 100-500 ns was used. Before any sample measurement the determination of the zero point was required. Here the transducers were set on each other, a measurement was taken to determine the travel time as zero point (without any sample). Then, the transducers were connected to the samples as illustrated and the P-wave velocity was measured by

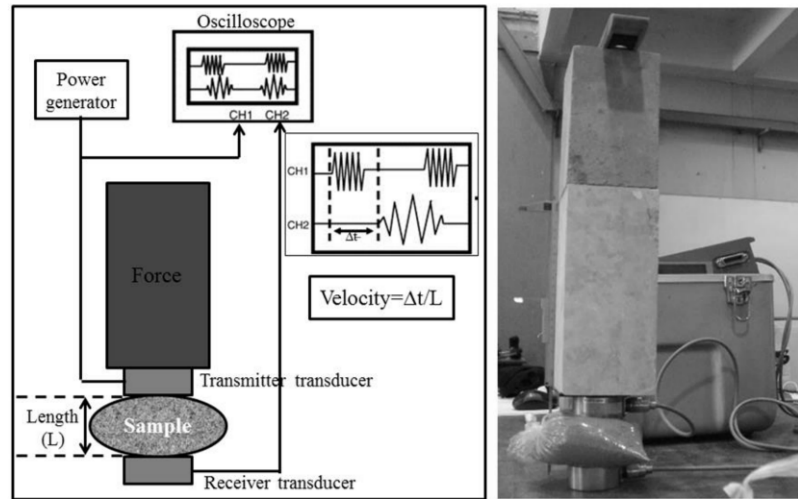


Figure 2. Schematic diagrams of the seismic laboratory measurements (left). Equipment set up in the laboratory (right).

identifying the first break. For VS measurements a similar procedure was carried out. Here the gain was 50-500, the filter a high cut 200 kHz and low cut 500 Hz. The ultrasonic velocity was determined under laboratory conditions with increasing water saturation from 0 to 100% for each sample in six steps. Each time after water was added the sample was compacted again for the measurement.

The wave velocity is calculated by using the time taken by the pulse to travel the measured distance between the transmitter and the receiver. The pulse velocity is given by the formula

$$v = \frac{s}{t} \quad (3)$$

where, v is velocity (km/s), s is length of sample (cm) and t is the travel time (μ s). This method was done at the School of Geotechnology, Institute of Engineering, Suranaree University of Technology, in Nakhon Ratchasima.

3 RESULTS AND DISCUSSIONS

The seismic velocities for the samples with increasing water saturation are shown in Figure 3 for samples from the granite site and in Figure 4 for samples from the sandstone site. For all samples and in compliance with Hook's law the P-wave velocities are in general higher than the S-wave velocities.

The seismic velocities with increasing water saturation for four samples from the granite site are shown in Figure 3a-d. The P-wave velocities at dry conditions are in the range of 500 to 800 m/s whereas the S-wave velocities for the same condition range between 300 and 500 m/s; published data provide similar values (e.g. Schön, 2011). Some data points seem not to reflect the overall trend of the velocities with increasing saturation highlighting the difficulties in the measurements of such samples.

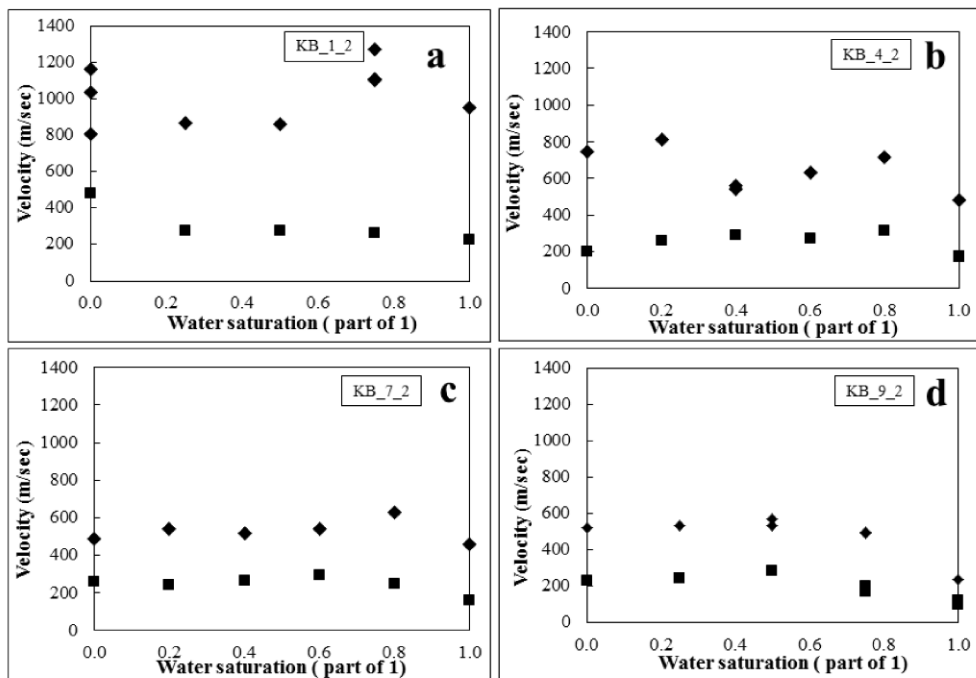


Figure 3. Velocity of granite site, crystal is V_P , square is V_S , (a) sample KB_1_2, (b) sample KB_4_2, (c) sample KB_7_2, and (d) sample KB_9_2.

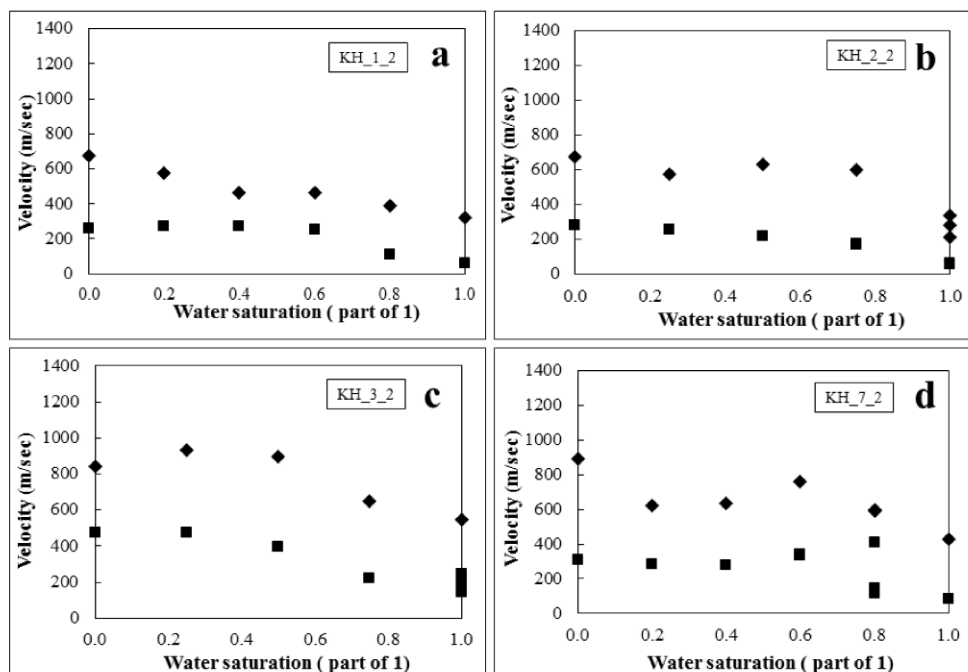


Figure 4. Velocity of sandstone site, crystal is V_P , square is V_S , (a) sample KH_1_2, (b) sample KH_2_2, (c) sample KH_3_2, and (d) sample KH_7_2.

Seismic velocities of unconsolidated sediments with clay

For three samples, KB_1_2, KB_4_2, and KB_7_2, it seems that V_P keeps almost constant before 80% water saturation, then increase at 80%, and then towards 100% water saturation decrease significantly, for sample KB_7_2 for example below the initial value. For sample KB_9_2, the increase is already at around 50% water saturation and after that the decrease is significant. The shear wave velocities mainly decrease with decreasing water saturation, however the gradient of decrease at almost 100% water saturation is for most samples significant larger (see Figure 3b-d).

The seismic velocities with increasing water saturation for four samples from the sandstone site are shown in Figure 4a-d. The P-wave velocities at dry conditions are in the range of 700 to 900 m/s and by this slightly higher. The S-wave velocities for the same condition range between 220 and 500 m/s; also in accordance to published data (e.g. Schön, 2011). Both V_P and V_S decrease with increasing water saturation. For the shear wave velocities the explanation provided above also applies here. However, the gradient of decrease is larger towards a saturation of 100%. For the P-wave velocities the values also decrease significantly towards 100% water saturation, but some samples exhibit an increase before at around 40-50% water saturation (Figure 4b-d).

The behavior of the P-wave velocity correlates with the macroscopic visible change of the sediment with increasing water saturation (not shown). With increasing water saturation first some grains stick together, and at about 80% water saturation almost all grains stick together correlating with increased V_P values. With a further increase in the saturation the sediments exhibit a state closer to liquid behavior which correlates with a sharp drop in the P-wave and S-wave velocities, and values of the Poisson's ratio reaching 0.48.

The decrease of the P- and S-wave velocities with increasing water saturation can be explained by the Biot-Gassmann effect, as the increase in the bulk density due to water replacing air in the pores is larger than the increase in the effective bulk moduli of the overall granular material (Wulff & Burkhardt, 1997). But the large change in the velocity values, especially with higher saturation values can be not fully explained by this.

Crane (2013) shows that for shallow sediments the added effect of the interparticle stress can suppress the Biot-Gassmann effect, which means that the seismic velocities can be higher than predicted; for clayey sediments the seismic velocities still decrease with increasing saturation. Interparticle stress is a combination of soil suction stress the apparent tensile stress at the saturated state of the sediment as a result of cohesive or physiochemical forces (Bishop et al., 1960), which combine van der Waals attractions, electrical double layer repulsion, and chemical cementation effects (Lu & Likos, 2006). In the shallow subsurface interparticle stress can be several orders of magnitude larger than the net overburden stress, which is the overburden pressure minus pore pressure (Ikari & Kopf, 2011). For clayey material this effect is significant to about 100 m depth (Crane, 2013). For this study the stress from the vertical loading in order to enhance the signal has to be taken in account as part of the overburden pressure.

4 CONCLUSION

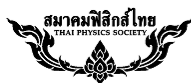
The velocity of clay bearing unconsolidated sediments is a complex phenomenon. Laboratory measurements have shown that the seismic velocities decreases when water saturation increase because of the Biot-Gassmann effect. However, the absolute changes are better explained when taken into account the interparticle stress, and here also the vertical loading. With a water saturation of more than 80% the seismic velocities decrease dramatically as the sediment samples approaching a state closer to liquid behavior.

ACKNOWLEDGEMENT

The authors would like thank the Department of Physics, Faculty of Science, Prince of Songkla University, for financial support and the Suranaree University of Technology for the use of equipment. Permission to publish this paper is gratefully acknowledged.

REFERENCES

- ASTM, 2003. ASTM Test Designation C 597-02, Standard Test Method for Pulse Velocity through Concrete, In Annual Book of ASTM Standards. American Society for Testing and Materials, ASTM International 04.02.
- Bishop, A.W., 1959. The principle of effective stress, *Teknisk Ukeblad* 106: 859–863.
- Crane, J.M. 2013. *Effects of stress and water saturation on seismic velocity and attenuation in near surface sediments*. PhD Thesis, Louisiana State University U.S.A. [Online]. Available: <http://etd.lsu.edu/docs/available/etd-08132013-190600/>
- Fratta, D., Fernández, A.L. & Santamarina, J.C. (2001). Geo-materials: Non-destructive evaluation in geo-system. In Thompson & Chimenti (Eds.), *AIP Conference Proceedings*, American Institute of Physics, pp. 1148–1155.
- Ge, S., Wenlue, S. & Dongquan, Y., 2003. Elastic wave velocity versus saturation and pore fluid distribution relationship, *Chinese Journal of Geophysics* 46: 192–198.
- Ikari, M.J. & Kopf, A.J., 2011. Cohesive strength of clay-rich sediment, *Geophysical Research Letters* 38: L16309.
- Immoor, L., 2006. Permeability, porosity and capillarity [Online]. Available: <http://jroberson.mssd14.wikispaces.net/file/view/Permeability,porosity,capilarity.pdf>
- Schön, J.H., 2011. *Physical Properties of Rocks*. United Kingdom: Oxford.
- Sheriff, R.E & Geldart, L.P., 1995. *Exploration Seismology*. United Kingdom: Press Syndicate of University Cambridge.
- Telford, W.M., Geldart, L.P. & Sheriff, R.E., 1990. *Applied Geophysics*. United Kingdom: Press Syndicate of University Cambridge.
- Wulff, A.M. & Burkhardt, H., 1997. Dependence of seismic wave attenuations and velocities in rock on pore fluid properties, *Physics and Chemistry of the Earth* 22: 69–73.



Electrical resistivity of unconsolidated sediments with clay

S. Suksawat^{1*}, H. Dürast^{1,2}

¹ Department of Physics, Faculty of Science, Prince of Songkla University, HatYai 90112, Thailand

² Geophysics Research Center (GRC), Prince of Songkla University, HatYai 90112, Thailand

The shallow subsurface, a few hundred meters in depth, comprises mainly of unconsolidated sediments, a porous material, with gravel, sand, silt, clay, and rock fragments, and it is the source for groundwater as well as the region of landslide hazards, and the main resource in agriculture, soil. For geophysical investigations of this region electrical methods are the first choices, for example soil moisture content in agriculture or vertical electrical sounding in groundwater exploration. For this study disturbed samples of unconsolidated sediments from different layers from bedrock to the top soil layer were taken from two location of the Khao Khohong mountain range near Hat Yai District, Songkhla Province. The two sample locations comprise different bedrock lithologies, sandstone and granite. The dried samples were characterized as following: main composition (X-ray diffraction), grain size distribution (sieve analysis for sand and hydrometer method for clay and silt content), grain matrix density (water pycnometer), bulk density, porosity, as well as pore structure (scanning electron microscopy). The electrical resistivity was determined under laboratory conditions with increasing water saturation (0–100%) of the sample. In general, the electrical resistivity decreases with increasing water content, with a larger gradient until about 40% saturation and a lower one above. The electrical resistivity of clay bearing sediments is the combination of electrolytic (water) and colloidal (wet clay) conductivity. Therefore, we used the modified Archie equation proposed by Sen et al. (1988) to model the laboratory derived data: $\sigma = S^n \phi^m a^{-1} [\sigma_w + A Q_v / (1 + C Q_v / \sigma_w)]$, with Q_v replaced by $Q^* = Q_v / S$ (for partial saturation; Günzel, 1994) where σ is the sediment conductivity (inverse of the resistivity), σ_w is the water conductivity, ϕ is the porosity, $A = 1.93 \times m$ (mho/m)(l/mol) and $C Q_v = 0.7$ (mho/m), m is the tortuosity factor (usually 2), S is the saturation degree, and n is the saturation index (usually 1.3), and a is constant (usually 1). In order to fit our experimental values for the electrical resistivity, respectively conductivity, with $m = 0.3-3.1$, $n = 1.4-2.2$ for sediments from the granite site, and $m = 1.0-3.9$, $n = 2.5-3.2$ for the sandstone site. The reduction in the tortuosity factor might show that larger grain sizes constrict the pathway of electrical current more than smaller grain size material resulting in higher resistivity values. Additionally, the larger grain size material might also result in a more uneven distribution of the clay content, which contributes significantly to the electrical pathway. The increase in the saturation index is mainly related to the too low resistivity values at lower water saturation values.

Keywords: Unconsolidated sediments, Resistivity, Clay, Water saturation

1. INTRODUCTION

Electrical resistivity method is one of the most used geophysical methods in shallow investigation, for example soil moisture content in agriculture, or as vertical electrical sounding in groundwater exploration. It is based on measuring the electrical potentials between one electrode pair while transmitting a direct current between another electrode pair [1]. Electrical resistivity is a parameter exhibiting a large range of values sensitive to various factors like the nature of material (e.g., gravel, sand, and clay), the water content and its conductivity, porosity, permeability, and the water or fluid saturation. The shallow subsurface is a few hundred meters in depth, comprises mainly of unconsolidated sediments, porous material, solid fragmental material from weathering of rocks, transported and deposited by air, but mainly by water, that form layers on the Earth's surface at normal temperature and pressure

conditions; near surface in unconsolidated form, e.g., sand, gravel, silt, mud, alluvium [2]. Unconsolidated sediment characteristics are composition, grain size, grain shape, grain arrangement, as well as pore size and shape. Important physical properties of unconsolidated sediments are density (bulk and mineral density), porosity, water saturation, and electrical resistivity, but also seismic velocities [3].

1.1 Study area

For this study disturbed samples of unconsolidated sediments from different layers from bedrock to the top soil layer were taken from two location of the Khao Khohong mountain range in Hat Yai District, Songkhla Province. The two sample locations comprise different bedrock lithology, first, mainly granite at a mountain site in different states of weathering and second, mainly sandstone with different layers from bedrock to top soil. From the later site samples have been collected as a profile from the

*Corresponding author.

E-mail: saowapa_suksawat@hotmail.com

top layer to the bottom layer (see Fig. 1). The top layer is top soil (KH_1_2), dark grey soil with roots, the second layer is yellowish brown unconsolidated sediment (KH_2_2), and bottom layer is brown unconsolidated sediment (KH_3_2). Below the last layer is bedrock, here a sand/siltstone (see Fig. 1).

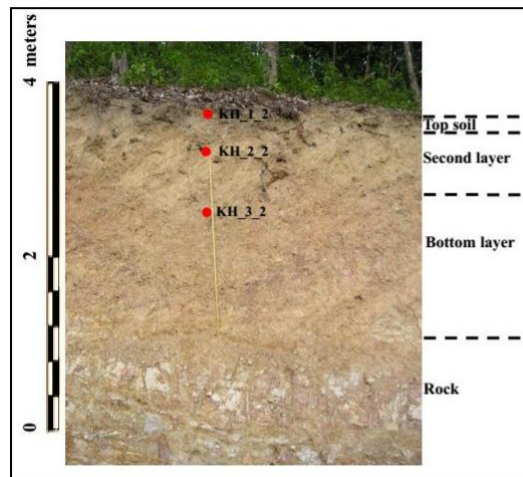


FIGURE 1. Samples of unconsolidated sediments from Khao Khohong Mountain. Bedrock is a sand/siltstone.

1.2 Electrical resistivity

The electrical resistivity (ρ , Ohm-m) of a homogeneous cylindrical solid of length L in meters and with a cross section area A in square meters, having resistance R in ohms between the end faces, is given as, [1]:

$$\rho = \frac{RA}{L} \quad (1)$$

The resistivity of a saturated porous rock can be expressed by Archie's law [1] as below

$$\rho = aS^{-n}\phi^{-m}\rho_w \quad (2)$$

where S is the degree of the water saturation, ϕ is porosity, ρ_w is the resistivity of pore fluid or water (it is temperature dependent), m is the tortuosity factor (m are used like porosity exponent, shape factor, or cementation degree), n is saturation exponent, a is the constant (reflects the influence of mineral grains on current flow) [4]. Eq. 2, or Archie equation, is valid only for clay free (clean) sediments as it describes the electrical resistivity of a sample only by the electrolytic conductivity of the pore filling water, respectively fluid.

However, for the interpretation of resistivity data of clay bearing material the factors saturation, porosity, and clay content were identified as crucial [5]. Clay minerals are hydrated minerals, which exhibit high porosity but quite low permeability values. Although clay minerals themselves are not very conductive, their surfaces can

generate an excess of cations in the pore fluid adjacent to the surfaces of the clay minerals. The result is a high conductivity space near to the clay surfaces, which can dominate the overall conductivity of the sediment even if the conductivity of the pore fluid is quite low. Following model for the conductivity of clay bearing sediments is proposed by [5]:

$$\sigma = S^n \phi^m a^{-1} [\sigma_w + A Q_v / (1 + C Q_v / \sigma_w)] \quad (3)$$

where, σ is Soil/sediment conductivity in S/m ($\sigma = 1/\rho$), S is degree of the water saturation, ϕ is porosity, σ_w is the conductivity of water, m is the tortuosity factor, n is saturation exponent, a is the constant, $A = 1.94 \times m$ in (S/m)/(mol/l) and $C = 0.7/Q_v$ in S/m, Q_v (in mol/l) is the concentration of Na-exchange cations relative to the water saturated pore space, which depends on the cation exchange capacity (C_{ex}) in mol/g and the matrix specific density ρ_m . Q_v replaced by $Q^* = Q_v/S$ (for partial saturation; [6]), with:

$$Q_v = C_{ex} \rho_m \frac{1-\phi}{\phi} \quad (4)$$

The dependence of the exchange capacity C_{ex} on the relative clay and silt content (mineral composition of clay) P_{clay} and P_{silt} is estimated by a relationship proposed by [6]:

$$C_{ex} = 0.47(P_{clay} + 0.2P_{silt}) \quad (5)$$

2. EXPERIMENT

The characterization of the unconsolidated sediments comprised the analyses of the main components, grain size distribution, grain shape, grain arrangement and pore structure (size and shape). The main physical properties of unconsolidated sediments investigated here are density (bulk and mineral density), porosity, water saturation, and electrical resistivity.

Semi-quantitative X-ray diffraction (XRD) analysis was used to identify the main components. Diffracted X-rays are used to measure the dimensions of the various atomic layers in the crystals, and different minerals have a distinct set of atomic layer spacing, which can be used to identify the mineral [7]

For analyzing the grain size distribution of the unconsolidated sediment, the distribution of the coarse particles (gravel and sand) was determined by sieve analysis. Fine particles (silt and clay), less than 0.063 mm in size, were analyzed by the hydrometer method. Grain sizes can occur in a wide range of sizes from micrometer to centimeters, and the assumption is that the particles are roughly circular with the diameter measured [8].

For the sieve analysis, weighed samples are poured into a top sieve which has the largest screen opening. Each lower sieve in the layer has smaller opening, at the base is a pan. The shaker shakes the column, usually for some fixed amount of time. After the shaking is complete the material on each sieve is weighed. The weight of the sample of each sieve is then divided by the total weight to give a percentage retained on each sieve. The hydrometer method

is based on the change of density of a soil and water suspension upon the settling of the soil particles. The hydrometer is gently placed into the cylinder containing the suspension after predetermined periods of time and a reading taken by determining where the meniscus of the suspension strikes the hydrometer.

The density, ρ , is defined as the ratio of its mass m to its volume V . If of a material can be separated into the matrix density (ρ_{Mineral}) that depends on the components (mineral) and the bulk density (ρ_{Bulk}), which depends on the minerals and the porosity.

The mineral density was determined by the pycnometer methods using water. First, the mass of the empty pycnometer was determined, then the sample was put in and the mass was measured. Distilled water was added to fill the pycnometer (with sample), removing entrapped air and weighted. Finally, the pycnometer was filled with distilled water only and weighted again. The density was calculated from the value of the sample mass per water mass and multiplied by the density of water. The bulk density of a sample was obtained by measuring the dimensions of a geometric sample container filled with the sediment and by this getting the volume and weight of the dry sample.

Porosity, ϕ , is a measure of the total void spaces in a material, and is the volume of voids over the total volume, between 0 and 1. The value for total porosity can be calculated from $\phi = 1 - (\text{bulk density} / \text{mineral density})$.

Pore space properties are controlling the fluid distribution in the pore space and are important for the characterization of the pore volume fractions of the fluids (porosity, saturation, bulk volume of fluids) [3]. The pore structure with pore space and pore size was analyzed using scanning electron microscopy (SEM). Samples needed to be made conductive by covering the sample with a thin layer of conductive material, here gold [9].

The electrical resistivity measurements were performed following a classical four-electrode-configuration. Electrical current (I) was injected by two electrodes named and the resulting electrical potential (ΔV) is measured by two other electrodes. This geometrical configuration offered a compromise between two contradictory constrains of a small contact (electrical) resistance that requires a large electrode diameter and the assumption of point electrodes needed for calculating the electrical resistivity (ρ) value. With A is cross sectional area in square meters, s is length in m, V in volt and I in ampere. The electrical resistivity was determined under laboratory conditions at room temperature with increasing (tap) water saturation (0–100%) of the air dried sample. The samples were always compacted by hand as much as possible before each measurement of the electrical resistivity.

3. RESULTS AND DISCUSSIONS

The grain size distributions of three of the unconsolidated sediment samples are shown in Fig. 2, their frequency and cumulative curves based on the logarithmic particle size method. The grain size distribution of the samples show that more than 50% of the unconsolidated sediment fraction exceeded 0.063 mm (gravel and sand). KH_1_2 contained less coarse particles (gravel) than KH_2_2 and KH_3_2 as it is the top soil (KH_1_2) and

because of weathering, erosion and transportation of particles. But KH_1_2 has a higher sand content than the other two samples, whereas KH_3_2 had the highest clay content.

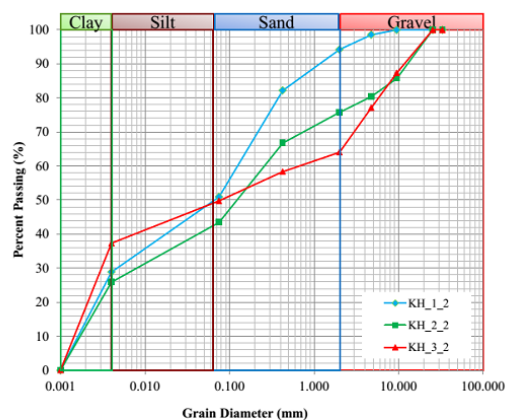


FIGURE 2. Grain size distribution curve for KH_1_2 (top soil), KH_2_2 (second layer), and KH_3_2 (bottom layer)

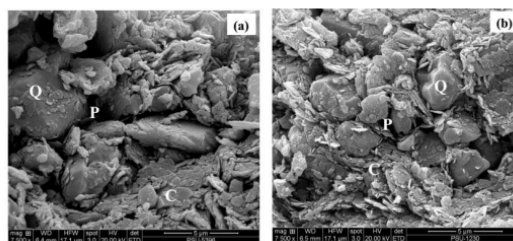


FIGURE 3. SEM microphotographs of unconsolidated sediment samples (a) KH_1_2, top soil, (b) KH_6_2, second layer (parallel sample to KH_2_2). P: pore, Q: quartz grain, C: clay mineral.

The main minerals of the unconsolidated sediments are quartz and clay minerals (illite and kaolinite) based on the XRD results. SEM microphotographs of the samples showed differences in micro texture and morphology due to the mineral content and grain size distribution. Mineral constituents identified under SEM are clay and quartz, consistent with the XRD results. Fig. 3(a) shows SEM microphotographs of KH_1_2 with pores and grains, which have a sub-rounded to angular grain shape, and show a fine to coarse grain size. Fig. 3(b) shows SEM microphotographs of sample KH_6_2 after 100% water saturation and subsequent drying under air. Smaller pores are seen than in the SEM microphotographs of KH_1_2 because the grains are arranged closer together than before due to the saturation.

Result from the resistivity measurements versus increasing water saturation are shown in Fig. 4 for the three samples, KH_1_2, KH_2_2, and KH_3_2 in semi-log graph. In general, the electrical resistivity decreases when the water content increases which is in accordance with the theory, see Eq. 2 and 3. It can be seen that for a water

content of 0-40% there is a larger gradient for the decrease of the electrical resistivity.

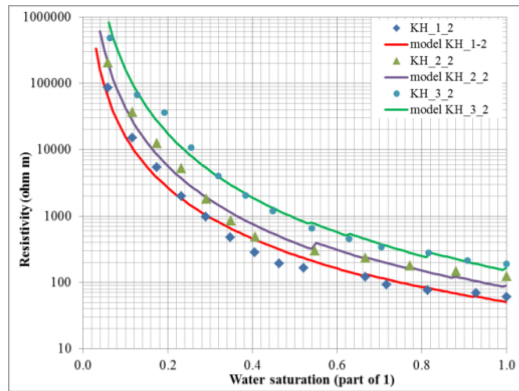


FIGURE 4. Relationship between the degree of water saturation and the electrical resistivity for different sample

Measured resistivity decreases logarithmically with increasing water saturation. The shape of the curve for all three samples is similar, but the absolute values are different, with the resistivity values showing following order: KH_3_2 > KH_2_2 > KH_1_2 (Fig. 4).

The shape of the resistivity curve can be attributed to a combination of electrolytic conductivity of the pore fluid and colloidal conductivity processes related to the clay content. In sediments with clay content, the electrical charges located at the surface of the clay texture lead to less electrical resistivity than in coarse-textured soils because of the magnitude of the specific surface [10]. A large specific surface area supports the surface conductivity because a number of cations in clay minerals are higher valence; electrical charge of the clay mineral surface is negative. It is compensated by the concentration of cations in the pore water in the mineral surface. This process is the cation exchange capacity (CEC). The calculation of the resistivity of clayey material is not trivial, since the electrical current flow is possible through clay minerals as well as through pore fluid [4]. However, for the three samples here the clay content is relatively similar, which might not explain the differences in the absolute resistivity values.

However, the three samples in Fig. 4 show significant difference in the gravel and sand grain size distribution. Sample KH_3_2 has a gravel content of 36% and a sand content of 15%, sample KH_2_2 has 24% and 36%, and sample KH_1_2 has 6% and 47%, respectively. A higher resistivity correlates with a higher content in gravel and vice versa. The larger gravel grains might obstruct the electrical pathway more than the sand grains and might also have an effect on the clay distribution in the sample (see Fig. 5). This would explain that the differences are more or less independent from the saturation degree.

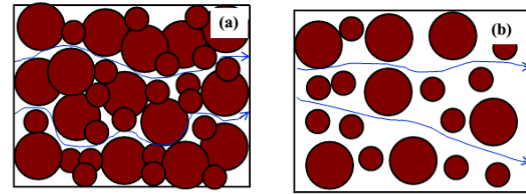


FIGURE 5. Relationship between the grain size and electrical current. a) higher content of larger grain size, b) lower content of larger grains size, white area represent smaller grain sizes.

In Fig. 4 the lines represent the calculations of the electrical resistivity using Eq. 3, using average parameters from the laboratory measurements: clay content (percent of clay and silt), porosity, matrix density, and conductivity of the water used. In order to fit a curve with the experimental values from the electrical resistivity measurements, the values m , n , and a in Eq. 3 were changed; it was tried not to change a significantly. When m was increased, the curve changed to higher resistivity values at higher degrees of saturation and the curve changed to much higher resistivity values at lower degrees of saturation when n was increased. For the three samples shown in Fig. 4 following order for the values m and n were obtained: KH_3_2 > KH_2_2 > KH_1_2. The tortuosity factor m increases with depth and with increasing larger grain size, making it more difficult for the electrical current to find a pathway, thus resulting in a higher resistivity. The increase in n value with depth might reflect the distribution of the pores associated with a larger portion of larger grains.

A summary of all m , n , and a values for nine samples from KH location and seven samples from KB location give following values: $m=0.3-3.1$, $n=1.4-2.2$, $a = 0.8-1.0$ for sediments from the granite site (KB), and $m=1.0-3.9$, $n=2.5-3.2$, $a=1.0-1.1$ for the sandstone site (KH) as shown in Fig. 6. Values of m for KB and KH are overlapping, whereas values of n for KB are less than for KH, illustrating that these values change with sediment type, in general, and that one set of these values cannot be applied to all sediments types.

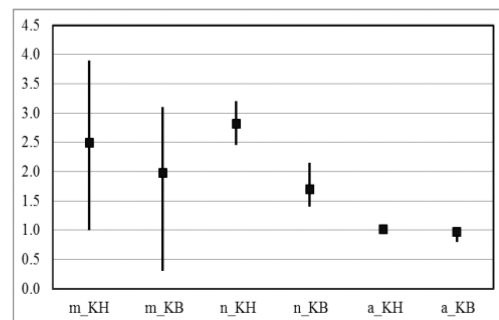


FIGURE 6. Comparison of m , tortuosity factor, n , saturation exponent, and a , a constant, of KH (9 samples) and KB (7 samples) location. Line reflects the range of all values, symbols represent the average value for each factor.

S. Suksawat, H. Dürrast

4. CONCLUSION

The electrical resistivity of clay bearing unconsolidated sediments is a complex phenomenon. Laboratory measurements have shown that the electrical resistivity decreases when the water content increases because of a combined effect from the electrolytic conductivity of the pore fluid and the colloidal conductivity from the clay mineral, and that the data follow current theory. However, the fitting parameter, m , n , and a , vary with different sediment type. With limited data the difference are clear. Further, the results of this study suggest that the grain size distribution has a significant effect on the absolute resistivity, independent from the water saturation.

ACKNOWLEDGMENTS

The authors would like thank the Department of Physics, Faculty of Science, Prince of Songkla University, for financial support and H. Schmidt, Christian-Albrechts-Universität, Kiel, Germany, supported by DAAD RISE, for her contribution to the measurements.

1. Telford, W.M., Geldart, L.P. and Sheriff, R.E., Applied Geophysics, Cambridge University Press, UK, 1998
2. Telford, W.M., Geldart, L.P. and Sheriff, R.E., Applied Geophysics, Cambridge University Press, UK, 1998

3. Telford, W.M., Geldart, L.P. and Sheriff, R.E., Applied Geophysics, Cambridge University Press, UK, 1998
4. Immoor, L., Permeability, porosity and capillarity, URL: http://jroberson.mssd14.wikispaces.net/file/view/Permeability_porosity_capillarity.pdf (March 22, 2014), 2006
5. Schön, J. H., Physical Properties of Rocks, Oxford, United Kingdom, 2011
6. Kirsch, R., Groundwater Geophysics – a Tool for Hydrogeology, Springer-Verlag Berlin Heidelberg, Germany, 2006
7. Sen, P.N., Goode, P.A. and Sibbit, A., Electrical conduction in clay bearing sandstones at low and high salinities, Journal of Applied Physics, Vol. 63, pp. 4832, 1988
8. Günzel, F., Geoelektrische Untersuchung von Grundwasserkontaminationen unter Berücksichtigung von Ton- und Wassergehalt auf die elektrische Leitfähigkeit des Untergrundes, PhD thesis Ludwig-Maximilians-Universität, München, Germany, 1994
9. Lewis, D.W. and McConchie, D., Analytical sedimentology, Chapman & Hall, New York, 1994
10. Wentworth, C. K., A scale of grade and class terms for clastic sediments, The Journal of Geology, Vol. 30, pp. 377, 1922
11. Schweitzer, J., Scanning Electron Microscope, <http://www.purdue.edu/rem/rs/sem.html> (March 22, 2014), 2010
12. Samouëlian, A., Cousin, I., Tabbagh, A., Bruand, A. and Richard, G., Electrical resistivity survey in soil science: a review, Soil & Tillage Research, Vol. 83, pp. 173, 2005

VITAE

Name Miss Saowapa Suksawat
Student ID 5510220162

Education

Degree	Name of Institution	Year of Graduation
B.Sc. in Geotechnology	Khon Kaen University	2012

List of Publication and Proceedings

Suksawat, S. and Dürrast, H. (2015). Seismic velocities of unconsolidated sediments with clay. Proceedings of the Fifth Thailand Symposium on Rock Mechanics, 22-23 Jan 2015, Nakhon Ratchasima, Thailand, 81-87.

Suksawat, S. and Dürrast, H. (2014). Electrical resistivity of unconsolidated sediments with clay. Thai Journal of Physics, Series 10, Art. No. 23001.